UNIVERSITY OF LEEDS

The Role of Wind Shear in Organised Deep Moist Convection in the West African Monsoon

by

Megan Bickle

Submitted in accordance with the requirements for the degree of
Doctor of Philosophy

The University of Leeds

Centre for Doctoral Training in Fluid Dynamics

May 2021

Intellectual Property

The candidate confirms that the work submitted is her own, except where work which has formed part of jointly authored publications has been included. The contribution of the candidate and the other authors to this work has been explicitly indicated below. The candidate confirms that appropriate credit has been given within the thesis where reference has been made to work of others.
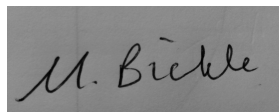
Research from the publication Bickle et al., 2021, *Understanding mechanisms for trends in Sahelian squall lines: Roles of thermodynamics and shear., Quarterly Journal of the Royal Meteorological Society*, 147(1), p983-1006, doi: https://doi.org/10.1002/qj.3955, jointly authored with John H. Marsham, Andrew N. Ross, David P. Rowell, Douglas J. Parker, Christopher M. Taylor, has been included in this thesis. The candidate performed all data analysis and produced all figures. Marsham, Ross, Rowell, Parker and Taylor contributed to method refinement and interpretation of results. Rowell extracted and provided Coupled Model Intercomparison Project 5 (CMIP5) data.

Research from the publication Bickle et al., 2021, *The Influence of the Diurnal Cycle in Wind Shear and Thermodynamics on Squall Lines in the West African Monsoon., Journal of the Atmospheric Sciences*, In Review, jointly authored with John H. Marsham, Andrew N. Ross, Stephen D. Griffiths, Julia Crook, has been included in this thesis. The candidate performed all data analysis and produced all figures bar analysis by Crook of observational data used in Crook et al. (2019). Marsham, Ross, Griffiths and Crook contributed to method refinement and interpretation of results.

This copy has been supplied on the understanding that it is copyright material and that no quotation from the thesis may be published without proper acknowledgement.

© 2021 The University of Leeds and Megan Elizabeth Bickle.

Signature:

Acknowledgements

Abstract

The West African Monsoon is characterised by mesoscale convective systems (MCSs) and a strong diurnal cycle in convection and wind shear. However, weather models struggle to provide skilful rainfall forecasts for the region, and climate projections are uncertain. Observational studies have linked recent decadal increases in extreme rainfall to stronger wind shear but this has not been reproduced in numerical models. Indeed, while wind shear is accepted to support organised convection, the underlying mechanisms are an active area of research. This thesis investigates the role of shear in diurnal and decadal trends in MCSs including examining the underlying mechanisms and theory.

The impact of environmental changes are investigated using an idealised model which allows thermodynamic effects to be isolated from those of shear. Greater shear led to increased MCS intensity and rainfall, but the effects of the thermodynamic changes dominated on both diurnal and decadal time scales. Our results explain the observed diurnal cycle, with the evening and night most favourable for MCSs, and are consistent with the decadal trend of increasing shear having enhanced storm severity.

A layer-lifting model correlated well with bulk ascent and rainfall rates of simulated MCSs. However, differences in microphysics and storm organisation are not accounted for and this is particularly clear when the thermodynamic profile is varied. Passive tracers reveal that inflowing air either descends in layers or is transported upward. Shear is shown to reduce entrainment dilution, but the effect is not captured well at coarse grid-spacings of $4\,\mathrm{km}$.

This thesis begins to reconcile different theories for the role of wind shear in organised convection where system-relative inflows explain bulk properties while the cold pool to shear balance indicates storm organisation. Thus, to correctly capture MCSs in global weather and climate models, they must include the diverse impacts of shear across scales.

Contents

List of Figures

12

List of Tables

14

Abreviations

AEJ African easterly jet

AEW African eaterly wave

AMMA African Monsoon Multidisciplinary Analysis

BL boundary layer

CAPE convective available potential energy

CFL Courant-Fredrichs-Lewy

CIN convective inhibition

CM1 Cloud Model 1

CMIP5 Coupled Model Intercomparison Project 5

CP4A convection permitting, 4.5km resolution modelling over Africa

DACCIWA Dynamics-Aerosol-Chemistry-Cloud Interactions in West Africa

ECMWF European Centre for Medium Weather Forecasting

EL equilibrium level

ERA ECMWF Re-Analysis

ICAPE integrated convective available potential energy

ITCZ inter-tropical convergence zone

ITD inter-tropical discontinuity

K-W Klemp-Wilhelmson

LCL lifting condensation level

LES large-eddy simulation

LFC level of free convection

LLJ low-level jet

LLMC layer-lifting model of convection

MCS mesoscale convective system

MERRA-2 Modern-Era Retrospective analysis for Research and Applications, Version 2

MIT Massachusetts Institute of Technology

NWP numerical weather prediction

PBL planetary boundary layer

PS propagation speed

RCP8.5 Representation Concentration Pathways Scenario 8.5

SAL Saharan air layer

SHL Saharan heat low

TKE turbulent kinetic energy

TRMM Tropical Rainfall Measuring Mission

WAM West African monsoon

Chapter 1

Introduction

1.1 Motivation

The Sahel, a semiarid region of western and north-central Africa, has one of the largest and fastest-growing populations on the continent. Subsistence farming is common across the region, the success of which relies heavily on the West African monsoon (WAM) which brings seasonal rains during the northern hemisphere summer. The monsoon is dominated by large, organised thunderstorms called mesoscale convective systems (MCSs), which contribute around 90% of the annual rainfall in the Sahel (Mathon et al. 2002b). Any annual variations in the number or severity of MCSs can cause critical differences in rainfall across the region.

MCSs, which regularly produce flooding, strong winds and lightning across the Sahel region, are frequent, extremely destructive and poorly forecast. Loss of life is common and can occur in frequent but less extreme events (Bevere et al. 2018) as well as in more extreme events such as the 2012 flood disaster in Nigeria in which 400 people lost their lives and over 1 million were displaced (World Health Organisation 2012). Additionally, as agricultural livelihoods become more precarious, urbanisation will likely cause a further expansion in informal settlements which are vulnerable to flash floods (Serdeczny et al. 2017). Recent increases in the frequency and intensity of extreme weather events have caused a 52% increase in economic damage due to hydro-met hazards across Africa in the decade 2009-2019 compared to 1970-2009 (Cullmann et al. 2019). This trend in extreme weather is predicted to continue with climate change (Vizy and Cook 2012).

Despite the drastic improvements in global numerical weather prediction (NWP) over the last fifty years (Bauer et al. 2015), NWP remains poor over northern Africa with

weather models often struggling to provide any real skill for rainfall forecasts, even for lead times of less than a day (Vogel et al. 2018). A patchy observational network hampers successful forecasting (Kniffka et al. 2020), but even during the 2006 African Monsoon Multidisciplinary Analysis (AMMA) campaign (Parker et al. 2008) (when models were initiated with a larger and more consistent set of observations), the gain in skill was lost after 24 hours of forecast time (Agustí-Panareda et al. 2010). Fink et al. (2011) suggest this is due to the models' inability to predict the genesis and evolution of convective systems. A recent evaluation of forecast products, which was run as part of the 2016 Dynamics-Aerosol-Chemistry-Cloud Interactions in West Africa (DACCIWA) field-campaign project, concluded that differences between the characteristics of the forecasts on days 1 and 2 are relatively small and hardly systematic, suggesting that forecasts respond quickly to errors in initialisation data and model physics (Kniffka et al. 2020). Vogel et al. (2018) found that there is little to no skill in precipitation forecasts from ten global NWP prediction systems over northern tropical Africa. For instance, not only do models often fail to accurately capture heavy rainfall events but they predict such events when no precipitation is observed (Haiden et al. 2012). These regular inaccuracies have resulted in a lack of public trust in short-range weather forecasts and have restricted the ability of national meteorological services to issue effective warnings.

The conditions which favour the growth of isolated cases of convection into organised MCSs include a favourable thermodynamic profile (i.e. a warmer and moister boundary layer) and vertical wind shear (Nicholls and Mohr 2010; Vogel et al. 2018). Despite the general consensus that environmental wind-shear plays a crucial role in supporting organised deep moist convection, there is of yet no full understanding of the underlying mechanisms of this process. Much of the study in this area has been based around a type of MCS called squall lines; long lines of organised convection that can last for days. It remains debated whether wind shear controls squall lines through its dynamic effect on the spread of the cold pool (Thorpe et al. 1982; Rotunno et al. 1988; Weisman and Rotunno 2004) or regulating the thermodynamic inflow of convectively unstable air and water vapour (Alfaro 2017).

In global weather and climate models, convection is parametrised as the processes involved occur on scales which are small relative to the grid size. However, although successful in the baroclinic extratropics, the small-scale processes involved in the triggering and growth of convective systems mean that NWP models often struggle to capture rainfall in the absence of a strong large-scale forcing, as is often the case in the tropics. For the Sahel, the poor representation of rainfall is in part due to how the parametrisation of convection represents MCSs, even though large MCSs occupy

many grid-cells. Parametrisation schemes also exclude the effects of shear on the convective systems. Parametrised models fail to accurately capture the intensity, size and propagation direction of West African squall lines (Crook et al. 2019). This results in parametrised NWP models performing poorly for climate, where extremes are underestimated, as well as failing to accurately capture the diurnal cycle. Taylor et al. (2017) used satellite data to show that the frequency of extreme Sahelian storms has tripled since 1982, with shear playing an important role in this increase. Shear is therefore expected to be key in future climate changes. A poor depiction of the diurnal cycle has upscale impacts including on mid-latitude weather forecasts (Marsham et al. 2013; Garcia-Carreras et al. 2013). Additionally, MCSs in the Sahel can trigger, and be triggered by, African easterly waves (AEWs) which are important for hurricane development over the tropical Atlantic (Russell et al. 2017).

To summarise, there is currently an incomplete understanding of how shear impacts the evolution and characteristics of severe MCSs that dominate the WAM. Additionally, the implications of variations in wind shear across different time scales (e.g. diurnal or decadal) are still unclear. In this thesis, an idealised model setup will be used to run high resolution simulations in which the initial environment can be altered. This setup provides an opportunity to test recent theories for the role of shear in extreme weather events in the WAM.

1.2 Idealised Simulations

The motivation behind this research includes gaining a more complete understanding of the complex part wind shear plays in the organisation of MCSs. Explicitly modelling convection in an idealised scenario provides an opportunity to isolate specific physical processes in order to test conceptual and mathematical theories. The results of which can be compared to observational studies.

In this thesis, large-eddy simulations are initiated with vertical profiles representative of the Sahel and line thermals are used to trigger mesoscale convective lines (or squall lines). Through applying different changes to the initial profile, it is possible to study how changes in 1) the Wind Profile, 2) the Thermodynamic Profile and 3) the Wind and Thermodynamic Profiles combined, impact mature squall lines. The changes applied include those representative of a diurnal cycle which are calculated from radiosonde data captured over the 2006 monsoon period as part of the AMMA campaign as well as recent and predicted decadal trends extracted from ECMWF Re-Analysis (ERA)-Interim and Coupled Model Intercomparison Project 5 (CMIP5) data. This provides

an opportunity to study the underlying mechanisms of what controls the intensity of squall lines as well as test existing theories on how wind shear impacts squall lines.

Additionally, simulations with varied resolution are also completed. These include passive tracers which are used to investigate how inflowing layers of air behave when flowing into the convective region and how this changes with different initial profiles of shear and resolution. It provided an opportunity to study the make up of the convective updrafts, the anvil cloud and the cold pool.

1.3 Research Topics

The focus of this work is on the most common type of squall line: lines of convective cells that continually grow and decay. Additionally, only mature systems are studied and initiation is not considered.

Alfaro (2017) describes a need for further investigation into the full spectrum of environments in which squall lines manifest, including variations in the environmental temperature profile, more diverse kinematic settings and tropical environments. Recent work has found promising results with the model outlined by Alfaro (2017) but in idealised settings (Mulholland et al. 2021). A large proportion of the literature which considers squall lines has been based on squall lines characteristics over the USA (Bryan and Fritsch 2000; Parker and Johnson 2004; Schumacher and Johnson 2005; Feng et al. 2018). In this thesis, we use idealised simulations of West African squall lines to bridge the gap between observations and theory and to shed some light on the fundamental processes that occur in this complex region. This also provides an opportunity to test the theory of Alfaro (2017) in a less idealised set-up.

Climate change is expected to increase extreme rainfall, but just by how much is still uncertain; a warmer climate allows greater concentration of water vapour in the atmosphere, allowing heavier rainfall, but this can be enhanced by changes in the storms themselves, which are much more complex and uncertain. Past observational studies implicate decadal trends in Sahelian temperature and its impact on vertical wind shear in the recent intensification of MCSs in the Sahel (Taylor et al. 2017) but previous modelling has not captured this (Fitzpatrick et al. 2020; Senior et al. 2021) and several theories exist for the role shear plays in deep moist convection. In particular, different theoretical models disagree over whether shear plays a dynamical role through balancing the cold pool or a thermodynamic one through modulating the system relative inflow of convective instability and moisture. In Chapter 4, through initiating simula-

tions with representative profiles from observations modified by changes derived from long-term trends in reanalyses or future climate projections, we isolate and examine how changes to the environmental wind or thermodynamic profile can affect the intensity of convection. Additionally, we investigate whether the system-relative inflow of convective instability and water vapour is key to determining squall line updraft speeds and rainfall. Finally, future increases in shear, temperature and humidity are simulated to test whether they could cause increases in storm intensity.

There is a clear diurnal cycle to the WAM including within MCSs which trigger in the evening and persist overnight, with an overall Sahel rainfall minimum in the late morning. Past studies have shown that the nocturnal low-level jet (LLJ) brings cool, moist air into the continent and produces vertical wind shear with the mid-level African Easterly Jet (Thorncroft and Blackburn 1999; Parker et al. 2005b). In Chapter 5, idealised simulations are used to test whether the LLJ supports storms by providing vertical wind shear and a low-level inflow of moisture to the storms that move towards it. Through initialising simulations with environmental profiles representative of different times of day, the effect of the diurnal cycle in temperature and humidity compared with wind shear on mature squall lines is explored. Additionally, the relative inflow of convectively unstable air and moisture and the ratio of cold pool strength to wind shear are quantified to provide insight into whether either theory holds and can be used to predict squall line intensity.

Finally, in Chapter 6, simulations with multiple layers of passive tracers are analysed to better understand how inflowing air from different heights travels through the convective region. This allows a diagnosis of the make-up of the convective cores of the updrafts and the resultant anvil cloud as well as what constitutes the downdrafts and cold pools. The simulations are repeated with different horizontal resolutions to explore whether this has any impact on the flow through the storm. Additionally, through only varying the wind profile, it is possible to investigate how the impact of shear on convective systems changes with resolution. Recent studies using a 4 km resolution climate model over Africa have found rainfall to have little sensitivity to shear which is at odds with observations (Senior et al. 2021). This study tests whether this result is a product of resolution or holds in general.

The structure of this thesis is as follows. Chapter 2 contains background information and a detailed review of the key concepts that have been used and built upon in this study. Chapter 3 describes Cloud Model 1, the idealised model used in this study, and its set-up while also outlining how a representative WAM pre-storm profile was obtained. In Chapter 4, recent and future predicted changes in the thermodynamics and environmental winds of the Sahel and their impact upon squall lines are explored.

Chapter 5 considers the diurnal cycle of the WAM and how it impacts upon the diurnal cycle observed in squall lines. The final results chapter, Chapter 6, analyses the transport of passive tracers through a simulated MCS and then compares how that changes with resolution and shear. A summary of this thesis and its conclusions are discussed in Chapter 7, including a section which outlines future possibilities for research which this study has uncovered.

Chapter 2

Review of Key Concepts

This chapter provides a review of the relevant literature and an overview of key processes that are necessary for the rest of the thesis. The thermodynamics and dynamics of convection are discussed in Section 2.1 including a summary of the different types of atmospheric instability and an introduction to variables that can be used to indicate convective instability. In Section 2.2, the existing literature on organised convective systems and how they organise, particularly with regard to wind shear, is reviewed. The West Africa Monsoon and its key features are described in Section 2.3. Finally, a summary of the results of explicit and parametrised convection in atmospheric models as well as resolution requirements is provided in Section 2.4.

2.1   Convection

Convection is the vertical motion which occurs due to buoyant parcels of air. If air rises in a thermodynamically unstable environment then buoyancy will result in continued upward movement i.e. convection. The atmosphere is composed of a varying quantity of several gases: water vapour can fluctuate between 0 and 4% and in doing so often has a profound impact on the behaviour of the air it constitutes. This is particularly the case when it condenses or freezes to release latent heat, or evaporates/melts/sublimates and in doing so cools the surrounding environment. This potential release or absorption of latent heat means that differences in moisture content between air masses can create and magnify instabilities within the atmosphere and so instigate or accelerate convective motion. The role of latent heating in moist convection is to enable rising air to reach far higher altitudes in the atmosphere than otherwise, producing cumulonimbus clouds which can extend through the depth of the troposphere.

2.1.1 Dry Convection

It is first worth considering the simpler situation of dry convection, where the air remains unsaturated despite vertical movement. A property of state which is useful to define is the virtual temperature (American Meteorological Society 2021a),

$$T_v \equiv T \frac{(1 + q_v/\epsilon)}{1 + q_v},\tag{2.1}$$

where T is temperature, $\epsilon = R_a/R_v$ is the ratio of the gas constant of dry air to that of water vapour, and $q_v = \rho_v/\rho_a$ is the water vapour mixing ratio where ρ_v and ρ_a are the mass of vapour and dry air per unit volume respectively. T_v allows the use of the dry-air equation of state for moist air, e.g. $p = \rho_m R_a T_v$ where $\rho_m = \rho_a + \rho_v$ is the density of the moist air. From this it becomes apparent that T_v is the temperature that dry air would have if its pressure and density were equal to those of a parcel of moist air (American Meteorological Society 2021a; Cotton et al. 2010).

As air moves through the atmosphere both its temperature and pressure will vary. Such occurrences can be idealised to be considered isentropic (reversible and adiabatic). It is therefore useful to define a thermodynamic coordinate: potential temperature, θ, in terms of temperature, T, and pressure, p,

$$\theta \equiv T \left(\frac{p_0}{p} \right)^{R_a/c_p},\tag{2.2}$$

where p_0 is defined as a specified reference pressure and c_p is the specific heat of dry air at constant pressure (Stevens 2005). θ is the potential temperature. It is the temperature the system would have if the air was isentropically moved to the reference pressure, p_0, and consequently it does not vary with pressure under isentropic displacements. The virtual potential temperature is defined as $\theta_v = \theta(1 + 0.61q_v - q_l)$ where q_l is the liquid water mixing ratio. The atmosphere is stable to unsaturated vertical motion if the potential temperature of the atmosphere increases with height, $\frac{\partial \theta}{\partial z} > 0$. Dry convection is generally limited to a thin boundary-layer, normally around $1\,\mathrm{km}$, in the daytime but reaching $5\,\mathrm{km}$ or more in the Sahara in summer (Garcia-Carreras et al. 2015).

2.1.2 Moist Convection

In dry convection, moisture content simply results in a higher buoyancy than dry air at the same temperature and pressure and it is possible to define neutral stability based on only potential temperature (Bryan and Fritsch 2002). In reality, the presence of moisture and its effects have a greater impact on atmospheric motion and the development of thermodynamics for moist air. Such impacts include changes to the partial pressures of the working fluid (gas constant, specific heats) as the composition of the fluid varies and, as was described at the start of this section, phase changes which result in the release or absorption of latent heat (Stevens 2005). It is therefore necessary to have some measure of the water within a control volume such as the total water mixing ratio (defined as the mass fraction of H_2O in the system),

$$q_t = q_v + q_l + q_i = \frac{\rho_v + \rho_l + \rho_i}{\rho_a},$$

(2.3)

where $\rho_\chi(\chi = v, l, i, a)$ represents the density of water vapour, liquid water, solid water and dry air respectively and those subscripts hold for the mixing ratio also. Similarly to the dry system, rather than temperature, it is useful to define thermodynamic coordinates which are invariant following reversible rearrangements of fluid parcels (Stevens 2005). In this project a moist generalisation of θ is used where the reference state is specified as $p = p_0$ where all water is liquid. The potential temperature obtained by isentropically moving to this reference state is the wet equivalent potential temperature (Bryan and Fritsch 2002),

$$\theta_e = T \left(\frac{p_a}{p_0} \right)^{-R_a/(c_p + c_{pl}q_t)} \exp \left[\frac{L_v q_v}{(c_p + c_{pl}q_t)T} \right],$$

(2.4)

where p_a is the partial pressure of dry air, q_t the total water mixing ratio and L_v the latent heat of vaporization. While c_{pl} is the specific heat of liquid water. This measure of temperature allows for the effects of latent heating as a parcel of air moves up and down in the atmosphere, as θ_e is conserved in reversible moist adiabatic processes. Since θ_e is insensitive to changes in the amount of condensate present it is suitable for the study of precipitating moist convection. Figure 2.1 shows vertical profiles of the potential temperature and the equivalent potential temperature (θ_e) typical of a tropical environment. θ can be seen to increase with height throughout the troposphere while initially θ_e decreases as the exponential component of Equation 2.4 which includes the mixing ratio of water vapour dominates. θ_e then begins to increase in line with θ.
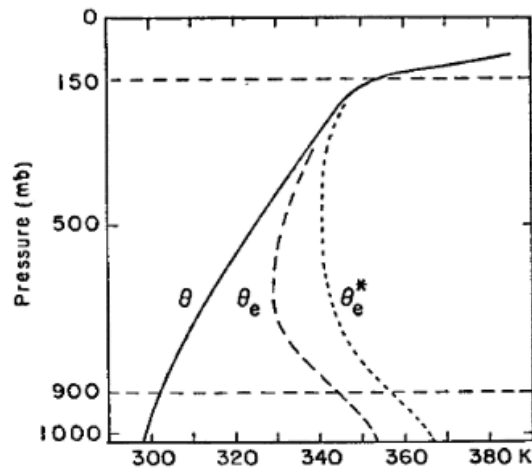
Figure 2.1: From Ooyama (1969), showing a typical stratification of the tropical atmosphere based on summer mean data over the the West Indies. Profiles of the potential temperature θ, the equivalent potential temperature θ_e and the saturated equivalent potential temperature $\theta_{es} = \theta_e^*$.

If q_v is replaced in Equation 2.4 with the saturation value of the water vapour mixing ratio, q_{sat}, this describes the atmosphere if it were saturated at the same temperature. This potential temperature, known as the saturated equivalent potential temperature θ_{es}, represents the theoretical maximum of θ_e (see Figure 2.1). If a parcel of air from the boundary layer is lifted pseudo-adiabatically (with no mixing) its θ_e path would be a vertical line upwards, after it intersects the θ_{es} curve the parcel will be more buoyant than its surroundings.

2.1.3 Describing Atmospheric Profiles and Convective Instabilities

To both understand and predict atmospheric motion, and convection in particular, it is useful to consider the vertical movement of a parcel of air. This conceptual model or 'parcel theory' neglects the pressure force and the small-scale mixing with the environment but is based on the theory that if a parcel rises it will experience decreased atmospheric pressure and so will expand and cool, with increasing pressure and warming and contraction if it falls, in accordance with the First Law of Thermodynamics. The decrease in temperature a parcel of air will experience while moving upward through the atmosphere is called the lapse rate of temperature. If the air is unsaturated and the movement is adiabatic this change of heat occurs at the dry-adiabatic lapse rate at constant θ and conserving θ_e (see Figure 2.2). If the parcel becomes saturated, latent heat will be absorbed by the parcel upon condensation. Once this occurs its temperature will change at the moist-adiabatic lapse rate, conserving θ_e. The point at which

condensation starts to occur is called the lifting condensation level (LCL).
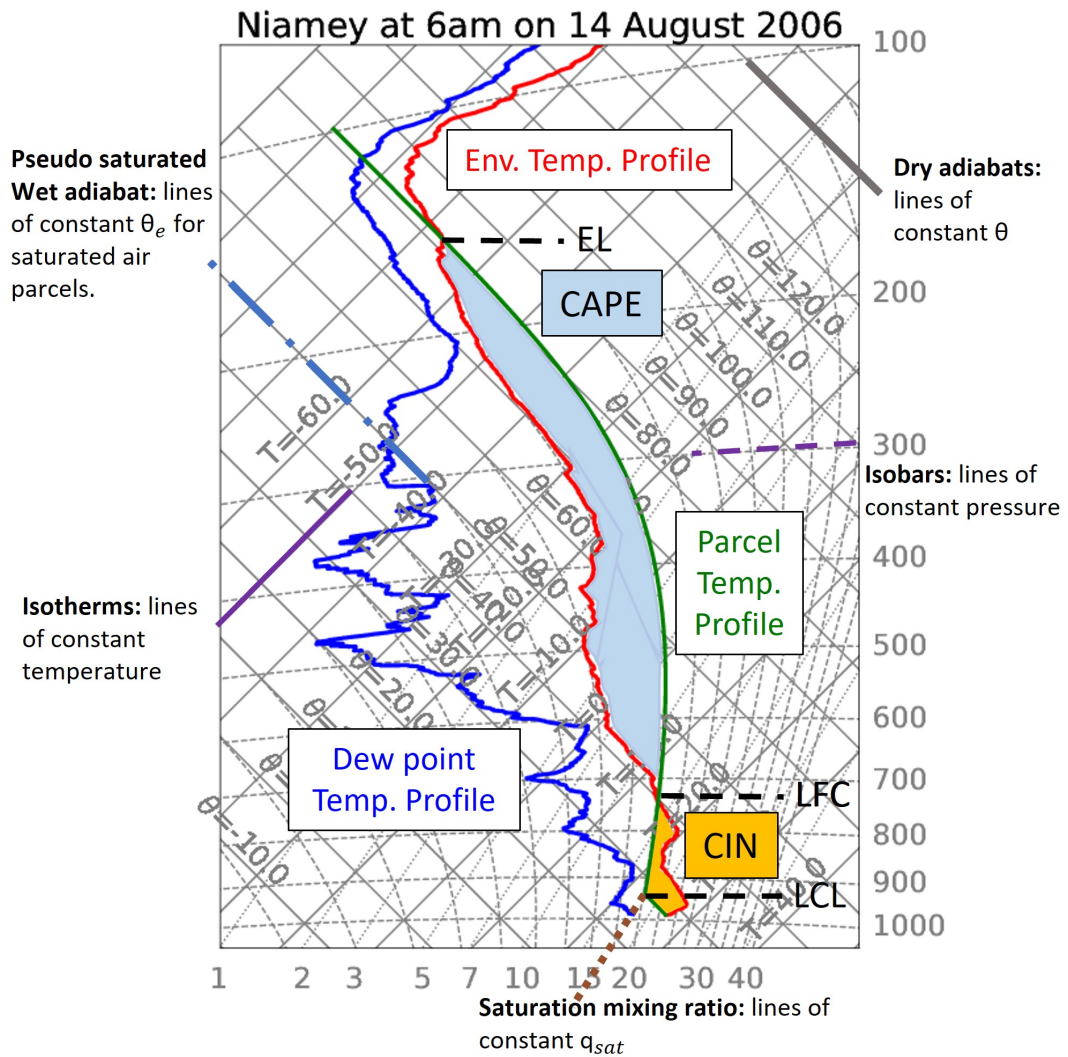
Figure 2.2: Radiosonde data from Niamey on 14th August 2006 at 0600 UTC plotted onto a tephigram. The red line represents the temperature of the environment and the green the temperature of a rising parcel of air from the surface under adiabatic ascent. The blue is the dew point temperature of the environment (the temperature a parcel of air would have to be cooled to, at constant pressure, to start condensing). On the tephigram the units are hPa for the y-axis, gkg^{-1} for the x-axis and °C for all temperatures shown.

An air parcel lifted from the surface may initially be cooler than the surrounding air and so will be denser than its environment and sink. However, if some mechanism forces the air to continue to rise to a height where it condenses and becomes warmer than the air around it then it will enter an unstable environment. This transition height is referred to as the level of free convection (LFC) (Figure 2.2). Once a parcel reaches

this height it will continue to rise until it becomes neutrally buoyant at the equilibrium level (EL). At this point, the surrounding air is the same temperature as the parcel and so it will begin to decelerate and eventually stop. Thus, the parcel will rise above the EL producing an overshoot at the top of the cumulonimbus cloud. Strong downward forces from negative buoyancy then lead to downdrafts that also overshoot the EL, with decaying buoyancy oscillations occurring after this (Cotton et al. 2010). In the absence of mixing a parcel of air would settle at the EL.

Convective inhibition (CIN) represents the amount of work needed per unit mass to lift an air parcel adiabatically to its LCL and then pseudoadiabatically from the LCL to its LFC (Figure 2.2).

$$CIN = -\int_{p_0}^{p_{LFC}} R_a(T_v - \bar{T}_v)\, d\ln p \,, \tag{2.5}$$

where T_v is the virtual temperature of a parcel of air which is lifted from an initial level of p_0, where the parcel originates, to p_{LFC}, the pressure at its LFC (American Meteorological Society 2021d). $\bar{T}_v$ is the virtual temperature of the environment. Virtual temperatures are used to account for the effect of moisture on air density.

Convective available potential energy (CAPE) represents the maximum buoyant instability of an undiluted air parcel and is related to the potential updraft strength of thunderstorms (American Meteorological Society 2021b). Generally calculated for near-surface parcels, it is the energy available per kg to convert to kinetic energy (vertical motion) once they have reached the LFC,

$$CAPE = \int_{p_{LFC}}^{p_{EL}} R_a(T_v - \bar{T}_v)\, d\ln p \,. \tag{2.6}$$

Energy and updraught speeds scale roughly with $\sqrt{CAPE}$ however the profile or shape of the positive area is also important. Two soundings with a similar value of CAPE could lead to different convective characteristics: a longer, narrower profile would likely produce a slower updraught acceleration but taller thunderstorms.

As air rises in updrafts varying amounts of environmental air are entrained via in-cloud turbulence. Through a near-global survey of tropical convection from satellite data, Takahashi and Luo (2012) found that although the ambient EL (calculated from soundings) provides a reasonable upper bound for convective development the maximum detrainment of mass occurs more than 3 km below this (Figure 2.3). The resultant

height that air parcels reach depends on the amount of air that is entrained on ascent and the type of air that is entrained.
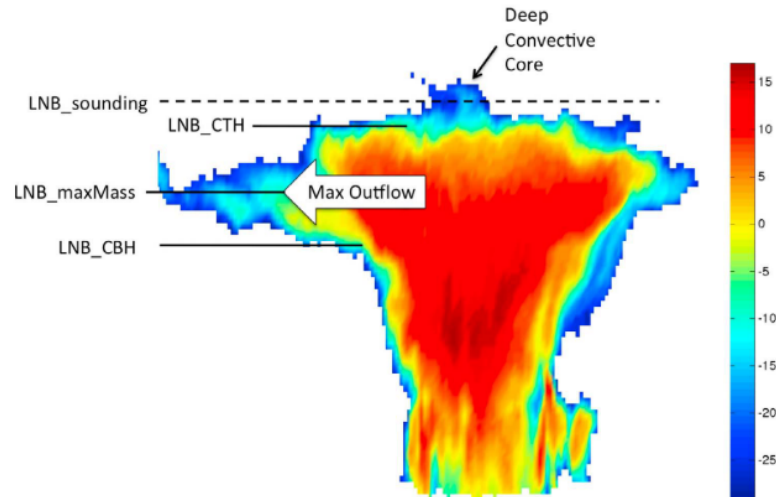
Figure 2.3: Figure and caption from Takahashi and Luo (2012), CloudSat radar reflectivity profile of a tropical deep convective cloud observed on February 24 2007 over Amazon (unit: dBZ). The size of the system is about 140 km and the highest point is about 17 km. Different observational equilibrium levels (or levels of neutral buoyancy, LNB) are marked up and illustrated on this example. LNB_{CTH}, $LNB_{maxMass}$ and LNB_{CBH} which refer, respectively to, the LNB defined by anvil cloud top height, maximum mass outflow (determined by radar reflectivity) and anvil cloud base height.

Thunderstorms need CAPE to occur but also have to overcome CIN. Sensible heat flux gradually shifts boundary layer (BL) air parcels ascent to the right on the tephigram, increasing CAPE. Surface latent heat flux increases q_v and in turn the CAPE. So if CIN delays the onset of convection, then larger CAPE will build up. Once convection does occur, more energy is available, and so it is more likely to be intense. Whether CAPE has any correlative effect on rainfall efficiency, the ratio of surface rainfall to water vapour inflow (Fankhauser 1988), is contested. Market et al. (2003) considered the precipitation efficiencies for mesoscale convective systems (MCSs) over the central United States and found little correlation with CAPE while CIN played a dominant role. They theorise that when CIN is minimised, even a modest amount of CAPE will produce updrafts strong enough to collect precipitation particles effectively while large values of CIN can ensure updrafts may never form. Thus, if CIN is high, updrafts will be rare or non-existent, but if they do occur in such a case they are likely to be more extreme. If CIN is low, there are often more storms but they tend to be less intense.
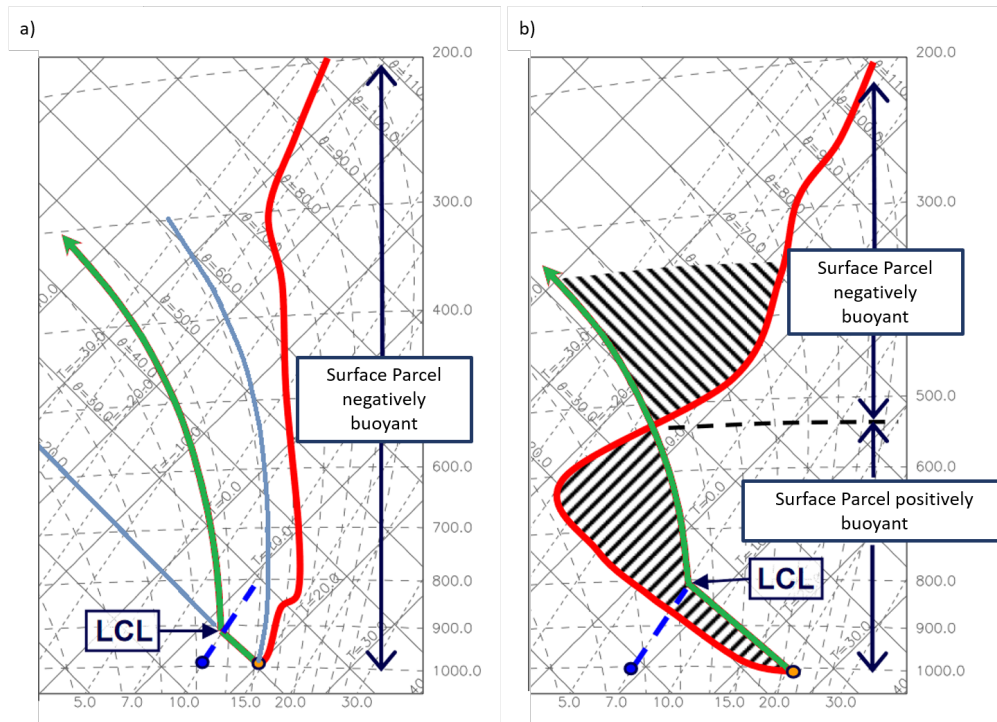
Figure 2.4: Adapted from Brooks (2011), idealised examples of (a) absolute stability and (b) absolute instability of air at the surface. The red line is the environmental temperature profile and the green line the surface parcel temperature profile. In (a) the solid light blue lines indicates the dry and moist-adiabatic lapse rate of the surface parcel.

2.1.3.1   Atmospheric Instability

If a parcel of air rises above its LCL, the water vapour will condense and latent heat is released to the surrounding air. This counteracts the simultaneously occurring adiabatic cooling. Thus, a saturated parcel of air cools less as it rises than an equivalent dry parcel and so will be more positively buoyant. The increased buoyancy will make it accelerate upward more than the dry parcel. This can often make the difference between a parcel being buoyant or not.

One method of judging atmospheric instability is to consider the environmental lapse rate and where it sits in relation to the dry-adiabatic and moist-adiabatic lapse rate. If the environmental lapse rate is less than a parcel's moist-adiabatic lapse rate (see Figure 2.4a) then there is absolute stability as the temperature of the air parcel will always be colder than the environment and lifting can only take place if forced. Alternatively, if the environmental lapse rate is greater than the dry-adiabatic lapse rate there is absolute instability (see Figure 2.4b) where any adiabatic lifting results in air that is warmer

than its environment. Finally, conditional instability occurs when the environmental
lapse rate of a layer of unsaturated air is between the moist and dry-adiabatic lapse
rates. This is the first of two definitions for conditional instability described in Ameri-
can Meteorological Society (2021c) and is described by (Sherwood 2000) as a statement
of uncertainty about instability. If the effects of moisture are included through consid-
ering the CAPE or potential instability this uncertainty can be resolved (Schultz et al.
2000). CAPE can be evaluated to determine the degree of instability. For instance,
if the conditionally unstable layer has a stable layer above it and so has CAPE near
zero, then no vertical displacement of parcels will produce positive buoyancy (Schultz
et al. 2000) and the state is described as stable conditional instability (Normand 1938).
The second definition of conditional instability occurs when the the parcel does have
CAPE (Figure 2.5) and is considered to possess latent instability. In this instance, it
must be possible for a parcel to be displaced adiabatically from some level and with
conservation of total water mixing ratio to attain the environmental temperature in a
saturated state. This latent instability can be further diagnosed if CAPE exceeds CIN,
whereby it is termed real latent instability. In the reverse, where more energy is needed
to lift parcels than is released through convection, it is termed pseudolatent instability.

2.1.3.1.1 Potential (Convective) Instability Potential instability was devel-
oped in response to the inability of the lapse-rate definition of conditional instability to
determine parcel stability. Potential instability occurs for an unsaturated layer or col-
umn of air in the atmosphere with $\frac{\partial \theta_e}{\partial z} < 0$ (as in Figure 2.1). If such a layer is forced to
lift adiabatically until saturated, it will become unstable as its temperature lapse rate
will exceed the moist-adiabatic lapse rate regardless of its initial stratification (Ameri-
can Meteorological Society 2021g). This layer-lifting process is not typically associated
with the development of upright deep moist convection but potential instability is often
diagnosed to be present in situations where deep, moist convection is likely (Schultz
et al. 2000).

θ_e is therefore a useful indicator of stability whereby $\frac{\partial \theta_e}{\partial z} > 0$ is analogous to stability.
If θ_e at the source level decreases with height to the level of saturation, then moist
convection can occur but it is not necessary for θ_e to decrease with height to the LCL
for there to be convection. The θ_e at the source compared with the saturated θ_e (or θ_{es})
of the environment indicates the buoyancy of the source at that level in the environment
and so is a useful measure of the instability of the column of air.
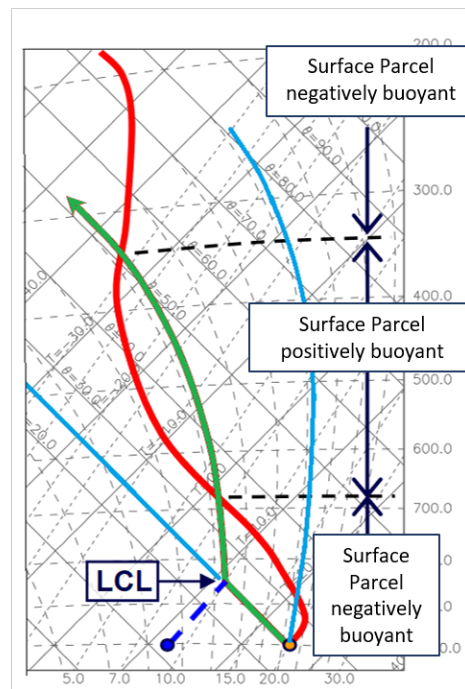
Figure 2.5: Adapted from Brooks (2011), idealised example of conditional stability of air at the surface. The surface parcel has CAPE so has latent instability. The red line is the environmental temperature profile and the green line the surface parcel temperature profile. The solid light blue lines indicates the dry and moist-adiabatic lapse rate of the surface parcel.

2.2   Organised Deep Convection

Moncrieff (1981) describes the basic thermodynamic feature of deep convection, in
contrast to shallow convection, to be the prevalence of downdrafts and cloud-scale
organisation. In order to produce this organisation, dynamic constraints operate to
impose a shape and character to the cloud-scale circulations resulting in the transport
of momentum being a key dynamic characteristic of deep convection. In storms with
multiple cells of convection, individual cells grow and dissipate, yet the ensemble of
cells can be interpreted as a quasi-steady system (Moncrieff 1978).

Through adding dry ambient air into moist updrafts, entrainment typically limits the
height and intensity of convection (Derbyshire et al. 2004). This occurs as entrainment
leads to an increase in vertical mass flux with height while typically diluting cloud
core properties and so contributing to decreases in both cloud moist static energy and
buoyancy with height. Through quantifying the change in θ_e as a function of height for
trajectories of inflowing air through a MCS, Fierro et al. (2009) showed that latent heat
released above the freezing level can compensate for initial decreases in θ_e due to mixing
at lower levels. A recent study using convection permitting simulations by Becker and
Hohenegger (2021) found that entrainment rates strongly increase with environmental
humidity over both ocean and land and with aggregation (except in squall lines where
they are generally high).

2.2.1   Mesoscale Convective Systems

The American Meteorological Society (2021f) defines a MCS as any ensemble of thun-
derstorms producing contiguous precipitation on the order of $100\,\mathrm{km}$ or more in the
horizontal scale in at least one direction. Markowski and Richardson (2010) state that
this length scale is approximately the scale at which the Coriolis acceleration (pro-
portional to wind velocity) becomes significant whereby perturbations produced by the
Coriolis force in the mid-latitudes approach the same order of magnitude as the original
wind. Mesoscale systems are often characterised by large wind accelerations and large
ageostrophic motions. Radar echoes have been used to show that MCS precipitation
divides distinctly into a convective region of intense, vertically extending cores and a
stratiform region of more uniform, lighter precipitation Houze Jr. (1977). Stratiform
precipitation is partly produced by the dissipation of older convective cells and partly
by broader-sloping mesoscale ascent (Houze Jr. 2014). Air cooled by evaporating rain
drops can form intense downdrafts in the convective-scale squall front regions of MCSs
while downdrafts in the region of net descent beneath the mesoscale stratiform region

are an order of magnitude weaker (Houze Jr. 1977; Kilpatrick and Xie 2015).

2.2.2   Squall Lines

The speed of MCS cloud lines, narrow bands of active thunderstorms, can vary greatly and are categorised as fast-moving, and therefore squall lines if they travel over $7\,\mathrm{ms}^{-1}$ (Barnes and Sieckman 1984) and are observed to last several hours. Squall lines frequently occur along an almost continuous line of deep convection and are prone to having a steady structure. They can self-organise, sustaining long-lasting deep convective motions in the absence of mesoscale forcing. Squall lines can extend to $1000\,\mathrm{km}$ in length and $100\,\mathrm{km}$ wide, and have life-times that can range from 12 to over 36 hours.

A squall line with trailing precipitation is shown in Figure 2.6, where the convection is fed by a front-to-rear storm-relative inflow in the lower troposphere, which partly ascends and weakly overturns. New cells can be seen to be forming at the front of the squall line. Squall lines with trailing precipitation tend to have a rear-inflow of low-θ_e air which enters from below the anvil cloud and gradually descends toward the leading convective line where it accelerates downward. A common characteristic of squall lines are convective downdrafts which transport horizontal momentum and relatively drier low-θ_e mid-level air to lower levels (Moncrieff and Miller 1976; Varble et al. 2020). Produced by evaporating condensate these downdrafts form cold pools which propagate outward. Studies have emphasised the importance of the cold pool at low levels in providing the extra lifting to sustain severe convection which is important in showing how a system can maintain itself without any large scale forcing (Crook and Moncrieff 1988).
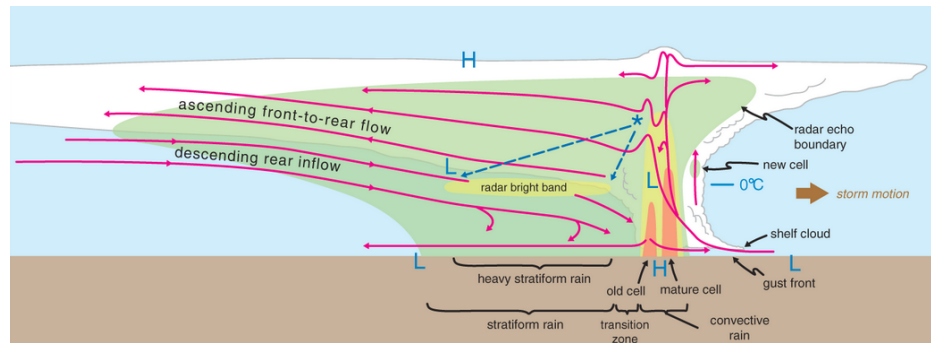
Figure 2.6: Schematic of a squall line moving to the right (westward) viewed in a vertical cross-section orientated perpendicular to the convective line. The green shading indicates the region of precipitation-sized hydrometeors, i.e. where radar echo is present. The yellow and orange shading indicates more intense radar echoes. The model also shows new cells forming on the leading edge of the squall line. From Markowski and Richardson (2010) adapted from Houze Jr. (1989).

Biggerstaff and Houze Jr. (1993) found that a transition region exists between the convective line and stratiform rain region which is characterised by mesoscale descent through a deep layer. This transition zone consists of two different types of average downdraft: one at upper levels that is mechanically forced by processes in the convective line and one at lower levels that is driven by microphysically induced negative buoyancy associated with melting and evaporative cooling in convective-scale downdrafts. Gallus and Johnson (1995) used numerical simulations of squall lines to analyse the microphysical processes within the stratiform region. Evaporation in mesoscale downdrafts was found to be the most important process in affecting the intensity of circulations (including the rear-inflow jet and precipitation). Their study also showed that environmental stability strongly controls vertical motion in the stratiform region. Greater instability increases the production of condensate, surface rainfall and low-level drying within the mesoscale downdraft producing the warm and dry (or onion) soundings of Zipser (1977). By considering dropsonde data through MCSs, Correia and Arritt (2008) demonstrated large variability within moisture and temperature profiles across the transition and stratiform regions, including near-saturated low-level conditions and unsaturated downdrafts. Correia and Arritt (2008) also discuss how the layered structure of the wet-bulb potential temperature implies that air in the lowest 4 km of an MCS originates from a variety of source regions.

Moncrieff and Green (1972) combined Bernoulli's theorem with the y-component of the vorticity equation to formulate a non-linear theory of steady, two-dimensional convection in shear based on the thermodynamic profile of the inflowing air. Through this they satisfactorily predicted the speed, and steering level, of different varieties of se-

vere convective events including squall lines. Moncrieff and Miller (1976) considered a mature squall line as a steady-state problem since although convective cells are comparatively short-lived, the density current produced by the downdraught outflow 'persists in a remarkably steady state... allowing the quasi-steady updraft/downdraft parts of the circulation to co-exist'. They suggest that this steady regime requires equivalent speeds of the cumulonimbus with the cold pool but that this will not often be satisfied as the propagation speeds (PSs) are each determined independently of the other. The speed of the density current depends on its depth and temperature deficit whereas the cumulonimbus is largely dependent on the CAPE. Any inequality between these two speeds will result in either impulsive behaviour or decay of the main convection. Moncrieff and Miller (1976) suggest a relationship for the PS of the cumulonimbus cloud which depends on attributing the source of entropy (and so changes to the log-potential temperature along a streamline) to saturated pseudo-adiabatic displacements.

2.2.2.1 Layer Lifting Theory

Houze Jr. (2014) stated the defining property of a convective cloud to be 'that condensation occurs in non-hydrostatic buoyant upward air'. One tradition is to view this as parcel lifting or buoyant bubbles of air emanating from the BL, see Section 2.1.3. However, while MCSs may begin in the form of such buoyant parcels rising high into the upper troposphere, the organised vertical circulation of a mature MCS is better described by layer lifting in the form of a deep slantwise ascending layer of air. A series of papers including Moncrieff and Miller (1976); Moncrieff (1978, 1981); Thorpe et al. (1982); Moncrieff (1992); Crook and Moncrieff (1988) quantified this view for the case of an idealised steady state convective storm with a prescribed decrease in hydrostatic pressure across the updraft at mid-levels. If the larger environment across an MCS is potentially unstable as well as sheared, air must flow through the system along a unique set of streamlines. The geometry of the streamlines can be deduced as entropy, mass, momentum and vorticity is conserved along streamlines (Houze Jr. 2014). The hydrostatic pressure differences across the storm are traced to the change in virtual temperature between the mesoscale updraft and the mesoscale downdraft zones (LeMone 1983).

In the two-dimensional model of Moncrieff (1992), θ_e is conserved along streamlines such that the thermodynamic stratification within the updraft layer does not change. As a layer of air rises and becomes saturated, small-scale convective cells will form if the rising air is potentially unstable (see Section 2.1.3.1.1). It is worth noting that without such a release of instability the highest θ_e air in the lowermost levels of the rising layer

of air would not, as in the parcel view, reach the tropopause (Houze Jr. 2014). Multiple studies using airborne Doppler-radar data have suggested that the layer lifting model does operate when the inflowing layers of air are potentially unstable (Kingsmill and Houze Jr. 1999; Bryan and Fritsch 2000). Kingsmill and Houze Jr. (1999) considered tropical MCSs and found the updrafts were almost always slantwise and consisting of finite layers of air rising over an apparent downdraft cold pool. Notably, Mechem et al. (2002) found that ascending inflow layers, (approximately 0.5 to 4.5 km in depth) into deep convective systems over the western tropical Pacific, do not merely consist of BL air and despite being potentially unstable maintained a well-defined layered structure.

One explanation for why a potentially unstable layer of air retains its coherent structure after becoming saturated is that the absolute instability which is created allows for overturning within the layer without breaking down the overall motion (Houze Jr. 2014). Mechem et al. (2002) found that moist mid-level air is critical to the development of the layer-lifting mode of inflow as when the layer meets the cold pool it quickly reaches saturation and so responds to lifting as a nearly moist neutral layer. Zipser et al. (2006) combined parcel thinking with the layer model to create a conceptual model which includes 'crossover zones' (see Figure 2.7) which exist when the ascending layer of air saturates and parcel processes become active. In this zone, a buoyant parcel will entrain air arriving in the zone with lower θ_e which will impact the EL and so the height of the horizontal trajectory downstream of the parcel.
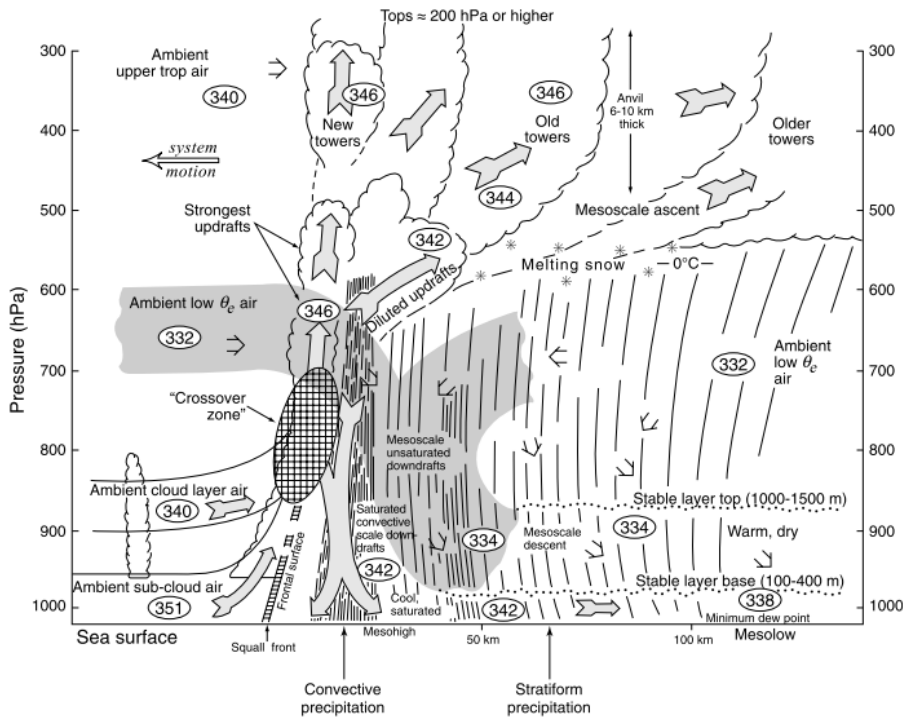
Figure 2.7: Idealisation of a tropical oceanic MCS. Parcels of air from the BL rise in convective updrafts and lower θ_e air is entrained into the updrafts. The updraft parcels rise till they lose their buoyancy by entrainment or by encountering a stable layer in the environment. Entrainment of ambient low-θ_e air weakens updrafts and forms convective-scale downdrafts, which sink to the surface in the convective precipitation zone. Note that the system has three-dimensionality such that the updraft and downdraft trajectories are not collocated, and the convective region contains a 'crossover zone' where convective-scale updrafts and downdrafts coexist. From Houze Jr. (2014) adapted from Zipser et al. (2006)
.

2.2.2.2 Dry Air Aloft

Dry air aloft, or the humidity above the cloud base, can have a key role in convection, in particular the influence of mid-level dry air on the production of cold pools and the overall strength of squall lines. Even in environments with identical CAPE and vertical wind-shear varied mid-tropospheric dryness can cause significant differences in the morphology and evolution of convective storms. Barnes and Sieckman (1984) showed that fast convective lines propagated in an environment where the mid-tropospheric θ_e was lower than that for slow lines, and where wind shear was significant and perpendicular to the fast lines. For supercell storms, low relative humidity above the cloud base aids the formation of strong downdrafts through evaporation (Gilmore and Wicker 1998),

which on reaching the surface create cold pools which can drive the development of new convective cells and so longer-lived and more intense systems.

In the tropics dry air aloft has been found to suppress convection due to the detrimental effects of entraining dry air (Brown and Zhang 1997) as while high θ_e air from the BL will ascend in convective updrafts, air above the BL with low θ_e will mix into convective downdrafts and may cause them to sink. Through idealised large-eddy simulation (LES) experiments, James and Markowski (2010) found that dry air aloft reduced the intensity of convection measured by upward mass flux and total condensation. However, this was inconsequential for high CAPE (in excess of $4000\,\mathrm{Jkg^{-1}}$) line-type scenarios where downdraught mass flux and cold pool strength were enhanced but only in the trailing stratiform region. In the Sahel, cold pools are stronger pre-monsoon than in the monsoon season and evidence suggests drier mid-levels play an important role (Provod et al. 2016).

2.2.3 Cold Pool interactions with Wind Shear

Strong shear at low levels, perpendicular to the convective line, can encourage squall line intensity and longevity (Browning and Ludlam 1962; Ludlam 1963). Ludlam (1963) initially observed that some thunderstorms thrive in strong shear. Thorpe et al. (1982) performed a numerical study on variations in mid and upper-level winds and constant low-level shear to better understand this phenomena. The severest and most prolonged storm occurred in the simulation with weakest mid and upper-level shear. From this they concluded that the lack of upper-level mean flow allowed for the cold pool to remain stationary relative to the deep precipitating convection where it can be continuously fed by the evaporative cooling of the downdraft. They describe the front of the downdraught, where the cold pool meets the inflowing air, as having a similar effect to orographic forcing. Rotunno et al. (1988) suggested that these processes do occur but that the cold pool and cloud are not passive but interact continuously with their environment. As numerical power expanded in the 1980s a large number of 3D simulations were undertaken with the conclusion that a broad range of convective structures could be produced in numerical models by changing only the environmental shear profile (Weisman and Klemp 1986; Weisman et al. 1988; see Figure 2.8).

Rotunno et al. (1988) expanded the theory of Thorpe et al. (1982) by suggesting that there is an optimal shear which counteracts the cold pool (this is often known as RKW theory; Figure 2.9). Through 2 and 3 dimensional simulations, a dependence of squall line strength and longevity on the wind shear was shown. The presence of shallow shear oriented perpendicular to the line resulted in the evolution of a long-
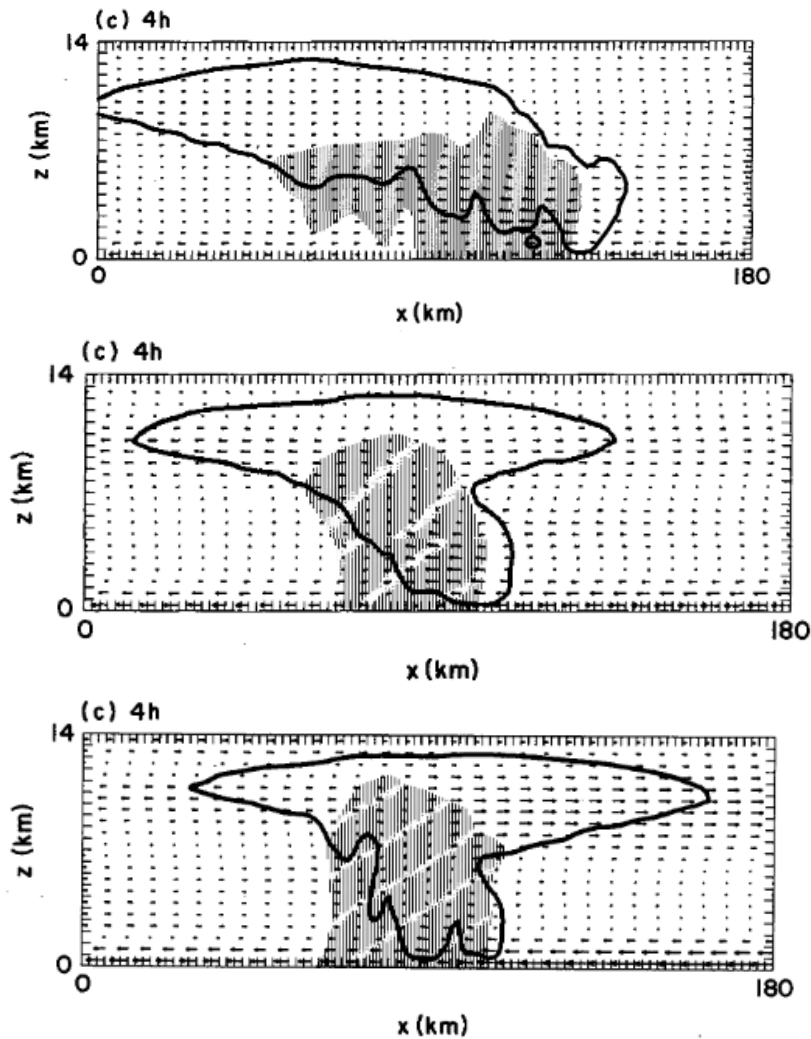
Figure 2.8: Adapted from figures in Weisman et al. (1988), line averaged vertical cross sections at 4 hours of model time with perpendicular shear applied with constant values above 2.5 km. The panels show (a) a weak shear case with $10\,\mathrm{ms}^{-1}$ maximum at 2.5 km, (b) a moderate shear case with $17.5\,\mathrm{ms}^{-1}$ maximum and (c) a strong shear case with $25\,\mathrm{ms}^{-1}$ maximum. The wind vectors are plotted with respect to storm speed, the thick line represents the boundary of the model-produced cloud water field and shading indicates rainfall.

lived line of convection containing individually short-lived cells. They theorised that alone both cold pools and environmental shear can inhibit convection. Cold pools induce circulations whereby near-surface air is accelerated horizontally over the top of the cold pool inhibiting vertical penetration of the air while wind shear alone can tilt updrafts downshear as shown in Figure 2.9. Rotunno et al. (1988) theorised that when combined these processes can counteract each other on the down shear side of the cold pool producing much-deeper and more vertical lifting than is possible without the low-level shear, making it easier for new cells to form and grow as old cells decay. Bryan et al. (2006) discuss that the most widely accepted components of the Rotunno et al. (1988) paper are the suggestions that: (1) when the cold pool effect is stronger than that of the wind shear it produces a trailing stratiform squall line where most rainfall occurs on the upshear side of the surface gust front, (2) when the wind shear is stronger a leading stratiform squall line emerges where the majority of rainfall occurs on the downshear side of the surface gust front and (3) when the most favourable 'optimum' state occurs it allows for an upright structure with convective cells roughly above the surface gust front.
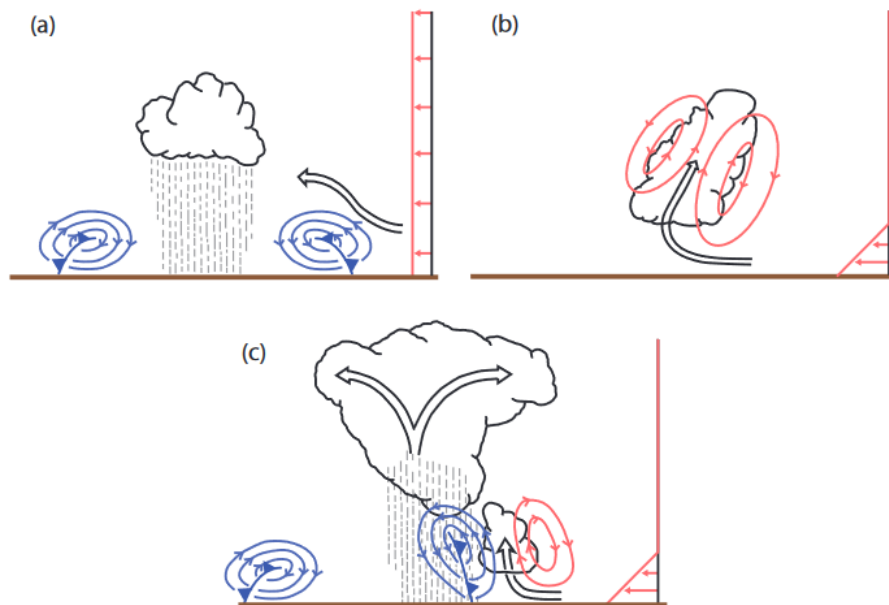
Figure 2.9: Figure adapted from Rotunno et al. (1988) by Bryan et al. (2006). Rotunno et al. (1988) suggest that (a) without low-level shear, the circulation induced by a spreading cold pool (blue streamlines) inhibits deep lifting and so cannot trigger a cell. (b) For an updraft in shear (without a cold pool), the thermally created vorticity together with the shear vorticity lead to a circulation (red streamlines) that tilts downshear. (c) The presence of low-level shear counteracts the circulation induced by the cold pool and promotes deep lifting that triggers new cells.
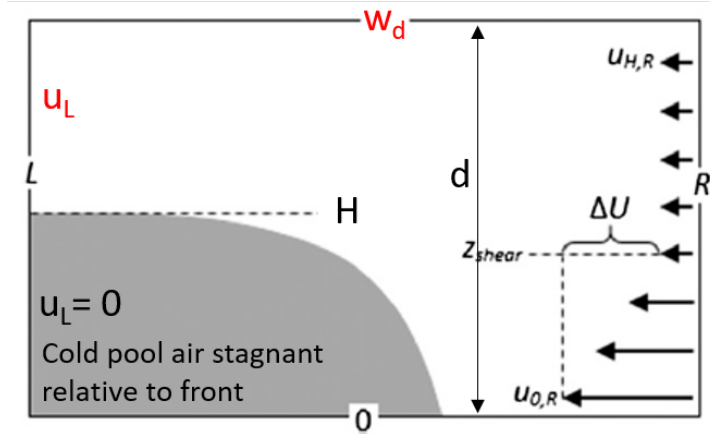
Figure 2.10: Figure adapted from Alfaro (2017). Schematic depiction of a two-fluid density current flow. The gray area represents the denser fluid and the frame of reference moves with the cold pool.

The Rotunno et al. (1988) paper also includes a quantitative section where the authors consider two-dimensional flow on a plane perpendicular to the deep convective line, see Figure 2.10. The vorticity equation for an inviscid Boussinesq fluid is considered,

$$\bar{\rho}\frac{d}{dt}\frac{\eta}{\bar{\rho}} = -\frac{\partial B}{\partial x}, \tag{2.7}$$

where $\eta = \frac{\partial u}{\partial z} - \frac{\partial w}{\partial x}$ and B is the buoyancy with respect to some reference density $\bar{\rho}$ (Bryan et al. 2006),

$$B = g\left(\frac{\theta - \bar{\theta}}{\bar{\theta}} + 0.61(q_v - \bar{q}_v)\right). \tag{2.8}$$

Over-bars indicate environmental conditions from the original base state e.g. at R in Figure 2.10. The problem is assumed to be steady while the buoyancy of the air approaching the cold pool is assumed to be negligible so that convection only occurs at the cold pool edge such that $\eta = \frac{\partial u}{\partial z}$ away from the cold pool. Therefore if Equation 2.7 is integrated over the area in Figure 2.10 the following is obtained,

$$0 = \frac{u_{L,d}^2}{2} - \left(\frac{u_{R,d}^2}{2} - \frac{u_{R,0}^2}{2}\right) - \int_L^R (w\eta)_d dx + \int_0^H B_L \, dz, \tag{2.9}$$

where $L, R, d, 0$ indicate the variable at either the left, right, at height d or at the

a) No shear (assume rigid plate at d)

$$u_{L,d}{}^2 = c^2 \equiv -2\int_0^H B_L\, dz$$

No vorticity
$u_{R,d} = u_{R,0}$

"The net generation of negative vorticity
is just balanced by the export of negative
vorticity on the downstream side"

b) With 'optimal' shear

$$u_{R,d} - u_{R,0} \equiv \Delta u = c$$

Flow is turned
exactly into the
vertical

Import of vorticity
$u_{R,d} < u_{R,0}$

"The import of the positive vorticity associated
with the low-level shear just balances the net
buoyant generation of negative vorticity by the
cold pool."

Figure 2.11: Figure adapted from Bryan et al. (2006). Schematic depiction of RKW theory for cases with (a) no and (b) 'optimal' shear.

surface.

Through control volume analysis Rotunno et al. (1988) then considered a case with no shear (i.e. $u_{R,d} = u_{R,0}$) such that the second and third terms in Equation 2.9 vanish (see Figure 2.11a). They also considered an 'optimal shear' case where there is an import of vorticity and the flow is turned exactly into the vertical so that $u_{L,d}, u_{R,d}$ and $\int_L^R (w\eta)_d\, dx$ are all zero, (see Figure 2.11b). The cold pool intensity (or the theoretical cold pool speed of a two-dimensional density current in an infinitely deep, unstratified environment) is defined at L in Figure 2.11b as (Benjamin 1968; Rotunno et al. 1988),

$$c^2 = 2\int_0^H B_L dz, \tag{2.10}$$

where H is the height above ground at which the buoyancy B_L is first observed to be $0\,\mathrm{ms}^{-2}$. The shear is quantified using $\Delta u = u_{R,d} - u_{R,0}$ and so the following is obtained for the 'optimum' case,

$$\Delta u = c. \tag{2.11}$$

Rotunno et al. (1988) suggests that Δu should be limited to low-levels as it is 'the actual shear within the air that makes contact with the cold pool that is influential'. There remains some ambiguity over how exactly to quantify environmental wind shear (or the depth to consider Δu) as several studies since have shown that mid- and upper-level shear are also important to consider (Fovell and Dailey 1995; Parker and Johnson 2004).

Fovell and Tan (1998) theorise that as convective updrafts generate vorticity and as the updrafts extend through mid and upper levels of the troposphere then shear throughout the troposphere can be influential on squall-line structure. The idealised simulations of Parker and Johnson (2004) indicated that although the lower-tropospheric shear has a greater effect, the deep-layer shear remains important. They theorise that this is particularly the case for the kinematic effects of environmental wind shear interacting with the, often downshear tilting, updrafts and contributing to an overturning mean updraft that is strongly influenced by shear in mid to upper levels of the troposphere. When considering precipitation efficiency with respect to cloud shear (the difference in the speed of the wind over the depth of the warm cloud), Market et al. (2003) found that increased shear impacted precipitation efficiency negatively. They argue that stronger winds aloft produce more tilted clouds allowing for more contact with drier environmental air which can increase evaporation and produce precipitation over a wider area. An additional consideration is the impact of the negative buoyancy within the cold pool inducing accelerations beyond its own confines. Weisman and Rotunno (2004) revised the original theory to consider shear to some layer "in close proximity to" (roughly 1.5-2 times) the depth of the cold pool.

Some criticisms of RKW theory include that such a strong connection between low level shear and squall line characteristics does not hold up to close scrutiny (Coniglio and Stensrud 2001). For instance, Fovell and Dailey (1995) found that without optimal conditions the model storms would be "weaker and more clearly multi cellular" but would still persist. Weisman and Rotunno (2004) attempted to address these arguments by arguing that although long-lived systems are produced over a wider range of environments than is strictly 'optimal' the strength of the systems is enhanced when moderate to strong surface based shear is confined to the lowest $2.5 - 5\,\mathrm{km}$. Weisman and Rotunno (2004) conclude that the optimum condition for a sustained squall lines is $C/\Delta u \approx 1$ however, although optimal, these conditions are not necessary for convective systems to be intense or long-lived. Indeed Bryan et al. (2006) states that system longevity can no longer be considered a part of RKW theory.

There has also been discussion over whether the focus on the cold-pool-shear interaction is an oversimplification as it neglects the mesoscale processes which also influence the longevity of squall lines. Lafore and Moncrieff (1989) examined the physical processes which generate and maintain mesoscale inflow at the rear of the squall line and found that horizontal potential temperature gradients (generated by a combination of latent heat release in the convective region and unsaturated mesoscale descent) cause a horizontal pressure gradient and generate horizontal, line-parallel vorticity, the consequence of which is a rear-inflow jet which can contribute a significant proportion of

mass to the cold-pool. Weisman (1992) suggests that for environments characterised by weak-to-moderate vertical wind shear and CAPE, the rear-inflow jet descends and spreads along the surface behind the leading edge of the storm while for occasions with high shear and high CAPE the rear inflow remains elevated to near the leading edge of the system. Depending on the vertical location of this rear-inflow jet it can both contribute or counteract the cold pool circulation (see Figure 2.12). However, Weisman (1992) also note that to have a significant impact in most occasions the rear inflow jet must exceed around $10\,\mathrm{ms}^{-1}$.

Finally, Alfaro and Khairoutdinov (2015) suggest that variations in the intensity of squall lines have been wrongly attributed to vorticity balance, particularly as latent heating often depends on shear strength. They argue that cold pool-shear balance alone is unlikely to represent as strong a constraint on the structure of mature squall lines as proposed by Rotunno et al. (1988). An alternative theory proposed in Alfaro (2017) which discusses how the shear can modulate the inflow of convective instability and moisture is described next in Section 2.2.3.1.

2.2.3.1   The Layer Lifting Model of Convection

Alfaro (2017) further investigated how the environmental low-tropospheric shear affects the structure and intensity of severe mid-latitude squall lines, focusing on the impacts of the strength of shear on the latent heating produced within the deep convective region of mature storms. He describes a layer-lifting model of convection (LLMC), a schematic of which is shown in Figure 2.13. Low-level shear modulates inflowing air in terms of water vapour and convective instability so that stronger shear leads to an increase of the total and mean storm-relative inflow of air being convectively unstable. The precipitation rate of the storm is strongly dependent on the water vapour inflow rate while the greater mean convective instability of the inflowing air leads to larger within-storm buoyancy. This theory places importance on the thermodynamic role wind shear can play in deep moist convection, but so far to the author's best knowledge has only been tested for mid-latitude conditions and for cases of idealised shallow shear.

Integrated convective available potential energy (ICAPE) measures the latent heating per unit area accomplished collectively by all unstable parcels as they ascend from their level of free convection to their EL.

$$\mathrm{ICAPE} = \int_0^{z_{tr}} \rho(z)\mathrm{CAPE}(z)dz\,, \tag{2.12}$$

a) Cold Pool Balanced by Shear

b) Cold Pool with Shear and Elevated Jet

c) Cold Pool with Shear and Surface Jet
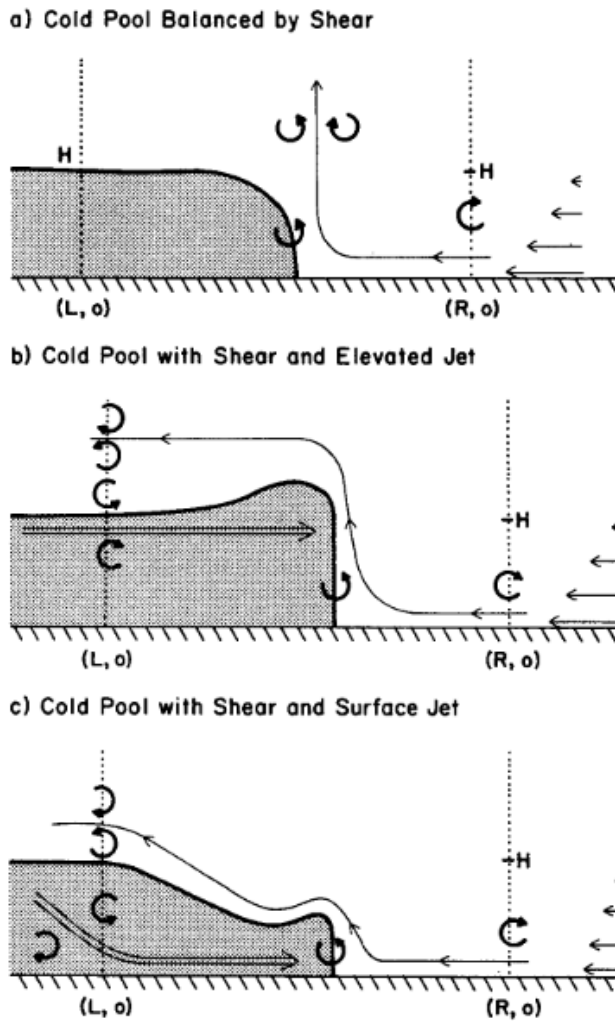
Figure 2.12: From Weisman (1992), schematic depiction of (a) a cold pool spreading in an environment with 'optimum' conditions, (b) a cold pool balanced by the ambient vertical wind shear and an elevated rear inflow jet, and (c) a cold pool in the presence of a surface rear-inflow jet. The shading denotes the region of negatively buoyant air. The thick arrows depict the sense of vorticity that is generated at the leading edge of the cold pool or that is advected through the boundaries.
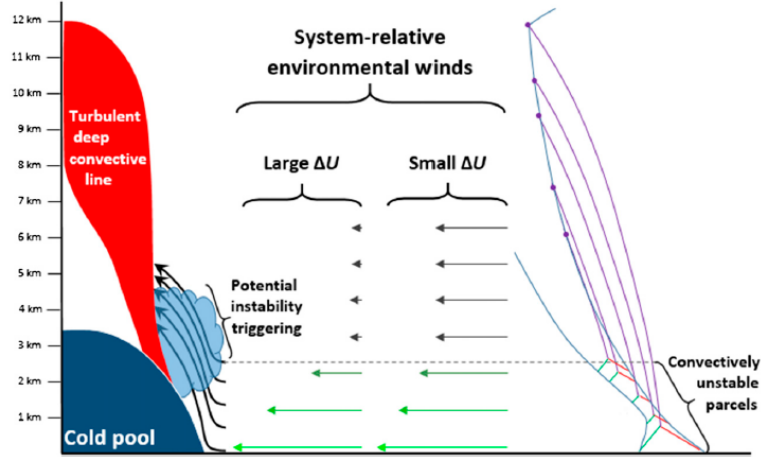
Figure 2.13: From Alfaro (2017), schematic representation of the LLMC. The cold
pool of a squall line lifts deep layers of air that mix turbulently throughout the deep
convective line. The thermodynamic environment is depicted in a skew $T - \ln p$ chart,
displaying pseudo adiabatic ascent by parcels originating at different levels. Two dif-
ferent cases of system-relative environmental winds with low-tropospheric shear are
shown, with the colour of the arrows representing the value of some relevant parameter
(e.g. CAPE or the water vapour mixing ratio). The strongly sheared environment
corresponds to greater inflow of convectively unstable air as a fraction of the total
storm-relative inflow.

where CAPE(z) represents the CAPE of a parcel originating at $z = 0$ while z_{tr} marks
the height of the tropopause. A layer-lifting index is then defined to measure the mean
convective instability of the storm-relative inflowing tropospheric air by,

$$\text{CAPE}_{ll} = \left(\int_0^{z_{tr}} \rho(z) \left| u_{env}(z) - \text{PS} \right| \text{CAPE}(z) dz \right) \left(\int_0^{z_{tr}} \rho(z) \left| u_{env}(z) - \text{PS} \right| dz \right)^{-1}. \tag{2.13}$$

The environmental wind component normal to the squall line is defined as u_{env} and
PS is the propagation speed of the storm. Alfaro (2017) defines an index for updraft
strength as,

$$w_{ll} = \sqrt{2\text{CAPE}_{ll}}. \tag{2.14}$$

Alfaro (2017) found w_{ll} to be predictive of the maximum vertical velocities produced in
simulated idealised squall lines. Mulholland et al. (2021) expands on Alfaro (2017) using
idealised simulations to show that stronger low-level shear results in greater horizontal

mass flux into the leading edge of the cold pool which produces wider updrafts, less entrainment-driven dilution and larger buoyancy than those with weak low-level shear.

2.2.3.1.1 Precipitation Alfaro and Khairoutdinov (2015) found that precipitable water is related to the surface precipitation rate. For constant low-tropospheric wind shear, the rate of water vapour processed by a squall line is the main factor affecting precipitation rate. However, Alfaro and Khairoutdinov (2015) also discuss that precipitation efficiency decreases with weaker shear, drier mid-tropospheric conditions and thus lower vertical velocities within the storm. To describe these processes, (Alfaro 2017) introduced a diagnostic for the precipitation rate,

$$\text{PR}_{ll} = \left(\frac{w_{ll}}{W}\right)^2 L_y \left(\int_0^{z_{tr}} \rho q_v(z) |u_{env}(z) - \text{PS}| \, dz\right), \qquad (2.15)$$

where PR_{ll} represents the total rainfall across the domain in kgs^{-1} and L_y is the length of the squall line in the along-line direction. The constant W should be selected such that the term $\left(\frac{w_{ll}}{W}\right)^2$ accounts for the efficiency of convection: the speed of upward-moving air, entrainment and the fraction of precipitable water that falls as precipitation. Thus, PR_{ll} defines a diagnostic for the precipitation rate which depends on the water vapour inflow rate per unit length in the along-line direction.

The Precipitation Rate scaling in Equation 2.15 is expanded below and is proportional to the system relative inflow of moist air and CAPE divided by the total relative system inflow of total air mass,

$$\text{PR}_{ll} = \frac{2L_y \left(\int_0^{z_{tr}} \rho \, |u_{env}(z) - \text{PS}| \, q_v(z) dz\right) \left(\int_0^{z_{tr}} \rho(z) \, |u_{env}(z) - \text{PS}| \, \text{CAPE}(z) dz\right)}{W^2 \left(\int_0^{z_{tr}} \rho(z) \, |u_{env}(z) - \text{PS}| \, dz\right)}.$$
$$(2.16)$$

As PR_{ll} describes the total rainfall rate for the domain, to convert this value into a mean rainfall rate in mmh^{-1} it is necessary to divide by an area A. In this work we have divided by L_y and the y-averaged storm width (that is the y-width of rain rates greater than $1\,\text{mmh}^{-1}$).

It is possible that a combination of the above theories will explain the formation of squall lines in the West African monsoon. It is also important to note that any role shear plays in the recent decadal increase in the intensity of squall lines could have been created by a specific set of changing environmental conditions which may not be reproduced diurnally, seasonally or in the future.

2.3   The West African Monsoon

Monsoons often occur in tropical regions and are distinctive due to extreme intra-annual
fluctuations in rainfall. They primarily occur in regions where there is a much greater
annual variation of temperature over large land areas compared with neighbouring
ocean surfaces. This leads to an excess of pressure over the continents in winter and
a deficit in summer, resulting in a seasonal reversal in wind (American Meteorological
Society 2021h) and a larger migration of the zone of peak rainfall, the inter-tropical
convergence zone (ITCZ), between the hemispheres. In the West African Sahel (shown
in Figure 2.14), the hot dry continental air masses originating from the low pressure
system above the Sahara Desert give rise to dusty winds during the winter (Lavaysse
et al. 2009). The West African monsoon (WAM) occurs during the summer months
when the daytime heating of the land produces a low-level pressure gradient between
the Saharan heat low (SHL) and the cooler Gulf of Guinea. The resultant monsoon
winds (lower tropospheric south-westerly circulations) bring cool, humid air into the
continent (Parker et al. 2005a). The inter-tropical discontinuity (ITD), also known as
the intertropical front, separates the hot and dry northerly surface flow to the north
from the moist and cool southwesterly monsoon flow to the south. In the summer the
ITD shifts inland from the Guinea coast and a baroclinic zone forms with a strong
meridional surface temperature gradient (Figure 2.14).

Two distinct convective regimes occur in the Sahara and toward the Gulf of Guinea
(Thorncroft and Blackburn 1999; Parker et al. 2005b). The Sahara is characterised by
a thermodynamic profile close to a dry adiabat with a deep, dry convective boundary
layer with well-mixed vertical profiles of θ and q_v from near the surface to approximately
5-6 km altitude (American Meteorological Society 2021e) (Figure 2.14). This Saharan
air layer (SAL) is deep where it merges with the Saharan boundary-layer in the north
and becomes thinner in the south where it is undercut by cooler, more humid marine
boundary layer air. The equatorward region has a profile that is closer to a pseudoadi-
abat, consistent with a strong influence of deep moist convection Parker et al. (2005b).
Parker et al. (2005b) describe a baroclinic region (where a temperature gradient exists
on a constant pressure surface) between these two extremes, the coherent air layers of
which can be seen in Figure 2.14. The monsoon layer, a humid zone connected to the
land surface is deeper towards the south and extends northwards into the Sahel where
it is capped by the SAL. Above the SAL, the troposphere is almost pseudoadiabatic.
There is also a diurnally varying convective mixing layer which grows upwards during
the day, into the monsoon layer in the south and into the Saharan residual layer in the
north.
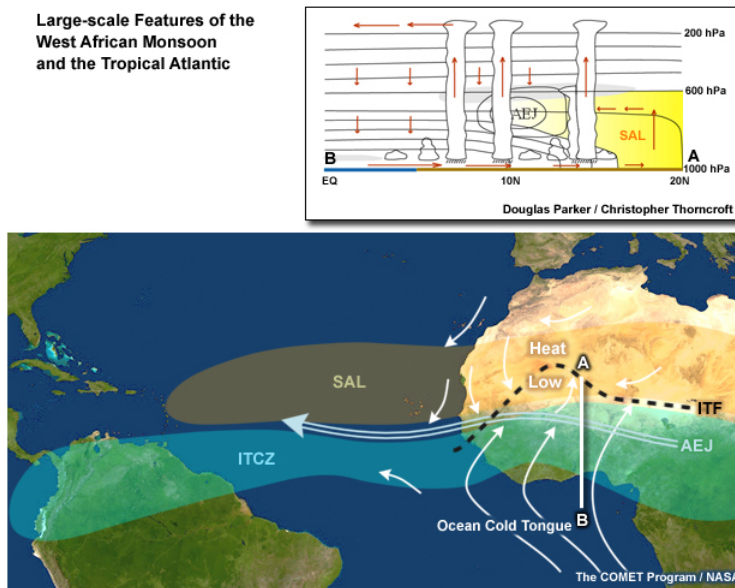
Figure 2.14: COMET® adaptation of Parker et al. (2005a), schematic of North-South vertical cross section along the Greenwich Meridian highlighting the heat low-African easterly jet (AEJ)-ITD system, the SAL and meridional variations in atmospheric boundary layer. The intertropical front in the figure (ITF) is another name for the ITD and refers to where the north-east and south-east trade winds converge.

The WAM is dominated by MCSs (Section 2.2.1) which contribute 90% of the annual rainfall in the Sahel (Mathon et al. 2002b). The MCSs observed over tropical Africa are mainly thought to initiate in the evening around 1700 and 1800 local time, with lifetimes that vary from a few hours to more than a day (Hodges and Thorncroft 1997). Once initiated they often persist, with cold pool outflows lifting inflowing environmental air to its LFC and so sustaining convection. They are most likely to be triggered by orography and elevated heating (Rowell and Milford 1993; Laing et al. 2012) or over convergent boundaries such as those produced by soil moisture anomalies (Taylor et al. 2013), gust fronts and cold pool outflow, synoptic weather systems such as African easterly waves (AEWs) (Birch et al. 2014) or the migration of the ITD. Recent work has shown that convective updrafts in West Africa have high entrainment (due to the prevalence of squall lines) as well as low buoyancy compared to other regions, due to convection originating from forced mesoscale convergence which results in large quantities of low θ_e air also being convected upwards (Becker and Hohenegger 2021).

Most regions of West Africa have a single diurnal peak of rainfall either in the afternoon or night while there is a minimum of rainfall in the morning (Zhang et al. 2016). Afternoon rainfall peaks are associated with locally initiated storms (Rickenbach et al. 2009), some of which can sustain into the night, developing into organised convective

systems that propagate westwards (Taylor et al. 2010) to give nocturnal rainfall peaks (Duvel 1989). Once deep moist convection has formed in the WAM it can, to a large extent, self-organise. On such occasions, long-lasting deep convective motions can be sustained in the absence of mesoscale forcing (Fink and Reiner 2003).

2.3.1 Synoptic Systems

2.3.1.1 The African Easterly Jet

The AEJ, a mid-tropospheric jet located over tropical northern Africa during the northern hemisphere summer, is a prominent and important feature of the zonal wind structure during the WAM. Thorncroft and Blackburn (1999) state the AEJ has a maximum around $12.5\,\mathrm{ms^{-1}}$ at 600-700 hPa and 15°N with a width of 5°-10° of latitude. However, there is some degree of uncertainty over the location, shape and intensity of the AEJ due to poor observational networks and discrepancies between reanalysis climatologies (Wu et al. 2009). Burpee (1972) attributed the AEJ to be a result of the baroclinic zone to the south of the Sahara and the reversal of the temperature gradient in the middle troposphere. Essentially, in the Northern Hemispheric summer, the West African land mass gets much hotter and drier than the coastal region to the south. This reverses the typical equator-to-mid-latitude temperature gradient and as a consequence, strong easterly geostrophic flow develops, creating strong shear with the monsoon westerlies below. The result is an easterly zonal wind maximum which is in approximate thermal wind balance with the lower tropospheric temperature gradient. Cook (1999) highlighted the importance of surface wetness contrasts between the Sahara and equatorial Africa in producing meridional temperature gradients which are strong enough to maintain the AEJ. Wu et al. (2009) revised the features necessary to the creation and maintenance of the AEJ to also include other geographical features including vegetation and orography.

Thorncroft and Blackburn (1999) demonstrated that the AEJ is associated with two separate diabatically forced meridional circulations, the low level heating and dry convection associated with the Saharan thermal low and the deep moist convection nearer the equator. The two different thermodynamic profiles, and the latitudinal temperature contrasts forced by these differences lead to the thermal wind that defines the AEJ (Parker et al. 2005a). There is a key transition zone between the peak in mean rainfall and deep moist convection, just south of the AEJ core, and the dry convection and the SAL to the north. In this zone the shallow monsoon layer undercuts the SAL resulting in high CIN (see section 2.1.3) and the build-up of CAPE. Maranan et al. (2018) argue

that this high CIN, high CAPE environment combined with the dryness of the SAL, which has a near-dry adiabatic lapse rate that aids stronger downdraft acceleration, contributes to making the region just north of the AEJ favourable for the formation of intense squall lines over localised rainfall. They also note that high wind shear, associated with the AEJ, is the best indicator for the horizontal extent, or organisation, of an MCS. Thorncroft and Blackburn (1999) discuss how any variations within the two types of diabatic heating in the Sahara and in the ITD region will impact the nature of the AEJ. The combination of this variability with the importance of soil moisture gradients, vegetation and orography helps to explain the discrepancies found in AEJ characteristics produced by different numerical models.

Thorncroft and Blackburn (1999) discuss how the AEJ plays a crucial role in the WAM as the vertical shears associated with the jet are crucial in organising moist convection while the associated meridional potential vorticity gradients are important in determining the nature of the mixed barotropic-baroclinic instability which gives rise to AEWs.

2.3.1.2   African Easterly Waves

AEWs, a type of convectively active atmospheric trough, develop in the region south of the AEJ core where the mean zonal flow is unstable. They can be observed from May to October but peak in intensity from August to September (Burpee 1974; Thorncroft and Hodges 2001). AEWs are most prominent in the lower troposphere with a maximum at around 650 hPa, the height of the AEJ. They have a period of 2-6 days and wavelengths of 2000-5000 km (Reed et al. 1977). Parker and Diop-Kane (2017) stress the diversity within AEW structures from case to case which occur due to differences in maturity, geographic location and the time of day. MCSs in West Africa are strongly modulated by AEWs: the western flank of the trough, characterised by diverging air, suppresses convection whereas convergence occurs on the eastern side of the trough, enhancing convection (Mathon et al. 2002a). Vizy and Cook (2018) associated 70-90% of nocturnal rainfall over the southern Sahel with MCSs that had developed in association with the ITD and were accompanied by a mid-tropospheric African easterly wave disturbance to the east. A schematic of the various observable elements of an AEW is shown in Figure 2.15 and highlights where MCSs are initiated relative to the trough of the wave. Fast-moving MCSs typically occur along the location of the AEJ core ahead of the trough where they are favoured by mid-level dry air. Slower-moving convective systems are found to the south, where wind shear is weaker and the monsoon depth is deeper (Parker and Diop-Kane 2017).
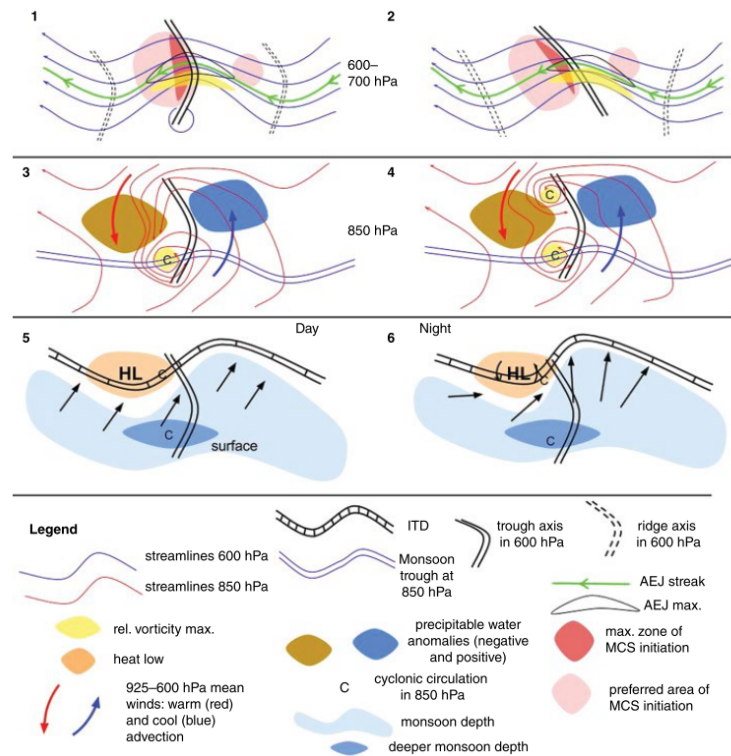
Figure 2.15: From Parker and Diop-Kane (2017), schematic of the various observable
elements of an AEW, and likely relationships between these. Left-hand panels show a
'normal' situation, as far as this exists, while right-hand panels show common alterna-
tives. For example, the structure in panel 2 would be expected in an environment with
additional barotropic shear, with a stronger easterly wind to the north.

While AEWs help to trigger MCSs the reverse also occurs with MCSs playing a role
in both triggering wave-like disturbances in the AEJ entrance region over the eastern
Sahel and in promoting the growth of the AEW trough during its westward propagation
across the subcontinent.

2.3.2 Diurnal Cycle within the West African Monsoon

Several studies have indicated how the diurnal cycle is intrinsic to the WAM (Parker
et al. 2005a; Klein and Taylor 2020). The strong surface heating during the day creates
a well-mixed, deep and turbulent convective boundary layer that inhibits the monsoon
winds and reduces CIN. Throughout the night radiative cooling of the surface results
in the formation of a shallow, stable boundary layer such that air aloft is decoupled
from the surface drag. From 0500 to 0700 UTC, the south-westerly low-level jet (LLJ)
which forms around 925 hPa is of maximum strength (Abdou et al. 2010) leading to

an increase in the low-level equivalent potential temperature and a large vertical shear with respect to the AEJ at around 600 hPa. During the morning, strong solar heating of the ground causes dry BL convection and erosion of the stably stratified layers formed overnight. Dry air is entrained from above into the boundary layer and there is downward mixing of momentum from the nocturnal LLJ and strong near-surface gusts (Knippertz 2008). By midday, deep BL mixing has produced drag on this deep layer of air and the vertical gradients of momentum and potential temperature are reduced. The LLJ and AEJ both weaken throughout the day with LLJ weakening rapidly after the morning and reaching a minimum in the late afternoon and early evening (Abdou et al. 2010). The AEJ has smaller diurnal variations but weakens to a minimum around 1800 UTC on average (Kalapureddy et al. 2010). Thus, the diurnal cycles of the LLJ and AEJ combine to produce a diurnal minimum in vertical wind shear in the late afternoon (Parker et al. 2005a). The build up of CAPE throughout the day, when combined with a daily minimum in the CIN barrier in the early evening, is conducive for the triggering of storms which then move westward overnight with the general direction of the mid-level AEJ (Zhang et al. 2016).

The Sahel ITD which separates dry air Saharan air masses and moisture-laden air flowing off the tropical Atlantic has a distinct diurnal cycle in the summer (Parker et al. 2005a). Daytime surface heating and the turbulent mixing it produces occur faster near the ITD where the moist layer is shallower compared to further south. This contrast can result in a low-level reversal in the meridional flow, enhancing convergence and the genesis of MCSs (Vizy and Cook 2018). Klein and Taylor (2020) conducted a systematic observational analysis of soil moisture feedback to show a strong positive impact of drier soils on convection within mature (westward) MCSs. Dry soils enhance sensible heating over latent heating, warming the overlying planetary boundary layer (PBL) and enhancing the climatological temperature gradient which once large enough accelerates the AEJ and creates a local shear anomaly. They also found that dry soil enhanced heating can draw the ITD anomalously south during the day, providing a large-scale source of moisture which when coupled with strong PBL temperatures can generate strong convective instability. The combined effect of this instability with enhanced shear is particularly strong during the afternoon-evening with soil moisture effects accounting for 1 in 4.8 of all cores in the late afternoon.

2.3.3 Past and Future Climate

Through studying rain-gauge recordings and Meteosat images for the region Lebel et al. (2003) concluded that on average 75- 90% of the Sahelian rainfall occurs in the monsoon

season, while over 90% of the rain in that period is produced by a small number of large and organized MCSs (12% of the total number of MCSs). Clearly for a region which is heavily dependent on agriculture, understanding how these large-scale systems may change in the future is vital. However, projections for Sahel rainfall changes in response to global warming are highly uncertain, with some coupled models predicting strong drying, others wetting and most more modest combinations of both (Biasutti et al. 2008).

Panthou et al. (2014) studied climatic trends for the Sahel by considering data from over 700 weather stations and validating against 43 that were continuously operated from 1950-2010. They concluded that over the period of 2001 to 2010 the Sahelian region has been characterized by a more extreme climate with the proportion of annual rainfall associated with extreme rainfall at 21% compared to 17% in the 1970-1990 period. The climate is drier in the sense of a persisting deficit in rainfall occurrence compared to 1950-1969 while at the same time there is an increased possibility of extreme daily rainfall. This was corroborated by Taylor et al. (2017) who used thirty-five years of satellite observations and rain-gauge readings from the West African Sahel to reveal a persistent increase in the frequency of the most intense MCSs over this period: this was inferred from a trend of $-0.78\,^\circ\mathrm{C}$/decade in cloud top temperatures. Intensification of MCSs was restricted to a narrow Sahelian belt in the months of June to September but extends to the Guinea Coast in the spring (Klein et al. 2021). This increase in the frequency of MCSs is only weakly related to the multi-decadal recovery of the Sahel annual rainfall but exhibits a similar trend to global land temperatures.

Taylor et al. (2017) calculated zonal means across $15^\circ\mathrm{E}-15^\circ\mathrm{W}$ of atmospheric variables from European Centre for Medium Weather Forecasting (ECMWF) ERA-Interim Re-analysis data (ERA-I). On considering the latitudes 5-25°N within the longitudes stated they found correlations at both event and inter-annual time scales between storm intensity and increased Sahelian temperatures, drying at mid-levels, and stronger wind shear. The correlating rising temperatures were within the Saharan PBL as well as the SAL which overlies the Sahelian PBL. This increase in temperatures results in a corresponding thermal wind which strengthens the AEJ, while the warmer (and deeper) Saharan Heat Low strengthens monsoon flow. Taylor et al. (2017) found no observable accompanying trend of increased precipitable water or specific humidity and concluded that the increase in wind shear has contributed to the observed rise in MCS intensity. As wet-season Sahelian temperatures have not risen and the meridional temperature gradient spanning the Sahel has increased in recent decades, Taylor et al. (2017) theorise that the changes in shear and storm severity are due to global temperature rises resulting from anthropogenic forcing rather than locally warmer conditions.

Recent work exploring climate change projections using convection permitting, 4.5km resolution modelling over Africa (CP4A) has suggested that dry and wet extremes over West Africa are expected to intensify in the future (Kendon et al. 2019). Through analysing CP4A data Fitzpatrick et al. (2020) found that WAM MCSs rain rates scaled with the product of time-of-storm total column water and in-storm vertical velocity. However, despite pre-storm wind shear modulating in-storm vertical velocity and the resulting cloud-top temperatures they found no direct correlation between wind shear and precipitation rates in CP4A, in contrast with observations for the Gulf of Guinea (Klein et al. 2021).

2.3.4 Observations of the West African Monsoon

The Sahel experiences some of the most regular and severe squall lines on Earth (Zipser et al. 2006). Mathon and Laurent (2001) recorded convective cloud clusters propagating over the Sahel with speeds of 8-12 ms^{-1}. In an earlier paper, which analysed eight year averages of satellite data during the WAM, Hodges and Thorncroft (1997) found mean speeds of squall lines to be from 10-17 ms^{-1} with the maximum speeds obtained around Lake Chad and the region of Burkino-Faso, Mali and Niger, which is roughly consistent with where the AEJ (see section 2.3.1.1) is strongest. Observations have suggested that the faster moving squall lines develop in environments which have drier mid-levels and where the vertical shear of the horizontal wind is normal to the leading edge of the squall line (Barnes and Sieckman 1984). Taylor et al. (2017) found a correlation between storm intensity and PS with MCSs categorised as the most extreme travelling at mean speeds of 18.3 ms^{-1}.

Chong (2010) considers a north-south MCS which was well-tracked by the Massachusetts Institute of Technology (MIT) Doppler radar as it passed over Niamey on the 11 August 2006. It was found to move with an advection speed of 13.7 ms^{-1} towards the west and 0.5 ms^{-1} southward. Radar reflectivity plots of the squall line in its mature state are shown in Figure 2.16 where it is composed of a north-south orientated line of convective cells (45 dBZ), a wide region of stratiform precipitation (25-40 dBZ) separated by a transition zone of lighter rain (< 25 dBZ). In the vertical cross-section there is a marked forward anvil.

For composite Sahelian squall lines observed at Niamey in the 2006 African Monsoon Multidisciplinary Analysis (AMMA) campaign, Provod et al. (2016) show mean rainfall rates between 10 mmh^{-1} at the leading edge to 1 mmh^{-1} at the trailing edge with the storms taking on average an hour to pass. In the same study, the maximum surface pressure and minimum potential temperature perturbations were measured to
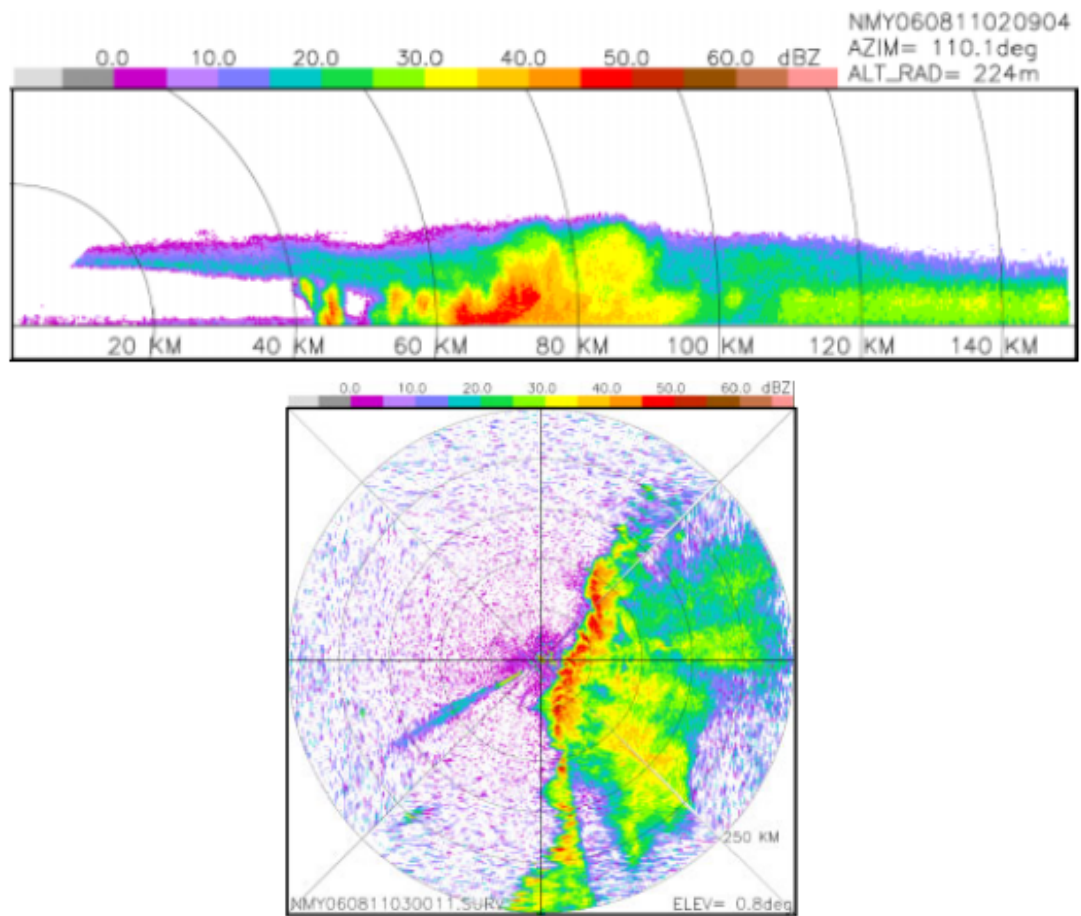
a

Figure 2.16: From Chong (2010), Radar reflectivity (dBZ) in (a) a vertical cross-section
along the azimuth of 110°, and at 0209 UTC 11 August 2006 and (b) a plan position
indicator at 0.8° elevation at 0300 UTC 11 August 2006.
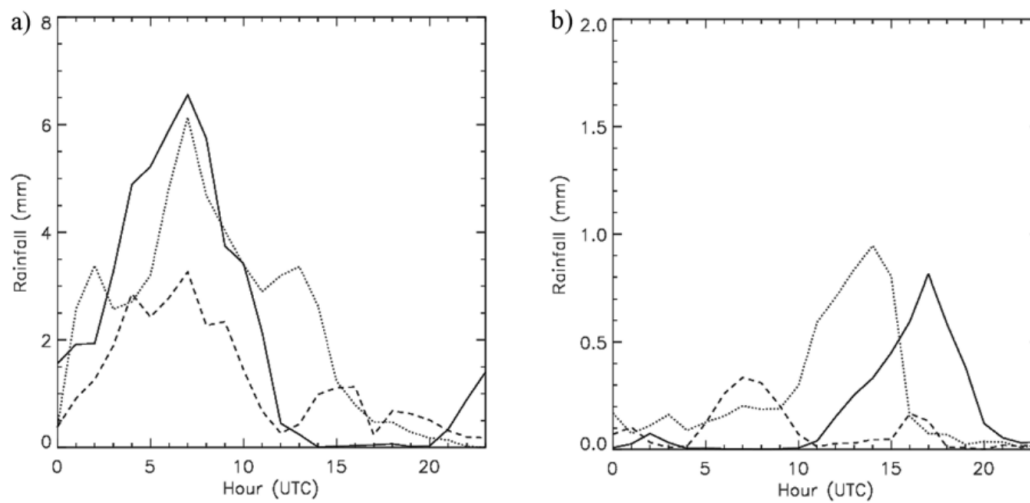
Figure 2.17: From Rickenbach et al. (2009), monthly composite diurnal cycle of precipitation observed by the MIT radar for (a) squall line MCS events, (b) non-MCS isolated convection. Solid curve is July, dotted curve is August, dashed curve is September. Local time equals UTC + 1 h

be around 2 hPa and 6 °C respectively.

Through using Tropical Rainfall Measuring Mission (TRMM) satellite rain estimates and MIT Doppler radar observations from near Niamey over the period of 5 July to 27 September 2006, Rickenbach et al. (2009) confirmed the bimodal structure of the diurnal rainfall cycle. The nocturnal maximum was found to be associated with propagating squall lines that formed in elevated terrain to the east of Niamey, the prior afternoon, while local isolated convection led to a smaller afternoon maximum (see Figure 2.17). Non-squall MCSs were found to be rare and short-lived.

2.4   Atmospheric Models

2.4.1   Weather and Climate Models

There has been significant improvements in global numerical weather prediction (NWP) in recent decades due to increased computing power and developments in model physics. However, Haiden et al. (2012) discuss how despite this being true for mass and wind fields it is not as straightforward for precipitation, where skill across models is poor in regions with prevalent deep convection and for the tropics in general. A striking result of their paper is that the skill of a forecast at day 1 in the tropics is similar to that of day 6 in the extra-tropics. Vogel et al. (2018) performed a verification study which

assessed the quality of operational ensemble precipitation forecasts from different NWP
centres over northern tropical Africa. They found that raw ensemble forecasts are of
no use for the prediction of precipitation over northern tropical Africa. Vogel et al.
(2020) investigated the potential of statistical ensemble post-processing to correct for
biases and dispersion errors and so improve the quality of precipitation forecasts in the
tropics in two leading operational ensemble predictions systems (ECMWF and the Me-
teorological Service of Canada). They found that post-processing leads to considerable
improvement almost everywhere but in tropical Africa where the skill remains close to
zero.

Representing moist convection accurately in weather and climate models is vital for
many reasons including the role it plays in: modifying local and large-scale circu-
lation patterns through latent heat release and the transport of heat, moisture and
momentum; regulating the water vapour in the atmosphere (which provides the largest
feedback for climate change); the hydrological cycle where the precipitation it produces
is of vital importance to human life and when extreme is accompanied by strong and
damaging winds, the transport of trace gases and aerosols, lightening production and
flash floods (Stensrud 2007). Despite the increase in resolution of atmospheric numer-
ical modelling in general, most global weather and almost all climate modelling does
not explicitly represent convective processes but rather include only the bulk effects of
convection over the model grid scale (typically 100s of kilometres for climate models)
which are inferred through parametrisation. Parametrisation is the process by which
important physical processes that can not be resolved directly are represented in a
numerical model (Stensrud 2007). Moncrieff (2013) argues that because of this, con-
vective organisation is almost completely absent from contemporary climate and global
weather models as the fundamental dynamics are not represented by parametrisations
and the model resolution is not sufficient to represent them explicitly. Even where
global convection-permitting modelling and time-slice climate change experiments are
and have been performed grid-spacings and run durations are limited (Senior et al.
2021) as is the representation of MCSs (Crook et al. 2019).

2.4.2 Parametrisation

Similarly to many tropical regions, there are substantial errors in global weather and
climate model predictions of the WAM. The convection parametrisations used in global
models struggle to capture MCSs leading to systematic errors (Peters et al. 2019;
Kendon et al. 2019; Pante and Knippertz 2019; Fitzpatrick et al. 2020). For example,
analysis of the UK Met. Office Unified Model has shown it has considerable difficulty in

capturing the observed phase of the diurnal cycle in convection (Yang and Slingo 2001; Senior et al. 2021). For the Sahel, parametrised numerical models currently predict the rainfall peak too early in the day, the rain too widespread, storms are rarely predicted to sustain past sunset and the most intense rainfall is not captured (Yang and Slingo 2001; Randall et al. 2003; Stephens et al. 2010). These errors are consistent with the convection parametrisation schemes that represent deep moist convection triggering too easily and typically lacking any representation of organisation.

Other aspects of convection which are not realistically modelled include cold pool initiation, land surface impact (Garcia-Carreras et al. 2013; Taylor et al. 2013; Trzeciak et al. 2017), poor representation of entrainment and, key to the efforts in this work, the effects of wind shear. Wind shear is understood to play a key role in the organisation of MCSs and in the formation of the most extreme MCSs (Nicholls and Mohr 2010). The lack of representation of cold pools in parametrised models leads to less northward advection of cooler air, and so systematic biases in temperature and humidity over the central Sahara (Marsham et al. 2013; Garcia-Carreras et al. 2013). Vogel et al. (2020) argue that the inability of convective parametrisation schemes to represent the vertically tilted structure crucial for the upscale growth and propagation of MCSs may explain why forecasts are only a little better than the climatological reference for tropical Africa even after post-processing.

Although shear is a parameter that is not usually accounted for in parametrisations there has been increased focus in recent years on how it might be included (Moncrieff et al. 2017). A recent study by Muetzelfedt et al. (2021) has focused on producing a climatology of tropical wind shear from climate-model output. The authors suggest that this methodology could be applied to re-analysis models to diagnose the wind shear profiles that are present when and where organised convection occurs with the aim of informing how convection parametrisation schemes could be adapted to include shear-induced organisation.

Convection-permitting models produce storms which have more intense rainfall, more realistic diurnal cycles and lifetimes than those from parametrised models as well as a better representation of propagation speed and direction (Crook et al. 2019). Indeed with a convection permitting model Zhang et al. (2016) were able to identify single peaks in the diurnal cycle in different regions in both the afternoon or at night. As would be expected a better representation of the diurnal cycle of convection has additional benefits including changes to the diurnal wind cycle through impacting pressure gradients. Marsham et al. (2013) and Birch et al. (2014) both found explicit modelling of convection in the Sahel in August resulted in stronger monsoon flow, an ITD which reached further north as well as the Sahel changing from a moisture source (as

in parametrised models; Meynadier et al. 2010) to a more realistic sink. It has also been demonstrated that mid-latitude weather forecasts improve if explicit modelling is used over West Africa (Pante and Knippertz 2019). Berthou et al. (2019b) compared convection parametrised against convection-permitting 4 km resolution climate models on a pan-African domain CP4A and found the latter drastically improved the distribution of precipitation over the Sahel particularly through portraying more short-lasting intense rainfall events linked to MCSs which increases the mean precipitation and gives a better representation of wet and dry spells. This intensification of rainfall is larger in CP4A and happens in regions of both increased and decreased mean rainfall (Berthou et al. 2019a). The repercussions of an incorrect representation of the diurnal cycle impact the entire monsoon system including pressure gradients, winds and the water budget (Marsham et al. 2013; Birch et al. 2014).

2.4.3 Resolution Requirements

Horizontal grid-spacing of 1 km is robust for processes such as gravity currents and net momentum and heat transports (Weisman et al. 1997). Several previous studies have tested the validity of different spatial resolutions for simulating convection (Bryan et al. 2003; Bryan and Morrison 2012) with a general consensus that below a horizontal resolution of $\mathcal{O}(500\,\mathrm{m})$ the peak in the vertical velocity energy spectrum is resolved (Lebo and Morrison 2015). Simulations with a horizontal grid-spacing of $\mathcal{O}(1\,\mathrm{km})$ produce systems with larger convective cells that do not entrain as much mid-level air and so produce more precipitation and have higher cloud tops (Bryan and Morrison 2012). Bryan et al. (2003) also list precipitation distribution and amount as well as convective cell structure, system phase speed, and the organizational mode of convective overturning as inconsistencies between $\mathcal{O}(1\,\mathrm{km})$ and simulations of $\mathcal{O}(100\,\mathrm{m})$ horizontal grid spacing. More recently this focus on how the resolution effects the size and properties of individual clouds and convective updrafts has been described as structural convergence by Panosetti et al. (2019).

Recent studies have shown that domain-averaged and integrated properties for a large ensemble of convective cells often converge at the $\mathcal{O}(1\,\mathrm{km})$ scale including idealised simulations of deep convection (Panosetti et al. 2018; Verrelle et al. 2015). Mean physical characteristics which begin to converge at $\mathcal{O}(1\,\mathrm{km})$ include intensity of convection and the area of cold pools. Such studies demonstrate that large-scale flow properties are relatively unaffected by further refinement of the mesh grid beyond the $\mathcal{O}(1\,\mathrm{km})$ scale. Langhans et al. (2012) considered the bulk convergence in real-case multi-day simulations of an ensemble of convective cells and found the mean diurnal cycles of bulk

heating/moistening and vertical fluxes are nearly resolution independent from 4.4 km to 0.55 km grid-spacing.

When considering orography and environmental wind shear in resolution tests which ranged from 8 km to 500 km Panosetti et al. (2018) found that the pronounced orographic forcing in the former and a higher degree of organisation in the latter reduced the differences in the simulated net exchange of heat and water vapour between the lower and upper troposphere. The higher degree of convective organisation in the presence of environmental wind shear led to the clustering of clouds and updrafts into larger-scale structures and to the removal of some energy at the small scales, rendering it less difficult to be captured even at coarse resolutions. However, a larger ensemble spread was generally observed for experiments with wind shear compared to all the other experiments. Recent work has shown that despite CP4A giving a greater and more realistic response of updraft strength to shear than convective parametrised simulations it does not capture the observed increases in MCS rainfall intensities with wind shear (see Figure 2.18; Senior et al. 2021).
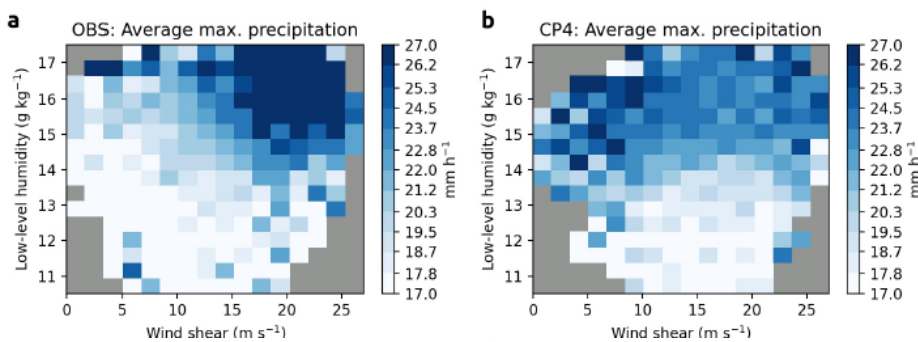
Figure 2.18: Figure and caption from Senior et al. (2021), MCS intensity scaling with atmospheric drivers for the CP4-Africa historical period and observations. 2d histograms for average maximum precipitation of (a) observations (OBS) and (b) CP4A as a function of pre-storm (1200 UTC) 925 hPa specific humidity and 650-925 hPa absolute zonal wind shear at storm location for more than 24,000 MCSs (active between 16-1900 UTC) over the Sahel (12° W-12°E; 9-19°N). Bins with less than 10 MCSs are shaded grey.

2.5   Summary

Current operational NWP forecasts for tropical Africa are only marginally more skilful than the climatological reference even after post-processing (Vogel et al. 2020). This is often due to convection parametrisation schemes struggling to capture the genesis and evolution of convective structures over multiple grid-boxes (Fink et al. 2011). This

culminates in rainfall predictions for the Sahel which are too widespread while failing to capture either the diurnal cycle or the most intense rainfall (Randall et al. 2003; Stephens et al. 2010; Stratton et al. 2018). Although a large body of literature exists which considers the role of shear in organising and promoting organised deep convection and particularly squall lines (Rotunno et al. 1988; Weisman et al. 1988; Bryan et al. 2006; Alfaro and Khairoutdinov 2015), there is little to no inclusion of the effects of shear in convection parametrisation schemes and the mechanisms behind how shear organises deep convection are still an active and debated area of research. Additionally, the majority of studies on the effects of shear have predominantly featured mid-latitude systems, idealised environments and have rarely focused on tropical Africa. Recent observational studies of the region have suggested that shear has played a key role in recent increases in extreme rainfall (Taylor et al. 2017) but this has not yet been reproduced by studies using numerical modelling (Fitzpatrick et al. 2020; Senior et al. 2021).

This Chapter has provided a summary of the literature on MCSs and the current debate around how vertical wind shear organises and supports them. The WAM and its main features have been discussed while an overview of the current difficulties in NWP for the Sahel region have also been covered. In the next chapter, the idealised model which is used throughout this thesis to explore the effects of wind shear on deep organised convection in the WAM will be discussed. Through running simulations which examines how the environmental profile affects MCSs this thesis bridges the gap between observations and theory with the aim of providing a greater understanding of why current weather and climate models often fail for this vulnerable region of the world.

Chapter 3

Experimental Design and Methodology

This chapter discusses the model, data and analysis methods used throughout this thesis. Section 3.1 gives an overview of idealised large-eddy simulations and the Cloud Model 1 (CM1) with which the idealised simulations discussed in Chapters 4-6 have been run. The model configuration used in this thesis is outlined in Section 3.2. Section 3.3 discusses the process by which a control simulation of a sustained storm was constructed using a representative profile from the Sahel during the West African monsoon (WAM) while Section 3.4.1 describes methods of quantitative analysis used throughout the thesis.

3.1   Idealised Modelling

As described in Section 2.4, current global weather and climate models struggle to accurately capture deep moist convection. A crucial challenge is that many of the processes involved occur on scales that are unresolved and so must be parametrised. Additionally, it is incredibly difficult to parametrise such processes unless the processes themselves and their interactions with one another are understood. It is important to note here that even a perfect understanding of such processes does not automatically make approximating or modelling them simple. Idealised cloud modelling provides an opportunity to investigate complex processes in a controlled and simplified environment and to isolate key variables to understand their importance.

In this study we have used an idealised model to isolate and compare how variations

within the initial thermodynamic (temperature and humidity) versus wind profile impact on the intensity of simulated squall lines. This idealised model is outlined in the next section.

3.1.1 The Cloud Model 1

The idealised model used in the project is CM1, a three-dimensional time-dependent non-hydrostatic numerical cloud model (Bryan and Fritsch 2002). This model is based on the third order Runge-Kutta time-integration scheme for compressible Navier-Stokes equations. In this study, a large-eddy simulation (LES) closure is used which solves a filtered Navier-Stokes equation where small-scale details of the turbulent flow have been removed from the solution (Bryan et al. 2003). This filtered equation is solvable with current computing resources but has an unknown term (the subgrid kinematic momentum flux) which must be parametrised. With this setup CM1 can be considered an LES model at horizontal resolutions below 1 km where boundary layer (BL) turbulence is resolved. Above this resolution, although the LES closure is still applied, the model can be considered cloud-resolving and still represents a more direct approach than conventional parametrisations. At such scales, the largest scale cumulus motions (at least) are resolved while fine-scale non-hydrostatic motions and their interactions with physical processes are still explicitly accounted for.

CM1's governing equations (Section 3.1.2) conserve mass and total energy in a moist atmosphere but not to machine accuracy. CM1 retains all terms in the pressure equation and several terms in the internal energy equation that many other numerical models neglect such as those associated with the heat content of hydrometeors and dissipative heating. Thus, the mass errors from CM1 are several orders of magnitude smaller than those from other cloud models that integrate pressure equations. In this study, the Morrison four-class double-moment explicit moisture scheme is used (Morrison et al. 2005). CM1 was originally designed to perform very-large domain simulations with high resolution and is a well established model for simulating propagating squall lines as the availability of inflow/outflow boundary conditions make it well suited for this (Alfaro 2017; Bryan and Morrison 2012; Letkewicz and Parker 2011).

3.1.2 The Governing Equations of Cloud Model 1

CM1 integrates governing equations for velocity (u, v, ω), pressure (π'), potential temperature (θ') and moisture (q_χ) where π is a non-dimensional pressure,

$$\pi \equiv (p/p_0)^{R_a/c_{pa}}, \tag{3.1}$$

and $q_\chi = \rho_\chi/\rho_a (\chi = v, l, f)$ represents the mixing ratios of moisture variables of water vapour, liquid water and solid water respectively with respect to dry air. We define p_0 as a reference pressure, c_{pa} as the specific heat of dry air at constant pressure and R_a as the gas constant for dry air. Superscript primes denote a perturbation from a base-state value (which are denoted by a subscript 0).

3.1.2.1 Properties of State

The base state, which varies only in z, is assumed to be in hydrostatic balance (the fluid is at rest initially due to a balance between vertical pressure gradient and buoyancy forces),

$$\frac{d\pi_0}{dz} = -\frac{g}{c_{pa}\theta_{\rho 0}}, \tag{3.2}$$

where g is gravitational acceleration. We define θ_ρ as a density potential temperature (Bryan 2017),

$$\theta_\rho = \theta \left(\frac{1 + q_v/\epsilon}{1 + q_v + q_l + q_f} \right), \tag{3.3}$$

where ϵ is the ratio of the gas constants R_a/R_v, and R_v is the gas constant for water vapour.

By combining the ideal gas law and Dalton's law of partial pressure, the equation of state for an air parcel at temperature T can be expressed as,

$$p = \rho_a R_a T + \rho_v \frac{R_a}{\epsilon} T = \rho_a R_a T (1 + q_v/\epsilon), \tag{3.4}$$

where ρ_a and ρ_v are the densities of dry air and water vapour respectively. Equation 3.4 may be equivalently written as,

$$\pi = \left(\frac{\rho_a R_a \theta (1 + q_v/\epsilon)}{p_0} \right)^{\frac{R_a}{c_{va}}}, \tag{3.5}$$

by using Equation 3.1 and as the temperature $T = \theta\pi$ and $c_{va} = c_{pa} - R_a$ where c_{va} is the specific heat of dry air at constant volume.

3.1.2.2 Conservation of Mass

For an arbitrary volume in space the material derivative, following a dry air parcel, is defined as,

$$\frac{D}{Dt} = \frac{\partial}{\partial t} + u_j \frac{\partial}{\partial x_j},$$

(3.6)

where u_j is the velocity. Einstein summation notation is used with indices i, j, k for the x, y, z co-ordinates. For dry air, the mass conservation equation is,

$$\frac{D\rho_a}{Dt} = -\rho_a \frac{\partial u_j}{\partial x_j}.$$

(3.7)

In contrast to an idealised dry atmosphere, the inclusion of moisture leads to the possibility of phase change (e.g. the evaporation of rainfall or the condensation of water vapour) and therefore the addition of multiple sources and sinks. Bannon (2002) defines a flow property χ which can move with a velocity u_j^χ that is different from the dry air velocity u_j. The conservation statement for χ can therefore be written as,

$$\frac{D}{Dt}\frac{\chi}{\rho_a} = \frac{\dot{\chi}}{\rho_a} - \frac{1}{\rho_a}\frac{\partial \chi v_j^\chi}{\partial x_j},$$

(3.8)

where v_j^χ is the velocity of χ relative to that of the dry air. The equation states that the amount of flow property per unit mass of dry air χ/ρ_a will change following the dry air if there is a source of χ or if there is convergence of χ moving relative to the air parcel. Thus, substituting the relevant densities for χ in Equation 3.8 the following conservation equations are obtained,

$$\frac{Dq_v}{Dt} = -\dot{q}_{cond} - \dot{q}_{dep} - \frac{1}{\rho_a}\frac{\partial \rho_v v_j^v}{\partial x_j},$$

(3.9)

$$\frac{Dq_l}{Dt} = \dot{q}_{cond} - \dot{q}_{frz} - \frac{1}{\rho_a}\frac{\partial \rho_l v_j^l}{\partial x_j},$$

(3.10)

$$\frac{Dq_f}{Dt} = \dot{q}_{dep} + \dot{q}_{frz} - \frac{1}{\rho_a}\frac{\partial \rho_f v_j^f}{\partial x_j}, \tag{3.11}$$

where $\dot{q}_{cond}$, $\dot{q}_{dep}$ and $\dot{q}_{frz}$ are the rates of change of condensation, deposition and freezing respectively.

3.1.2.3 Conservation of Momentum

The total momentum is defined as, $M_i \equiv \rho_a u_i^a + \rho_v u_i^v + \rho_l u_i^l + \rho_f u_i^f = \rho u_i^a + \rho_l v_i^l + \rho_f v_i^f$ where v_j^χ is the velocity of a property χ relative to that of the dry air such that $u_j^\chi = u_j^a + v_j^\chi$ and $\rho = \rho_a + \rho_v + \rho_l + \rho_f$. Water vapour is assumed to move at the same velocity as dry air. A conservation equation for the total momentum can therefore be defined as (Cotton et al. 2010),

$$\frac{\partial M_i}{\partial t} + \frac{\partial M_i u_j^a}{\partial x_j} + \frac{\partial p}{\partial x_i} - \epsilon_{ijk}M_j f_k + \delta_{i3}\rho g - \frac{\partial \tau_{ij}}{\partial x_j} = -\frac{\partial \rho_l u_i^l v_j^l}{\partial x_j} + \frac{\partial \rho_f u_i^f v_j^f}{\partial x_j}, \tag{3.12}$$

where f_k is the Coriolis vector, g is the acceleration due to gravity, τ_{ij} is the viscous stress tensor, ϵ_{ijk} the Levi-Civita symbol in three-dimensions and δ_{i3} the Kronecker delta. Often, the horizontal velocity is about the same as the air; in this case v_j^χ is pointed straight downwards and termed the terminal fall velocity. Equation 3.12 can be solved for the velocity of air in terms of π using Equations 3.3 and 3.4:

$$\frac{Du_i^a}{Dt} + c_{pa}\theta_\rho \frac{\partial \pi'}{\partial x_i} - \epsilon_{ijk}u_j^a f_k + \delta_{i3}\rho g - \frac{\partial \tau_{ij}}{\partial x_j} = 0 \tag{3.13}$$

where changes in momentum due to moisture effects have been neglected.

3.1.2.4 Conservation of Internal Energy

The total thermodynamic energy per unit volume is $E = \rho_a e_a + \rho_v e_v + \rho_l e_l + \rho_f e_f$, where the total energy e in each case is equal to the sum of the kinetic and internal energy. Cotton et al. (2010) define an equation for the total energy of cloudy air as,

$$\frac{\partial E}{\partial t} + \frac{\partial}{\partial x_j}\left(Eu_j + \rho_l e_l v_j^l + \rho_f e_f v_j^f\right) + p\frac{\partial u_j}{\partial x_j} - \rho Q_r = \tau_{ij}\frac{\partial u_i}{\partial x_j} + Q_{vt} + \frac{\partial}{\partial x_j}\left(\kappa\frac{\partial T}{\partial x_j}\right),$$

$$(3.14)$$

where Q_r represents radiative tendencies. The terms on the right include respectively:

- the dissipative heating term often small at low winds and over time scales shorter than a day

- Q_{vt} which represents the tendencies to internal energy from hydrometeor/air interaction processes as condensate falls at terminal velocity

- the heat conduction term where κ is the thermal conductivity and is often only important at small scales (order $1\,\text{mm}$)

Through using the material derivative and Equations 3.7 and 3.9-3.11 as well as the following relationships for the specific heats,

$$\frac{de_a}{dT} = c_{va}, \qquad \frac{de_v}{dT} = c_{vv}, \qquad \frac{de_l}{dT} = c_l(T_l), \qquad \frac{de_f}{dT} = c_f(T_f), \qquad (3.15)$$

the following can be obtained for air temperature T,

$$c_{vm}\frac{DT}{Dt} = -\frac{p}{\rho_a}\frac{\partial u_j^a}{\partial x_j} + Q_r + \dot{Q} + (L_{lv} - R_v T)\,\dot{q}_{cond}$$

$$+ (L_{fv} - R_v T)\,\dot{q}_{dep} + L_{fl}\dot{q}_{frz} - q_l v_j^l\frac{\partial e_l}{\partial x_j} + q_f v_j^f\frac{\partial e_f}{\partial x_j},$$

$$(3.16)$$

where $\dot{Q}$ represents the entire right-hand side of Equation 3.14 divided by ρ_a and T is assumed to be the same as the hydrometer temperatures. The latent heat, L_{ab}, is the change in internal energy during a phase change of a to b and $c_{vm} \equiv c_{va} + c_{vv}q_v + c_l q_l + c_f q_f$ is the specific heat of cloudy air at constant volume.

3.1.2.5 Pressure Equation

A prognostic equation for pressure is derived in Cotton et al. (2010) by using the equations of mass continuity, internal energy and the equation of state,

$$\frac{Dp}{Dt} = -\frac{c_{pm}}{c_{vm}}p\frac{\partial u_j^a}{\partial x_j} + \frac{p}{c_{vm}T}(Q_r + \dot{Q} + W_T)$$
$$+ \frac{p}{c_{vm}T}(L_{lv}\dot{q}_{cond} + L_{fv}\dot{q}_{dep} + L_{fl}\dot{q}_{frz}) - \frac{R_v c_{pm}}{R_m c_{vm}}p(L_{lv}\dot{q}_{cond} + L_{fv}\dot{q}_{dep}), \tag{3.17}$$

where $c_{pm} \equiv c_{pa} + c_{pv}q_v + c_l q_l + c_f q_f$ is the specific heat of cloudy air at constant pressure. While W_T represents the transport of internal energy by condensate that falls relative to the dry air,

$$W_T \equiv -q_l v_j^l \frac{\partial e_l}{\partial x_j} - q_f v_j^f \frac{\partial e_f}{\partial x_j} \cong q_l v_{tl} \frac{\partial c_l T}{\partial z} + q_f v_{tf} \frac{\partial c_f T}{\partial z} \tag{3.18}$$

where $v_{t\chi}$ is the terminal fall velocity of χ and where it is assumed that the hydrometeor temperature is equal to the air temperature.

3.1.2.6 All Governing Equations

To summarise, the governing equations solved for velocity and moisture in the numerical model are listed below,

$$\frac{\partial u_i}{\partial t} + c_p \theta_p \frac{\partial \pi'}{\partial x_i} = ADV(u_i) + \delta_{i3}g\left(\frac{\theta_p}{\theta_{\rho 0}} - 1\right) + T_i + D_i + N_i, \tag{3.19}$$

$$\frac{\partial q_v}{\partial t} = ADV(q_v) - \dot{q}_{cond} - \dot{q}_{dep} + T_{qv} + D_{qv},$$
$$\frac{\partial q_l}{\partial t} = ADV(q_l) + \dot{q}_{cond} - \dot{q}_{frz} + \frac{1}{\rho_a}\frac{\partial \rho_l v_j^l}{\partial x_j} + T_{ql} + D_{ql}, \tag{3.20}$$
$$\frac{\partial q_f}{\partial t} = ADV(q_f) + \dot{q}_{dep} + \dot{q}_{frz} + \frac{1}{\rho_a}\frac{\partial \rho_f v_j^f}{\partial x_j} + T_{qi} + D_{qi}.$$

The advection operator used in the model for a variable α is,

$$ADV(\alpha) = -u_j\frac{\partial \alpha}{\partial x_j} + \frac{1}{\rho_0}\left[-\frac{\partial \rho_0 u_j \alpha}{\partial x_j} + \alpha\left(\frac{\rho_0 \partial u_j}{\partial x_j}\right)\right]. \tag{3.21}$$

Equation 3.16 can be expressed in terms of the potential temperature perturbation (θ'), where $\theta \equiv T/\pi$, by using the equation of state,

$$\frac{\partial \theta'}{\partial t} = ADV(\theta) - \theta \left(\frac{R_m}{c_{vm}} - \frac{R_a c_{pm}}{c_{pa} c_{vm}} \right) \frac{\partial u_j^a}{\partial x_j} + T_\theta + D_\theta + N_\theta + \frac{c_{va}}{c_{vm} c_{pa} \pi} (Q_r + \dot{Q} + W_T)$$

$$+ \frac{c_{va}}{c_{vm} c_{pa} \pi} (L_{lv} \dot{q}_{cond} + L_{iv} \dot{q}_{dep} + L_{il} \dot{q}_{frz}) - \theta \frac{R_v}{c_{vm}} \left(1 - \frac{R_a c_{pm}}{R_m c_{pa}} \right) (\dot{q}_{cond} + \dot{q}_{dep}). \quad (3.22)$$

Here the reference potential temperature is from the base-state the model is initiated with. Equation 3.17 can be expressed with the non-dimensional pressures π as,

$$\frac{\partial \pi'}{\partial t} = ADV(\pi) - \frac{R}{c_p} \frac{c_{pm}}{c_{vm}} \pi \frac{\partial u_j^a}{\partial x_j} + \frac{R\pi}{c_v \theta} (T_\theta + D_\theta + N_\theta + Q_r + \dot{Q} + W_T) +$$

$$\frac{R}{c_p} \frac{c_{pm}}{c_{vm}} (L_{lv} \dot{q}_{cond} + L_{iv} \dot{q}_{dep} + L_{il} \dot{q}_{frz}) - \frac{R}{c_p} \frac{R_v c_{pm}}{R_m c_{vm}} \pi (\dot{q}_{cond} + \dot{q}_{dep}) + \frac{R}{c_v} \frac{\pi}{\epsilon + q_v} (T_{qv} + D_{qv}).$$

$$(3.23)$$

Bryan and Fritsch (2002) discusses how the advection terms are written in this form rather than as the advection term (the second on the left hand side) in Equation 3.6 as it has been shown to sometimes improve conservation of the variable being advected. The T_i terms represent tendencies from turbulence (see Section 3.1.4.1), the D terms represent optional tendencies from other diffusive processes and have been excluded in the simulations in this study and N represents Newtonian relaxation (i.e Rayleigh damping). The Coriolis force has been disregarded as it is not used in the simulations discussed in this study. W_T as described in Section 3.1.2.5 represents the transport of internal energy by condensate that falls relative to air and is neglected in this study.

3.1.3   Pressure Solver

The advection of velocities and scalars is integrated with fifth-order horizontal and vertical advection schemes with implicit diffusion, with a Klemp-Wilhelmson (K-W) time-splitting, vertically implicit, horizontally explicit pressure solver. The details of this are explained in the following paragraphs.

Motions within the atmosphere occur with a wide range of frequencies. One way to account for this is to use time-splitting methods, such that terms associated with faster modes are integrated on a smaller time step which maintains stability, while terms associated with slower modes are integrated on a larger time step for efficiency. As CM1 is a non-hydrostatic model, it solves equations which are fully compressible and therefore includes sound waves. While sound waves are not meteorologically significant

they travel at high speeds which require a smaller time step to maintain numerical
stability.

In this study, the K-W (Klemp and Wilhelmson 1978) time-splitting method has been
used. In the K-W method the fast and slow mode operators are never completely
split, instead all the terms in the governing equations are left coupled together and
those terms governing slowly evolving processes are updated less frequently than those
responsible for the propagation of high-frequency, physically insignificant waves (Dur-
ran 2013). The advection, diffusion and buoyancy tendencies in the momentum and
pressure equations are kept constant during the K-W sub-steps, allowing for a reduced
equation set during these shorter time steps and higher efficiency. The horizontal prop-
agation of the sound waves has a time-centred explicit treatment while the vertical
propagation is treated implicitly. The vertically implicit differencing scheme allows the
shorter time step to be independent of the vertical resolution which is important for
efficiency, and thus the step only depends on the horizontal grid length (Georg et al.
1994). Only the momentum and pressure equations need to be split, as although all
the terms in Equations 3.19-3.23 have some influence on sound waves, only the pres-
sure gradient terms in the momentum equations and divergence terms in the pressure
equation control rapid sound wave propagation Durran and Klemp (1983).

3.1.4   Turbulence

3.1.4.1   Sub-grid Turbulence Scheme

The turbulent kinetic energy (TKE) sub-grid turbulence scheme is used. The American
Meteorological Society (2021i) defines TKE as the mean kinetic energy per unit mass
associated with eddies in turbulent flow. The CM1 scheme is based on that described
in Deardorff (1980) with grid increments denoted by Δx, Δy and Δz. The subgrid-
scale turbulence energy is defined as $\bar{E} = \frac{1}{2}(\overline{u_i' u_i'})$ where over-bars signify the Reynolds
average over a volume $V = \Delta x \Delta y \Delta z$ centred at the point of interest while primes
indicate the local deviations from that point.

The predictive equation for $\bar{E}$ is (Bryan 2017),

$$\frac{\partial \bar{E}}{\partial t} = -\frac{\partial}{\partial x_i}(\bar{u}_i \bar{E}) + K_m S^2 - K_h N_m^2 + \frac{1}{\rho}\frac{\partial}{\partial x_i}\left(2\rho K_m \frac{\partial \bar{E}}{\partial x_i}\right) - \epsilon$$

where ϵ is the dissipation which is parametrised as,

$$\epsilon = \frac{c_\epsilon e^{3/2}}{l}, \tag{3.24}$$

and $S^2 = 2S_{ij}S_{ij}$ is the deformation with $S_{ij} = \frac{1}{2}\left(\frac{\partial u_i}{\partial x_j} + \frac{\partial u_j}{\partial x_i}\right)$. N_m^2 is the squared Brunt-Väisälä frequency which has different formulae for saturated and sub-saturated air. The eddy viscosity,

$$K_m = c_m l \bar{E}^{1/2},$$

is the subgrid-scale eddy coefficient for momentum. While,

$$K_h = c_h l \bar{E}^{1/2},$$

is the eddy diffusivity, a sub-grid eddy coefficient for scalar quantities. Parameters c_m, c_h, l must be specified to close these equations. In CM1, while c_m has a default value of 0.10 the other parameters have a stability dependence that is formulated to reduce sub-grid-scale mixing in statically stable conditions and $N_m^2 > 0$,

$$\begin{aligned}
c_h &= 1 + 2\frac{l}{\Delta}, \\
c_\epsilon &= 0.2 + 0.787\frac{l}{\Delta} \\
l &= \left(\frac{2}{3}\frac{e}{N_m^2}\right)^{1/2},
\end{aligned} \tag{3.25}$$

where Δ is a measure of the grid size, e.g., $\Delta = (\Delta x \Delta y \Delta z)^{1/3}$ and when $N_m^2 \leq 0$, $l = \Delta$. The settings for c_m, c_h and l ensure that turbulence is inactive when the Richardson number ($Ri = \frac{N_m^2}{S^2}$), is greater than 0.25. The Richardson number is defined by the American Meteorological Society (2012) as the dimensionless ratio of buoyant suppression of turbulence to shear generation of turbulence.

The scheme is extended from Deardorff (1980), with the adaptation described in Sullivan et al. (1994), whereby the model preserves the usual sub-grid-scale eddy viscosity but explicitly includes a contribution from the mean flow and a reduction of the contributions from the turbulent fluctuations near the surface in order to address the common problem of excessive mean vertical wind shear near the surface in LESs.

3.1.5 Microphysics

Microphysics describes the phase changes between different states of water and the formation and growth of liquid and solid cloud droplets and hydrometeors, the accurate representation of which is of key importance when modelling the state of the atmosphere. The vast majority of models employ bulk schemes in which the particle size distribution for each species is specified separately (Wang 2002). To account for phase changes, Bryan and Fritsch (2002) describe how the model uses a saturation adjustment technique whereby the equations are advanced forward in two steps: a dynamical step and a microphysical step. In the dynamical step, the terms involving phase change are neglected and are the sole inclusion in the microphysics step. Pressure tendencies due to phase changes are included in the microphysics step. Since changes in pressure affect the saturation vapour pressure, an iterative scheme is used to approach a value for the condensation for which θ converges.

CM1 includes all terms in the pressure and thermodynamic equations in order to conserve total energy. The Morrison four-class double-moment explicit moisture scheme is used (Morrison et al. 2005), which predicts the number concentrations, N, and mixing ratios, q, of four hydrometeor species (droplets, cloud ice, rain and snow). The microphysical processes shown in Figure 3.1 between the various water species represent the source and sink terms for q and N in the kinematic equations.
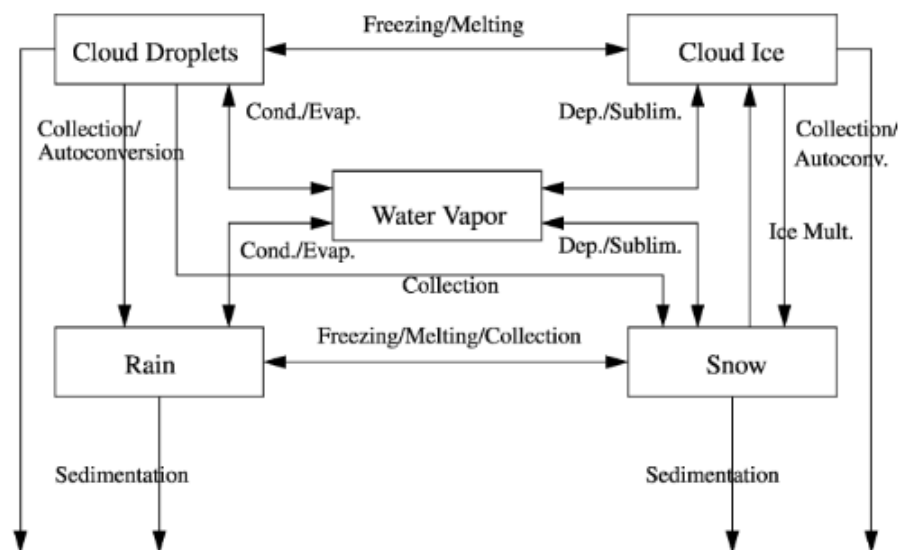
Figure 3.1: From Morrison et al. (2005), box diagram of the microphysics scheme.

3.1.6 Boundary Conditions

3.1.6.1 Open-Flow Radiative Boundaries

The locations of both the lateral boundaries and the top of the domain have been chosen somewhat arbitrarily as it is impractical to include all of the surrounding fluid. It is therefore important for these boundaries to mimic the presence of the surrounding fluid which would exist there. In order to obtain this, boundary conditions should follow the 'radiation condition' and allow outward travelling disturbances to pass through without generating spurious reflections that propagate back toward the interior (Durran 2001). However, it is difficult to design boundaries where the energy radiated from the simulated convection scatters to infinity while no energy is radiated back into the domain. Therefore, an approximation of this radiation condition must be introduced.

3.1.6.1.1 Open-Flow Lateral Boundaries The Durran-Klemp formulation (Durran and Klemp 1983) is used for the open-radiative lateral boundaries in this study which allows gravity waves to exit the computational domain with minimal reflection. In this approach, the phase speed c of a gravity wave impinging on the east boundary (without loss of generality) is estimated, and the flow variables are advected out at the speed $c^* = u + c$ ($c^* = u - c$ at the west boundary). c^* is chosen to be representative of the dominant modes and therefore will be incorrect for certain nodes and so produce reflections which will increase with the deviation of each particular c from c^*. At each vertical level k, c^* is estimated as in the original theory of Orlanski (1976), for an arbitrary prognostic variable ψ, by numerically calculating a propagation velocity from the neighbouring grid points,

$$c_k^* = -\frac{\partial \psi/\partial t}{\partial \psi/\partial x} = \frac{\Delta x}{\Delta t} \frac{u_{b-1,k}^{t-\Delta t} - u_{b-1,k}^t}{u_{b-1,k}^{t-\Delta t} - u_{b-2,k}^{t-\Delta t}}, \qquad (3.26)$$

where ψ has been replaced with u and b is the grid-point at the right of the domain. The speed of propagation is then calculated by averaging c_k^* vertically. In order to maintain stability c^* is bounded by zero, and the maximum speed for which the numerical time step is stable,

$$c^{*t} = \sum_{k=1}^{N} min\left[u_{max}, max(0, c^*)\right], \qquad (3.27)$$

(Durran and Klemp 1983). The maximum speed $u_{max} = \Delta x/\Delta t$, following the Courant-Fredrichs-Lewy (CFL) condition, which requires that the solution of a finite-difference equation must not be independent of the data that determines the solution to the associated partial differential equation (Durran 2013). Through theoretical analysis, Klemp and Lilly showed that the error about $c^* = c$ is asymmetric and that it is therefore better to overestimate rather than underestimate the magnitude of c^*. Therefore the calculations have been biased toward an outward directed phase speed by setting any inward phase speeds to zero prior to averaging.

3.2 Overview of Cloud Model 1 Configuration

3.2.1 Boundary Conditions

The lower boundary condition is set to a flat, rigid no-slip surface while a free-slip boundary condition is applied to the top of the domain. If the upper boundary condition is totally reflective, then vertically propagating internal gravity waves which are artificially reflected may significantly distort the evolving storm structure (Klemp and Durran 1983). The radiation boundary condition is approximated by adding an absorbing layer, which gradually increases in strength, to the top of the domain. In these simulations a Rayleigh damping sponge layer has been used from $20\,\mathrm{km}$ with an e-folding frequency of $1/300\,\mathrm{s}^{-1}$. The damping zone acts on u, v, w and θ only. Horizontal boundaries are open-radiative in the across-line (west to east) direction and periodic in the along-line direction. The latter allows the squall line to extend across the entire domain in this direction.

3.2.2 Microphysics

The Morrison four-class double-moment explicit moisture scheme is set with hail for the large ice category. No radiation, surface heat and moisture fluxes are included in the simulations analysed in this thesis. This is to both aid in the isolation of the role of shear and as simulations were intended to represent nocturnal squall lines.

3.2.3 Default Resolution and Domain Size

3.2.3.1 Domain Size

In the vertical, the domain is 23.4 km deep. This height has been limited by the radiosonde data available from the African Monsoon Multidisciplinary Analysis (AMMA) campaign used in this study to produce the control profile the simulations are initiated with. The domain extends 1600 km × 60 km in the horizontal (across squall line, x, and along squall line, y, directions respectively) with 1 km grid-spacing. The much larger domain size in the x direction has been chosen in order to limit the impact of reflections from the open-flow lateral boundaries. The y-domain has been selected in consistency with previous studies (Bryan et al. 2003).

3.2.3.2 Resolving the Boundary Layer

The model includes an analytic stretching function (Wilhelmson and Ching-Sen Chen 1982) to create smoothly varying grid spacing as well as a smooth geometric stretching for the vertical direction. Vertically, the stretching layer may be placed arbitrarily in space i.e. in the middle. The number of vertical levels must follow,

$$n_z = \frac{s_b}{dz_b} + \frac{z_t - s_t}{dz_t} + \frac{s_t - s_b}{0.5(dz_b + dz_t)},$$

where s is the level, z_t the total height of the domain, dz the grid-spacing and the subscripts b, t indicate the bottom and top of the stretching region respectively. The values used in this study, unless otherwise stated, included a stretching layer which starts at the surface, $s_b = 0$ km, with grid spacing of $dz_b = 25$ m to 500 m from $s_t = 8.4$ km upwards. This results in 62 vertical levels.

3.2.4 Tracer Setup

Ten different passive tracers have been inserted into the domain in some simulations. One set of five tracers initiated â€˜westâ€™ of the storm beginning at 0 km to 825 km and one set east of the storm beginning at 900 km to the end of the domain. This set-up has been chosen to clearly differentiate the inflow from the rear and the front of the squall line. Additionally, throughout this study the focus has been on mature squall lines, therefore the tracers have been initiated at two hours after initiation, and are therefore undisturbed by the spin-up. Each tracer is initiated with a constant value

of $1\,\mathrm{gkg}^{-1}$ mixing ratio and there are no sources, sinks or sedimentation of the tracers.

3.2.5 Base-state Sounding

To initiate the model a sounding requires values at the surface for pressure, potential temperature and water vapour mixing ratio, q_v. At increasing heights θ, q_v and components of west-east and south-north velocities u, v are required.

3.2.5.1 Configuration of Test cases

To ensure the model was working as expected two simulations were completed to imitate cases discussed in Weisman and Rotunno (2004) and Bryan and Fritsch (2002). A quantitative assessment of the differences suggested structural differences of a magnitude which were likely repercussions from the initial random noise.

3.3 Creating a Representative Profile

The initial conditions used as a control for the model were taken from radiosonde measurements made at Niamey in Niger, latitude 13° 29'N and longitude 2°10'E, during the AMMA 2006 field campaign (Parker et al. 2008). Niamey which is west of a mountainous area, see Figure 3.2, may not give a profile that is representative of the whole of West Africa. However, these are by far the most comprehensive observations of the atmospheric profile over West Africa; a region where analyses exhibit major biases (Roberts et al. 2015). As it is an idealised simulation and it is the variations from the control run that are of real interest an initial profile that roughly represents an area of the Sahel is considered satisfactory.

Figure 3.2: ©TEAM welt-atlas.de, physical map of Niger. Niamey is in the south-west of the country.

It is generally agreed that the humidity measured by radiosondes can have some errors depending on sonde type, relative humidity, temperature and age of the sensor. In particular, dry biases in radiosonde measurements have been identified for a long time (Crutcher and Eskridge 1993). Agustí-Panareda et al. (2009) found that dry bias in radiosonde relative humidity over the Sahel region was found to have a strong seasonal cycle, indicating a need to consider dependence of bias on magnitude of observed relative humidity. They found dry biases that are typically between 5% and 30% for relative humidity. This group applied a refined empirical correction method to the AMMA data which takes the dependence of the bias on the observed humidity into account. The correction method was validated using global positioning system signals; total column water vapour confirmed the method is able to correct for a large part of the dry biases associated with the different sonde types.

The corrected humidity radiosonde data is used in this project due to the impact of humidity on the development of convection and therefore its importance in the WAM. Only the six hour interval radiosondes (starting from midnight) which used the newer, and more reliable, RS92 sondes were used to find the average profiles. Each individual profile was smoothed using the Savitzky-Golay filter (Savitzky and Golay 1964) before it was fit to the grid-size used in the model. This process was repeated for the final average profile obtained.

Provod et al. (2016) generated a seasonal characterisation of cold pool properties by quantifying related changes in surface meteorological data including temperature decreases of $2° - 14\,°C$, pressure increases of $0 - 8\,hPa$, and wind gusts of $3 - 22\,ms^{-1}$. Through applying these characterisations 38 cold pools that passed over Niamey dur-

ing the AMMA campaign (1 June to 30 September 2006) were identified. To produce
atmospheric profiles representative of those in which squall lines were observed to oc-
cur, only soundings from within the twelve hours immediately before cold pools passed
over Niamey, as identified by Provod et al. (2016), were considered. Furthermore, only
soundings from the evening, night and early morning (1800, 0000 and 0600 UTC) are
considered since squall lines usually form in the evening and persist overnight. The
model will be run for eight hours and so this profile is representative of that period.
Throughout this study, all times will refer to UTC with sunrise and sunset in Niamey
(where local time is UTC+1) occurring at approximately 0530 and 1815 UTC respec-
tively.

As this profile did not produce a sustained squall line, several different methods were
tried to construct a control profile from the radiosondes. Eventually, the method chosen
included finding the average of the top 25% of pre-storm nocturnal profiles with the
highest convective available potential energy (CAPE). This mean profile, Figure 3.3, has
a CAPE of 1860 J/kg and convective inhibition (CIN) of 52 J/kg. There is a decrease
in humidity from 750-600 hPa which is indicative of the Saharan air layer (SAL). The
hodograph shows south-westerly winds above the surface with the nocturnal low-level
jet (LLJ) spanning from 960-900 hPa with a peak in westerlies at 950 hPa. Above
900 hPa there is a continuous decrease in westerly winds while southerly winds sustain
around $3.8 \, \text{ms}^{-1}$ until 800 hPa when they start to weaken. The African easterly jet
(AEJ) spans from 725 hPa to a maximum at 600 hPa which can more easily be seen in
Figure 3.4. It is also worth noting the easterly winds above 250 hPa as these control
the spread of the cloud anvil.

If compared to the mean July-August Niamey profile the pre-storm profile has higher
CAPE and lower CIN and a stronger westerly component of the LLJ but weaker AEJ
at 600 hPa. The profile allows persistent mesoscale convective systems (MCSs) in this
idealised environment with no imposed large-scale convergence. In reality there will
probably be some large-scale convergence to aid convection. Thus, in the absence
of large-scale forcing a slightly more favourable profile is required in order to get a
sustained squall line. This is preferable to applying large-scale forcing as it keeps the
set-up in these idealised simulations simple. Additionally, selecting the top 25% of
profiles provides the best method of studying the most extreme storms, which are of
the most interest.

The CAPE and CIN (calculated for parcels of air at different height levels of the profile)
and water vapour mixing ratio (q_v) are shown in Figure 3.4. There is moist air with
CAPE from the surface to above the surface air's lifting condensation level (LCL) at
900 hPa and just below the surface air's level of free convection (LFC). A system speed
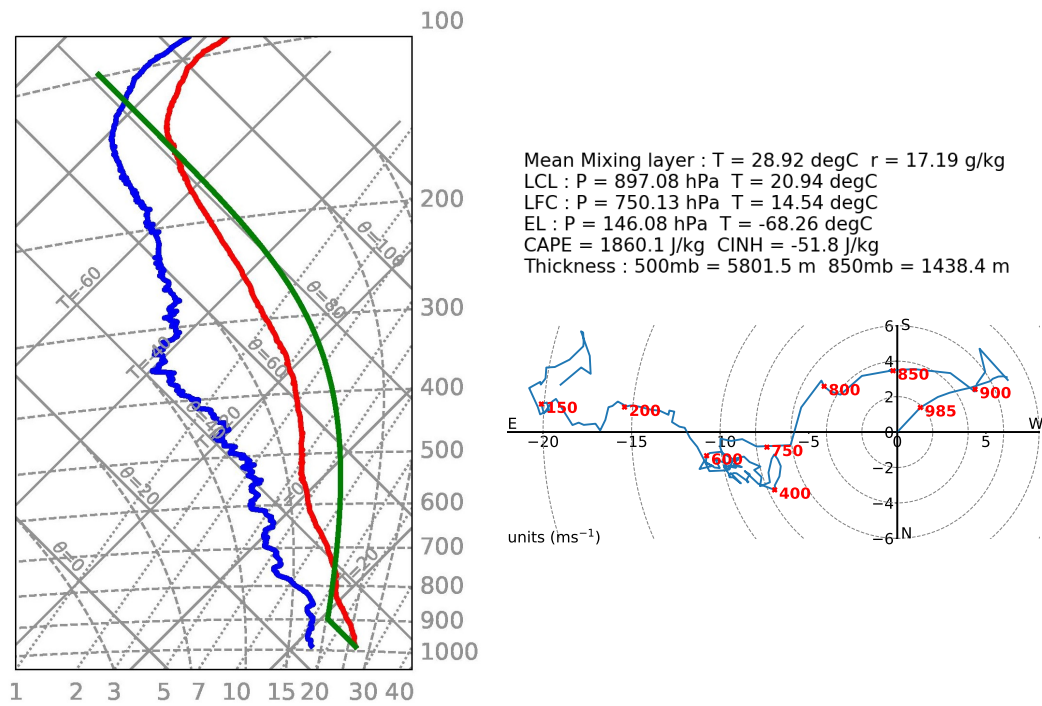
Figure 3.3: Tephigram and hodograph of the control profile created from selecting the top 25% of profiles with the highest CAPE and lowest CIN and finding the average. The selections were made from evening, night and early morning (18:00, 00:00 and 06:00 UTC) radiosonde profiles from 12 hours before cold pools were recorded at Niamey in July and August 2006. On the tephigram the units are hPa for the y-axis, gkg^{-1} for the x-axis and °C for all temperatures shown. Wind direction on the hodograph represents winds from that direction. q refers to the water vapour mixing ratio.
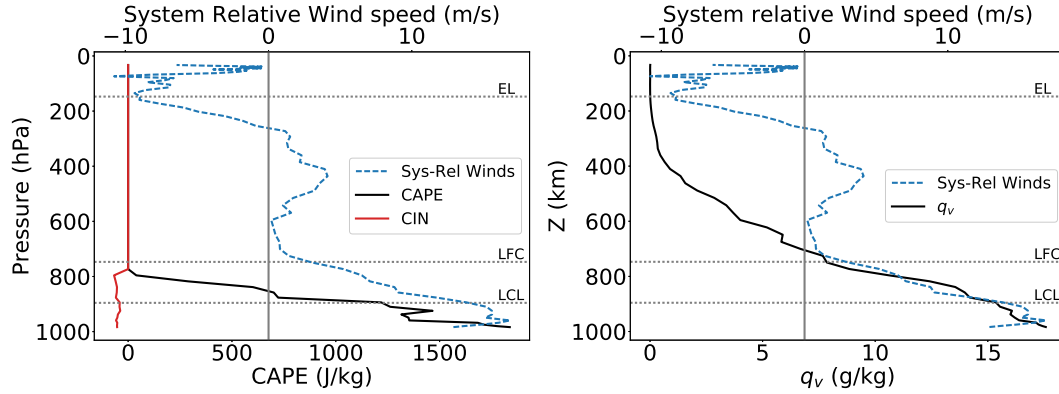
Figure 3.4: The CIN, CAPE and water vapour mixing ratio at different heights for the
control profile. The LCL, LFC and equilibrium level (EL) for a parcel at the surface
have been marked. The system relative wind speed at each level is relative to a system
speed of $10.7\,\mathrm{ms}^{-1}$. This is the average speed when sustained of systems produced by
the control profile.

of $10.7\,\mathrm{ms}^{-1}$, the average speed of squall lines produced with the control profile when
sustained, has been used. The system relative wind speed is also plotted and shows
that the majority of the inflowing air comes from below $750\,\mathrm{hPa}$ and particularly at the
height of the LLJ. Although the CAPE of the air above $800\,\mathrm{hPa}$ is zero there is still
moisture flowing into the storm at this level.

3.4 Exploring Regional Decadal and Diurnal Trends through Modifying the Control Profile

Having obtained a realistic and representative profile of the Sahel region from radioson-
des taken in Niamey (Figure 3.3), this profile could then be modified to explore how
changes to the region's environmental thermodynamic and wind profiles, over a decadal
or diurnal time frame, could affect mature squall lines. Changes that are considered in
this study include linear trends calculated from ECMWF Re-Analysis (ERA)-Interim
data (Berrisford et al. 2011) for the period of 1982 to 2017, high future concentra-
tion scenario predictions from the Coupled Model Intercomparison Project 5 (CMIP5)
(Taylor et al. 2012) for the Niamey region for the end of this century (both discussed
in Chapter 4) and diurnal variations within those measured in the AMMA campaign
(Chapter 5).

3.4.1 Quantitative Analysis of Numerical Simulations

In order to quantify the impact of temperature and humidity variations as well as the role of environmental wind shear and in particular the roles of the African Easterly Jet and the nocturnal monsoon winds, methods were established to quantitatively compare simulations of squall lines and their cold pools. The change in pressure and potential temperature from the original profile can be used to give an indication of cold pool intensity. Comparing maximum vertical velocities and cloud top heights gives an indication of the strength of updrafts. Finally, the total accumulated rainfall and the rate of rainfall can indicate rain intensity. Other comparisons that can be made include the speed and the height of the cold pool.

Measures of maximum rainfall or velocity can be calculated over the whole domain, as an average of the maximum at each cross-section along the line of the storm or over a vertical cross-section which has been averaged along the line of the storm. These diagnostics describe quite separate aspects of the storm. For instance a maximum upward vertical velocity across the whole domain will indicate the strength of the strongest updrafts while averaging along the line of the storm will represent bulk measures. The statistics used in this study, and listed in Table 3.1, give an indication of the intensity of the storm. This table also includes diagnostics from the layer-lifting model of convection (LLMC), Section 2.2.3.1.

In this study, the cold pool front is identified where the temperature perturbation from the original profile changes from positive to negative at $25\,\mathrm{m}$ altitude. Then the propagation speed (PS) of the system is defined as the average speed of the front edge of the cold pool during the period the storm is considered to be steady which is consistent with Alfaro (2017).

Table 3.1: Table describing diagnostics and variables.

Variable	Description
ICAPE	From Alfaro (2017), system-relative inflow of CAPE integrated over all z (Equation 2.12).
$CAPE_{ll}$	From Alfaro (2017), a diagnostic which describes the system relative inflow of CAPE (Equation 2.13).
w_{ll}	From Alfaro (2017), an indicator for updraft strength (Equation 2.14).
PR_{ll}	From Alfaro (2017), an indicator for precipitation rate (see Equation 2.15).
$\bar{w}_{max}$	The vertical velocity is averaged over the y domain (along the line of storm). The maximum in the x-z plane is then found of this average.
w_{max}	The maximum value of vertical velocity across the entire domain
$\hat{w}_{max}$	The maximum vertical velocity (in the x-z plane) averaged over (the along squall-line) y-direction.
$\bar{R}$	Mean rain rate where raining. The mean value of all rain rates above a threshold of $1\,\mathrm{mmh}^{-1}$.
R_{tot}	The rate of total rainfall across the domain.
$\hat{R}_{max}$	The maximum rain rate (in the x-z plane) averaged over (the along squall-line) y-direction.
Upward Mass Flux	The sum of all upward mass flux across the domain. As this includes the entire domain the magnitude will be much larger than the convective mass flux.
ΔU	The maximum vertical difference in the wind vector from the LLJ to the AEJ
Total liquid and solid water content	Marks the edge of the cloud in cross-sections of simulations and is calculated where the sum of the total cloud, snow, ice, rain and graupel in each grid-space is above $0.01\,\mathrm{gkg}^{-1}$.
Precipitable content	Marks the edge of the precipitating region in cross-sections of simulations and is calculated where the sum of the total snow, rain and graupel in each grid-space is above $0.01\,\mathrm{gkg}^{-1}$.

3.4.1.1 Triggering Convection

There was some difficulty in producing squall lines that reached a steady state for the thermodynamic profile measured during the AMMA campaign with changes representative of the end of the 21st century added on (CMIP5 changes). Warm and cold line thermals of varying temperatures were tested to find whether the unexpectedly quick demise of the storms were a consequence of the initiation or could be considered a characteristic of the environmental changes predicted for the end of the century.

All the line thermals considered were created in the shape of an ellipse with a major horizontal axis of 40 km in the x direction and a minor axis of 3 km in the vertical and continuous in the y direction. Additionally, a combination of a cold and warm line

thermal was also tested. The cold line thermal was always placed $80\,\mathrm{km}$ downstream or 'west' of the warmer bubble. Storms were considered to no longer be sustained when $\hat{w}_{max}$ fell below $5\,\mathrm{ms}^{-1}$. The largest line thermals tested initially caused intense convection but after the initial spin-up failed to sustain. From the perturbations tested, Table 3.2, it was found that cold line thermals produced longer lasting storms. Applying forced convergence as an alternative method was also attempted with a maximum intensity of u-forcing of $0.2\,\mathrm{ms}^{-2}$ over a radius in z of $10\,\mathrm{km}$ and with varied x-radius of 10, 20 and $40\,\mathrm{km}$ tested. The forcing continued with maximum intensity for $50\,\mathrm{min}$ and then was turned off completely at one hour. For the CMIP5 case none of the setups with forced convergence produced squall lines which sustained for longer than 3 hours. A greater maximum u forcing with $0.4\,\mathrm{ms}^{-2}$ was applied but with no more success. It can therefore be concluded that the thermodynamic profile with the predicted CMIP5 changes applied is not conducive to producing long lasting storms in this simple experiment which could be due to a lack of large scale flows although lack of representation of radiation or synoptic variability may also be important.

Table 3.2: Initial perturbation and the lifetime of storms (h) in the CMIP5 predicted environment. Storms are only considered to be 'active' when $\hat{w}_{max}$, see Table 3.1, is above $5\,\mathrm{ms}^{-1}$.

Perturbation	0K	-0.25K	-0.5K	-1K	-2K	-3K
0K	0	4.75	5	5.25	5	4.5
0.25K	4.5	–	–	–	4.5	–
0.5K	3.75	–	–	–	–	–
1K	3.25	–	–	3.25	3.25	–
2K	2	–	–	3.25	3.25	–
3K	1.5	–	–	–	–	3.25

From evaluating the results shown in Table 3.2, a north-south $-2\,\mathrm{K}$ line thermal was selected as it produced one of the longest lived storms with the CMIP5 profile and had been previously used for simulations with the control profile. The perturbation had a maximum amplitude of $-2\,\mathrm{K}$, and is located $3\,\mathrm{km}$ above ground and at $x = 912\,\mathrm{km}$. The perturbation decreases to zero in a radius of $40\,\mathrm{km}$ in the horizontal and $3\,\mathrm{km}$ vertically. The temperature perturbation of the line thermal is at a maximum at the centre, (x_0, z_0), and decreases to zero at the edges with a sinusoidal shape deter-

mined by $\cos^2(\frac{\pi}{2}\beta)$ where $\beta = \sqrt{(\frac{x-x_0}{x_r})^2 + (\frac{z-z_0}{z_r})^2}$. A random seed number generator is used to add random noise of maximum amplitude $0.2\,\mathrm{K}$ to the line thermal perturbation at every point to break the symmetry and encourage more rapid development of three-dimensional flows. Over the remainder of the domain the initial conditions are horizontally homogeneous.

Chapter 4

Understanding mechanisms for trends in Sahelian squall lines: Roles of thermodynamics and shear

Recent observational studies have revealed a persistent increase in the frequency of extreme rainfall during the West African monsoon (WAM) over the last fifty years while showing evidence of a simultaneous deficit in rainfall occurrence (Panthou et al. 2014; Taylor et al. 2017). This trend is predicted to continue under climate change, but by how much is an active area of research. A warmer climate will allow for a greater concentration of water vapour in the atmosphere, allowing heavier rainfall. Temperature increases, including the magnification of the Saharan heat low (SHL) during the summer months, will produce other effects including a stronger low-level jet (LLJ) and African easterly jet (AEJ) and thus an increase in the vertical wind shear across the Sahel region. Increased wind shear has been suggested to have been a key driver of the recent intensification of squall lines experienced in the Sahel (Taylor et al. 2017). However, previous modelling has not yet corroborated this (Fitzpatrick et al. 2020) and as is discussed in Chapter 2.2.3 several theories exist for the role shear plays in deep moist convection. Thus, the changes to temperature, moisture and the environmental wind profile under climate change will influence the mechanisms of the storms themselves which are complex and uncertain due in part to ambiguity over the role shear plays.

In this chapter, idealised simulations of squall lines will be used to bridge the gap

between observations and theory and to shed some light on how decadal trends in Sahelian temperature and its impact on wind shear have affected the fundamental processes of the region's squall lines. The chapter has four main hypotheses that are tested: (1) recent increases in shear from both strengthened monsoon south-westerlies and the AEJ, caused by Saharan warming, have increased the intensity of squall lines (Taylor et al. 2017), (2) recent changes to the environmental thermodynamic profile may have influenced squall line intensity and could be comparable with the effects of shear, (3) the system-relative inflow of convective available potential energy (CAPE) and water vapour is key to determining squall line updraft speeds and rainfall so that the layer-lifting model of convection (LLMC) can explain the modelled impacts of changing profiles, (4) predicted future increases in shear, temperature and humidity will cause an increase in storm intensity.

This chapter uses the Cloud Model 1 to run idealised large-eddy simulation (LES) experiments to investigate the impact of changing environmental thermodynamic and wind profiles on squall lines representative of those seen in the West African Monsoon. Section 4.1 outlines the control profile that is used and the sensitivity simulations based on historical and future climate changes. The changes considered are those from reanalysis from the period of 1982 to 2017 to allow comparison with the results of Taylor et al. (2017). Whether the idealised simulations produce consistent changes in storm intensity to those discussed in Taylor et al. (2017) from a small environmental change taken from trends in reanalyses is tested. Further experiments consider possible future changes to squall line intensity by adding, to the control profile, environmental changes predicted by the Coupled Model Intercomparison Project 5 (CMIP5) for the end of this century under a high emissions scenario in order to explore possible future impacts on this vulnerable region. The LLMC (Chapter 2.2.3.1) is applied to the LES results to investigate whether it successfully captures variations in modelled squall line intensities. This is a recent theory and in this study a unique test of this LLMC in tropical conditions is performed. Section 4.2 discusses the relative roles of wind shear and thermodynamic environments on squall lines and whether the LLMC is consistent with the changes in squall line characteristics seen in the results from the idealised simulations. Finally, Section 4.3 presents some conclusions.

4.1 Methods

4.1.1 Past Decadal Trends in Thermodynamics and Shear from ERA-Interim Analyses

Having obtained a realistic and representative profile of the Sahel region from radiosondes taken in Niamey in Chapter 3.3 (Figure 4.8a), how that profile may have changed over recent decades is now considered. Figure 4.1 shows changes in winds and humidity in ECMWF Re-Analysis (ERA)-Interim from 1982 to 2017 at selected pressure levels across the wider region. Low-level moisture has increased north of and around Niamey (Figure 4.1a), consistent with an increase in the low-level south-westerly monsoon winds north of Niamey (Figure 4.1d). Changes in the AEJ west of 10°E are small, with a weak $0.9\,\mathrm{ms}^{-1}$ increase in AEJ north of Niamey (Figure 4.1b). There is an increase in the magnitude of the shear vector (Figure 4.1c) of 0.7×10^{-3} s^{-1} north of Niamey (16 to 18°N) and a smaller change of 0.2×10^{-3} s^{-1} around Niamey (10 to 14°N). Within the marked white box, (15°E-15°W and 16-17°N), there is an increase in low-level water vapour mixing ratio and shear (Figures 4.3a and 4.4).

To allow comparison with Taylor et al. (2017), and test hypothesis-1, changes in the mean profiles of water vapour mixing ratio, potential temperature and horizontal winds over the period 1982-2017 were calculated using the months of June to September at 1200 UTC across 15°E- 15°W and 16-17°N from ERA-Interim data (Berrisford et al. 2011). Higher latitudes than that of Niamey were used for the reanalysis data as the strongest trends in variables and strongest correlations with mesoscale convective system (MCS) intensity exist between 15-20°N.

Baroclinicity and day to day variability are characteristic of the Sahel region. Both factors matter and can cause changes in the environmental profile in the same zone on the same day. Given the innate uncertainty across the region, the changes calculated from the ERA-Interim data for 16-17°N over the period of 1982 to 2017 can be interpreted as plausible ranges for each parameter over this period. Thus, we have calculated a particular trend that we can apply to our control profile to explore how such changes in temperature, humidity as well as the environmental wind profile could affect storms in the region. They are also some of the more extreme variations within the ERA-Interim data for the Sahel area and thus provide a higher signal-to-noise ratio in the idealised simulations in this study. However, we do not link these changes explicitly to decadal variability, climate change or a mixture of the two. The validity of the ERA-Interim data will be considered in Section 4.1.1.1 when it is compared with alternative re-analyses for the same region. Applying these changes to the control

(a) Mixing Ratio at 850hPa

(b) Horizontal winds at 600hPa

(c) Wind Shear (600-925)hPa

(d) Horizontal Winds at 925hPa
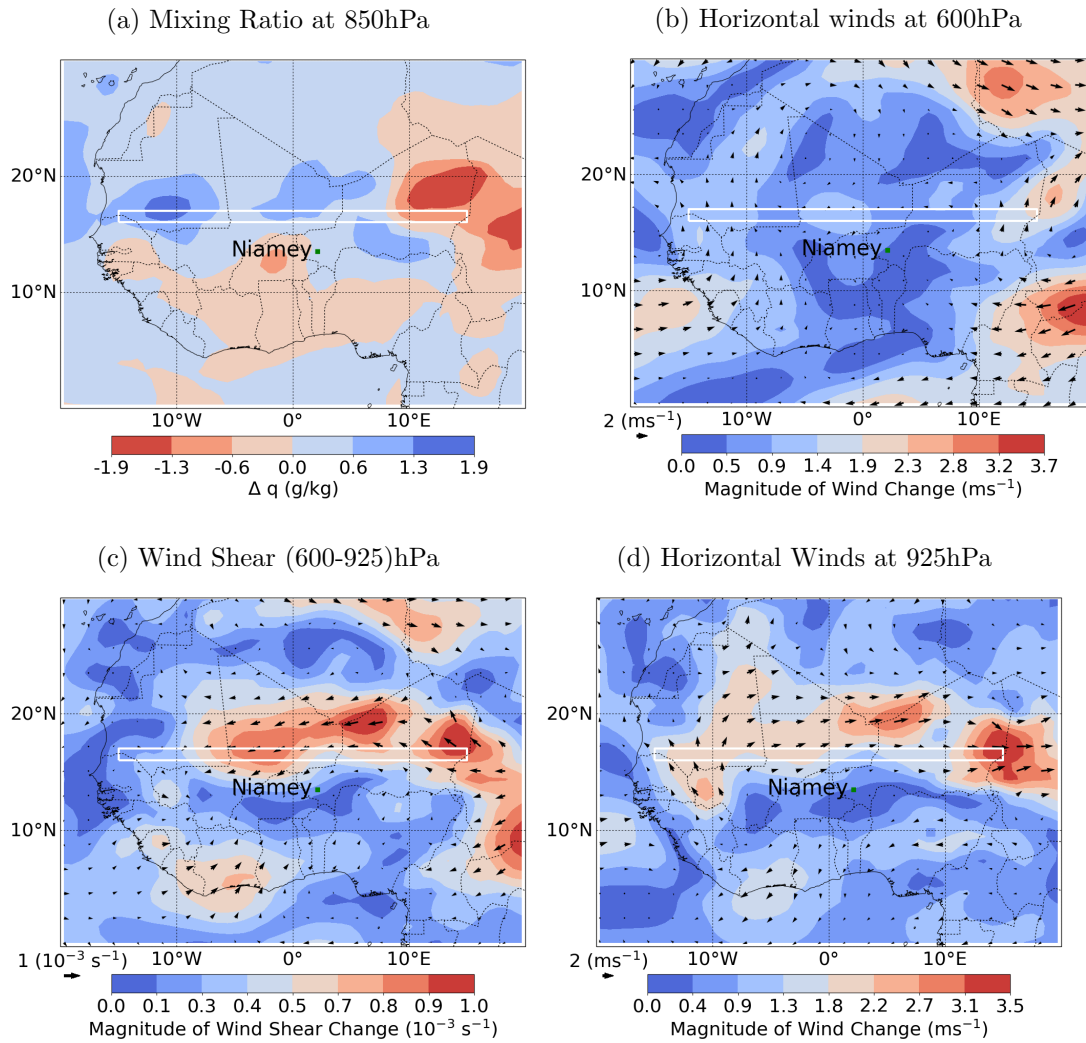
Figure 4.1: Linear trend calculated from an annual mean from 1982 to 2017 of ERA-Interim reanalysis data at 12:00 UTC over the months of June-September. The region marked by a white box, 15°W-15°E and 16°N-17°N, defines the region used to determine the final change applied to the control profile.

Table 4.1: Table detailing the number of repeated experiments which were run for each wind and thermodynamic profile combination. Each profile combination was run five times with a different random seed generator to produce unique random noise at every point in the line thermal perturbation.

| | | Thermodynamics | | |
		Control (2000s)	ERA-I (1980s)	CMIP5 (2100s)
	Control (2000s)	5	5	5
Winds	ERA-I (1980s)	5	5	-
	CMIP5 (2100s)	5	-	5

allows direct comparison with the changes considered by Taylor et al. (2017) and a means of testing their suggestion that increases in westerly wind speeds of $0.4\,\mathrm{ms}^{-1}$ decade^{-1} in the lower troposphere from 15-22°N caused higher wind shear and correlated most significantly with MCS intensity across the region. Additionally, the highest correlation between increases in mid-level temperatures and MCS intensity were found at similar latitudes. Once the linear ERA-Interim changes were calculated for each of the variables, the profiles were interpolated onto the finer grid of the African Monsoon Multidisciplinary Analysis (AMMA) control profile using cubic interpolation. A profile representing the 1980s conditions was then obtained by deducting the change from the control profile. The experiments run are listed in Table 4.1.

The AMMA control profile is compared against the same with the ERA-Interim changes subtracted in Figure 4.3a. The buoyancy profile change is negative throughout, such that the 2006 profile has both higher convective inhibition (CIN) and lower CAPE compared to the 1980s. This suggests storms are more likely in the 1980s profile and could also be more intense. Figure 4.4 shows that from the 1980s to the 2006 control profile there is an increase in the westerly component of the low-level monsoon winds of $1.8\,\mathrm{ms}^{-1}$ as well as a slight increase of $0.4\,\mathrm{ms}^{-1}$ in the AEJ at $600\,\mathrm{hPa}$. Also evident is an increase in shear since the 1980s. The changes to the southerly component of the winds are less marked with only an increase of $0.18\,\mathrm{ms}^{-1}$ in the monsoon winds and a decrease of $0.57\,\mathrm{ms}^{-1}$ in the northerly component of the AEJ. To conclude, the 2006 profile has higher CIN, lower CAPE and increased shear compared to the profile representative of the 1980s.

4.1.1.1 Uncertainty in past trends from Reanalyses

Considering the sparsity of weather stations and radiosondes which regularly measure atmospheric conditions across the African continent it is necessary to view re-analysis such as ERA-Interim for these regions with caution (Roberts et al. 2015). Additionally,

changes in satellite observation systems may have adversely affected the ERA-Interim reanalyses making trend analysis difficult. This is particularly true for temperature and humidity in the tropics, (Trenberth et al. 2001). In order to gain some perspective, data from the Modern-Era Retrospective analysis for Research and Applications, Version 2 (MERRA-2) (Rienecker et al. 2011) for the months of June to September at all times across 15°E-15°W and 16-17°N were compared to ERA-Interim and ERA-5 analyses for the same region. On a direct comparison of variables at set heights, it can be seen that not only do the three reanalyses disagree on mean values, they also give different magnitudes and indeed signs in trends over time. For instance, Figure 4.2a shows similar values for specific humidity at $850\,\mathrm{hPa}$ in all models after the year 2000, however, the higher values of $0.011\,\mathrm{kgkg^{-1}}$ in ERA-Interim compared to $0.009\,\mathrm{kgkg^{-1}}$ in MERRA-2 at the start of 1990s and particularly the low of $0.008\,\mathrm{kgkg^{-1}}$ in ERA-5 ensure a slight increasing trend in humidity in MERRA-2, a somewhat more significant one in ERA-5 and a decrease in ERA-Interim. Similarly, ERA-Interim and MERRA-2 show slight increases in temperature at $850\,\mathrm{hPa}$ in Figure 4.2b while ERA-5 remains fairly constant. It is the trend in thermodynamics that dominates the results in Section 4.2.2, but significantly these trends, taken from re-analyses, are uncertain. Figure 4.1 reveals large spatial variability in water vapour mixing ratio over the region that has been averaged over which creates added complexity. Although decadal trends for the region could be obtained directly from radiosondes, this was not pursued as it is unclear how representative that would be. Humidity measurements are sensitive to the type of radiosonde used (as seen in the spurious diurnal cycle in AMMA sondes, Agustí-Panareda et al. 2009). Additionally, observations would be from a single location. Taylor et al. (2017) considered what trends could be inferred from different collections of radiosonde observations from across the Sahel region and summarised them to be a warming of the SAL relative to the underlying Sahelian planetary boundary layer and increased easterlies at $700\,\mathrm{hPa}$, since the 1980s.

The trends in wind speeds can also be compared between re-analyses. The magnitude of the AEJ increases at $600\,\mathrm{hPa}$ by approximately $1.5\,\mathrm{ms^{-1}}$ for ERA-5 and MERRA-2 while remaining fairly constant for ERA-Interim (Figure 4.2c). The lack of a marked increase in westerlies at both $850\,\mathrm{hPa}$ (Figure 4.2d) and $925\,\mathrm{hPa}$ (Figure 4.2e) in MERRA-2 and ERA-5 is also notable compared to ERA-Interim. When the wind shear is compared in Figure 4.2f however, despite the disparities between wind speeds at different heights between the two European Centre for Medium Weather Forecasting (ECMWF) cases, the shear increase is similar compared to the fairly constant shear in MERRA-2. These differences highlight that the uncertainty in past trends in both thermodynamics and shear is large enough that it may change their relative roles for storm trends.

(a) Specific Humidity at 850hPa

(b) Temperature at 850hPa

(c) Westerlies at 600hPa

(d) Westerlies at 850hPa

(e) Westerlies at 925hPa

(f) Westerlies Wind Shear (925 -600 hPa)
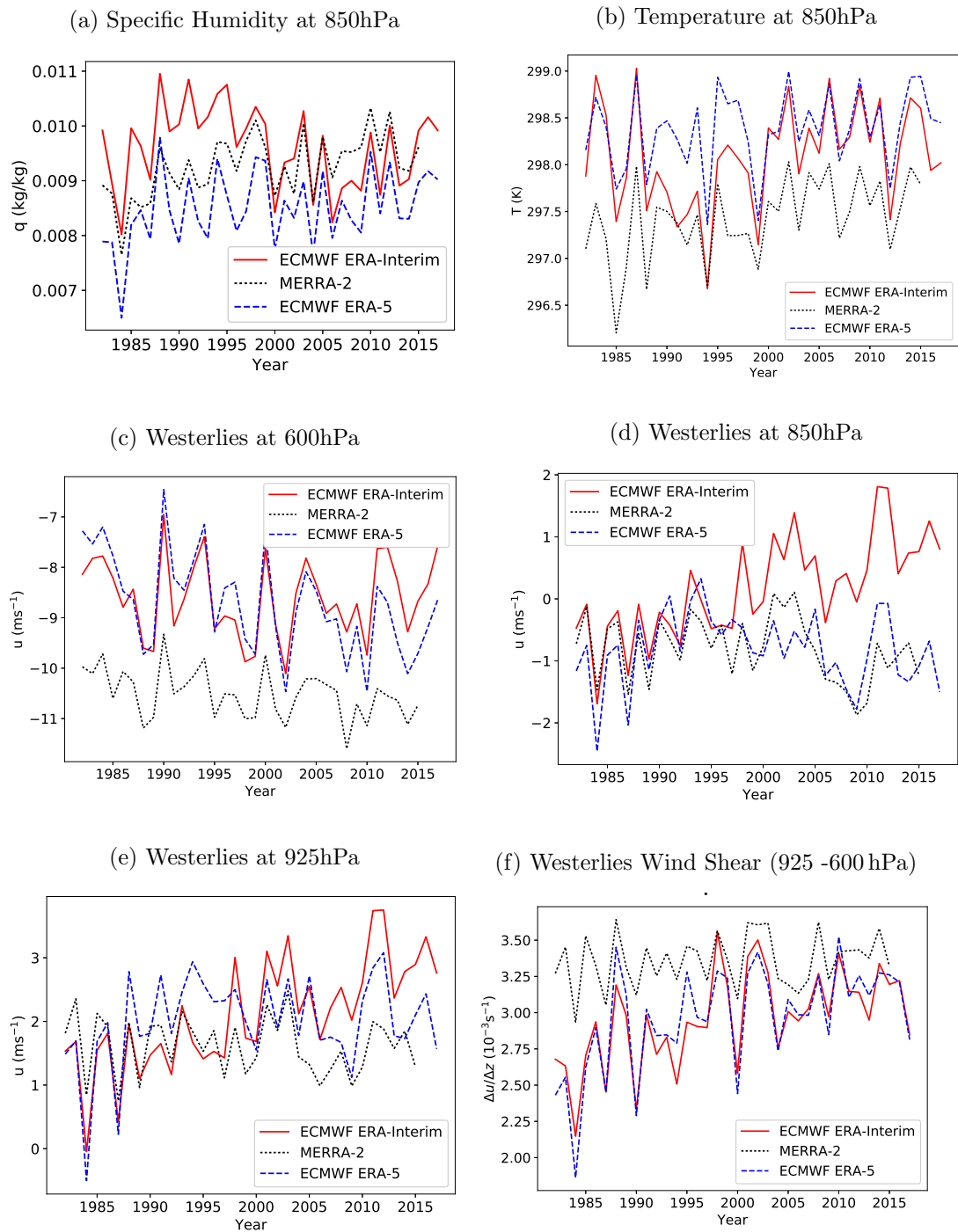
Figure 4.2: Comparison of mean annual values from 1982 to 2017 of ERA-Interim data against MERRA-2 and ERA-5 reanalysis for June-September monthly averages for the region 15°W-15°E and 16°N-17°N (all times of the day included).

4.1.2 CMIP5 Predicted Change

Monthly profiles were obtained from 34 CMIP5 models (Taylor et al. 2012) representing both the historic (1950-1999 average) case and a predicted future (2070-2099 average) case from the Representation Concentration Pathways Scenario 8.5 (RCP8.5). The RCP8.5 scenario has been chosen as it represents high future emissions and large global temperature change and thus provides a good signal to noise ratio.

The CMIP5 profiles studied are averages for the months of July and August for the two time periods using the temperature, specific humidity and horizontal winds at 11 pressure levels to the near-surface to 12.5 km and the temperature and specific humidity at the surface. The averages have been calculated for a 3x3 grid box around Niamey from 1.875°E- 3.75°E and 13.75-15°N The average across models for each time period was calculated and the mean change predicted found from these averages. The average changes for potential temperature, humidity and wind were interpolated onto the higher resolution grid of the AMMA control profile using cubic interpolation. The different variations of the control profile with the CMIP5 environmental changes applied were simulated and repeated with five different random seeds (Table 4.1).

The CMIP5 models provide our best current estimate of possible changes for this emissions scenario and the best method of testing hypothesis-4. The changes from CMIP5 were applied to the control profile: this is preferred to studying the actual profiles as the CMIP5 models have significant biases and relatively coarse resolution. Thermodynamic and wind changes were applied individually and together in order to study the effect each has independently and combined.

The AMMA control profile is plotted against the control with the CMIP5 changes applied in Figure 4.3b. The buoyancy profile change is negative near the surface but is positive above the level of free convection showing increased CAPE and increased CIN in the future profile. From this, it can be anticipated that convection is less likely to occur in the future but when it does it will be more extreme. At the same time Figure 4.5 shows an increase in the low-level monsoon winds of $1.8\,\mathrm{ms}^{-1}$ in the westerlies of the future profile as well as an increase of $1\,\mathrm{ms}^{-1}$ in the AEJ at $500\,\mathrm{hPa}$. There is an increase in both wind magnitudes, in opposite directions, at the altitudes mentioned and thus shear increases compared to the current profile. There is also some indication that the maximum of the AEJ may extend higher in the future or that the maximum is predicted at varied altitudes between CMIP5 models. However, as can be seen from the standard error of the average across the different models there is uncertainty in these predictions. In some cases, this includes disagreement between models over whether the change in a variable will be of positive or negative magnitude.
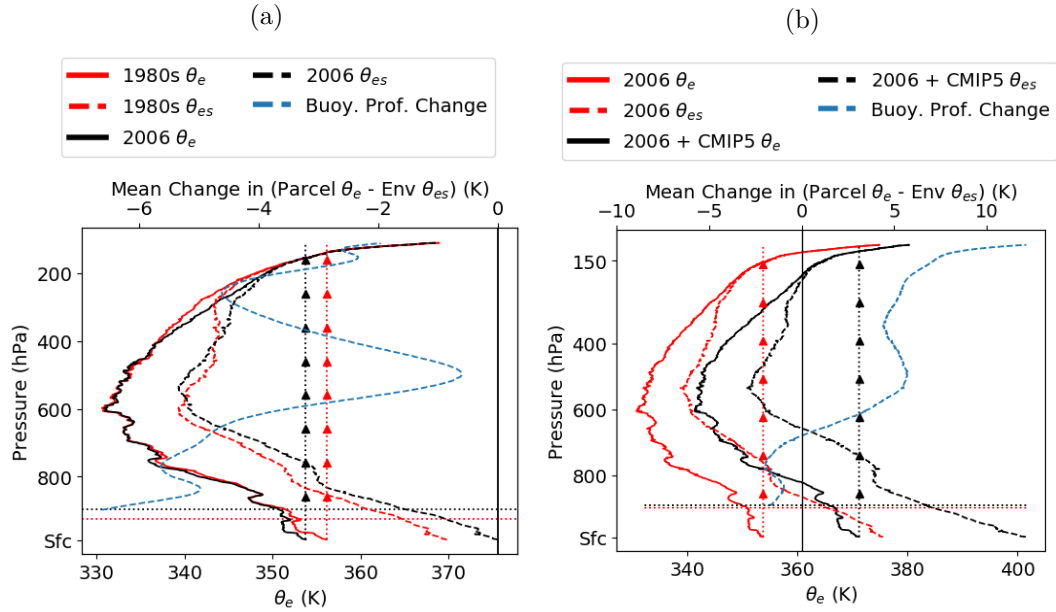
Figure 4.3: Average equivalent potential temperatures across past (red) and future (black) for the Niamey region. The comparisons include the 2006 Control profile obtained from the AMMA campaign and a) the linear trend of ERA-Interim reanalysis from 1982 to 2017 deducted from it and b) the average calculated change across CMIP5 models applied. The saturated equivalent potential temperature is plotted (dashed). The vertical lines indicate the equivalent potential temperature of a surface parcel if it were to be lifted pseudo-adiabatically, after it intersects the θ_{es} curve the parcel can be considered more buoyant than its surroundings. The horizontal dotted lines mark the lifting condensation level. The blue dashed line represents the change in buoyancy profile (buoyancy calculated as the difference between a surface parcel's θ_e and the environment θ_{es} at levels above the lifting condensation level (LCL)).

4.2   Results

In this section, the control simulation and whether the squall line produced is consistent with observations of Sahelian MCSs during the WAM (Section 4.2.1) is described. Once this is determined, Section 4.2.2 considers hypothesis-1 that recent increases in shear from both strengthened monsoon south-westerlies and the AEJ have increased the intensity of squall lines and hypothesis-2 how recent changes to the environmental thermodynamic profile may have influenced squall line intensity and may have been comparable with the effects of shear. Using the same set of simulations from profiles representative of wind and thermodynamic profiles from the 1980s and 2000s, hypothesis-3 whether the system-relative inflow of CAPE and water vapour is key to determining squall line updraft speeds and rainfall so that the LLMC can explain the modelled impacts of changing profiles is tested in Section 4.2.3. Finally, hypothesis-4 that pre-
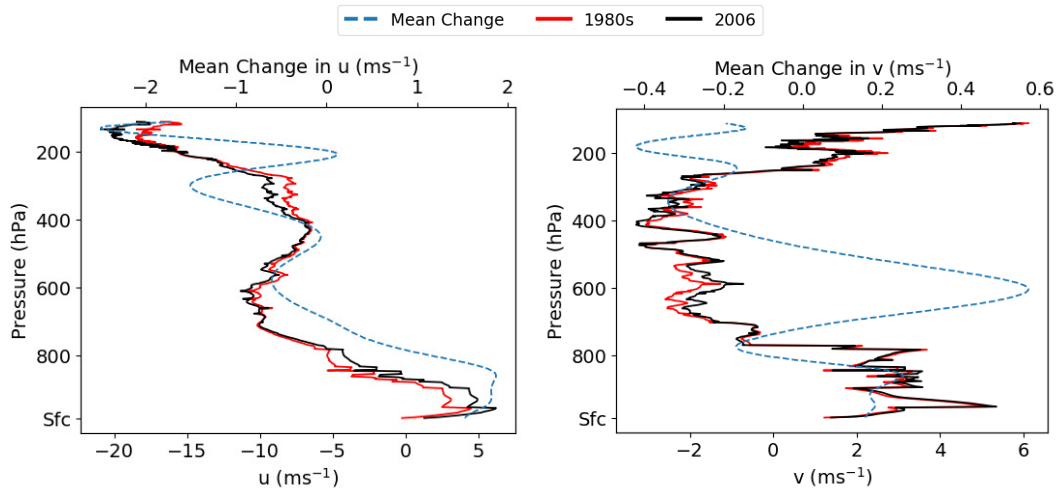
Figure 4.4: Control profile (black) for u and v respectively with the ERA-Interim reanalysis trend from 1982-2017 deducted (red). The change between profiles is shown in blue (dashed).
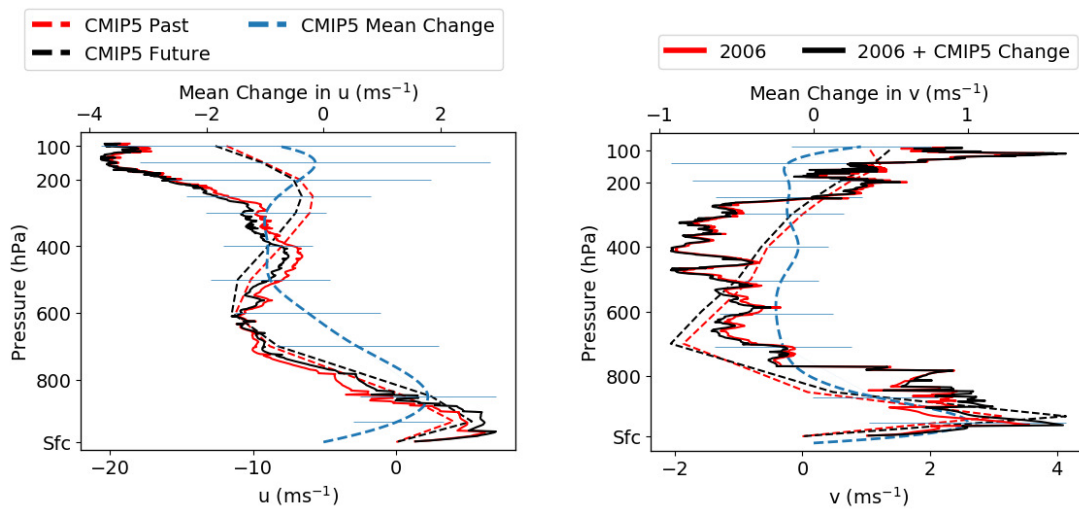
Figure 4.5: CMIP5 average across models of period (1950-1999) vs future (2070-2099) of u, westerlies and v, southerlies respectively (dashed). The AMMA control profile (red solid) and the same with CMIP5 changes applied (black solid). The mean interpolated change across models is also plotted with standard error of the mean shown.

dicted future increases in shear, temperature and humidity will cause an increase in
storm intensity is tested in Section 4.2.5.

4.2.1   2006 AMMA Campaign Control Profile Simulation

The resulting simulation from the control profile (Figure 3.3) can be seen in Figure 4.6.
The cold bubble results in two separate updrafts that can be seen to merge completely
by hour 3. After this, the squall line begins to enter a more mature and steady state.
The main convective updraft moves towards the front edge of the storm and appears
to shrink slightly from around 20km to 10km wide. The system speed is defined as the
speed of the front edge of the cold pool moving at the front of the storm. A maximum
surface pressure perturbation of $1.6\,\mathrm{hPa}$ occurs at around four hours which coincides
with the squall line moving at its maximum speed and the main convective updraft
jumping forward. The updraft appears to extend over the whole troposphere and an
overshoot can be seen around $13\,\mathrm{km}$ while there is weak mesoscale ascent in the anvil.
The anvil spreads out mainly westwards as a result of the strong Tropical Easterly Jet
(around $100\,\mathrm{hPa}$ in Figure 3.3) to be hundreds of kilometres wide. There is an area
of descending flow at the rear of the convective zone but this appears to be moving at
the same speed as the storm rather than providing a system relative inflow. The area
of precipitation of the storm spreads to about $80\,\mathrm{km}$ behind the front at 6 hours and
then shrinks slightly again.

Whether the simulated storm produced with the control profile was consistent with
those found in the West African Sahel and previously discussed in Chapter 2.3.4 was
considered. The control profile produced cold pools with an average propagation speed
of $10.7\,\mathrm{ms^{-1}}$ across repeated experiments when in a steady state which is consistent
with the propagation speeds of convective cloud clusters in Mathon and Laurent (2001).
The mean rainfall rate, maximum surface pressure perturbation and minimum poten-
tial temperature perturbations of the storms simulated using the control profile are
$7.2\,\mathrm{mmh^{-1}}$, $2.8\,\mathrm{hPa}$ and $6.8\,\mathrm{°C}$ respectively. This is consistent with the storm com-
posites of Provod et al. (2016) from the AMMA monsoon period which include mean
rainfall rates between $10\,\mathrm{mmh^{-1}}$ at the leading edge to $1\,\mathrm{mmh^{-1}}$ at the trailing edge,
temperature decreases of $2° - 14\,\mathrm{°C}$, pressure increases of $0 - 8\,\mathrm{hPa}$, and wind gusts of
$3 - 22\,\mathrm{ms^{-1}}$.
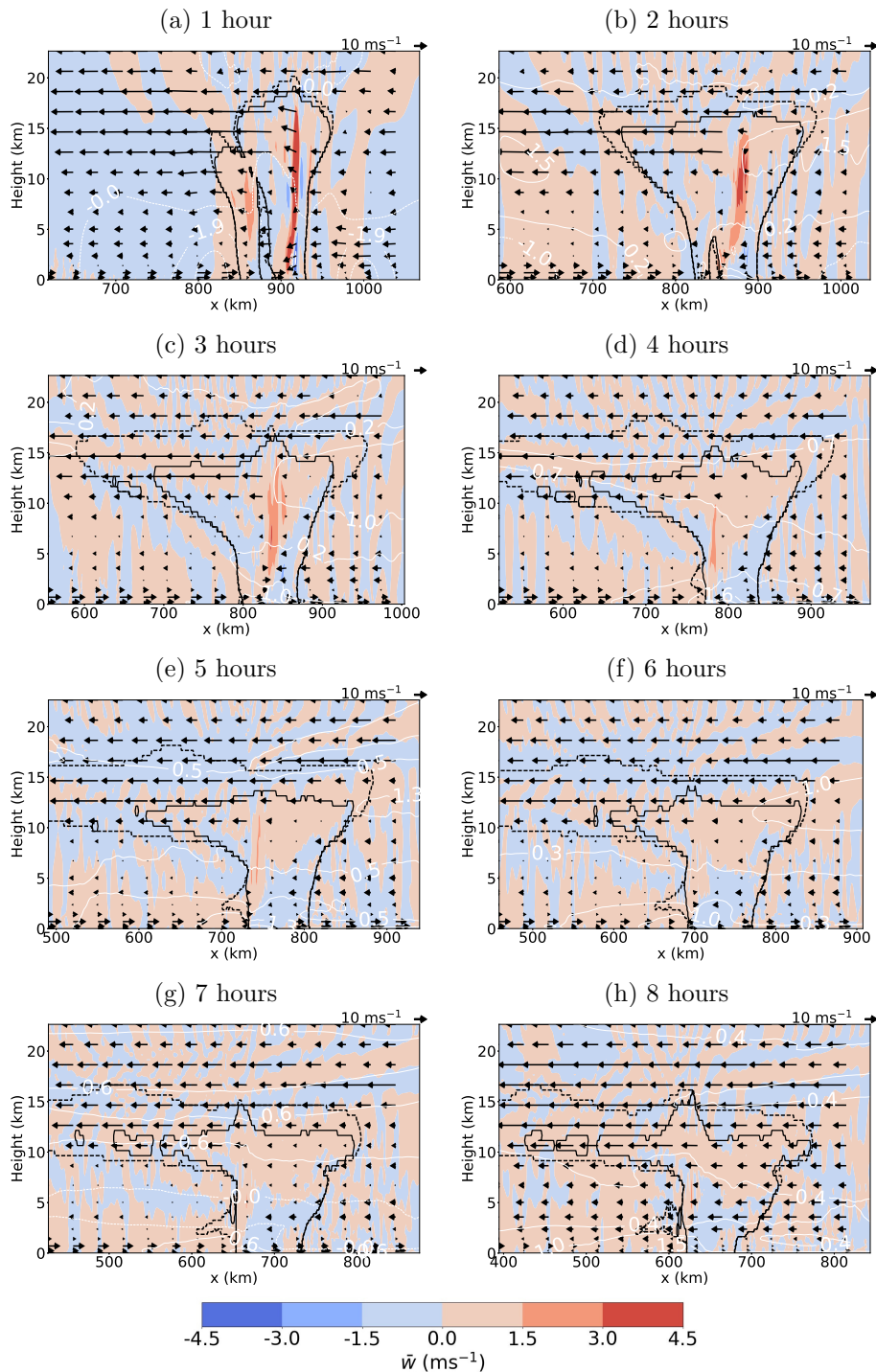
Figure 4.6: Simulation with the control profile from the 2006 AMMA campaign from one hour after initiation to eight hours in hourly intervals. A slice through the storm in the x-z plane is shown with y-averaged values shown (y-average is indicated by a bar e.g. $\bar{w}$). Vertical velocity is shaded, pressure perturbation (hPa) in white contours, total liquid and solid water (dashed) and precipitable content (solid) both plotted where above $0.01\,\mathrm{gkg}^{-1}$ (see Table 3.1 for details of variables). The arrows represent $((\bar{u}_r, \bar{w}))$ where $\bar{u}_r$ are the system relative wind speeds. Only a) had vertical velocities higher than $4.5\,\mathrm{ms}^{-1}$ where the highest magnitude reached was $15.0\,\mathrm{ms}^{-1}$.

4.2.2 Effects of past decadal changes in thermodynamics and shear from ERA-Interim Analyses

Simulations were run with thermodynamic and wind profiles produced by deducting recent decadal changes in ERA-Interim data from the 2006 control profile in order to isolate the effect of recent thermodynamic changes against those within the wind profile and to test hypothesis-1 and hypothesis-2. This allows for the comparison of four simulation configurations with two different thermodynamic environments, each with two wind profiles (Table 4.1). Maximum vertical velocities, $\bar{w}_{max}$ and $\hat{w}_{max}$, maximum rain-rates $\hat{R}_{max}$ and mean rain-rates (where raining), $\bar{R}$, are described in Table 3.1 and plotted in Figure 4.7. All storms can be considered long-lived and can be categorised as being in a steady-state from 4-6.25 hours with $\bar{w}$ values staying within a range of $1\,\mathrm{ms}^{-1}$. It appears as if the control case with 1980s winds begins to die after this point ($\bar{w}$ consistently below $1\,\mathrm{ms}^{-1}$) and so times after 6.25 hours were not considered.

In Figure 4.7 the thermodynamic change dominates the wind-shear change: the cases with 1980s thermodynamics (*i.e.* with higher CAPE and lower shear: red lines) have $\bar{w}_{max}$ and $\bar{R}$ values of over $3\,\mathrm{ms}^{-1}$ and $5\,\mathrm{mmh}^{-1}$ higher, respectively, than those with 2006 thermodynamics (*i.e.* with lower CAPE and higher shear: black lines). This supports hypothesis-2 that changes to the thermodynamic profile may have influenced squall-line intensity and could be comparable to the effects of shear. While the impact of increasing wind shear for a constant thermodynamic profile (*i.e.* solid versus dashed lines) is less dramatic it does result in higher rain rates and vertical velocities; approximately $2.5\,\mathrm{mmh}^{-1}$ and $0.5\,\mathrm{ms}^{-1}$ respectively. This supports hypothesis-1 that stronger wind shear has strengthened the intensity of squall lines. The bulk indicators, $\bar{w}_{max}$ and $\bar{R}$, (Table 3.1, Figures 4.7a-4.7b) involve first averaging over the y domain and so lose the detail of extreme cases of velocity/rainfall in single convective cells. However, they tend to show more distinct differences between experiments. The difference in the noisier $\hat{w}_{max}$ and $\hat{R}_{max}$ (Table 3.1, Figures 4.7c-4.7d) is less obvious, as expected,st but there is still an increase in $\hat{w}_{max}$ with constant thermodynamic environments but increased wind-shear. The standard error of the mean bars on Figure 4.7 show that the variation between the repeated experiments with different random seeds is less significant than the variations from different initial environments.

Vertical cross-sections through the simulated squall lines are now examined, Figure 4.8, to provide a qualitative examination of changes of squall-line structure as a function of the changes in thermodynamics and shear. All cases show squall lines with cold pools and a spreading anvil cloud to the west. The area usually associated with the rear inflow jet has downward movement with a similar horizontal velocity to that of the system.

(a) (b) (c) (d)
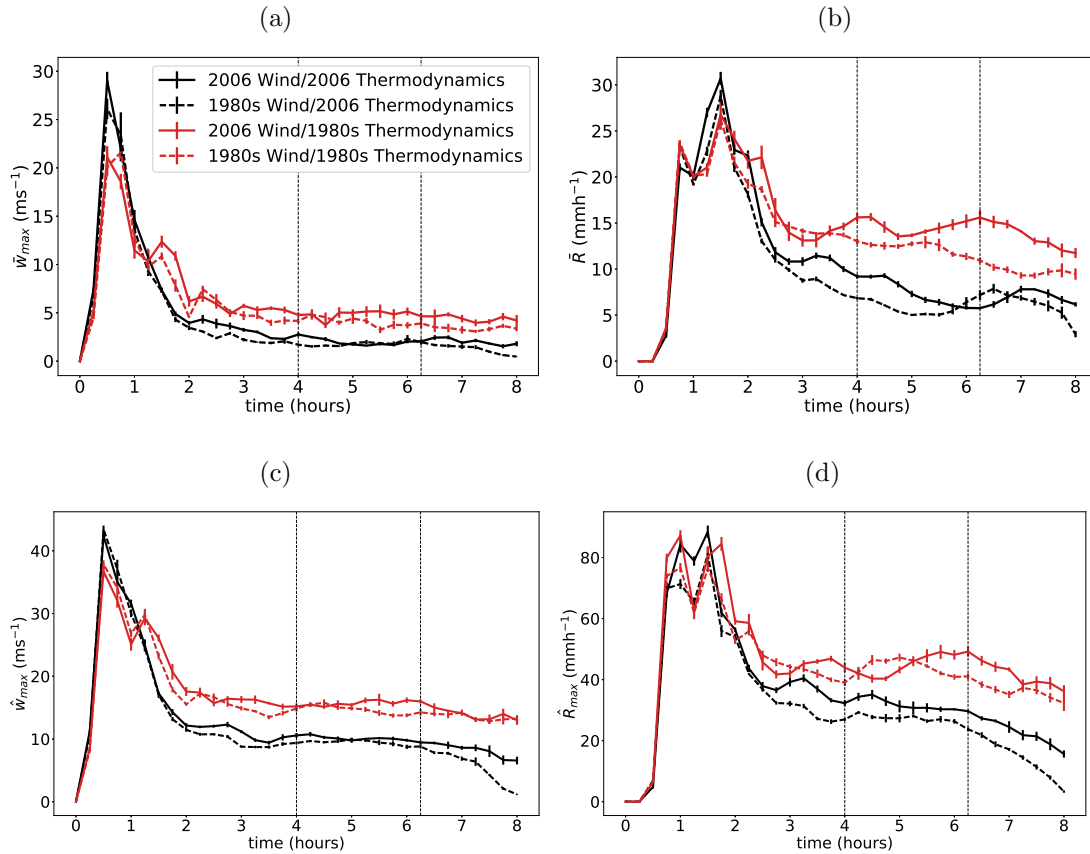
Figure 4.7: The top two figures show a) the maximum vertical velocity and b) the mean rain rate (where raining) in the y-averaged profile. See Table 3.1 for further descriptions of variables. The bottom figures show c) y-averaged values of the maximum velocity, $\hat{w}_{max}$, and d) maximum rain rate, $\hat{R}_{max}$ in the $x - z$ plane. The mean of the five repeated experiments for each environmental profile is marked with the standard error of the mean shown by a vertical bar. This includes the control, control with ERA-Interim winds deducted, control with ERA-Interim thermodynamics deducted, and control with both deducted. The dashed vertical lines indicate the period during which the storms are considered to be in a steady state from 4 to 6.25 hours.

If the 2006 control thermodynamic cases (Figures 4.8a-4.8b; lower CAPE/higher CIN)
are compared with the 1980s cases (Figures 4.8c- 4.8d; higher CAPE/lower CIN) there
are weaker updrafts, a wider precipitation area, a drier Rear Inflow Jet (0.5-3 km),
lower overshoots, a moister cold pool and a weaker meso-low ahead of the squall line.
These differences are consistent with what would be expected for storms which occur
in environments with lower CAPE.

4.2.3   Testing the Layer Lifting Model of Convection

The layer-lifting model of convection, and so hypothesis-3, was tested by plotting di-
agnostics w_{ll} and PR_{ll} against statistics calculated from the different simulations and
time-averaged over the period when the storms were considered steady (Figure 4.9).
The propagation speed (PS) used was the speed of the cold pool for each storm aver-
aged over the period when the MCS is considered to be in a steady-state (from 4 to 6.25
hours in the ERA-Interim experiments). The increased wind shear of the 2006 profile
(circles versus squares) produces higher velocities, $\bar{w}_{max}$ in Figure 4.9a, and rainfall,
$\hat{R}_{max}$ in Figure 4.9b; this change is small when compared to that from the thermo-
dynamics (red versus black). The mean rain rate above a threshold of $1\,\mathrm{mmh}^{-1}$, $\bar{R}$,
consistently increases for higher wind shear across constant thermodynamic profiles
(Figure 4.9c). However, the impact of changing wind shear on $\hat{R}_{max}$ is less clear for the
cases of constant 1980s thermodynamics (high CAPE). Thus, $\hat{R}_{max}$ is more thermody-
namically controlled as it captures the rain rate of the most intense cumulonimbus cell,
and thus less sensitive to MCS structure (and so to shear) than $\bar{R}$. The LLMC is there-
fore a useful indicator of vertical velocities and mean rainfall rates in these idealised
experiments. This is particularly true for the bulk indicators of storm intensity.

The precipitation rate diagnostic, Equation 2.15, can not necessarily be universally used
across thermodynamic profiles as the constant W may vary. A constant value of $W =
58.5\,\mathrm{ms}^{-1}$ is used for all cases and despite this PR_{ll} is still a clear indicator of mean
rainfall rates (Figure 4.9c). The value of W was chosen in order to fit the magnitude
of PR_{ll} for the control profile experiments in Figure 4.9d to $\bar{R}$. The constant does not
affect correlation, only the gradient of the best-fit line. PR_{ll} is also a useful indicator
of storm intensity for cases of varied wind shear in a constant thermodynamic profile
(circles versus squares). Furthermore, considering the linear relationship shown in
Figure 4.9c, W can be concluded to be almost constant between these relatively similar
environments. The average storm widths (where raining along y) were calculated for
each individual storm (when considered steady). The width of raining area varied from
46 km for the higher shear/higher CAPE case to 70 km for the lower shear/lower CAPE.
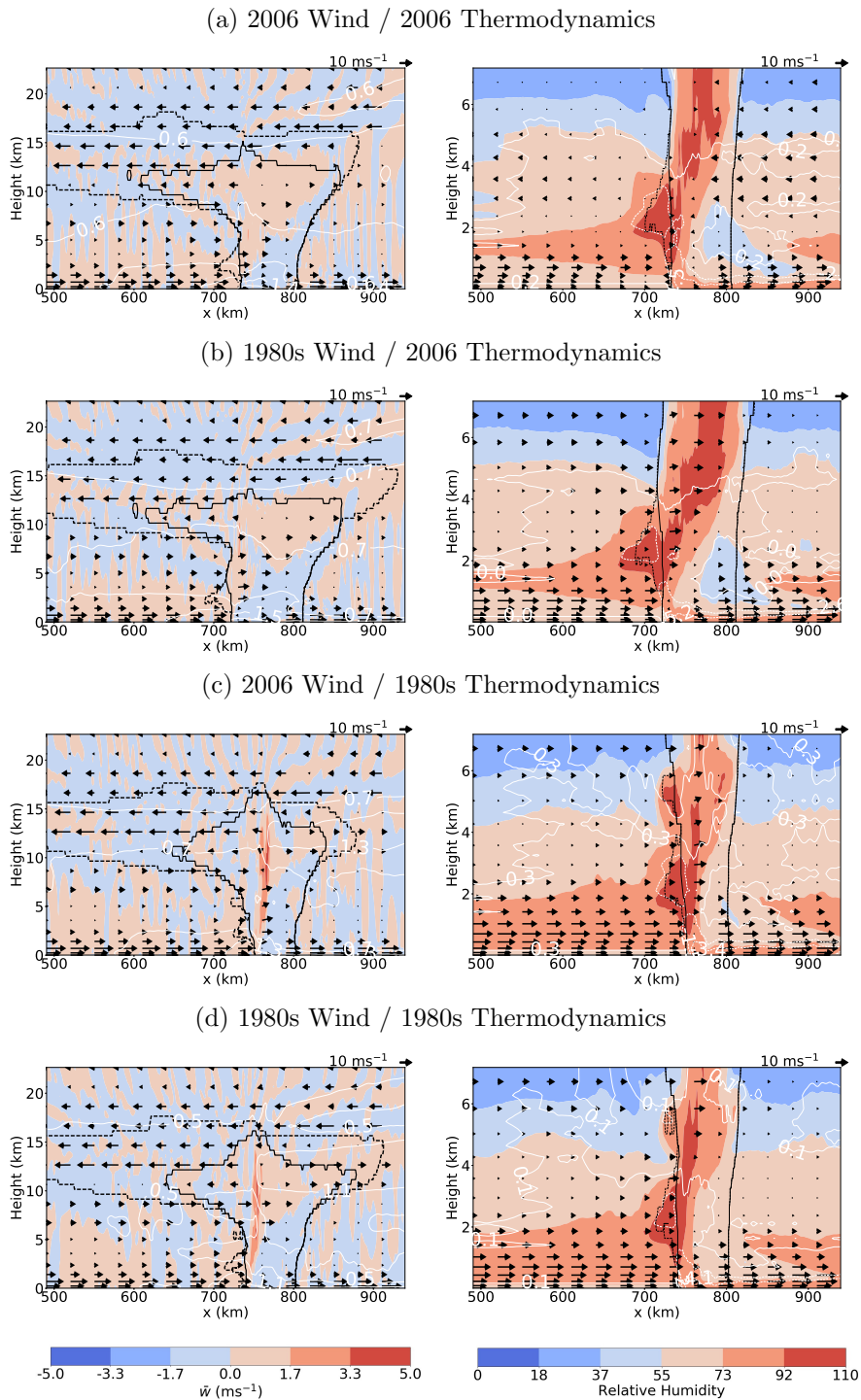
Figure 4.8: *y*-averaged values for the ERA-I set of experiments shown at 5 hours. Vertical velocities (left) and relative humidity (right) shown by shaded contours, total liquid and solid water content (dashed) and precipitable content (solid black). White contours indicate perturbations from the original pressure profile. The arrows represent $((\bar{u}_r, \bar{w}))$ where $\bar{u}_r$ are the system relative wind speeds.
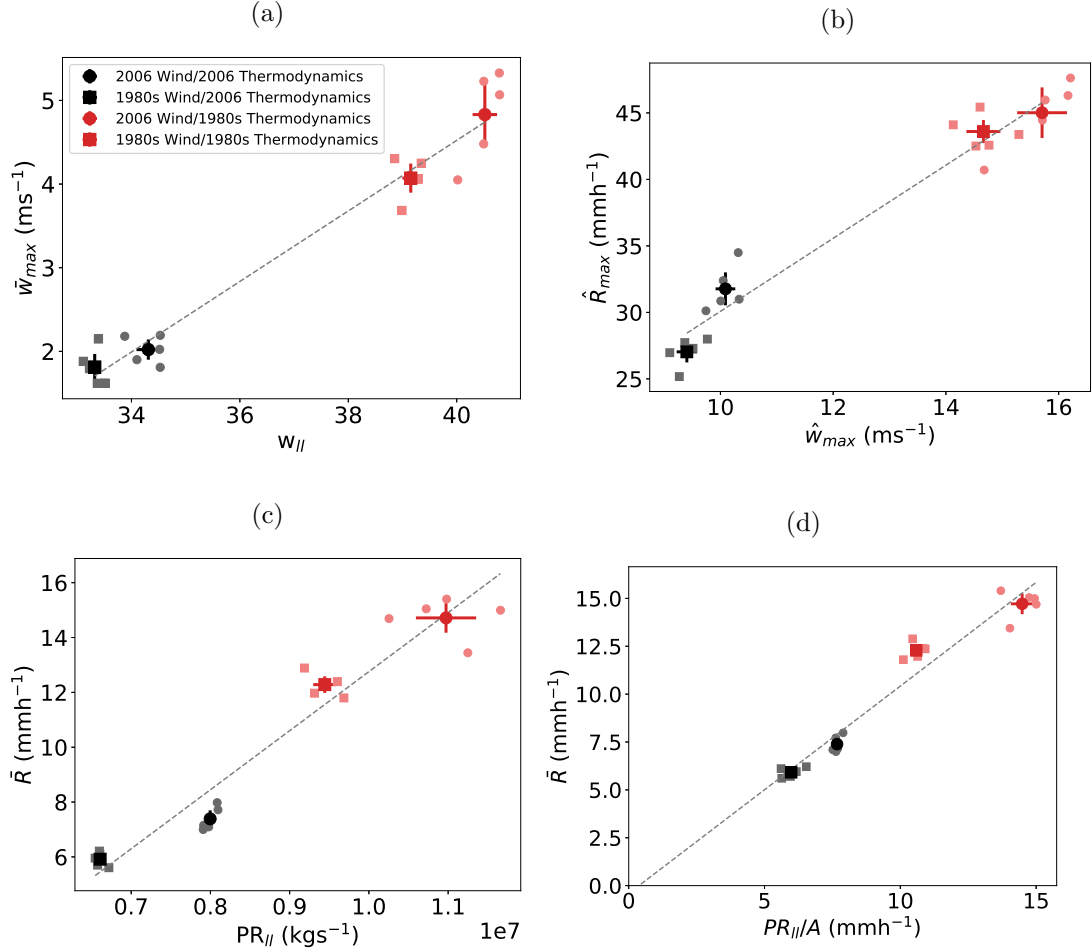
Figure 4.9: Time-averaged statistics for the duration the storms are steady in the ERA-Interim experiments. The mean of the five repeated experiments for each environmental profile are plotted with error bars equal to $\pm 1.6 \times$ the standard error of the mean equivalent to a 90% confidence interval. Figures include a) The index for updraft strength, $w_{ll} = \sqrt{\mathrm{CAPE}_{ll}}$, plotted against $\bar{w}_{\max}$, b) $\bar{w}_{\max}$ against $\bar{R}_{\max}$, c) the precipitation rate diagnostic PR_{ll} against the mean rain rate $\bar{R}$ and the same with d) PR_{ll}/A - calculated through division by raining area width (where raining) for each individual case.

These values were then used to calculate PR_{ll}/A in mmh^{-1}, Figure 4.9d displays how the diagnostic loses some skill through including this time-averaged value with the correlation coefficient of the mean values falling from 0.98 to 0.97.

The difference in cloud tops (maximum height reached by the cloud) can be viewed in the cross-sections shown in Figure 4.8. The 1980s (higher CAPE/lower shear) experiment in Figure 4.8d shows a higher overshoot, with a cloud top difference of $3\,km$, than the 2006 thermodynamics equivalent in Figure 4.8b (low CAPE/low shear). However, an increase in wind shear (from the 1980s to 2006) with the constant 1980s thermodynamics also results in a $1\,km$ increase in cloud top height. This impact of increasing shear is representative of the results of Taylor et al. (2017), which have been corroborated by Fitzpatrick et al. (2020), whereby satellite data reveals growing numbers of clouds with colder cloud top temperatures and thus higher cloud top height over time, as shear increases.

PR_{ll} was expanded in Section 2.2.3.1 Equation 2.16 and the terms of interest have been plotted in Figure 4.10. The first three figures explore the relative inflow of mass, CAPE and moisture at each height for the different environments. The strong southwesterly nocturnal winds dominate for mass with a maximum inflow of $17.5\,kgm^{-2}s^{-1}$ in Figure 4.10a at $975\,hPa$ and only beginning to decrease at $925\,hPa$. This is also true for inflowing CAPE and moisture which both have secondary maxima at the low-level jet.

The higher CAPE near the surface in the 1980s thermodynamic cases results in maximum inflows of $10\,000\,Jm^{-2}s^{-1}$ higher than their equivalent 2006 wind profiles (red versus black in Figure 4.10b). Increasing the low-level winds for a constant thermodynamic profile (solid versus dashed lines) results in a smaller but still significant increase of inflowing CAPE. Above the near-surface maximum, the inflowing CAPE in Figure 4.10b then drops more dramatically than the mass in Figure 4.10a which corresponds to a similar drop in CAPE at $920\,hPa$ in Figure 3.4. The inflowing mass is a dominant factor here as it controls the fraction of convectively unstable air within the storm. As the fractional change in water vapour mixing ratio from the 1980s to 2000s is less substantial than that of the CAPE, the wind profile is more important for changes in the system-relative inflow of water (Figure 4.10c) than for CAPE (Figure 4.10b). In fact for the system-relative inflow of water, the change in shear dominates the change in thermodynamics. However, lower values of specific and relative humidity at mid-levels in the 2006 profile (Figure 4.11) could also be responsible for suppressing convection through entrainment. These processes are not directly captured by the LLMC.

In order to calculate the layer-lifting indices such as $CAPE_{ll}$ and PR_{ll} the propagation
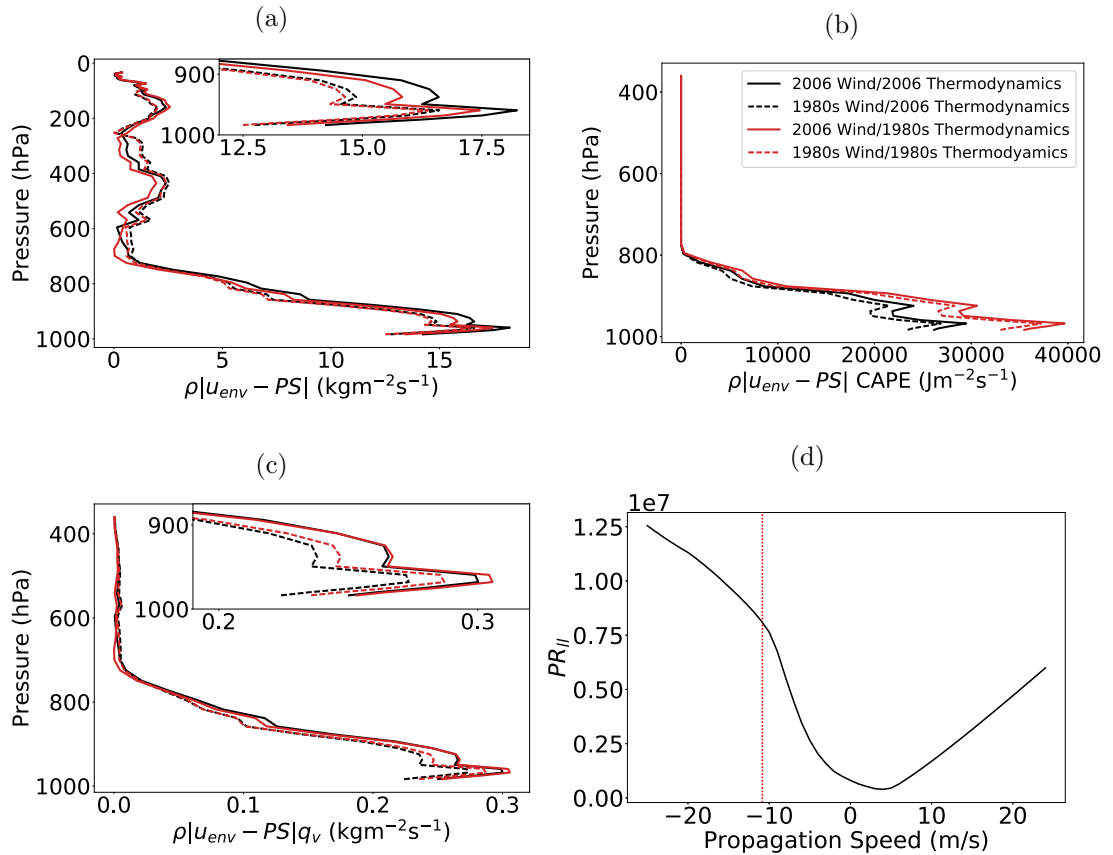
Figure 4.10: System relative inflows of: a) mass, b) CAPE and c) water vapour at different heights for the different profiles. Panel d) explores the relationship between the chosen propagation speed PS and the resultant PR_{ll} for the control profile. The red dotted line represents the mean speed of the control profile storm when it is in a steady state.
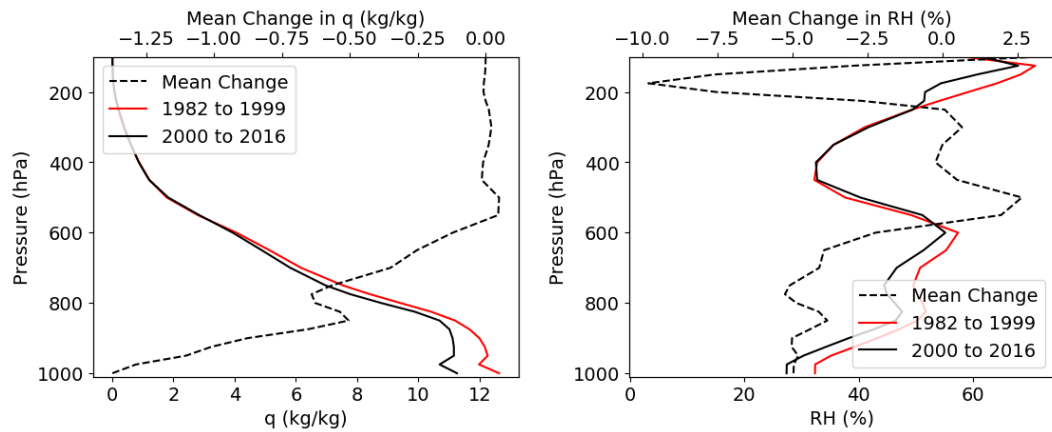
Figure 4.11: Linear trend in mixing ratio and relative humidity calculated from an annual mean from 1982 to 2017 of ERA-Interim reanalysis data at 12:00 UTC over the months of June-September.

speed of the MCS is required, and this is not predicted by the LLMC. Different choices for PS are considered and the resultant PR_{ll} plotted for each of the experiments against $\bar{R}$ as in Figure 4.9c (not shown). The different PS investigated included the speed of the storm when steady for each individual experiment; the average speed across repeated experiments with the same environment but unique small-scale random noise and the average across all experiments over all environments. The correlation coefficient was similar, approximately 0.98, for cases looking at the same environment and 0.97 for the average over all environments. To summarise, although environment-specific PS values result in more accurate values for PR_{ll} there is no stark change in result since variations in PS are small throughout the experiments in this study where one control profile is modified.

Although the PSs did not vary greatly across the simulations in this study it is not clear that this would hold in general as squall lines can travel both slower and faster than seen here (Barnes and Sieckman 1984). Therefore, the sensitivity of PR_{ll} to PS in Equation 2.16 was further investigated in Figure 4.10d for the control run, where it is evident that an accurate value of PS is required. If the PS used is multiplied by a factor of 2 or 0.5 this results in the PR_{ll} being out by a factor of 1.5 and 0.3 respectively. If PS is set to zero the PR_{ll} is 1/11 of the original value. This complicates the process of parametrising convection as the resultant rainfall of the storm is a function of not only the environmental thermodynamics but also storm motion, which may be a function of storm dynamics as well as the profile.

The line plot in Figure 4.10d is somewhat artificial as not all propagation speeds are realistic for this profile. Figure 4.12 more fully explores sensitivities to shear and propagation speed within the LLMC. The shear has been varied by multiplying the entire wind profile by factors of 0.5 to 1.5 and the resultant magnitude of the AEJ is plotted on the y-axis of the figure. The sensitivity of rainfall to shear is much lower than the sensitivity to propagation speed. Overall Figure 4.12 suggests that theoretically, shear is expected to increase rain consistent with Taylor et al. (2017), unless the PS barely increases with shear in which case the quantity of air entering the storm from above the LFC (Figure 3.4) will increase at a greater rate as $|u_{env} - PS|$ will no longer be near zero at the AEJ. More air from above the LFC results in a reduction in the total fraction of convectively unstable air entering the storm. However, Taylor et al. (2017) showed that systems with colder cloud top temperatures (*i.e.* of higher intensity) were indeed associated with significant increases in PS. Whether a faster system facilitates increased storm intensity or is a consequence of it is unclear but fundamentally PS and system intensity are coupled. The solid line on Figure 4.12 marks the AEJ as the steering level of the storm (e.g. the PS is equal to the maximum of the AEJ) which is
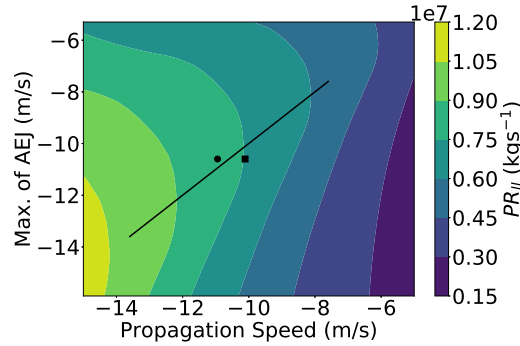
Figure 4.12: Sensitivity Test of Equation 2.15 for PS vs Shear using the 2006 temperature and humidity profiles. For each case the environmental wind profile has been multiplied by a factor so that although only the value of the AEJ is shown the nocturnal jet has also been increased. The black line indicates where the AEJ maximum is equal to the propagation speed. The experiments with the 2006 wind profile are plotted - control (circle) and ECMWF thermodynamics (square).

supported by the black markers (indicating the PS of the simulated squall lines with the control wind profile). If the AEJ does control the PS of storms then an increase in the AEJ could result in more rainfall and a correlating increase in shear. Although the LLMC appears to support the hypothesis that shear has increased storm intensity it is worth noting that in a potential scenario with a strengthening LLJ but constant shear (weakening AEJ), the fraction of moisture and convectively unstable air entering the storm would also increase.

In conclusion, the effects of plausible past decadal changes in humidity and shear were quantified, to test hypothesis-1 that increased shear may have increased severe storms in the Sahel over the period from 1982 to 2017, while also testing hypothesis-3 whether the LLMC can explain the modelled impacts of changing environmental profiles through calculating the system-relative inflow of CAPE and water vapour. Thus, neither hypothesis can be rejected, and increased shear is seen to increase both measures of convective intensity (i.e. updrafts and rainfall) although for the changes used temperature and humidity changes are the dominant drivers of the total rainfall changes. Given the innate variability across the Sahel region, including on a daily scale, understanding the potential effects caused by these changes in wind profile and thermodynamics is enlightening.

4.2.4 Horizontal Resolution

As discussed in Section 4.1, experiments were repeated to investigate the integrity of the results when changing the horizontal resolution. Figures 4.9a and 4.9c were

(a)

(b)
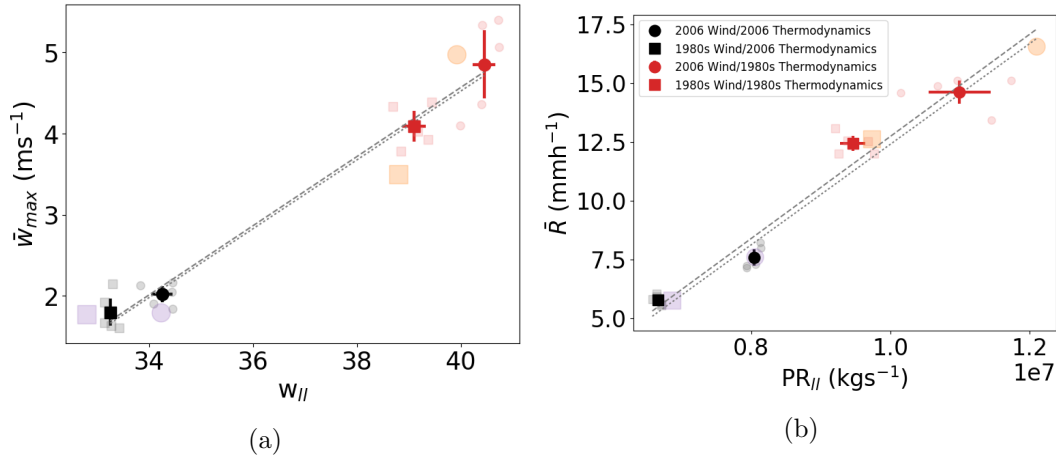
Figure 4.13: As in Figure 4.9 but with repeated simulations at 200 m horizontal resolution also plotted (large pale symbols), alongside those at the original 1km grid spacing (small symbols, with the mean of the five repeated experiments shown as a darker symbols with error bars equal to $\pm 1.6\times$ the standard error of the mean). Figures include a) The index for updraft strength, $w_{ll} = \sqrt{\mathrm{CAPE}_{ll}}$, plotted against $\bar{w}_{\max}$, b) the precipitation rate diagnostic PR_{ll} against the mean rain rate $\bar{R}$. The dashed line is the line of best fit for the 1 km simulations and the dotted line for the 200 m simulations.

Table 4.2: Table of gradients for best fit lines for different resolutions.

Resolution	Figure 4.13a	Figure 4.13b
200 m	0.42	2.14×10^{-6}
1 km	0.43	2.18×10^{-6}
2 km	0.36	1.58×10^{-6}

reproduced for cases with horizontal resolution of both 200 m (see Figure 4.13) and 2 km (not shown). The gradient of the best-fit straight line in both cases was within 10% of that of the 1 km case, and within 2% for the 200 m experiments. Thus, the LLMC continues to accurately predict the relative intensity of the storms and the results support the conclusions made from the lower resolution simulations (Table 4.2). However, the vertical velocities were consistently slightly lower for the 2 km resolution, consistent with the effects of the vertical velocity energy spectrum not being as well resolved. Interestingly, the gradient was less steep for the 2 km runs, suggesting that large grid-spacings can decrease the modelled effects of shear, consistent with a lack of shear effects in the 4 km simulations used in Fitzpatrick et al. (2020) when compared with observations. Given the need to run long duration large domain convection-permitting simulations for future climate projections, this potential sensitivity merits future investigation.

4.2.5 Implications for Future Rainfall

The previous sections have shown that shear changes can drive intensification of rainfall. Under climate change, warming allows for higher water vapour mixing ratios leading to increased rain rates (Kendon et al. 2019). The Sahara is expected to continue to warm faster than the Gulf of Guinea under climate change (Dong and Sutton 2015) which is expected to increase shear. It is important to question to what extent such changes in shear may affect future Sahelian MCSs, alongside effects from the change in the thermodynamic profile. Given the success of the LLMC indices in Section 4.2.2, the possible role of shear changes versus thermodynamic changes under climate change are now investigated.

Figure 4.14 shows that the future climate thermodynamic change imposed dominates the shear change imposed. When compared with the current climate thermodynamic profile (black), the future thermodynamic profile (red) results in higher bulk measures of vertical velocities and rainfall in the spin-up but the storm does not remain sustained for as long and dies off first. This results in a shorter period for which the storms can be considered as 'steady'. During the period of 3-4.5 hours which have been marked the future thermodynamic storms (red) are 'dying' and thus the vertical velocities and rain rate are lower than for the current period.

Vertical cross-sections of the experiments at three hours are shown in Figure 4.15. Again all cases show squall lines with cold pools and anvil clouds spreading to the west. In the 2006 control case (lower CIN/lower CAPE/lower shear) compared with the future (higher CIN/higher CAPE/higher shear) there are: stronger updrafts, a drier Rear Inflow Jet (0.5-3 km), drier cold pool and a weaker meso-low ahead of the squall line. The difference in CIN explains these variations, in that after the spin up the lower CIN in the control 2006 profile allows a more sustained storm.

Figure 4.14 shows that increased wind shear (dashed lines) produces an increase in vertical velocities and rain for the control run thermodynamics; this is only seen for rain in the future thermodynamic experiments, and here it is smaller and more short-lived (consistent with the earlier demonstrated greater role of shear for the system-relative inflow of water than for the system-relative inflow of CAPE). In both thermodynamic environments the future wind profile causes the storms to die earlier. Similarly to the analysis of experiments investigating recent ERA-Interim trends in Section 4.2.2 the thermodynamic changes dominate compared to applied environmental wind changes, although the effects of shear can still be seen. It is also worth noting that although the ERA-Interim experiments are longer-lived than the future climate cases the Control with ERA-Interim wind case begins to die out after 6.25 hours and thus does not sustain

for that much longer.
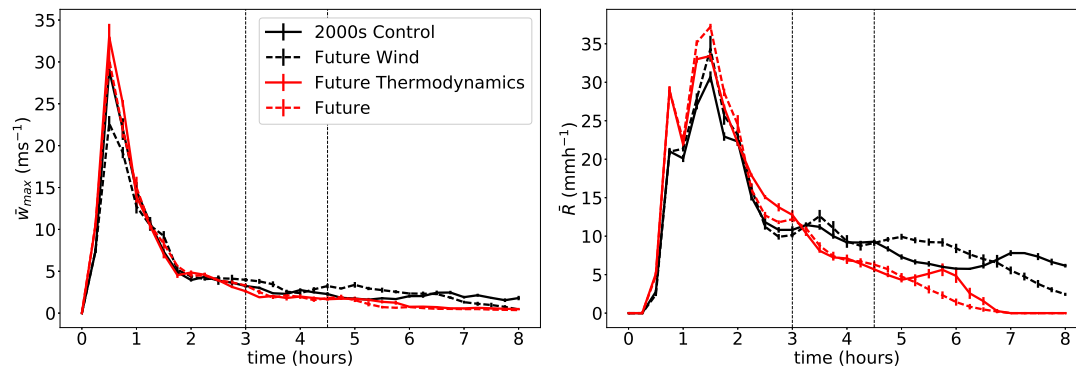
Figure 4.14: Maximum y-averaged (bulk measure) of vertical velocity and the mean rain rate (where raining). Mean values are plotted and the error bars mark the standard error of the mean for all CMIP5 experiments including the control, control with CMIP5 winds applied, control with CMIP5 thermodynamics applied, and control with both applied. The dashed vertical lines indicate where the storms are considered to be in a steady state.

4.3   Conclusion

Previous studies have suggested that increased shear in the Sahel has caused a recent intensification of Sahelian squall lines (Taylor et al. 2017) while predicting that a warming Sahara (through climate change) will result in stronger wind shear over the Sahel (Dong and Sutton 2015). Large-eddy simulations of squall lines in an environmental setting representative of night conditions in the Sahel during the West African Monsoon were analysed in order to investigate the suggested role of shear for past and future climate change. Initial profiles were based on soundings from the 2006 AMMA campaign observations made in Niamey. This control profile was then modified using environmental thermodynamic and wind profile changes calculated from ERA-Interim data for the period of 1982 to 2017, giving a 1980s profile with decreased shear, increased CAPE and decreased CIN when compared to the control 2006 environment. Additionally, the profile was also modified with long term predictions from CMIP5 for the Niamey region. The CMIP5 mean predicts increased low-level south-westerly winds, a stronger AEJ whose maximum extends higher than currently and an increase in both CAPE and CIN.

In the idealised experiments, for constant thermodynamic profiles, the increased wind shear of the 2006 control caused greater values of storm vertical velocities and rainfall which supports hypothesis-1 that recent increases in shear from both strengthened

(a) Past Wind / Past Thermodynamics

(b) Future Wind / Past Thermodynamics

(c) Past Wind / Future Thermodynamics

(d) Future Wind / Future Thermodynamics
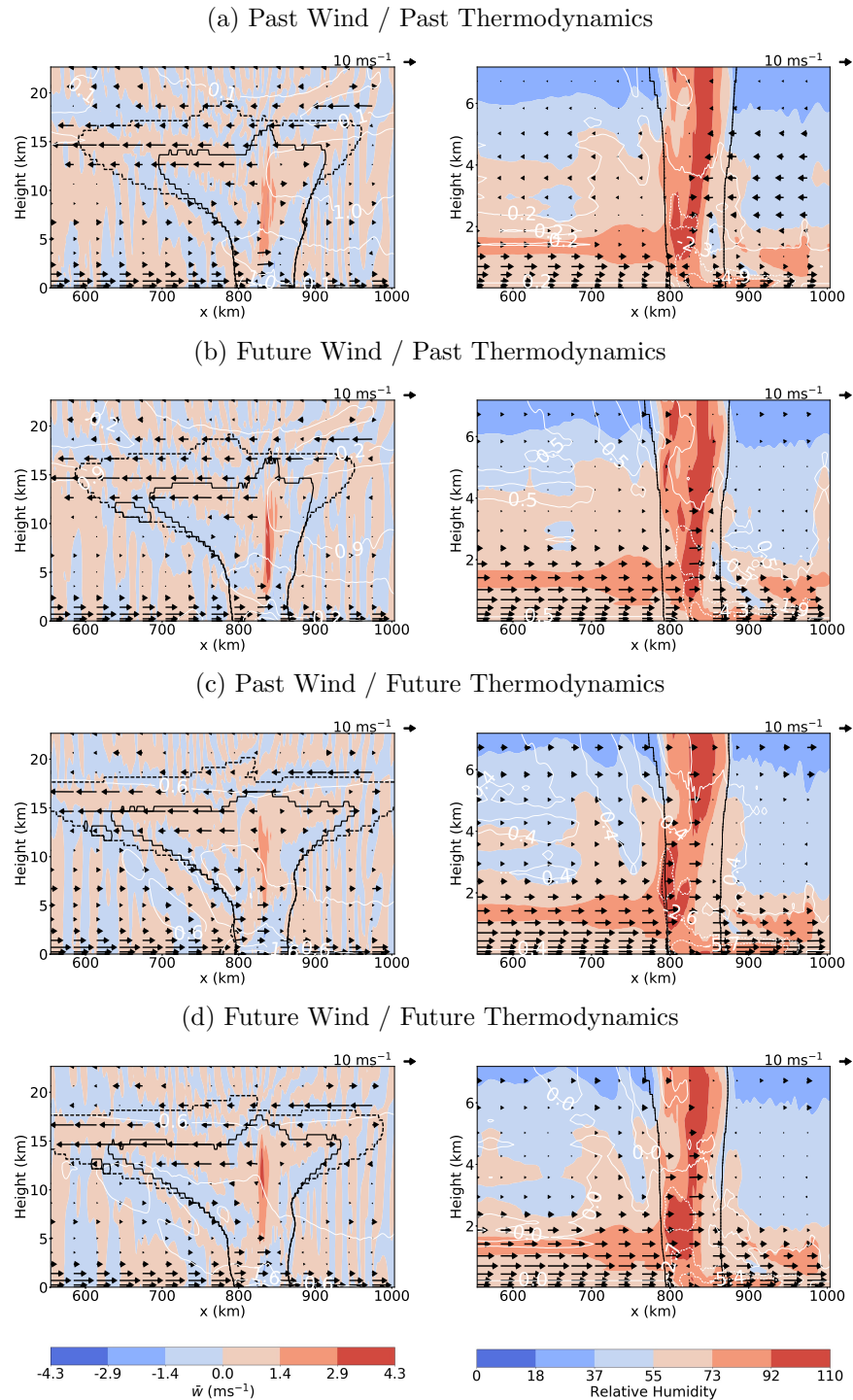
Figure 4.15: y-averaged values for the CMIP5 experiments shown at 3 hours. Relative humidity (shaded contours), total liquid and solid water content (dashed black) and precipitable content (solid black). White contours indicate perturbations from the original pressure profile. The arrows represent $((\bar{u}_r, \bar{w}))$ where $\bar{u}_r$ are the system relative wind speeds.

monsoon south-westerlies and the AEJ caused by Saharan warming have increased the intensity of squall lines. However, in the simulations in this study the effects of the thermodynamic changes imposed dominated the effects of the shear changes imposed: for the 1980s cases, the higher CAPE and lower CIN resulted in higher vertical velocities and mean rainfall. Comparison of the ERA-Interim, MERRA-2 and ERA-5 showed that there were significant differences between the three datasets, including in the signs of decadal trends in both humidity and shear (although shear tends to increase). The results in this study, therefore, support the conclusions made in Taylor et al. (2017) that increased wind shear could be the main driver of decadal changes in storm intensity in the Sahel. The results also do not allow for a rejection of hypothesis-2, that recent changes to the environmental thermodynamic profile may have influenced squall line intensity and could be comparable with the effects of shear, but an increase in humidity might be expected to increase moderate and severe storms, whereas shear is more compatible with the increase in severe and not moderate storms seen in Taylor et al. (2017). This leads to the conclusion that quantifying the past thermodynamic change is vital to understanding past trends in squall line intensity. This highlights the need for an improvement in measurements for the region.

The LLMC, including indices for vertical winds and rain, was tested to gain an understanding of changes in shear and thermodynamics. It was found that the diagnostics of Alfaro (2017) were an excellent indicator of squall line average ascent and rain-rate, with maximum ascents and rain rates less well predicted, as expected. This agreement with the theory is an indicator that rainfall and heating in mature squall lines is primarily determined by the system relative inflow of the environmental air and is consistent with hypothesis-3 that the LLMC can explain the modelled impacts of changing environmental profiles. The relative inflow of mass, CAPE and moisture for each of the environments were considered at different heights. The maximum inflow of all the properties entered the storms with the low-level jet, showing the importance of the jet for Sahelian MCSs. The precipitation rate diagnostic was found to be dependent on the propagation speed of the storm, which is not predicted in the LLMC. This suggests that using the environmental thermodynamic profile alone to parametrise convective events is problematic since the resultant rainfall of the storm is also a function of the storm's motion, and so internal dynamics and wind speeds, and that to predict storm intensity it is also necessary to predict storm speed. Finally, the accuracy of the LLMC raises questions over whether increases in storm intensity are correlated with stronger shear or the congruent increase in the low-level jet.

Simulations perturbed with the future thermodynamics predicted by CMIP5 models resulted in shorter-lived squall lines. This is consistent with the increase in CIN predicted

across the CMIP5 models and accordant with large-domain convection-permitting future climate simulations (Kendon et al. 2019; Fitzpatrick et al. 2020). These short-lived storms suggest that large-scale convergence and synoptic variability may play an important role for storms in a future climate and more work is needed to understand this relationship. Similar to the ERA-Interim experiments, the thermodynamic changes dominated the wind shear changes. Increased wind shear did increase rain, however, but also caused storms to die earlier for both thermodynamic profiles. It is important to note that there are large disparities across the different CMIP5 model predictions, not only on the magnitude of future changes, including wind-shear but whether they will be negative or positive. However, positive feedback between changes in temperature and water vapour are generally expected to enhance the Saharan Heat Low and so increase shear (Dong and Sutton 2015; Evan et al. 2015) which is consistent with hypothesis-4 that predicted future increases in shear, temperature and humidity will cause an increase in storm intensity.

Finally, the simulations throughout this Chapter are idealised and so ignore influences such as large-scale convergence, variations in the synoptic state, and the diurnal cycle including surface fluxes and radiation. Thus further study is required on testing the layer-lifting scalings in less idealised settings, to more fully understand squall-line dynamics, and controls on past and future trends in squall line properties.

Chapter 5

The Influence of the Diurnal Cycle in Wind Shear and Thermodynamics on Squall Lines in the West African Monsoon.

As discussed in Chapter 2.3.2, the West African monsoon (WAM) has a clear diurnal cycle in boundary-layer properties, synoptic flow and moist convection. A nocturnal low-level jet (LLJ) brings cool, moist air into the continent and mesoscale convective systems are mostly triggered in the evening and persist overnight, with an overall Sahel rainfall minimum in the late morning. It is theorised that the LLJ may support storms by providing vertical wind shear and a low-level inflow of moisture to the storms that move towards it. The morning erosion of the LLJ is similarly expected to reduce shear and so provide a less favourable environment for mesoscale convective systems (MCSs).

Parker (2008) investigated nocturnal-like convective systems representative of the central United States through examining the effects of low-level cooling in idealised simulations. He found that as convective systems transitioned from surface based to elevated (inflowing air comes from the lowest 500 m initially then from above that altitude) the mechanism responsible for lifting inflowing parcels evolved from a cold pool to a trapped internal gravity wave. Interestingly, as the cold pool temperature deficit decreased the cold pool slows but also produces more intense lifting due to being more nearly balanced by the lower-tropospheric shear. French and Parker (2010) expanded on this study to discuss the effect of a developing nocturnal LLJ, the main impacts of which are to alter the wind shear and the magnitude of the storm-relative inflow in

117

the jet layer. They note that changes in the system relative inflow correlate well with changes in total upward mass flux, while changes in shear seem to better describe the changes in updraft intensity. Thus, nocturnal squall lines in the central United States are supported by the LLJ providing higher system-relative inflows while also dynamically controlling storms. Furthermore, nocturnal thermodynamic changes alone can produce more intense systems.

In this Chapter, idealised simulations are used to investigate how the diurnal cycle in temperature and humidity compared with wind shear can impact on mature Sahelian squall lines. In Chapter 4 changes in vertical wind shear over recent decades were shown to intensify MCS. In this Chapter, we consider representative profiles of the Sahel at different times of the day and use idealised simulations to study whether the diurnal cycle of shear is significant for MCSs and how this compares to the role of the diurnal cycle in thermodynamics. This idealised framework provides an opportunity to test: 1) whether the nocturnal LLJ supports nocturnal storms and 2) whether the layer-lifting model of convection (LLMC) (Alfaro 2017) can be used to explain the modelled characteristics of the MCSs. Finally, what insights can these tools and analysis provide into the actual diurnal cycle of the WAM which includes both the wind and thermodynamic changes? In Section 5.1 the methods used in the study are outlined including how the control profile (Figure 3.3) is adapted to represent different points in the diurnal cycle. Section 5.2.1 contains results from varying wind profiles alone, thermodynamic profiles alone (Section 5.2.2), and with variations combined (Section 5.2.3). Using these results we test the LLMC in Sections 5.2.2.1 and 5.2.3.1.

It is important to note that these simulations are idealised and so we do not consider the diurnal cycle of synoptically driven convergence, radiation or mesoscale flows from inhomogeneous surfaces. Neither do we consider a continually changing profile but rather our experiments provide an opportunity to isolate key diurnal features and their effects on mature MCSs.

5.1   Method

5.1.1   Diurnal Cycle from AMMA profiles

The diurnal cycle in wind and thermodynamic profiles are shown in Figures 5.1, 5.2 and 5.3. African Monsoon Multidisciplinary Analysis (AMMA) campaign radiosonde measurements at 0600, 1200, 1800 and 0000 UTC from every day of July and August 2006 have been used to produce both an overall mean profile as well as mean profiles at

(a) 0600

(b) 1200

(c) 1800
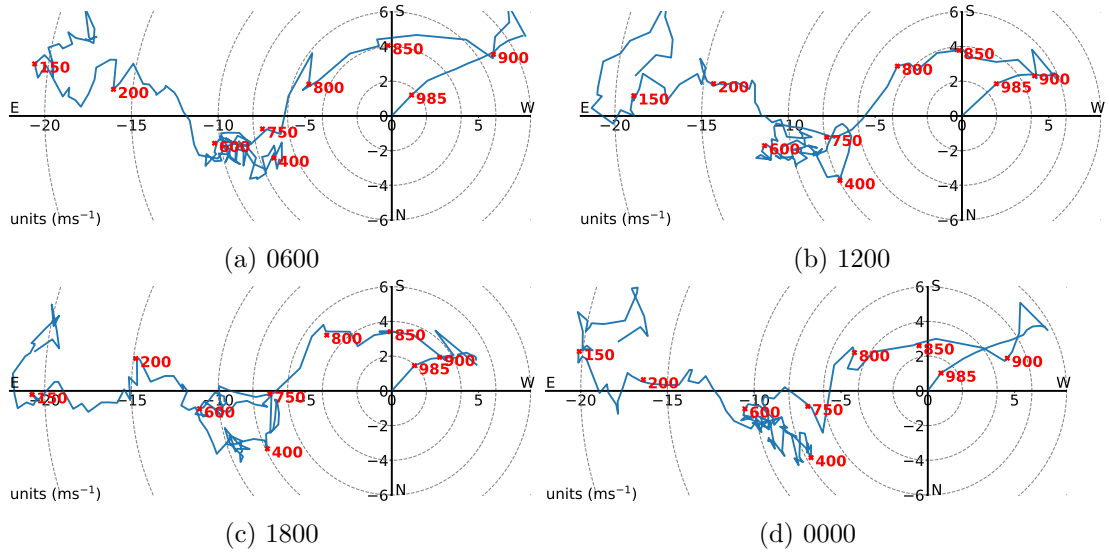
(d) 0000

Figure 5.1: Hodographs for the diurnally varying profiles used. The profiles have been obtained by applying the average at 0600, 1200, 1800 and 0000 UTC (over July and August with the overall average over those months deducted) to the control profile. As in Figure 3.3 wind direction on the hodograph represents winds from that direction and the red numbers are pressure in hPa.

each of the six hourly intervals to generate diurnal anomalies. The diurnal variations from the overall mean at each time have then been applied to the nocturnal pre-storm control profile (Figure 3.3). This approach was selected as it provided a pre-storm profile to be used for the control, which allowed an MCS to be sustained in our simulations while producing an unbiased sample of the mean diurnal cycle in wind and thermodynamics.

At 0600 the near-surface air is cool and moist (Figure 5.2a) with a stable boundary layer (BL) such that there is a maximum of $90\,\mathrm{Jkg}^{-1}$ in the magnitude of convective inhibition (CIN) at the surface and a daily minimum in convective available potential energy (CAPE) for air at all levels (Figure 5.3a). The LLJ is at its sampled diurnal maximum of $10\,\mathrm{ms}^{-1}$ (Figure 5.1a) and the vertical shear between the level of the LLJ and the African easterly jet (AEJ) is also at a maximum (Table 5.1). There is a decrease in humidity from 820-600 hPa indicating the Saharan Air Layer (Figure 5.3c) and the profile is almost dry-adiabatic over these levels (Figure 5.2a). By 1200 UTC surface heating has resulted in increased temperatures at the surface, to around $30\,°\mathrm{C}$, and a well-mixed, turbulent convective BL, Figure 5.2b). The vertical CAPE profile has increased at all heights while the magnitude of the vertical CIN profile has decreased from the surface to 925 hPa (Figures 5.3a and 5.3b). Entrainment has deepened and dried the convective BL and the LLJ has weakened to below $5\,\mathrm{ms}^{-1}$ in the westerly direction but wind speeds both near the surface and within the AEJ are
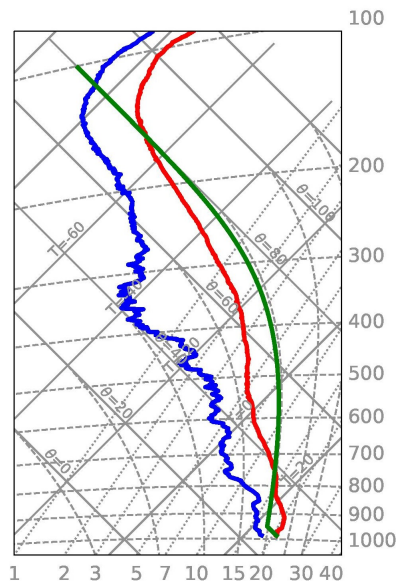
Mean Mixing layer : T = 25.67 degC q = 17.82 g/kg
LCL : P = 948.49 hPa T = 22.44 degC
LFC : P = 746.13 hPa T = 13.84 degC
EL : P = 154.51 hPa T = -66.16 degC
CAPE = 1593.3 J/kg CINH = -90.0 J/kg
Thickness : 500mb = 5792.8 m 850mb = 1434.6 m

(a) 0600
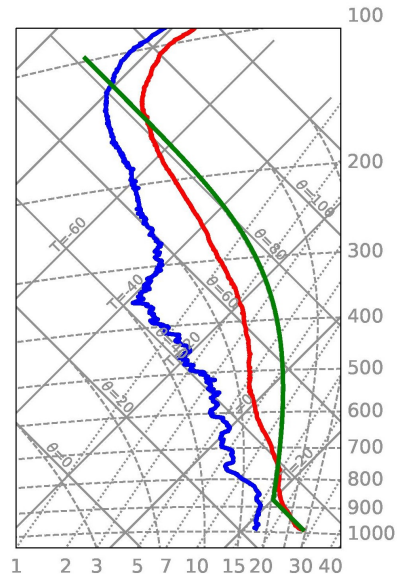
Mean Mixing layer : T = 30.46 degC q = 16.79 g/kg
LCL : P = 873.73 hPa T = 20.13 degC
LFC : P = 749.42 hPa T = 14.63 degC
EL : P = 145.34 hPa T = -68.27 degC
CAPE = 2021.9 J/kg CINH = -26.4 J/kg
Thickness : 500mb = 5797.8 m 850mb = 1433.5 m

(b) 1200
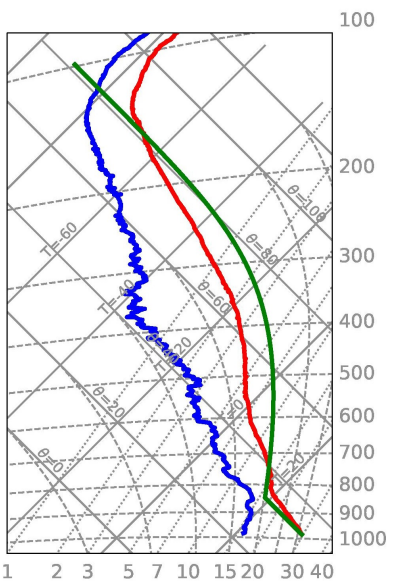
Mean Mixing layer : T = 31.67 degC q = 16.01 g/kg
LCL : P = 845.78 hPa T = 18.84 degC
LFC : P = 740.57 hPa T = 14.04 degC
EL : P = 152.96 hPa T = -65.66 degC
CAPE = 1652.5 J/kg CINH = -27.9 J/kg
Thickness : 500mb = 5819.3 m 850mb = 1450.1 m

(c) 1800
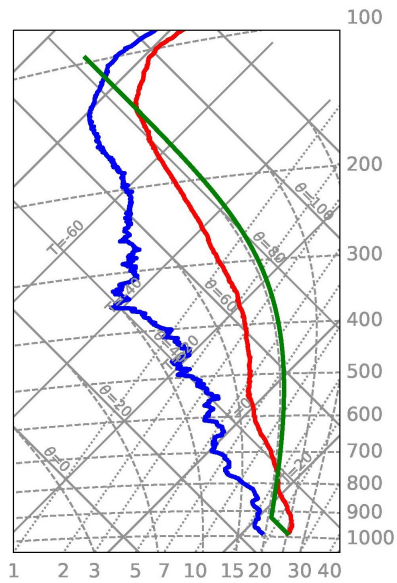
Mean Mixing layer : T = 27.86 degC q = 18.16 g/kg
LCL : P = 923.55 hPa T = 22.31 degC
LFC : P = 762.09 hPa T = 15.51 degC
EL : P = 134.27 hPa T = -72.19 degC
CAPE = 2177.7 J/kg CINH = -72.9 J/kg
Thickness : 500mb = 5803.3 m 850mb = 1436.1 m

(d) 0000

Figure 5.2: As in Figure 3.3. Tephigrams for the diurnally varying profiles used. Profiles created as in Figure 5.1
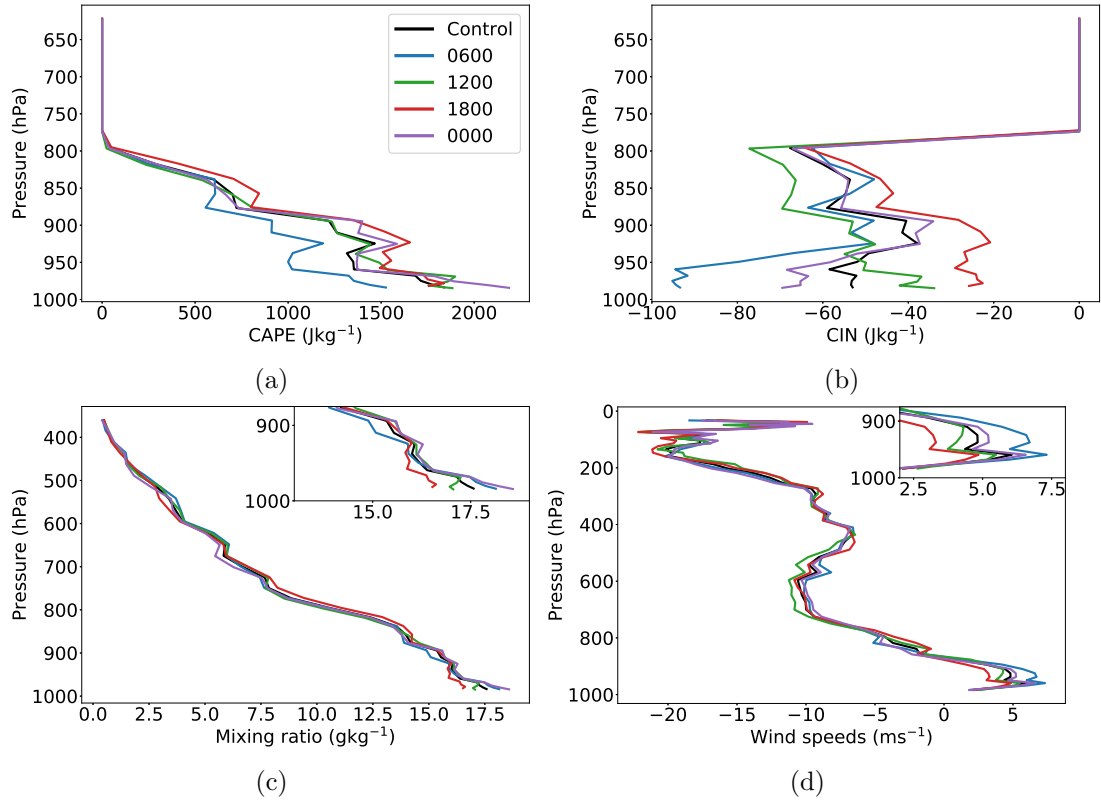
Figure 5.3: Profiles of (a) CAPE (b) CIN (c) water vapour and (d) westerly wind speeds at different heights. In (a) and (b) the profiles show the CAPE and CIN of idealised parcels ascents from the levels indicated. 'Td' indicates the thermodynamic and 'W' the wind profile from time of day stated.

at their maximum (Figures 5.1b and 5.3d).

At 1800 UTC the decrease in the convective BL humidity produces a higher lifting condensation level (LCL) of 845 hPa (Figures 5.2c and 5.3c). The boundary layer has continued to deepen and air from all levels has the lowest magnitude of CIN of the day while the CAPE at 950-890 hPa is at a maximum (Figures 5.3a and 5.3b). The LLJ and the vertical shear between this and the AEJ are both at a minimum (Figure 5.3d). After sunset, the surface cools again so that by 0000 UTC a stable nocturnal boundary layer has formed allowing a strengthened LLJ and an increase in the near-surface water vapour mixing ratio, q_v, which in turn increases CAPE near the surface to 2177 Jkg^{-1}, the highest for any time of the day (Figures 5.2d and 5.3a-5.3d). The increased q_v and lower temperature of near-surface air results in a lower LCL at 923 hPa.

In this study we have triggered squall lines in environments with constant vertical profiles which are characteristic of one time of day. This idealised setting provides an opportunity to isolate the defining features of the diurnal cycle and compare how their

Table 5.1: The maximum strength of the AEJ (ms^{-1}), the LLJ (ms^{-1}) and $\Delta U = |U_{AEJ} - U_{LLJ}|$ (ms^{-1}) for each environment. The average propagation speed (PS) of squall lines (ms^{-1}) as defined in Section 3.4.1, the maximum theoretical cold pool speed (c_{max}, ms^{-1}) as defined in Equation 2.10, the ratio of ΔU to c_{max} and the PS which maximises w_{ll} ($PS(w_{ll}^{max})$, ms^{-1}) for each environment are also shown.

	Winds				Thermodynamic				Combined			
	06	12	18	24	06	12	18	24	06	12	18	24
AEJ	9.8	10.8	10.1	9.9	10.3	10.3	10.3	10.3	9.8	10.8	10.1	9.9
LLJ	6.7	4.5	3.3	5.2	4.8	4.8	4.8	4.8	6.7	4.5	3.3	5.2
ΔU	16.5	15.3	13.4	15.1	15.1	15.1	15.1	15.1	16.5	15.3	13.4	15.1
PS	10.8	11.1	10.6	10.8	9.7	10.4	11.6	11.1	9.7	10.7	11.6	10.8
c_{max}	23.5	24.1	22.9	23.4	16.3	23.5	24.1	24.0	18.1	23.9	24.2	23.5
$\Delta U/c_{max}$	1.43	1.58	1.71	1.55	1.08	1.55	1.60	1.59	1.10	1.56	1.80	1.56
$PS(w_{ll}^{max})$	9.7	10.7	9.9	9.6	9.8	9.8	9.8	9.8	9.7	10.7	9.9	9.6

relative strengthening and weakening throughout the day can impact on a mature squall line. In particular, it provides a method to understand what environments may support the longevity and strengthening versus the decay of squall lines in the WAM. In order to isolate and explore the contributions of the diurnal cycle in the wind and thermodynamic profiles to the development of squall-line MCSs three sets of simulations were run. These included: (1) the 'Wind Experiments' where the thermodynamic profile was kept constant (pre-storm control) while the wind profile was varied to represent the six-hourly intervals of 0600, 1200, 1800 and 0000 UTC, (2) the 'Thermodynamic Experiments' where the wind profile was constant (control) and the thermodynamic profile varied to represent the six-hourly intervals and (3) the 'Combined Experiments' where both the thermodynamic and wind profiles were varied to represent each of the six-hourly intervals. Each experiment was repeated five times with different random noise applied to the initial temperature perturbation and the average across these five used in quantitative analysis.

5.2   Results

In Section 5.2.1 we first detail experiments investigating how the diurnal wind cycle of the Sahel region can impact the severity and longevity of squall lines in the WAM. In Section 5.2.2, we consider the impact of the diurnal thermodynamic cycle alone and in Section 5.2.3 we consider the impact of the combined (wind plus thermodynamic) diurnal cycle. In each case, we consider whether the LLMC explains variations in storm updrafts and rainfall.
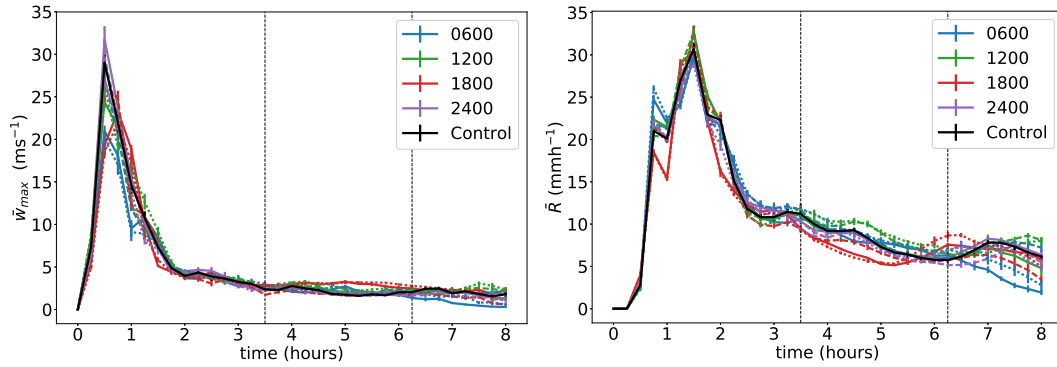
Figure 5.4: Time evolution of y-averaged maximum vertical velocity and mean rain
rate, for Wind (dash dot), Thermodynamic (solid) and Combined (dashed) simulations.
Vertical dashed lines indicate the analysis period. Error bars indicate the standard error
of the mean.

Line-averaged maximum updraft speeds and mean rain rates from all simulations are
shown in Figure 5.4 including the 'spin-up' and mature phases. All cases sustain grad-
ually weakening convection after the initial "spin-up" although the 0600 UTC ther-
modynamic case begins to decay after 6.25 hours ($\bar{w}$ consistently below $1\,\mathrm{ms}^{-1}$). We
therefore only consider and compare the systems when they are steady between 3.5 and
6.25 hours, which we call the analysis period.

5.2.1 Effects of varying the wind profile with constant thermodynamic profile

Vertical cross-sections of the y-averaged vertical velocity for the wind profile experi-
ments are shown in Figure 5.5. The profiles have been time-averaged over the analysis
period. The most upright and consistently strong updraft occurs at 1200 UTC. In all
cases there is a region of descent at the rear of the squall line as well as rear-to-front
system relative inflow near the surface of the cold pool.

5.2.1.1 Layer Lifting Indices

The LLMCwas tested by plotting w_{ll} and PR_{ll} against updraft and rain rates (Fig.5.6)
calculated from different simulations and time-averaged over the period when the storms
are considered steady (Fig.5.4, see Table 3.1 for details of variables). The PSs of the
storms (calculated using the method outlined in Section 3.4.1) are noted to be close to
the AEJ speed in each case (Table 5.1). There is little variation in PS for the different
wind profile cases with the 1800 UTC cold pool moving slowest at $10.6\,\mathrm{ms}^{-1}$ and the
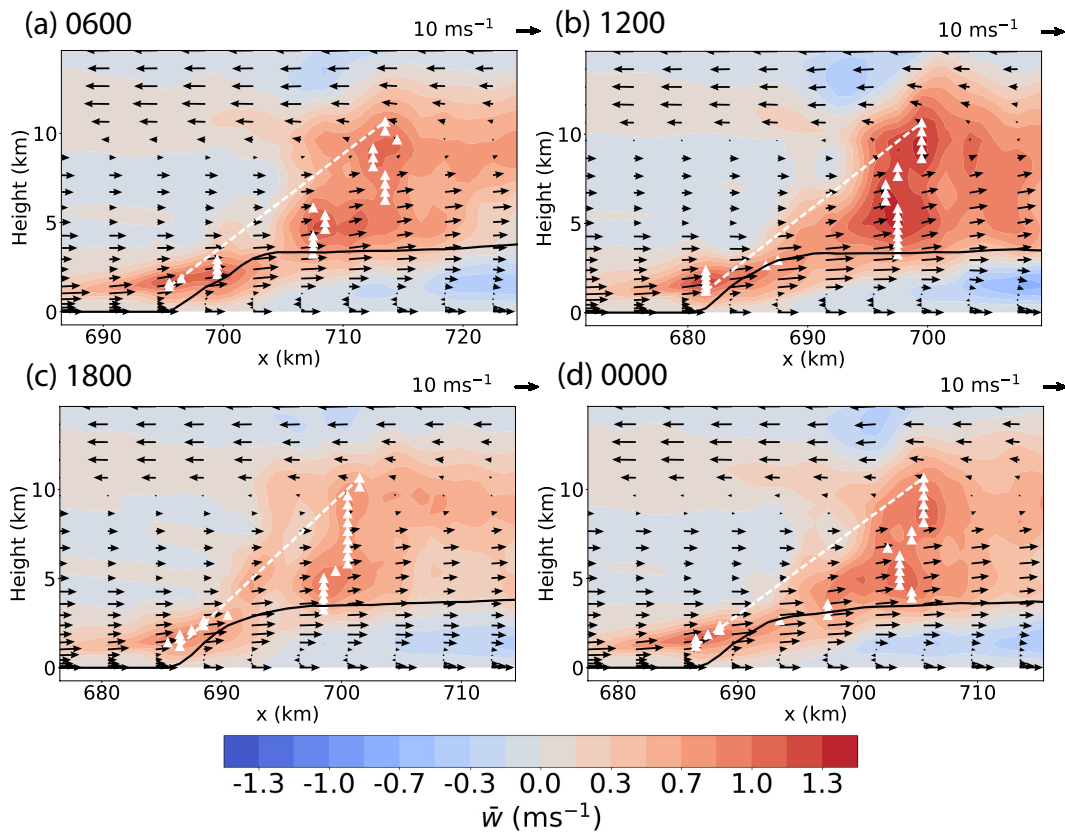
Figure 5.5: Comparing Wind Experiments. Time and y-averaged profiles of vertical velocity (shaded contours) with diagnosed cold pool depths (solid black lines). The white triangles indicate where the maximum of $\bar{w}_{max}$ occurs at each height level. The dashed white line is drawn from the location of the maximum $\bar{w}_{max}$ at cloud base to 11km. The black arrows represent $((\bar{u}_r, \bar{w}))$ where $\bar{u}_r$ are the system relative wind speeds. The y-integrated domain is time-integrated over the analysis period, and the x-axis runs from 10 km in front of the cold pool (where $c > 0$) to 40 km behind.
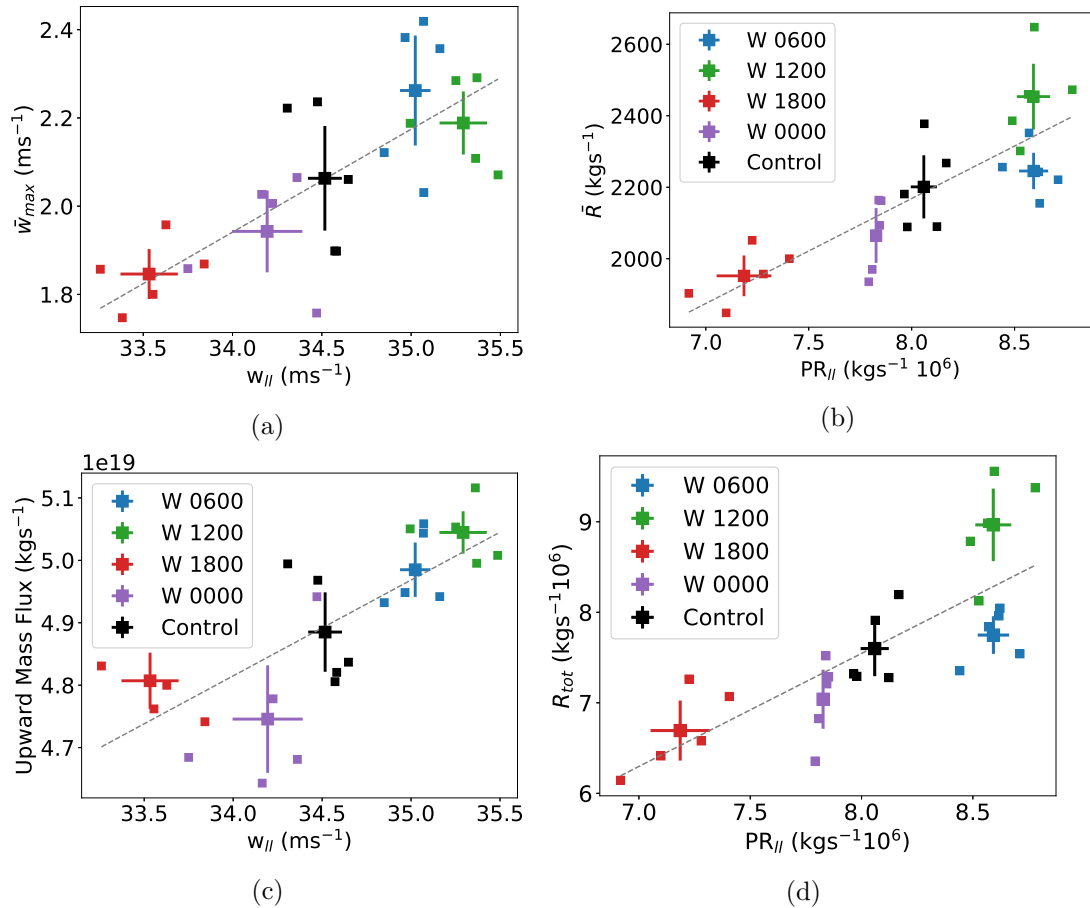
Figure 5.6: Results from Wind Experiments (W) averaged over the analysis period. (a) w_{ll} plotted against the maximum of the y integrated velocity for heights of 4-10 km within the updraft. The correlation co-efficient, r, for the mean across runs is 0.94 (b) PR_{ll} plotted against the mean rain rate, $r = 0.90$ (c) w_{ll} plotted against the total upward mass flux across the domain, $r = 0.84$ and (d) PR_{ll} plotted against the mean total rainfall across the domain, $r = 0.83$. Error bars indicate $\pm 1.6\times$ the standard error of the mean, with a confidence interval of 90%.
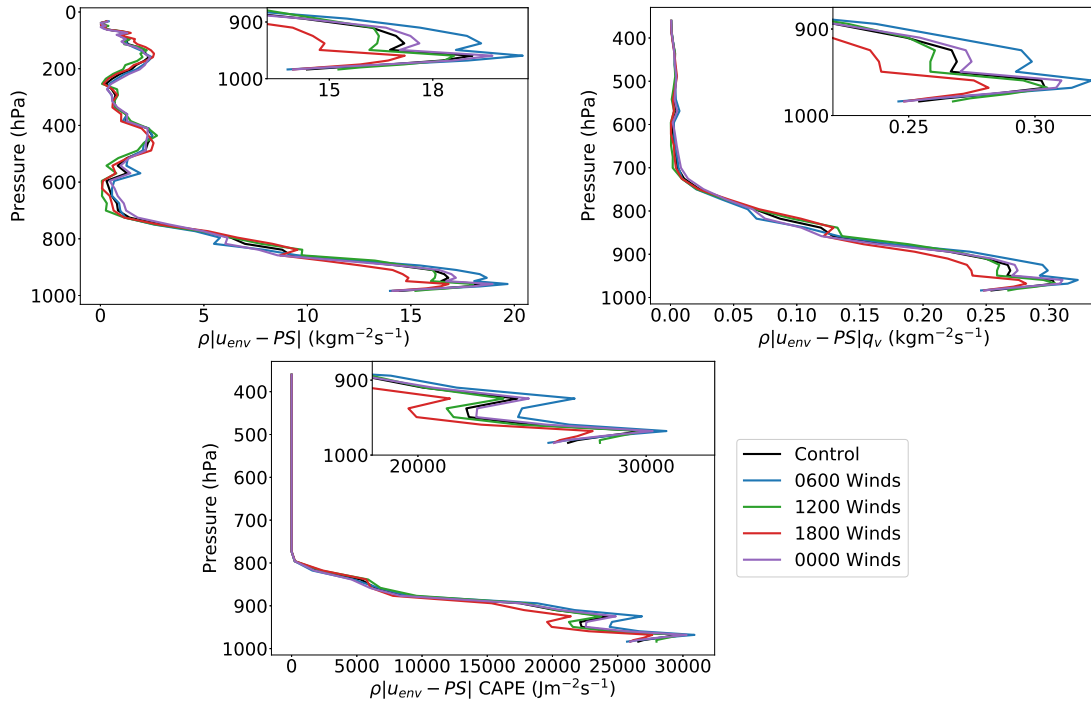
Figure 5.7: Wind Experiments. System relative inflows of (a) mass, (b) water vapour mixing ratio and (c) CAPE, calculated using the propagation speed PS (as defined in Section 3.4.1) averaged over the analysis period.

1200 UTC travelling fastest at $11.1\,\mathrm{ms}^{-1}$ when the AEJ is also at its strongest (see Table 5.1).

For the Wind Experiments, the indices from Alfaro (2017) correlated well with the mean behaviour across repeated runs of the average ascent and rain rates ($\bar{w}_{max}$ and $\bar{R}$ respectively) as well as the bulk quantities including the upward mass flux and the total rate of rainfall (R_{tot}) with correlation coefficients of 0.83 to 0.94 (Figure 5.6). However, despite the 0600 and 1200 UTC cases having the greatest upward mass fluxes, these do not produce equally high rainfall with the 0600 UTC case producing less (Figure 5.6). Due to the strong winds near the surface, the inflow of CAPE at that level is higher for 1200 UTC (Figure 5.7) which combined with the faster PS gives this profile high w_{ll} and PR_{ll} values. Indeed, when comparing the updrafts in Figure 5.5 it can be seen that the updraft in 1200 UTC has consistently strong vertical velocities from $4\,\mathrm{km}$ to $11\,\mathrm{km}$. The 0600 UTC case has a similar maximum $\bar{w}_{max}$ but only near $6\,\mathrm{km}$, explaining why despite the high $\bar{w}_{max}$ value for 0600 UTC in Figure 5.6 the upward mass flux and both mean and total rainfall are lower than for the 1200 UTC case.

5.2.2 Effects of varying the thermodynamic profile, with a constant wind profile

Simulations were run where the thermodynamic profile was varied with the wind profile held constant. In all cases, the storms were sustained, although the 1800 UTC case re-intensifies from hour 5 to 6 and the 0600 UTC case begins to die out at 6.25 hours (Figure 5.4).

5.2.2.1 Layer Lifting Indices

As in the Wind Experiments (Figure 5.6), the LLMCcorrelated well with bulk measures, particularly upward mass flux (Figure 5.8c), but also total rainfall rates (Figure 5.8d) for all except the 1800 UTC case. The LLMC did not correlate well with average ascent rates (Figure 5.8a) or mean rain rates (Figure 5.8b) well. The main difference between the mean and bulk measures is that the rain or updraft area matters for the former which the LLMC does not account for. In the following discussion, we show that varying the thermodynamic profile varies these quantities, as well as affecting evaporation, causing a poorer fit for the $\bar{w}_{max}$ and $\bar{R}$ than for runs when only winds were varied.

The 0600 UTC thermodynamic case has unexpectedly high $\bar{w}_{max}$ and $\bar{R}$ values compared to those of the other cases when w_{ll} and PR_{ll} are considered (Figures 5.8a and 5.8b). Vertical cross-sections in Figure 5.10 show that the 0600 UTC case is a more horizontally compact storm so that mean rain rates are higher relative to the total rain rate as they depend on the area of the storm (where raining). This lower value for total rainfall rate correlates better with PR_{ll} (Figure 5.8d). The 0600 UTC low-level environment is the coolest of the profiles with the potential temperature near the surface about 10 °C lower than for the 1800 UTC case (Figures 5.2 and 5.12). The colder low-level environment at 0600 UTC results in a reduced cold pool buoyancy deficit. Furthermore, the rate of rainfall evaporation at 0600 UTC is just above 80% of that of the other profiles (Fig. 5.9b) resulting in a warmer and so less dense cold pool that therefore has further reduced negative buoyancy.

The 0600 UTC cold pool is therefore slower (Fig. 5.12), and shallower, with the ascent of environmental air in front of the cold pool feeding directly into the updraft (Figure 5.10). Since the height of the cold pool is lowest for 0600 UTC it has a lower maximum theoretical cold pool intensity (c_{max} in Table 5.1). This results in a slower system overall with the front of the cold pool travelling slower at 0600 UTC (Fig. 5.12 and Table 5.1). Due to the cold pool being weaker than the other cases the ratio of c_{max}

(a)

(b)

(c)

(d)
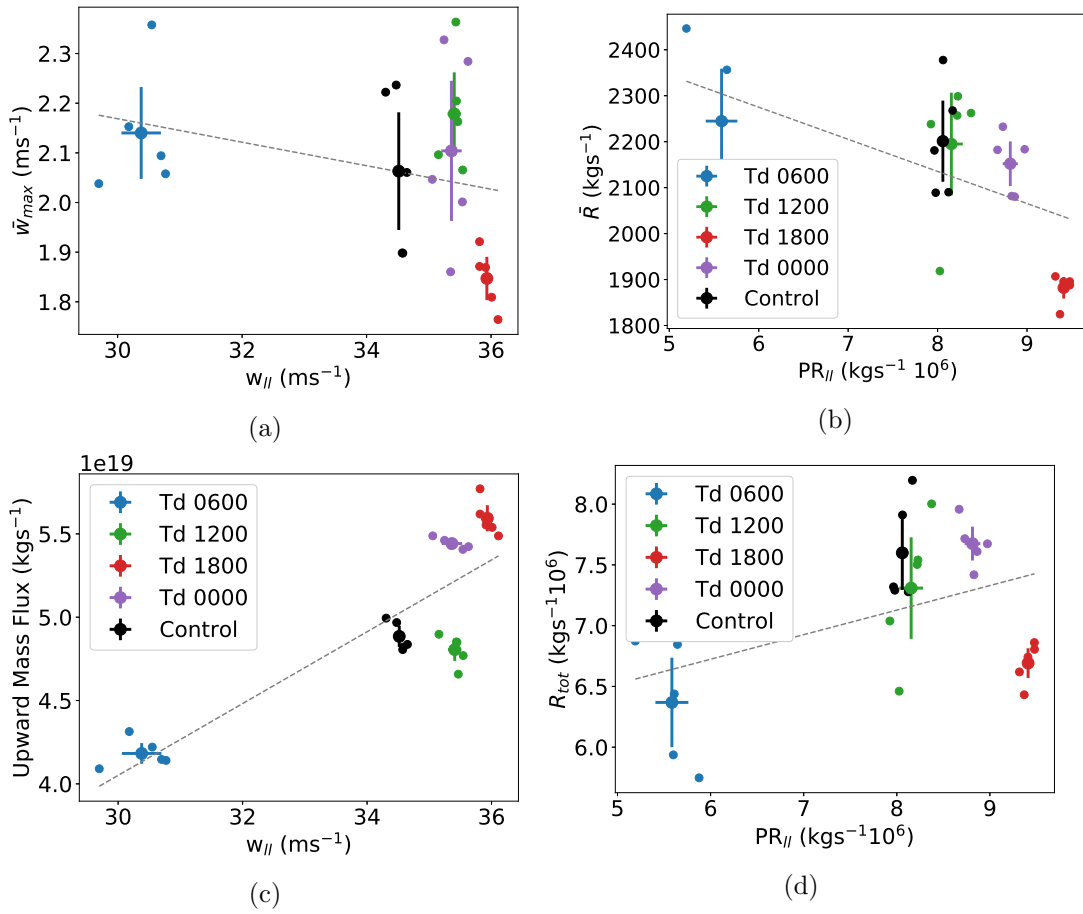
Figure 5.8: As Figure 5.6 but for Thermodynamic Experiments (Td) with r values (a) -0.42, (b) -0.70 (c) 0.88 and (d) 0.51.

(a)

(b)
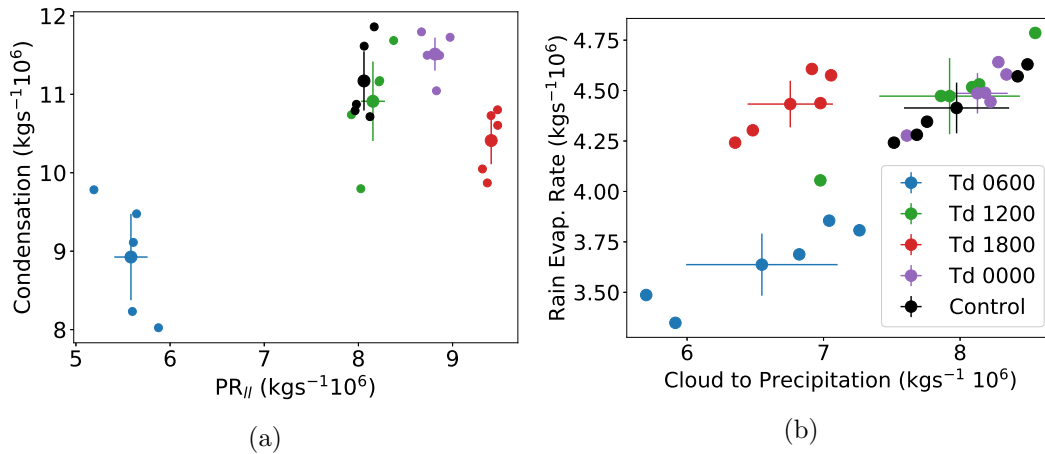
Figure 5.9: Thermodynamic Experiment (Td) results averaged over the analysis period with (a) PR_{ll} plotted against the rate of condensation (total over domain) and (b) total cloud to precipitation rate vs rain evaporation rate. Error bars indicate $\pm 1.6\times$ the standard error of the mean, with a confidence interval of 90%.

to wind shear (represented by the maximum vertical difference in the wind vector, $\Delta U = |U_{AEJ} - U_{LLJ}|$) is nearer 1 for the 0600 UTC runs compared with the other runs in Fig. 5.11. According to RKW theory this balance should result in a more upright updraft. The spread in the value of this ratio within the wind shear experiments was much smaller than for the thermodynamic experiments (Table 5.1).

Another consideration is that the near surface stable layer that exists at 0600 UTC (Figures 5.2 and 5.3) and the weak temperature deficit between the cold pool and its environment produces a system that acts differently to the other cases. These differences include the much smoother wave like shape of the 0600 UTC cold pool (Figure 5.10). At 1200, 1800 and 0000 UTC there is a system-relative rear-to-front flow near the surface in the cold pool which follows the definition of a density current of Crook and Moncrieff (1988). At 0600 UTC the system-relative flow is front-to-back i.e. a gravity wave according to the definitions of Crook and Moncrieff (1988) and similar to what is described in Parker (2008). To summarise, although the LLMC can explain the total rainfall amount in its current form it does not predict storm structure nor storm area and thus cannot predict average ascent and rainfall rates across the storm. The 0600 UTC case, which has a cold pool with a weaker temperature deficit as well as a near-stable environment at the surface, gives more intense rain and ascent due to a narrower storm. The more vertical and intense updrafts are likely the product of a weaker cold pool which is more wave-based rather than density current based and, as in Parker (2008), better balanced by the lower-tropospheric shear.

Even considering the total rainfall, the 1800 UTC case has lower rainfall than expected from its value of PR_{ll}. This profile also produces the fastest moving cold pool (Table 5.1). To gain insight into differences between the storms, we considered their condensation and evaporation rates and found that for the 1800 UTC case the total condensation of vapour to cloud (Figure 5.9a) is around 1.5×10^6 kgs^{-1} lower than expected from PR_{ll} when compared to the other cases. The lifting condensation level of near surface air is at its highest at this time of the day. Additionally, the amount of cloud which evaporates at 1800 UTC is around 50% of the cloud mass that becomes precipitation while it is nearer 40% for the other cases (not shown). A larger fraction of this precipitation then evaporates at 1800 UTC, about 0.75×10^6 kgs^{-1} more than would be expected from the rate of conversion of cloud to precipitation (Figure 5.9b). We conclude that the anomalous values of high rain and cloud evaporation and low condensation explain the low values of total rainfall in the 1800 UTC case, compared to the value of PR_{ll}. The inflow from above $800\,\mathrm{hPa}$ is larger for this case (Figure 5.13) and so more convectively stable and drier air enters the storm which explains the higher cloud evaporation. The updraft is leaning upshear (over the cold pool) to 80km

further upstream (Figure 5.10). RKW theory would suggest this is due to the cold pool being stronger than the shear profile and indeed the value for $c_{max}/\Delta U$ in Figure 5.11 is 1.45.

To summarise, the LLMC correlates well with total upward mass flux while deviations from R_{tot} are explained by the LLMC not considering rain evaporation. The LLMC does not correlate well with average values across the storm, including $\bar{w}_{max}$ and $\bar{R}$, as it does not take the area or structure of the storm into account. The high $\bar{w}_{max}$ value for 0600 UTC is due to a horizontally compact storm structure and a weaker cold pool which, while not currently explained by the LLMC, is consistent with RKW theory.

We now consider what controls the variations in w_{ll} and PR_{ll} shown in Figure 5.8. The 1800 and 0000 UTC thermodynamic cases have the greatest w_{ll} and upward mass flux (Figure 5.8c) with the w_{ll} values explained by the high levels of CAPE in these profiles. The 1800 UTC case also has very low magnitudes of CIN for air up to 900 hPa, which when combined with the high CAPE values at that time may explain the strong vertical velocities in-front of the cold pool (at 1-3 km altitude in Figure 5.10c). However, this does not produce equivalently strong vertical velocities above the cold pool. The 0000 UTC case has the largest system-relative inflow of moisture (Figure 5.13) which translates into high rainfall. Despite the 0600 UTC thermodynamic profile having enhanced moisture due to the presence of the LLJ overnight, the slow PSs (around $9.7 \, \mathrm{ms^{-1}}$) ensure that the system-relative inflow of moisture is not as great as for other times.

5.2.3   Combined Thermodynamic and Wind Experiments

Time-averaged properties for the three sets of simulations (Wind, Thermodynamic and Combined) are shown in Figure 5.14b. For both mass flux and rainfall, the thermodynamic change tends to dominate the wind change for the runs with the combined profile applied. The 1800, 0000 and 1200 UTC combined profiles produce storms with greater mass flux and rainfall than at 0600 UTC (Figure 5.14) and rainfall is at a maximum for the 1200 UTC case. The PSs of the storms are similar to their thermodynamic experiment counterparts (Table 5.1).

5.2.3.1   Layer Lifting Indices

The upward mass flux is very well explained by the LLMC (Figure 5.14a) with consistent lines of best fit between the three sets of simulations. The rainfall results are
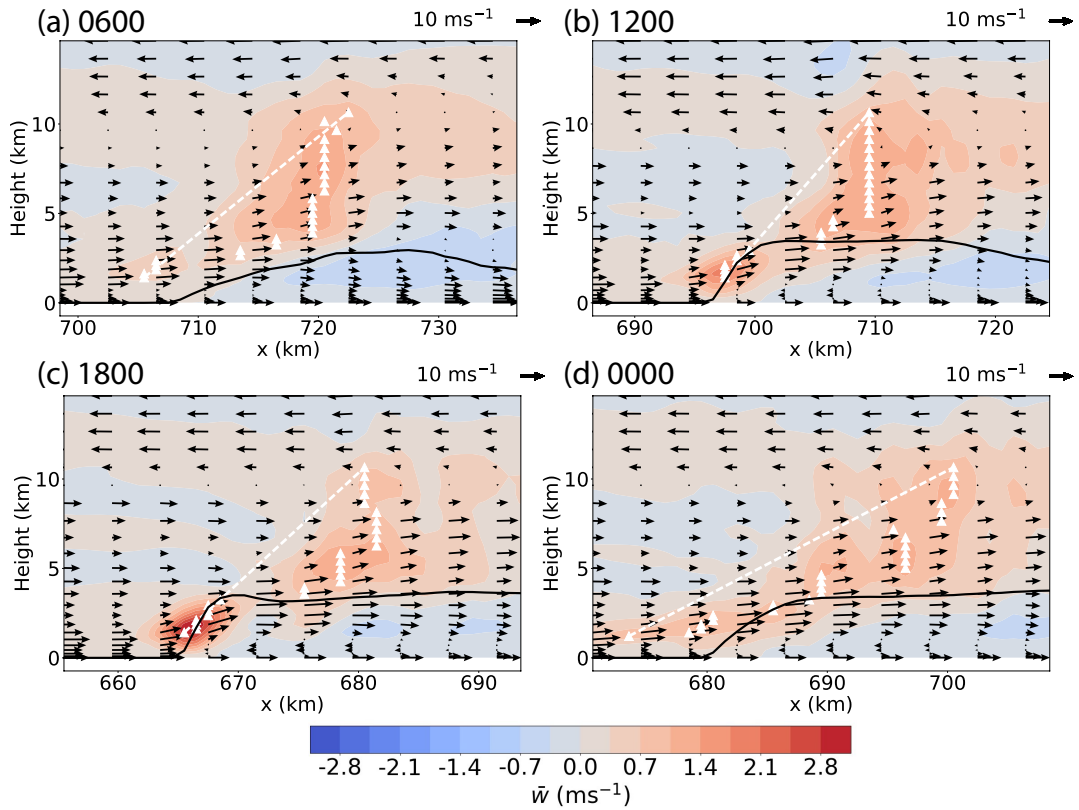
Figure 5.10: As Figure 5.5 but for the Thermodynamic Experiments.
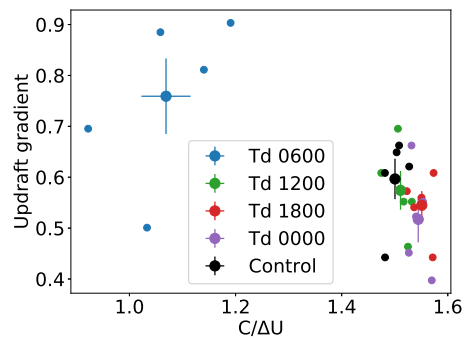
Figure 5.11: Slope of the updraft (e.g., dashed white line in Figure 5.10) for the Thermodynamic experiments, with $c_{max}/\Delta U$ as defined in Table 5.1. Error bars indicate $\pm 1.6 \times$ the standard error of the mean, with a confidence interval of 90%.
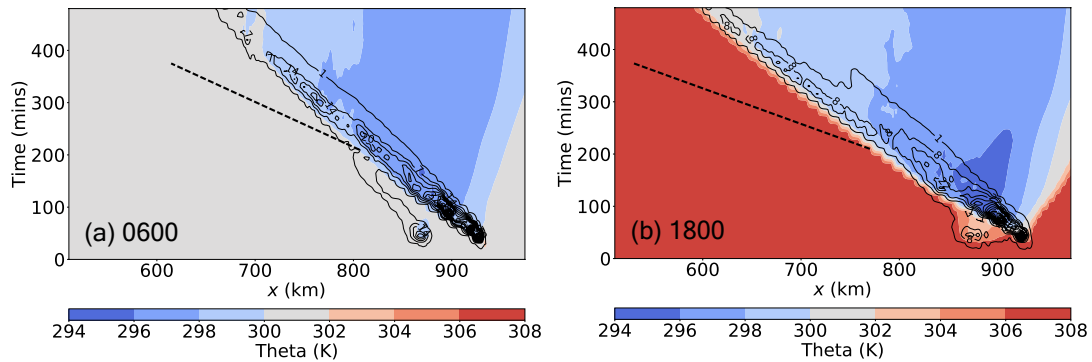
Figure 5.12: Hovmöllers for the 0600 and 1800 Thermodynamic Experiments. Potential temperature at $93\,\mathrm{m}$ (shaded contours), and surface rainfall in mmh^{-1} (black contours). The black dashed line shows the maximum theoretical cold pool speed c_{max} (Equation 2.10) averaged over the analysis period.
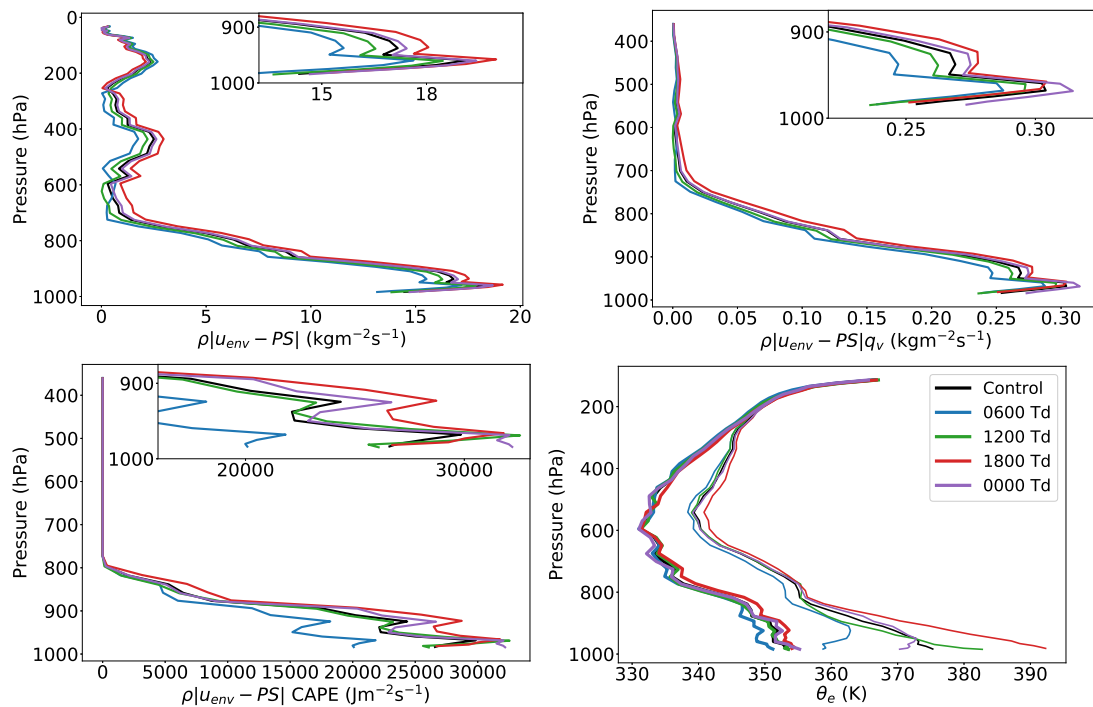
Figure 5.13: Thermodynamic Experiments (Td). System relative inflows of: (a) mass, (b) water vapour mixing ratio and (c) CAPEcalculated using the propagation speed PS (as defined in Section 3.4.1) averaged over the analysis period. Figure (d) shows the θ_e (thick lines) and θ_{es} (thin lines) for the different profiles.

(a)

(b)
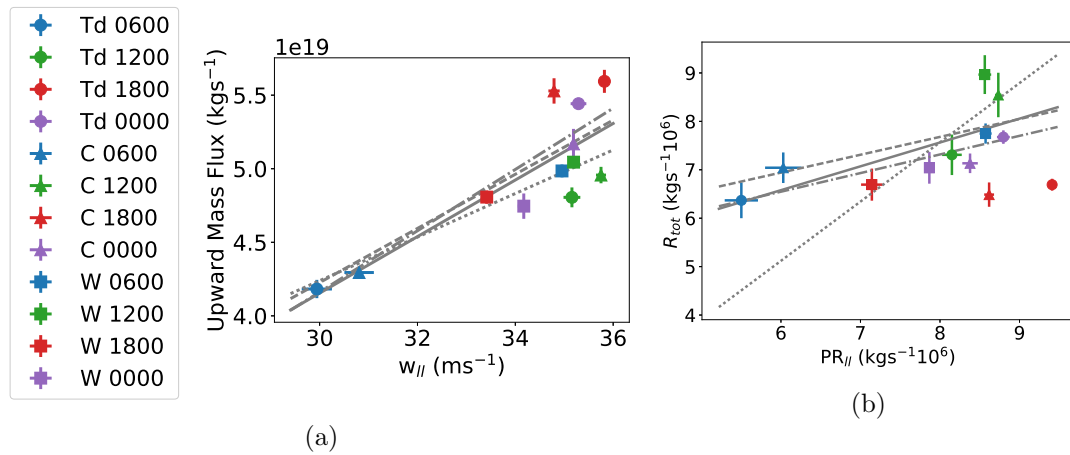
Figure 5.14: (a) Index w_{ll} plotted against the total upward mass flux across the domain.
Correlation coefficients, r, for the mean values are 0.84 for Wind runs (W), 0.89 for
Thermodynamic runs (Td), 0.80 for Combined runs (C), and 0.83 when all runs are
used together. (b) PR_{ll} plotted against the mean total rainfall across the domain. With
$r = 0.83$ for Wind runs, 0.99 for Thermodynamic runs, 0.64 for Combined runs, and
0.72 when all runs are used together. Statistics from experiments are for duration when
storm is steady from 3.5 to 6.25 hours. The best fit lines have been plotted for all cases
(solid), Combined Experiments (dashed), Thermodynamic Experiments (dash-dot) and
Wind Experiments (dotted). For (b) cases with the 1800 UTC thermodynamics have
been ignored when finding r due to the high precipitation evaporation rate in this case.
Error bars indicate $\pm 1.6 \times$ the standard error of the mean, with a confidence interval
of 90%.

accordant with the role of evaporation discussed in Section 5.2.2 for cases with 1800 UTC thermodynamics which have anomalously low rainfall (red triangle and circle in Figure 5.14b). Despite not including these two points when calculating lines of best fit, there are greater differences in the lines of best fit for rainfall than for mass flux (Figure 5.14a), with wind runs giving a steeper gradient, or larger inferred value of W (Equation 2.15). Similarly to the thermodynamic experiments, it was found that the indices from Alfaro (2017) did not correlate well with average ascent rates or mean rain rates (not shown). The effect of using the overall mean PS, rather than the specific PSfor each run, in calculations of w_{ll} and PR_{ll} was investigated in Figures 5.14a and 5.14b (not shown) and using a non-specific PS reduced the correlation co-efficient by less than 10%.

The 0600 UTC combined case has low values for w_{ll} despite the strong nocturnal jet. If the total inflow is considered (Figure 5.15) it can be seen that although the inflow of moisture is high and the total inflow of mass is also high compared to other profiles. Thus, the minimum inflow of CAPE at 0600 UTC (Figure 5.15) produces a low value of w_{ll} as the fraction of convectively unstable air as a proportion of total inflow is smaller. The case also has notably lower bulk measures of mass-flux and total rainfall compared to the other storms (Figure 5.14). This could be a result of the low equivalent potential temperatures (Figure 5.13) which occur despite the higher levels of q_v produced by the overnight advection of moisture.

Recent observational studies have linked decadal trends in shear to decadal trends in extreme storm rainfall (Taylor et al. 2017). According to the LLMC it is not simply shear, but the system-relative inflows of mass, CAPE and water vapour that determine the rainfall, which are themselves a function of shear. For the mean values of all runs, $\bar{R}$ is better correlated with ΔU ($r = 0.72$, Figure 5.16a) than PR_{ll} ($r = 0.19$, not shown). However, a similar plot of R_{tot} against ΔU gives a correlation of 0.51 (not shown), compared with 0.72 for PR_{ll} (Figure 5.14). We conclude that PR_{ll} provides a better scaling for the mean behaviour of R_{tot} across runs than ΔU alone, but that ΔU is better for $\bar{R}$. Future work should seek to understand these differing controls, but we note that variations in ΔU may change the structure of a storm, potentially resulting in higher values of $\bar{R}$, for a given R_{tot}.

The PS of storms is not predicted by the LLMC and the impact of varying PS on the scaling w_{ll} is explored in Fig. 5.16. The value of PS that maximises w_{ll} appears mainly dependent on the wind profile and is generally slower but within $1\,\mathrm{ms^{-1}}$ of the speed of the AEJ (Table 5.1). Travelling close to the speed of the AEJ provides an enhanced inflow of low-level air compared to a minimum inflow from mid-levels (i.e. the height of the AEJ). Any further increases in PS, i.e. greater than the AEJ, will increase the
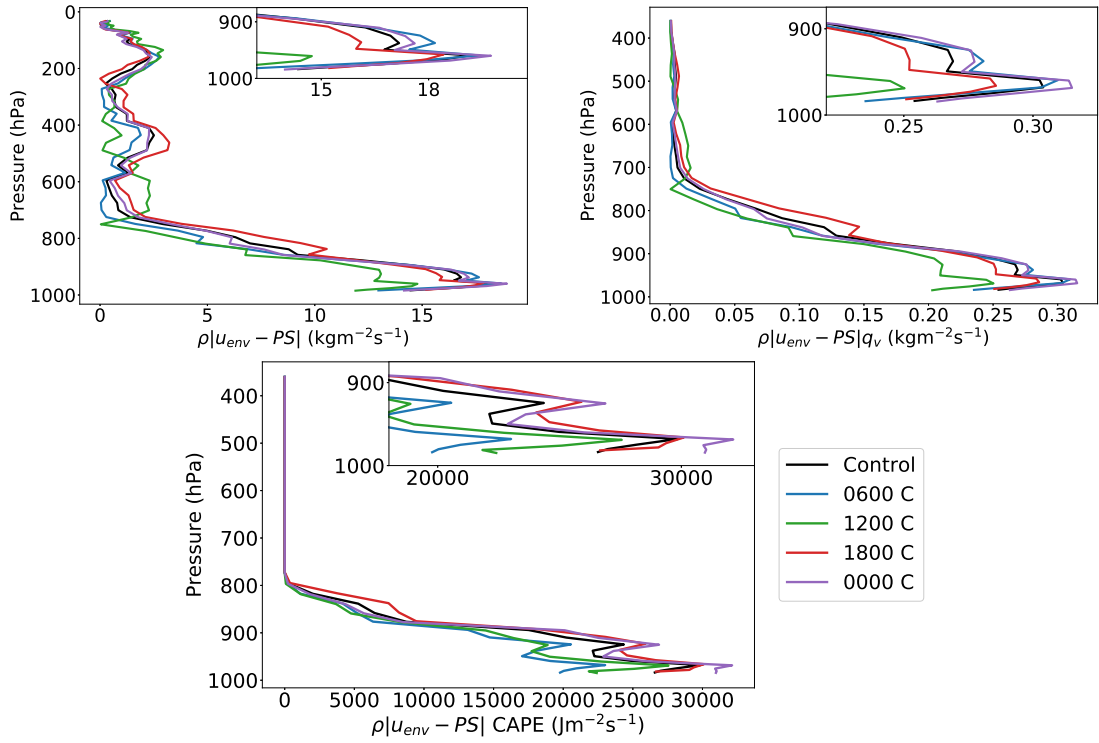
Figure 5.15: As Figure 5.7 but for the Combined Experiments.
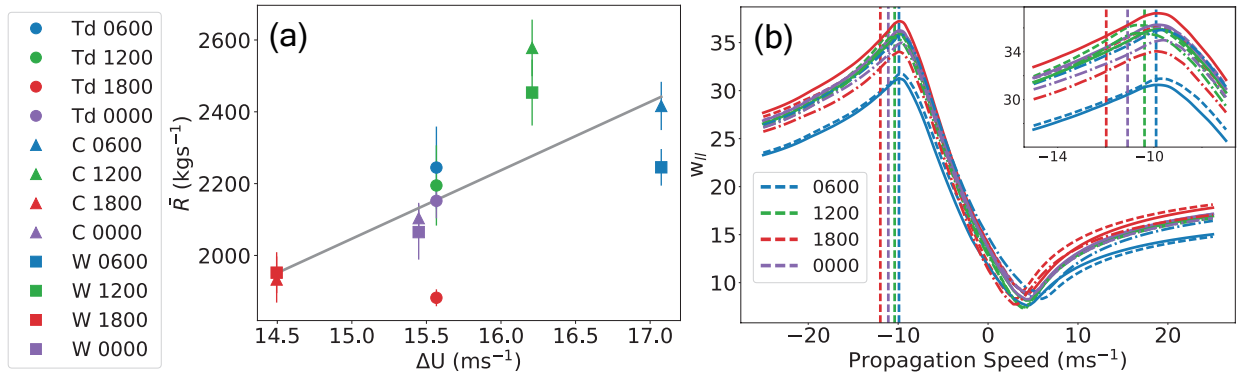
Figure 5.16: Combined (C), Thermodynamic (Td) and Wind experiments (W) including (a) ΔU versus mean rainfall with $r = 0.72$ and (b) changing propagation speed for Wind (dash dot), Thermodynamic (solid) and Combined (dashed) cases and its impact on w_{ll}. Vertical lines indicate the average PS of the front of the cold pool, over the analysis period, for the combined case at each time. Error bars in (a) indicate $\pm 1.6 \times$ the standard error of the mean, with a confidence interval of 90%.

system-relative inflow into the front of the system of both moist low-level air with high CAPE and dry mid-level air with no CAPE. Thus, the optimum PS is close to the AEJ as further increases will cause a greater fraction of the total inflow to be from mid-levels. From Figure 5.16 and Table 5.1b it can be seen that storms do move within $2\,\mathrm{ms}^{-1}$ of this optimum PS but whether this is because the AEJ simply 'steers' the storm or whether the storms tend towards this optimal speed is unclear and requires further study with more varied environmental profiles. The PS of the 0600 UTC combined case is closest to this optimal PS while its ratio of c_{max} to ΔU is also close to 1 (Table 5.1). The value of c_{max} in this case is within $2\,\mathrm{ms}^{-1}$ of $\Delta U = |U_{AEJ}| + |U_{LLJ}|$ while the PS is slower, and closer to the speed of the AEJ. This disparity is due in part to the presence of the LLJ, which flows in opposition to the motion of the leading edge of the cold pool. This provides an alternative understanding of the theory of Rotunno et al. (1988), in that $c/\Delta U$ is not optimal due to vorticity balance (or, not optimal only due to this) but because it often coincides with strong storm-relative inflow in the CAPE-bearing layer, or maximisation of w_{ll}, which explains the efficiency of this storm, see Fig. 5.16b.

5.3   Discussion

The LLMC was tested to see whether the relative inflow of moisture and convective instability could be used to explain rates of rainfall and updraft strength. The LLMC correlated well with bulk measures of upward mass flux and the total condensation. However, the total rainfall was not as well correlated as the LLMC does not account for the rate of evaporation or the fraction of cloud that becomes rain. Additionally, as the LLMC neither predicts storm structure nor the area of the storm, LLMC indices correlated poorly with average ascent and rainfall rates unless only the wind profiles were varied. In particular, the 0600 UTC thermodynamics case had faster updrafts and stronger rainfall than would be expected from the LLMC and this was found to be due to its compact structure. The cold pool at 0600 UTC had a more wave-like form than the other thermodynamic cases due to its weak temperature deficit as well as the near stable surface layer. The lower evaporation and weaker cold pool produced a structurally different and slower-moving storm. When the theory of cold pool and wind shear strength balance (Rotunno et al. 1988) was considered it appears to hold for this case, explaining the more upright updrafts and efficient storm. Thus, we have some insight into the reconciliation of theories concerning the dynamic (Rotunno et al. 1988) and thermodynamic (Alfaro 2017) role of wind shear in deep moist convection. Interestingly, shear alone gave a better indication of the mean rainfall rate than any

particular theory and the reasons for this require further investigation. Our results are also in agreement with French and Parker (2010) where system-relative inflow correlated with mass flux and shear with updraft intensity.

The 1800 UTC thermodynamic case had lower rainfall than the LLMC indicated would occur. This is due to a lower rate of condensation and a higher relative rate of cloud and rainfall evaporation compared to the other cases. Despite the LLMC accounting for moisture moving into the storm this case shows that more consideration of the fraction that will condense and reach the surface as precipitation is needed.

The combined simulations suggest that the 1800, 0000 and 1200 UTC profiles are all favourable for convection to occur. For the 1200 UTC case, this is due to the wind profile where strong near-surface winds and a maximum in the AEJ result in the maximum total rainfall of all the profiles. The fact that the 1200 UTC profile supports strong rainfall is in apparent disagreement with the observed minimum in Sahel-wide rain at around 1100 to 1200 UTC (Birch et al. 2014). However, analysis of observational data used in Crook et al. (2019) shows that there is a daily minimum of about 10% in the probability of an active storm dissipating at 1100 to 1200 UTC, compared with a probability of 22% from 0500 to 0700 UTC (Figure 5.17). So although our results suggest the 1200 UTC profile would be supportive for mature systems very few remain by this point in the day. Thus, our results are consistent with the observed decline in rainfall from 0000 through to 1100 UTC, storms triggering in the evening and persisting overnight and observed storms having a higher probability of dissipating at 0600 than at 1200 UTC.

In the WAM, we know that the low CIN barrier and build up of CAPE that characterise the afternoon indicate an environment which is favourable for storms to develop but one question we address in this paper is whether the LLJ supports them overnight. We have shown that although the diurnal cycle in the LLJ does support nocturnal convection, overall the most supportive profiles are 1800 and 1200, then 0000 with 0600 UTC being the least favourable, consistent with observed storms dying through the late-night and morning. This is explained by the maximum in surface CAPE and the minimum in the CIN barrier at 1800 and the reverse at 0600 UTC.

It is important to note that our experiments consider artificially triggered storms existing in an unchanging environment. Clearly, while our set-up allows us to isolate specific characteristics of the diurnal cycle it does not explore the effects of shear and buoyancy profiles changing in time. Future work should consider a temporally varying environment which would reveal how the life-cycle of storms depends on different environments.
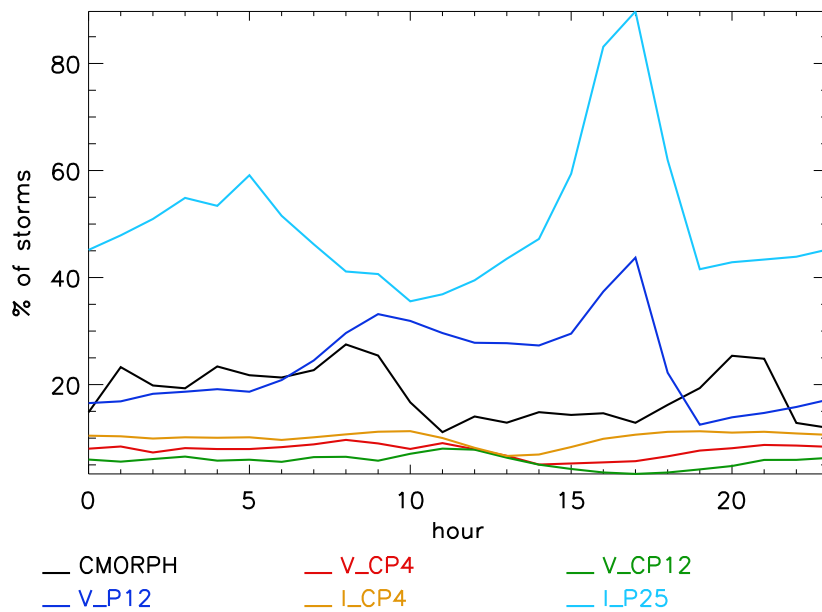
Figure 5.17: Figure courtesy of Julia Crook showing the percentage of storms present in each time bin that dissipated in that time bin for observations (CMORPH) and simulations. Simulations include those from the UK Met Office atmosphere-only Unified Model (UM v8.2) over a single season with instantaneous temporal resolution (V) at 4 and 12 km. Additionally, simulations using the UM Met Office regional model (I) at 4.5 and 25 km resolution with mean temporal resolutions have also been plotted. Whether convection is permitted (CP) or parametrised (P) is also indicated. See Crook et al. (2019) for further details on simulations. The percentage storm dissipation has been calculated by counting a storm whenever it is seen at a given time and counting the storms that dissipate in each time bin for all days and months of the simulations and then dividing number of dissipations by number of storms present.

5.4   Conclusions

Previous studies have shown that there are strong diurnal cycles in winds, vertical wind-shear and MCSs in the WAM. Idealised simulations were run with environmental profiles representative of different points in the day in order to isolate and study the effects of both combined and isolated diurnal variations in thermodynamics and shear. A particular motivation was to test whether the nocturnal LLJ supports MCSs overnight in the Sahel. Additionally, the LLMC and whether it provides useful indices for storm updraft speeds and rainfall was investigated.

We ran idealised simulations to isolate the effect of diurnal changes in the wind profile and we conclude that the LLJ winds do support nocturnal storms. Increasing the magnitude of the LLJ also increases the system-relative inflow of CAPE and water vapour. However, the variation in thermodynamics is large diurnally and so dominates when combined with that of the wind.

The LLMC correlates well with upward mass flux but not average values of vertical velocity due to variations in storm area and storm organisation. Variations in these appeared to be explained by differences in the ratio of the cold pool speed to shear (Rotunno et al. 1988). For the 0600 thermodynamic case, this ratio was close to 1 and this coincided with more vertical updrafts and a horizontally compact storm, however this arrangement also maximises w_{ll} for the profile, possibly offering an alternative, or additional, understanding of RKW theory. To summarise, the upward mass flux does depend on wind shear and although the effect of the diurnal wind cycle is weaker than that of the thermodynamics it still plays a role.

The LLMC better explains R_{tot} than $\bar{R}$, which can again be understood partly as $\bar{R}$ is a function of storm area whilst R_{tot} is not. R_{tot} is not as well explained as mass flux, however, and our analysis shows that this can largely be explained by variations in thermodynamics affecting microphysical processes: in particular, our 1800 UTC runs had a deep, dry and warm BL and much greater fractional evaporation of rainfall, reducing surface rain rate and producing a strong and fast cold pool, which led to low condensation for its PR_{ll} .

We conclude that the LLMC does provide useful scalings for squall line mass fluxes and rainfall, with results showing these properties are strongly controlled by shear, a parameter that is not usually accounted for in parametrisations. However, differences in microphysics and storm organisation are not accounted for and this is particularly clear when the thermodynamic profile is varied, rather than the wind profile alone.

Our results indicate that for convection parameterization schemes to account for the diurnal cycle, which they currently struggle with, they must capture the shear effects. The LLMC has been shown to give a useful indicator of bulk measures of convection. There is also some measure of reconciliation between the theories of Alfaro (2017) and Rotunno et al. (1988) as storms where the cold pool intensity was comparable with shear strength were more compact resulting in a more efficient storm with higher mean rainfall rates and as we have discussed this was not well explained by the LLMC. Further investigation showed these storms to be travelling nearer a speed which maximised their value of w_{ll} while a weaker cold-pool temperature deficit produced variations in the structure and form of the cold pool such that it was more wave-based than density current based (Crook and Moncrieff 1988). Finally, we also found shear alone was by far the best indicator of $\bar{R}$ highlighting the need for further study.

Although our idealised simulations allow us to isolate how key features of the diurnal cycle in thermodynamics and wind shear can control the intensity of squall lines they do not include all the factors that control the diurnal cycle of even mature MCSs in the real world. In reality, storms tend to form in regions of synoptic and mesoscale convergence (Birch et al. 2014) which vary diurnally (Vizy and Cook 2018), as does radiation which both interacts with clouds directly and produces the surface fluxes which drive BL circulations. Nevertheless, our simulations provide insight into the real world, indicating that the environmental profiles at 1800 and 0000 UTC are most favourable for strong updrafts, consistent with the intense storms and rainfall at this time from storms which are generated in the afternoon/evening when the CIN barrier is at a minimum. Although the 0600 UTC thermodynamic profile is not conducive to higher total rainfall and mass flux, the LLJ does help support storms overnight, a feature that models with parametrised convection struggle to represent. Our 1200 UTC profile supports high rainfall due to environmental wind features which include strong surface winds and a maximum in the AEJ, the latter of which results in stronger shear despite the LLJ weakening as the surface heats up and the boundary layer increases. This is in apparent disagreement with the observed minimum in Sahel-wide rain at this time. However, analysis of observational data used in Crook et al. (2019) shows that observed storms are twice as likely to die-out at 0600 than 1200 UTC (not shown). Thus, our results are consistent with the observed decline in rainfall from 0000 through to 1100 UTC, with storms triggering in the evening, persisting into the night and dying out through the night and early morning, with the fraction of storms which die out at 1200 being much lower than 0600 UTC.

We note that by moving with the AEJ, storms maximise their system-relative inflow of CAPE, and produce ratios of $c/\Delta U$ which are closer to 1, providing an additional,

or alternative, understanding to the RKW theory. Whether there are mechanisms that create a tendency for storms to move at a speed that maximises the system-relative inflow of CAPE, or whether this is simply because storms move with the AEJ and this maximises the inflow is unclear and needs further research to investigate. Finally, we note that the LLMC combined with RKW theory appear useful in explaining our results, with the LLMC explaining mass fluxes and rainfall, with RKW useful for explaining storm organisation and structure.

Chapter 6

Tracing Transport in Modelled Squall Lines

As discussed in Chapter 1, the flow of air through a mesoscale convective system (MCS) and how this depends on the environmental wind shear is still an active area of research. Kingsmill and Houze Jr. (1999) investigated tropical MCSs using Doppler-radar data and found the updrafts were almost always slantwise and that the ascending air nearly always maintained a well-defined layered structure. In this chapter, passive tracers are added to the experiments to investigate if this holds for idealised experiments representative of the West African monsoon (WAM). Since mass transport is key to diabatic heating, rainfall and the transport of trace gases, a better understanding of the movement of layers of air through Sahelian squall lines will provide valuable insight.

This chapter analyses passive tracers in key large-eddy simulation (LES) experiments from Chapter 5 to diagnose the transport of environmental air by the modelled MCS and so gain insight into which layers of air are transported upwards, and which form the downdrafts and subsequent cold pool. The ability to trace where the air from different levels ends up provides an opportunity to better understand the ratio of low-level to entrained air in convective updrafts. Tracers also provide a method to compare the mixing of air from different levels throughout the convective region. Finally, experiments are run with different wind profiles at multiple resolutions which allows testing of the combined effect of varying resolution and shear on tracer transport.

Through considering satellite data of cloud-top temperatures over West Africa, Taylor et al. (2017) showed that over the last few decades there has been an increase in the height of MCS anvils which correlates with an increase in shear over the same

period. The study argues that cloud-top temperatures can be viewed as a indicator of intense rainfall as they found the likelihood of intense rainfall (measured by rain gauge measurements) coinciding with an MCS (at a temperature threshold of -40 °C and an areal threshold of $25\,000\,\mathrm{km}^2$) was 85.5%. Ongoing analysis of observations is showing that shear allows MCS anvils to be higher relative to their equilibrium level (EL) (Baidu 2021). In recent convection permitting, 4.5km resolution modelling over Africa (CP4A) increases in shear have produced higher anvils but not greater rain intensity (Fitzpatrick et al. 2020; Senior et al. 2021) unlike the simulations discussed in Chapters 4 and 5 of this study. There is uncertainty about the reasons for this discrepancy within the literature on the effects of shear on rainfall in MCSs.

This recent work suggesting that low-resolution convection permitting models may struggle to capture some shear effects on MCSs, combined with the results of the investigation into the effects of horizontal resolution in Chapter 4.2.4, has motivated further investigation into the effects of horizontal grid-spacing in this chapter. Bryan and Morrison (2012) included passive tracers in the boundary layer in their simulations of squall-lines in order to investigate the entrainment process with different resolutions. The final passive tracer distribution was notably different for grid-spacings of $0.25\,\mathrm{km}$, $1\,\mathrm{km}$ and $4\,\mathrm{km}$. They found that for the $0.25\,\mathrm{km}$ case there were higher levels of tracer throughout the troposphere while the lower-resolution simulations deposited more tracer in the upper troposphere and lower stratosphere. Thus, it is clear that resolution impacts the rate of entrainment which controls the EL of the ascending air. In this chapter, simulations will be repeated at different resolutions to gain some insight into whether the effects of shear are consistent across different horizontal resolutions. If resolution does control the effects of shear by influencing the rate of entrainment this may provide an explanation for this key discrepancy between recent simulations at $4\,\mathrm{km}$ and observations.

In Section 6.1 the set-up of the tracers is discussed as well as the thermodynamic make-up for each of the layers of air that are considered. The transport of each of the tracers in the control $1\,\mathrm{km}$ simulation are described in Section 6.2.1. How the transport of the tracers changes with horizontal grid-spacing is then examined for the control profile simulations at $4\,\mathrm{km}$ and $100\,\mathrm{m}$ resolutions in Section 6.2.2. The tracer transport at different horizontal grid-spacings with the control profile thermodynamics but with environmental wind profiles representative of 0600 and 1800 (Chapter 5) are then considered. Finally, the results are discussed in 6.3.

Table 6.1: Table detailing the different passive tracers which the experiments were initiated with.

		Width	
		A: 0-825 km	B: 900-1600 km
	Surface - 1.5 km (830 hPa)	Tracer 1A	Tracer 1B
	1.5 - 3 km (830 - 700 hPa)	Tracer 2A	Tracer 2B
Height/Pressure	3 - 6 km (700 - 470 hPa)	Tracer 3A	Tracer 3B
	6 - 9 km (470 - 320 hPa)	Tracer 4A	Tracer 4B
	9 - 12 km (320 - 210 hPa)	Tracer 5A	Tracer 5B

6.1 Methods

6.1.1 Tracer Setup

As described in Section 3.2.4, ten different passive tracers have been inserted into the domain. The tracers become active two hours after the start of the simulation to avoid the spin-up and so to include only the flow of a mature system. Each tracer is initiated with a constant value of $1 \, \text{gkg}^{-1}$ mixing ratio and there are no sources, sinks or sedimentation of the tracers. The cold line thermal which initiates the storm spans from 872-952 km originally and the storm moves west from there. The tracers have been placed in front of and behind the storm (indicated by A and B respectively, see Table 6.1) so the inflow into the mature MCS from both in front and behind the storm can be studied. The different tracers can all be combined and generally tracers from one level, e.g. Tracer 1A and 1B, will be combined and so referenced together e.g. Tracer 1. These experiments have been repeated with horizontal grid-spacing of 100 m, 1 km and 4 km. These three grid-spacings have been chosen as we expect the mesoscale flows of the squall line, which span 100 km, to be reasonably resolved at 4 km grid-spacing, whilst individual cores of convection will only really start to be resolved with finer grid-spacings, and studies show that 100 m is needed to resolve mixing (Petch et al. 2002; Bryan and Morrison 2012). In Section 6.2.2 the impact of increasing the resolution, and the associated flow features, are explored. The 4 km and 1 km simulations have each been repeated five times with random noise of maximum amplitude 0.2 K to the line thermal perturbation at every point. The 100 m simulations have been repeated three times.

In order to explore how horizontal grid-spacing influences the effects of shear, the 0600 and 1800 Wind profiles which represent the extremes in shear of the diurnal cycle discussed in Chapter 5 are also used here. The single thermodynamic profile used in

the experiments and multiple wind profiles are shown in Figure 6.1, as only the wind profile is varied in this chapter. The air from nearest the surface to 830 hPa has been marked by Tracer 1 (T1) as it contains almost all of the convectively unstable air which enters the storm (Figure 6.2) with the air above approximately 780 hPa having convective available potential energy (CAPE) of zero, Figure 6.1. Figure 6.1 shows a distinct change in the vertical gradient of θ above 810 hPa where the monsoon layer ends. T1 therefore categorises the inflow of monsoon layer air. As the south-westerly low-level jet (LLJ) is at a maximum in this region, the greatest quantity of air will enter the westward propagating storms with T1.

Above T1 there is an increase in stability and a drop in humidity (Figure 6.1), marking the start of the Saharan air layer (SAL), which extends to approximately 500 hPa and defines Tracer 2 (T2) and Tracer 3 (T3). T2 has been defined to include this fairly convectively stable region which extends to 650 hPa with q_v values of 12.7 gkg^{-1} at 810 hPa decreasing to 5.5 gkg^{-1} at the top of the layer. T3 has been placed from 650 hPa, roughly around the freezing level, and at which height there is a local decrease in $\frac{d\theta}{dz}$ in Figure 6.1, and so a decrease in stability, to 450 hPa. This layer includes no CAPE and is marked by the maximum of the African easterly jet (AEJ), which occurs at approximately 600 hPa with a strength of around 11 m s^{-1}. In Chapter 5, it was found that the propagation speed (PS) of the storms are often similar to the speed of the AEJ. Thus, the greatest inflow of mass from Tracer 3 (T3) occurs toward the top of the layer (Figure 6.2). The water vapour mixing ratio continues to decrease through the T3 layer to 1 gkg^{-1}. T3 describes the mid-level air of the troposphere which will provide useful insight into both upward mixing and entrainment as well as whether this important layer of air experiences descent including in the form of a rear-inflow jet.

Tracer 4 (T4) has been added from 450 hPa to 320 hPa, a level which includes a high inflow of mass (Figure 6.2) but little inflow of moisture. Finally, T5 has been placed at 320 hPa to 200 hPa which includes the height of the maximum outflow from the convective updrafts. This allows the study of how the detrainment of air that originates from different levels and is transported upwards by convective updrafts reaches its EL and impacts the environmental air at that height.
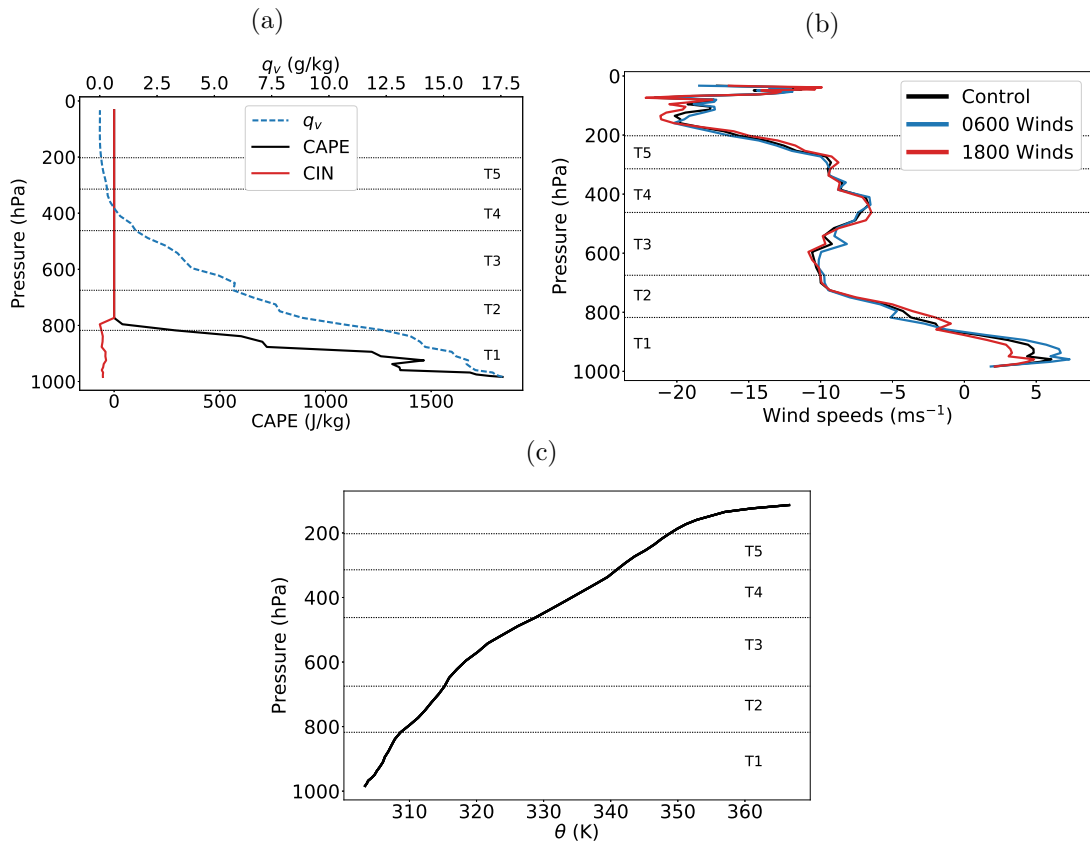
Figure 6.1: (a) The vertical profiles of CAPE (black solid), convective inhibition (CIN) (red solid) and the water vapour mixing ratio (blue dashed) for the control profile, (b) Vertical wind profiles representing different times of day and (c) the vertical potential temperature profile for the control profile. The heights of each of the tracers shown by black solid lines.
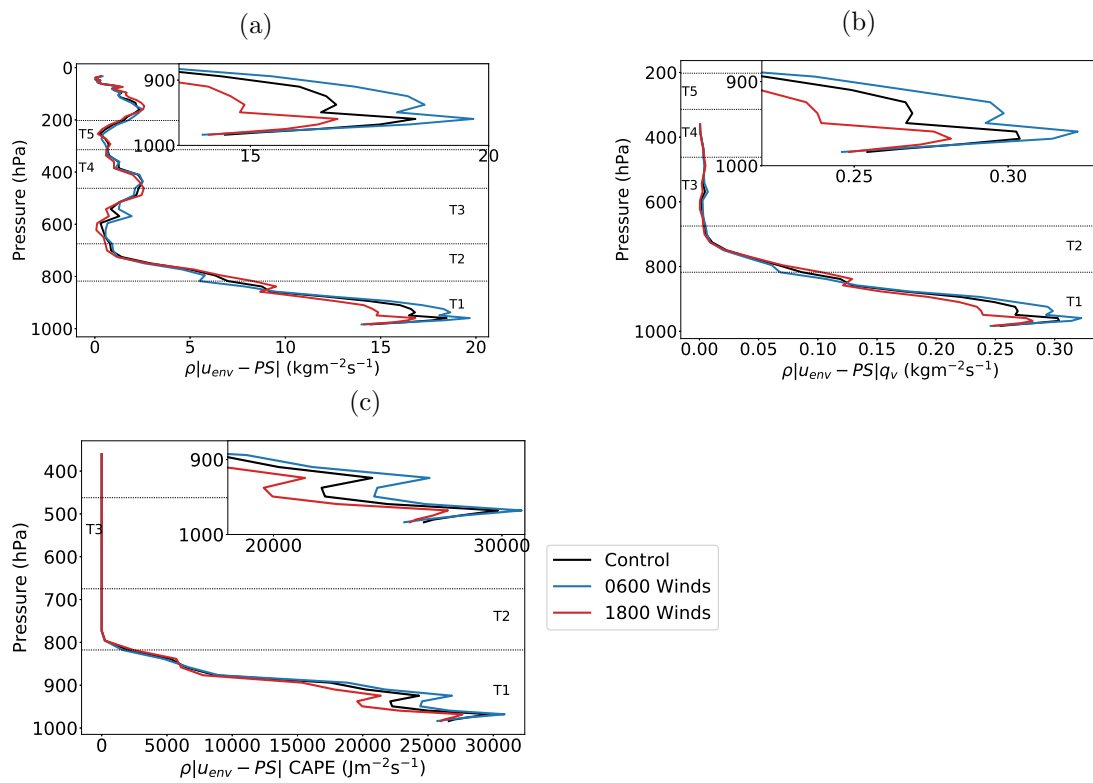
Figure 6.2: 4 km Wind Experiments. System relative inflows of (a) mass, (b) water vapour mixing ratio and (c) CAPE at different heights for the different profiles. The propagation speed of the storm, PS, is defined as the average speed of the cold pool whilst the storm is considered steady (as in Chapter 5).

6.2 Results

6.2.1 Model Tracer Transport in the Control Run

In this section, the transport of each of the tracers in the 1 km control run simulation is considered in order to better understand the general flow through the convective region. Figure 6.3 shows the time evolution of Tracers 1, 2 and 3 (averaged over the y-domain) from two to eight hours. Tracers are initiated at two hours. At three hours it is possible to see the near-surface air with T1A (at the front of the convective region) moving up and over the remnants of the cold line thermal and entering into the updraft. The higher system-relative inflow of air near the surface is clear here with T1 entering the convective region before the tracers at other heights. By four hours some of the T1A air has reached near the top of the anvil while the rest descends back down toward the surface as it moves toward the rear of the convective region. As Figure 6.3 only shows whichever tracer is at a maximum concentration at that height, it indicates that T1A makes up the majority of the updrafts, anvil as well as the lowest portion of the cold pool at these times. Boundary-layer air to the east of the storm (to its rear, T1B) quite quickly disappears from the domain shown as the westerly winds are strongest at that level. From 4 hours both T2A and T3A can be seen to be flowing into the storm. T2A and T3A can also be seen to descend toward the back of the convective region from five hours to a height of around 1-2 km. There is also a clear rear-inflow jet of mid-level T3B air which descends and flows into the rear of the storm before reversing to be swept away from the storm at lower levels. Although the quantity of T3 in the storm at heights of 3-5 km dominates T1 from six hours in Figure 6.4, it can be seen that T1 is still present in this region. Despite some mid-level air with T2 and T3 being entrained into the convective updrafts from four hours (Figure 6.5) T1 air from near the surface dominates the content of the anvil as can be seen at 6-8 hours in Figure 6.3, while T3 air moves below T2 at the rear of the convective region. In Figure 6.4, T4 can be seen to descend into the convective region from five hours while Figure 6.5 shows that some of T4 is also entrained upward as it flows into the front of the storm. After reaching the anvil T1 air moves horizontally outward, forcing the T5 air at the rear eastward and upward so that from 6 hours it flows over the top of T1 (Figure 6.4).

Figures 6.3-6.5 display properties which have been averaged over the y-domain. In Figure 6.6, horizontal cross-sections of the T1, 2 and 3 are shown at different heights at five hours. This time has been chosen as the storms are well-established by this point and so are in the 'steady' phase (Figure 4.7) but it is also long enough before some cases begin to 'die out'. From the cross-sections at 3 km and 7 km it is clear that there are sections along the line of the squall line where there are significantly stronger
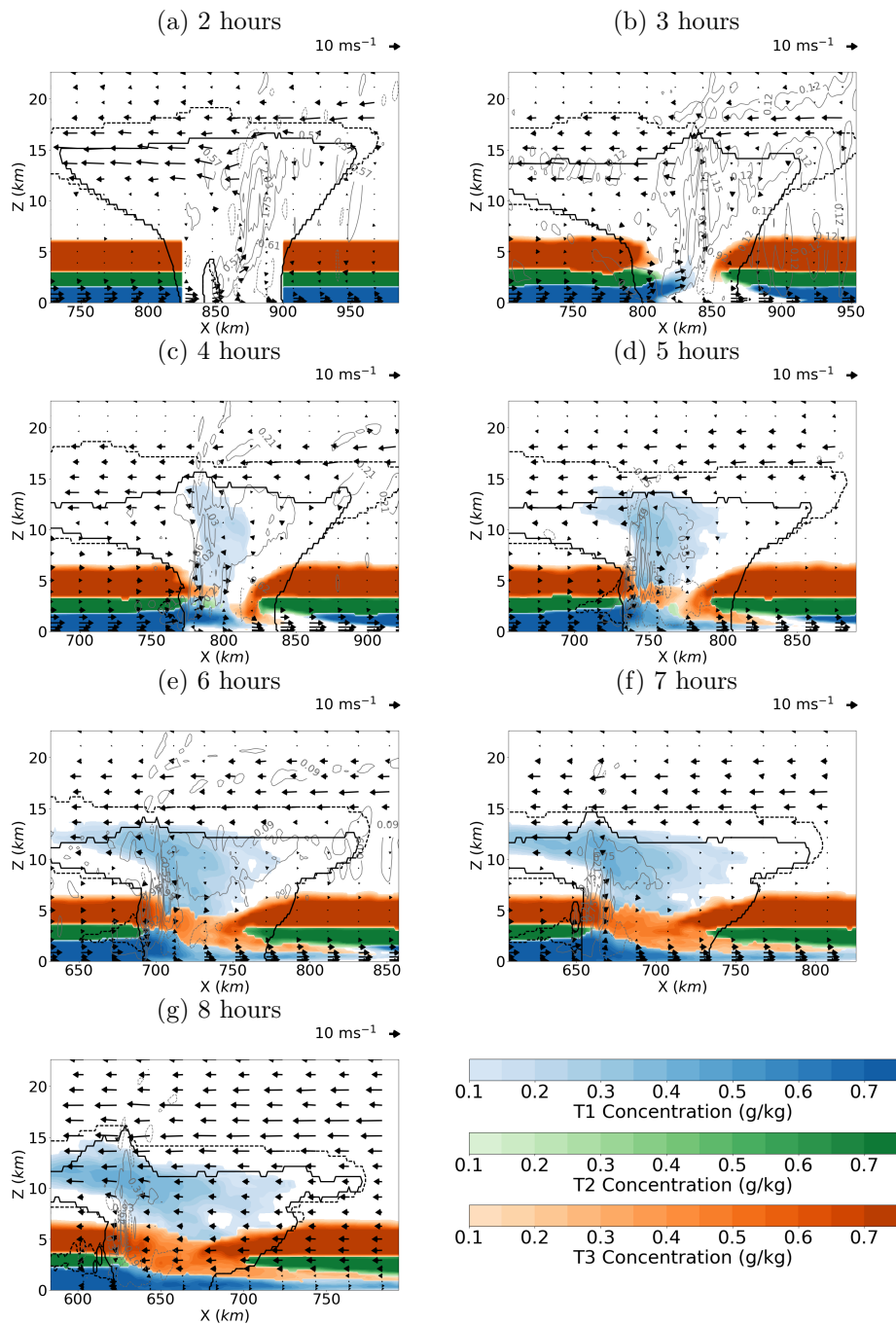
Figure 6.3: Simulation with the control profile from the 2006 African Monsoon Multidisciplinary Analysis (AMMA) campaign with $1\,km$ grid-spacing and averaged over the y-domain. Concentrations of Tracer 1, 2 and 3 shown by blue, green and orange shading respectively. At each point only the tracer with the highest concentration (and above $0.1\,gkg^{-1}$) is shown. Total liquid and solid water content where above $0.01\,gkg^{-1}$ (dashed contours) and precipitable content where above $0.01\,gkg^{-1}$ (solid contours). Vertical velocity is shown by grey contours ($m\,s^{-1}$). The arrows represent $(\bar{u}_r,\ \bar{w})$ where $\bar{u}_r$ are the system relative wind speeds.
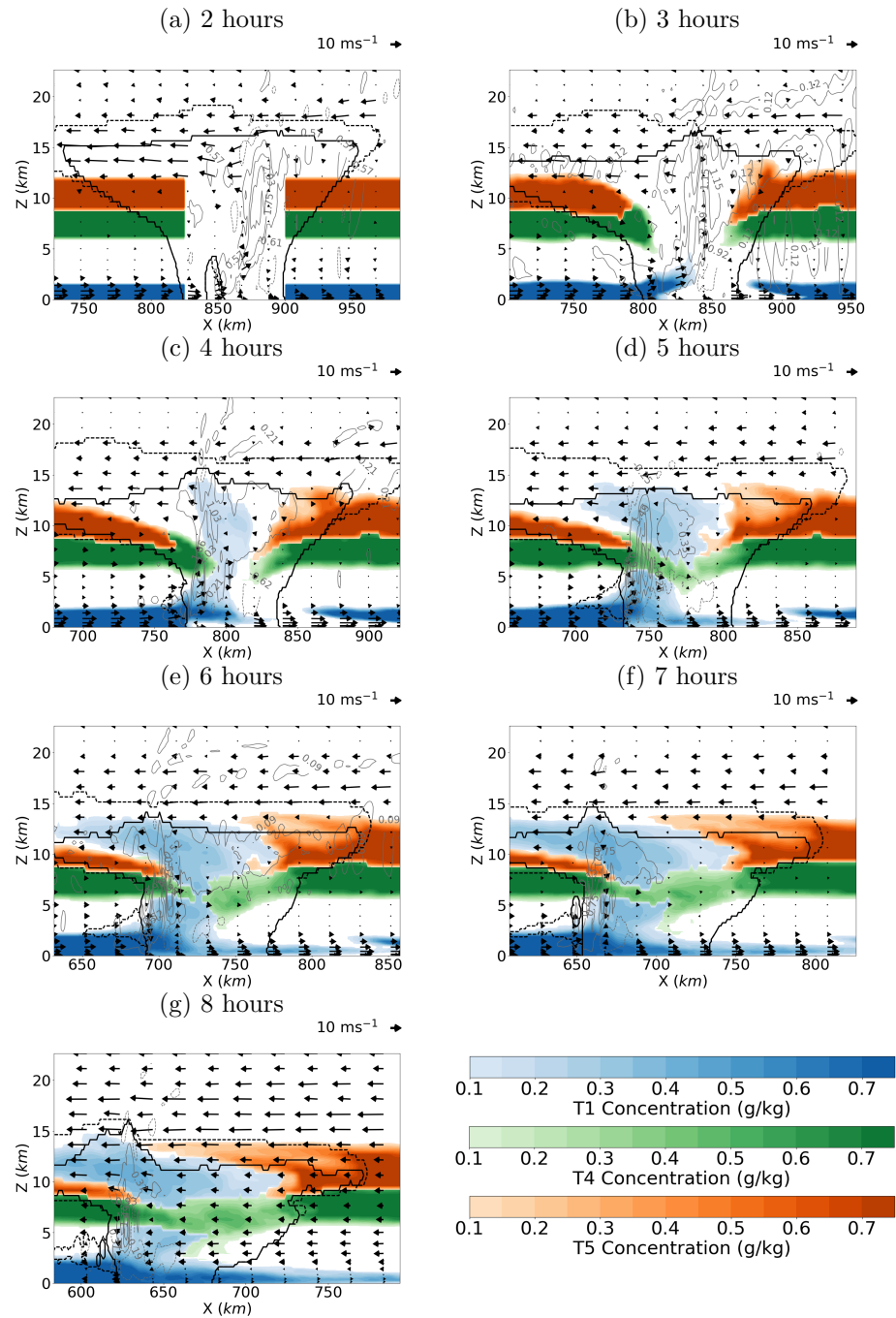
Figure 6.4: Simulation with the control profile from the 2006 AMMA campaign with 1 km grid-spacing and averaged over the y-domain. Concentrations of Tracer 1, 4 and 5 shown by blue, green and orange shading respectively. At each point only the tracer with the highest concentration (and above $0.1\,\mathrm{gkg}^{-1}$) is shown. Total liquid and solid water content where above $0.01\,\mathrm{gkg}^{-1}$ (dashed contours) and precipitable content where above $0.01\,\mathrm{gkg}^{-1}$ (solid contours) are shown. Vertical velocity is shown by grey contours $(\mathrm{m\,s}^{-1})$. The arrows represent $(\bar{u}_r, \bar{w})$ where $\bar{u}_r$ are the system relative wind speeds.
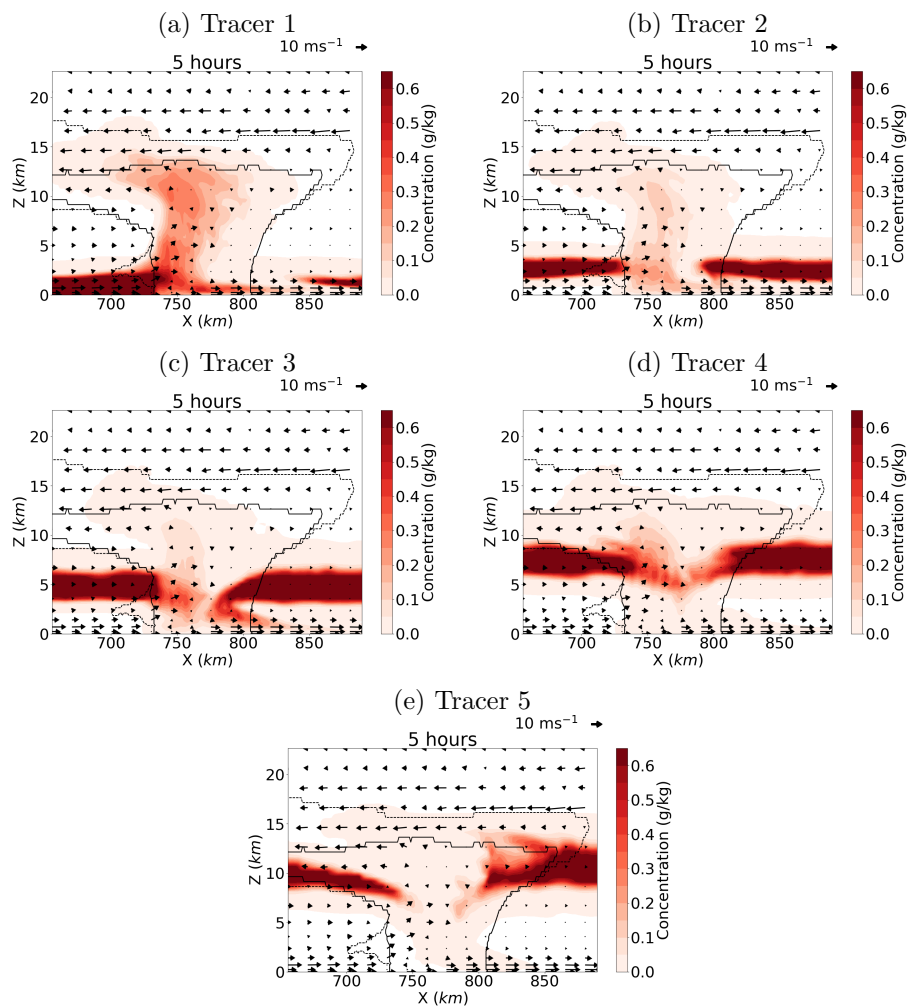
Figure 6.5: Simulation with the control profile from the 2006 AMMA campaign with 1 km grid-spacing at five hours. Concentrations of each tracer are shown by red shading. Total liquid and solid water content where above $0.01\,\mathrm{gkg}^{-1}$ (dashed contours) and precipitable content where above $0.01\,\mathrm{gkg}^{-1}$ (solid contours) are shown. The arrows represent $(\bar{u}_r, \bar{w})$ where $\bar{u}_r$ are the system relative wind speeds.

convective cores as well as sections with little upward motion. Figure 6.7 indicates
that rainfall occurs within, or close to, regions with strong convective cores and is not
continuous across the whole length of the storm. To better understand the differences
at different points along the line of convection, vertical cross-sections have been plotted
at two specific y points, one of which cut through a convective core and one that cuts
through a part of the squall line without a core (Figure 6.8). The characteristics of the
convective core at $y =58$ km in Figure 6.8a) include a deep convective updraft of T1
very near the front of the storm which reaches up to 13 km, has a maximum vertical
velocity of $20.4\,\mathrm{ms}^{-1}$ and which has entrained very little T2 or T3 air. T1 dominates
both T2 and T3 air in the mid-level region although some has ascended upward behind
the strongest convective core. In contrast, at $y =45$ km (Figure 6.8b), convective cores
are shallower (only reaching 7 km), and are dominated by an inflow of T2 and T3
air. There is also a region of stable T3 air near the surface at 750 km in Figure 6.8a
indicating a strong downdraft and likely supporting the convective core. Indeed, if
Figures 6.6b and 6.6c are compared then locations where T3 is present in the middle
of the convective region at 3 km produce less intense convection and include less T3 at
1 km.

From Figure 6.5 where the concentration of each tracer is shown individually at five
hours, it is clear that T1 moves both up and down when entering the storm and while
this is also the case for T2, more appears to descend. The majority of T3A descends
when entering the front of the storm while T3B can be seen to almost completely
descend. Figure 6.6 suggests the cold pool is predominantly made up of T1. However,
there appears to be a consistent downward flow of T3 at 3 km at five hours (Figures 6.5
and 6.6b) which has reached 1 km at some points along the line with some green T2
mixed in (Figure 6.6c). From Figure 6.8 there are clear downward flows of the pink T3
from the rear of the storm at points along the storm with both strong convective cores
and without (Figure 6.8a and 6.8b). However, there is a greater presence of the yellow
T2A in the convective region where there is no strong convective core (Figure 6.8b) and
this appears to determine the top of the cold pool. There are scattered centres of T1
representing convective cores along the front of the line of convection at 3 km (Figure
6.6b) interspaced with regions of T3. Behind the front of the storm is a wide region of
descent of predominantly T3 air. At 1 km in Figure 6.6c, the majority of T3 is behind
the storm with some present within the convective region.

Figure 6.9 contains tephigrams and vertical wind profiles of the 1 km control squall
line at different x points cutting through the line of the storm at five hours. In front
of the cold pool at 720 km shallow updrafts are triggered consistently along the line
of the storm such that there is a layer of ascent which has moistened the region of

(a) 7 km

(b) 3 km

(c) 1 km
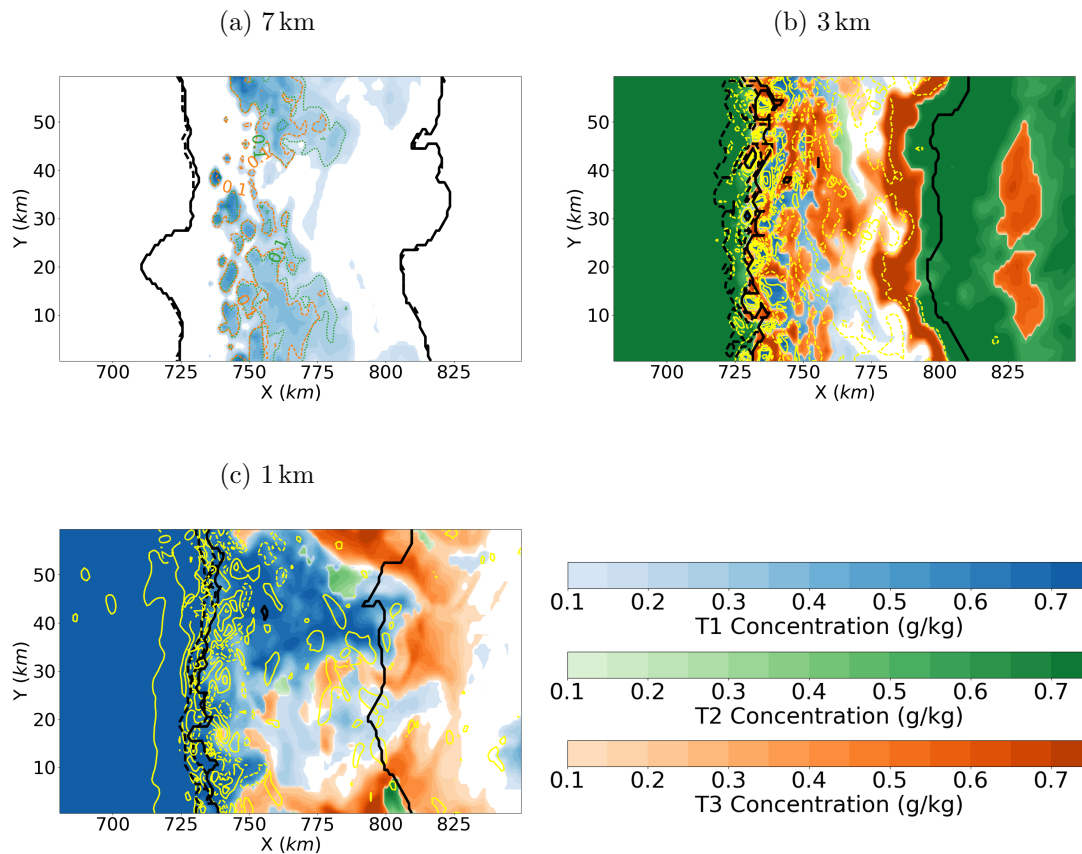
Figure 6.6: Horizontal cross-sections at 1, 3 and 7 km from the control simulation at 5 hours with 1 km grid-spacing from the 2006 AMMA campaign. Concentrations of Tracer 1, 2 and 3 shown by blue, green and orange shading respectively. At each point only the tracer with the highest concentration (and above $0.1\,\mathrm{gkg}^{-1}$) is shown. Total liquid and solid water content is shown where above $0.01\,\mathrm{gkg}^{-1}$ (dashed contours) and precipitable content is shown where above $0.01\,\mathrm{gkg}^{-1}$ (solid contours). In panel (a) as T1 dominates, contour lines of T2 (green dotted) and T3 (orange dashed) have been plotted to show the mixing which occurs. In figures (b) and (c) vertical velocity is shown by yellow contours $(\mathrm{m\,s}^{-1})$.
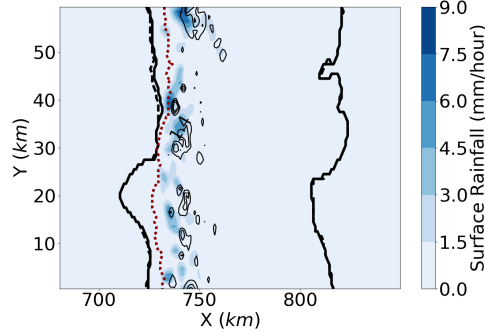
Figure 6.7: Surface rainfall rate at 5 hours (averaged over the next fifteen minutes) in
the control simulation with $1\,\mathrm{km}$ grid-spacing from the 2006 AMMA campaign. The
thin black contours show vertical velocity at $7\,\mathrm{km}$ with contours from -4.5 to $19.3\,\mathrm{ms}^{-1}$.
The total liquid and solid water content where above $0.01\,\mathrm{gkg}^{-1}$ (heavy dashed con-
tours) and precipitable content where above $0.01\,\mathrm{gkg}^{-1}$ (heavy solid contours) are shown
at $7\,\mathrm{km}$. The front of the theoretical cold pool, as defined by Equation 2.10, is shown
by a heavy red dotted line.

(a) $y = 58\,\mathrm{km}$ (b) $y = 45\,\mathrm{km}$
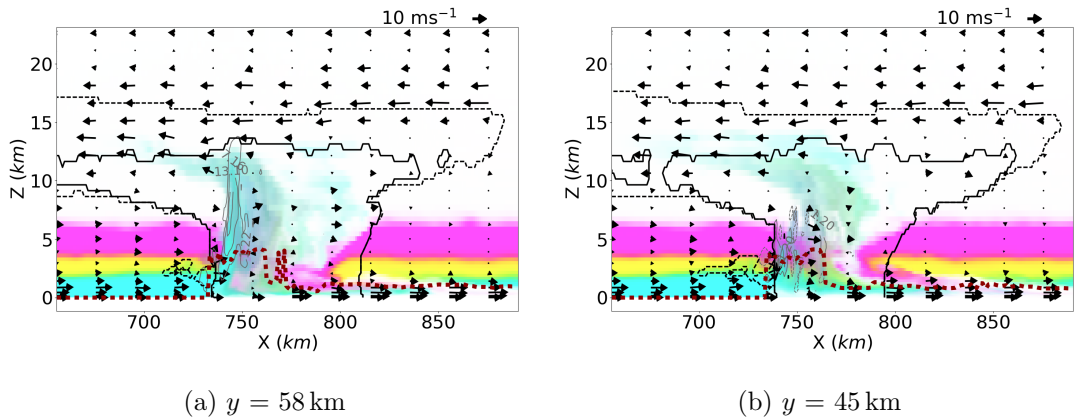
Figure 6.8: $1\,\mathrm{km}$ Control Simulation. Vertical cross-sections at key points on the y-
axis of (a) through a convective core and (b) a region with no convective core, with
coloured contours of Tracer 1, 2 and 3 indicated by cyan, yellow and pink respectively.
All colours are plotted here rather than only that with the highest concentration so
that 'mixing' can be seen. Vertical velocity is shown by grey contours $(\mathrm{m\,s}^{-1})$. The
arrows represent $(\bar{u}_r, \bar{w})$ where $\bar{u}_r$ are the system relative wind speeds. The front of
the theoretical cold pool, as defined by Equation 2.10, is shown by a heavy red dotted
line.

825-700 hPa. Above this there is little change to the initial profile (Figure 3.3) until 325 hPa where the moist anvil can be seen to be reducing the CAPE. At 740 km the lower near-surface temperatures indicate the cold pool which is strongest at $y=58$ km. This region appears to be highly turbulent with no consistent vertical motion indicating that only a few of the shallow updrafts have developed into deep convection. If consecutive vertical velocity profiles along the x-domain are considered (not shown) it becomes clear that the updrafts are slantwise and so do not show well in these plots. Notably, the y-averaged vertical motion is very close to zero which could be a product of gravity waves not penetrating out of the domain due to its periodic nature. Finally, at 760 km the tephigram shows an 'onion profile' with a thin cold wet layer near the surface, made up of T1 and some T2, which has not moved significantly but has been cooled and moistened by evaporation. The layer above is close to dry adiabatic and is predominantly formed of T3 air which has been warmed as it is forced into adiabatic descent by the convective activity. The mid-troposphere is where the maximum descent occurs and the maximum warming occurs around 900 hPa. Above this layer of warmer and direr air is the moist adiabatic anvil.
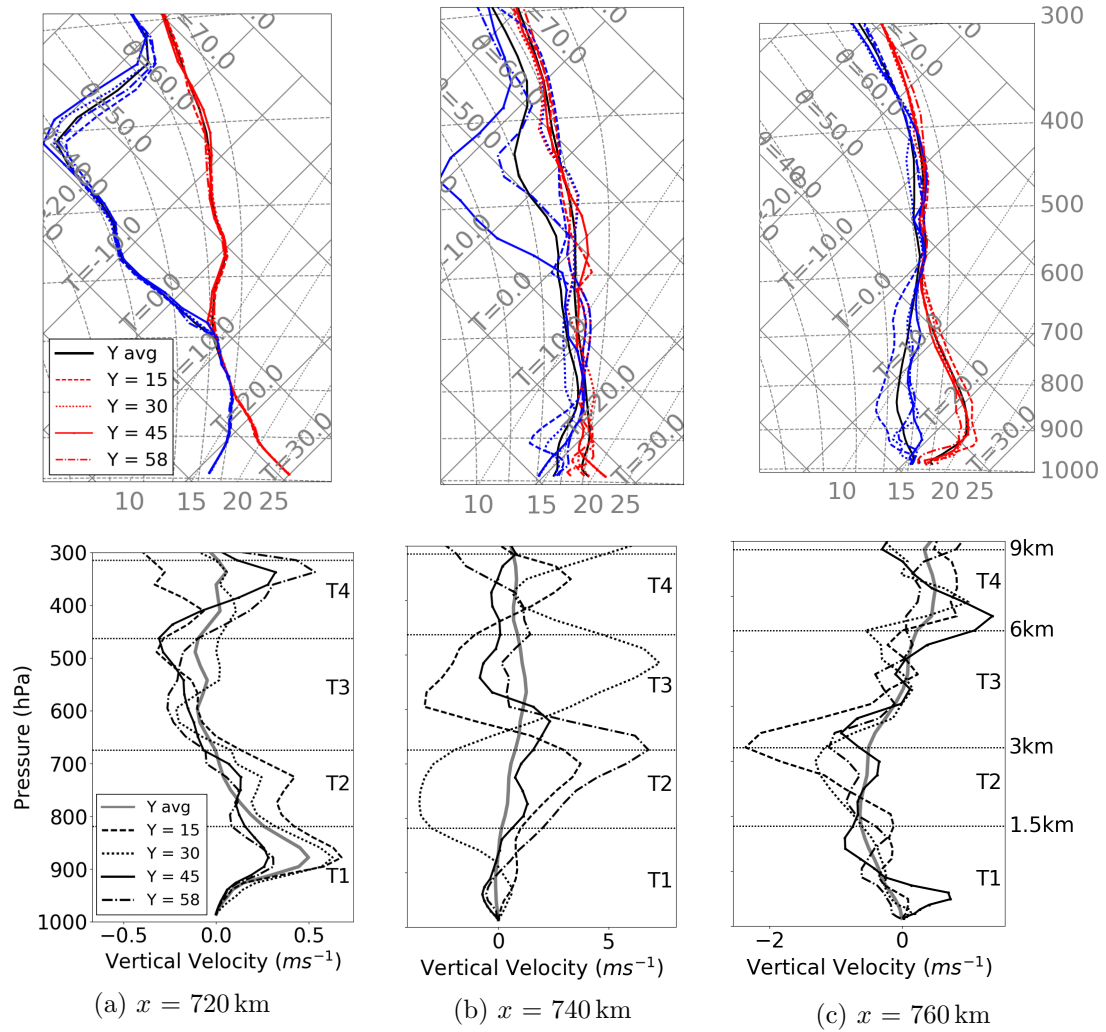
Figure 6.9: Tephigram and vertical wind profile for the 1 km control simulation at 5 hours for different y points along the line of the storm as well as the y average. The profiles are shown at x points of a) 720 km which is below the anvil but ahead of the cold pool and mid-troposphere cloud front, b) 740 km toward the front of the cold front and the region of deepest convection and at c) 760 km in a stratiform region of mesoscale descent. The heights of the original layers of the tracers are indicated by dotted lines in the vertical velocity profiles.

6.2.2 Changes to Model Transport with Horizontal Grid-Spacing

The control (1 km) profile simulation was repeated with 4 km and 100 m horizontal grid-spacing. The maximum vertical velocities across the y-averaged domain, $\bar{w}_{max}$, and mean rain rates (where raining see Table 3.1), $\bar{R}$, are plotted in Figure 6.10. All storms can be considered long-lived but the 4 km resolution case begins to die after six hours. For all cases the simulated storms can be categorised as being in a steady-state at five hours and therefore the different cases will be compared at this time throughout this section. The bulk properties $\bar{w}_{max}$ and $\bar{R}$ are consistent after spin-up across horizontal resolutions for the control profile.

Horizontal and vertical cross-sections with the 4 km and 100 m horizontal grid-spacing simulations at five hours after initiation are shown in Figure 6.11. Only the tracer which is at highest concentration is plotted. The width of the updraft as well as the precipitating region is smaller in the 4 km (Figure 6.11a) simulations where T1 covers a horizontal distance of approximately 25 km, and the precipitating region is approximately 60 km at 7 km height compared with 40 km and 85 km respectively at 1 km and 100 m horizontal grid-spacing cases (Figures 6.3 and 6.11c). The 100 m horizontal grid-spacing updraft appears to tilt further backward in the mid troposphere than the control (1 km) and 4 km case with the convective core further from the front of the storm (Figure 6.3 and 6.11). There is less T5B present at 100 m resolution at five hours (Figure 6.12b) due to a higher system-relative flow at that level and resulting in T5B being forced both above and below the expanding anvil. This occurs at a later time at 1 km grid-spacing (Figure 6.4).

The horizontal cross-sections at 4 km grid-spacing contain large 'blobs' of convection, T1 and rainfall in contrast to the 100 m case (Figures 6.11 and 6.13) where there are distinct convective cores and the rainfall is more consistent across the line of the storm. On comparing the 100 m simulation to the 1 km case (Figures 6.6 and 6.7) the line of convection is narrower and also more consistent along the line of the storm. The amount of T2 and T3 that reach 7 km increases as the grid-spacing becomes finer (Figures 6.11b, 6.11d and 6.6a): with a concentration exceeding $0.2\,\mathrm{gkg}^{-1}$ at 100 m, $0.1\,\mathrm{gkg}^{-1}$ at 1 km and above $0.08\,\mathrm{gkg}^{-1}$ at 4 km. In fact, at 4 km, only T2 appears above $0.02\,\mathrm{gkg}^{-1}$ and only co-located with the strongest convective core. In the 100 m case, an overall larger proportion of T1 also moves upwards, with less of T1 forming the rear of the cold pool, as can be seen in Figure 6.12b. The front of the cold pool is closer to the edge of the precipitable area at 100 m and 1 km grid-spacing (Figures 6.13a and 6.7 respectively) while lagging behind at 4 km (Figure 6.13a).

Next we compare the vertical cross-sections at points with and without convective cores
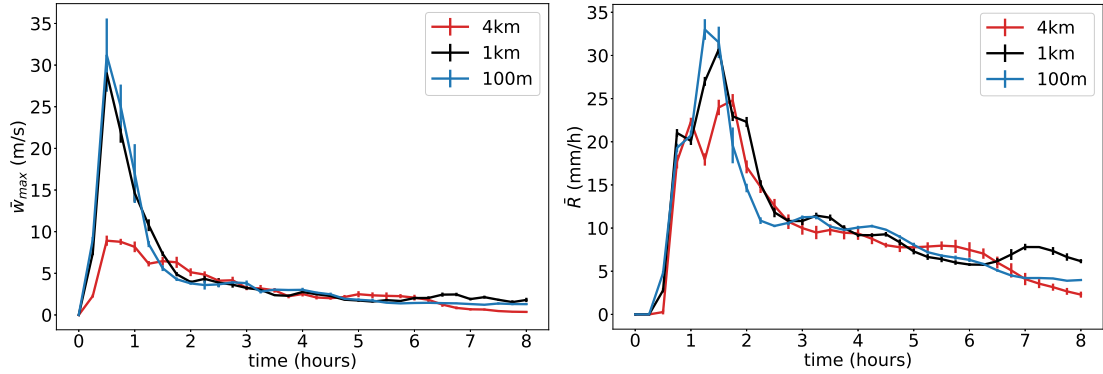
Figure 6.10: Time evolutions of (a) the maximum vertical velocity and (b) the mean
rain rate (where raining) in the y-averaged profile with the control profile from the 2006
AMMA with 4 km, 1 km and 100 m grid-spacing. See Table 3.1 for further descriptions
of variables. The mean of the repeated experiments for each environmental profile is
marked with the standard error of the mean shown by a vertical bar.

for the 4 km horizontal grid-spacing experiments. Less tracer from the lower tropo-
sphere has been transported upwards at all heights in the 4 km horizontal grid-spacing
simulations (Figures 6.14a and 6.14b) in comparison to the 1 km simulations (Figures
6.8a and 6.8b). Additionally, there is no evidence of deep or shallow convection at $y =$
45 km in Figure 6.14b, which confirms the lack of consistent convection along the line
of the squall line seen in the horizontal cross-sections for the 4 km grid-spacing (Figure
6.13a. Equivalent cross-sections have also been plotted for the 100 m grid-spacing sim-
ulations in Figure 6.15. The strongest updrafts at both $y = 22$ and 48 km are located
approximately 50 km behind the front of the storm. However, the updraft in Figure
6.15a is less titled, wider and with higher vertical velocities. In Figure 6.15b there is
less of T1 near the surface below the updrafts but there appear to be shallower updrafts
near the front of the cold pool, which may indicate new convective cores beginning to
take form. This shallow convection does not reach the 7 km height displayed in Figures
6.11d and 6.13b, which is why the majority of T1, T2 and T3 shown as well as the
convective cores lag behind the front of both the cold pool and precipitating cloud.

To gain a better understanding of how changes in horizontal grid-spacing impact the
flow of air from different heights through a squall line, the mean values of the tracers
at five hours at each vertical level for the control profile simulations are compared in
Figure 6.16. Increased resolution results in higher quantities of T1 at all levels from
2.5-13 km, particularly at mid-levels. While the 100 m horizontal grid-spacing results
in a greater quantity of T2, T3 and T4 in the anvil compared to the cases with coarser
grid-spacing, a greater quantity of these tracers also descends at 100 m grid-spacing so
there is generally more vertical mixing. Due to the higher system-relative flow at 12 km,

(a) 4 km grid-spacing

(b) 4 km grid-spacing at 7 km altitude

(c) 100 m grid-spacing

(d) 100 m grid-spacing at 7 km altitude
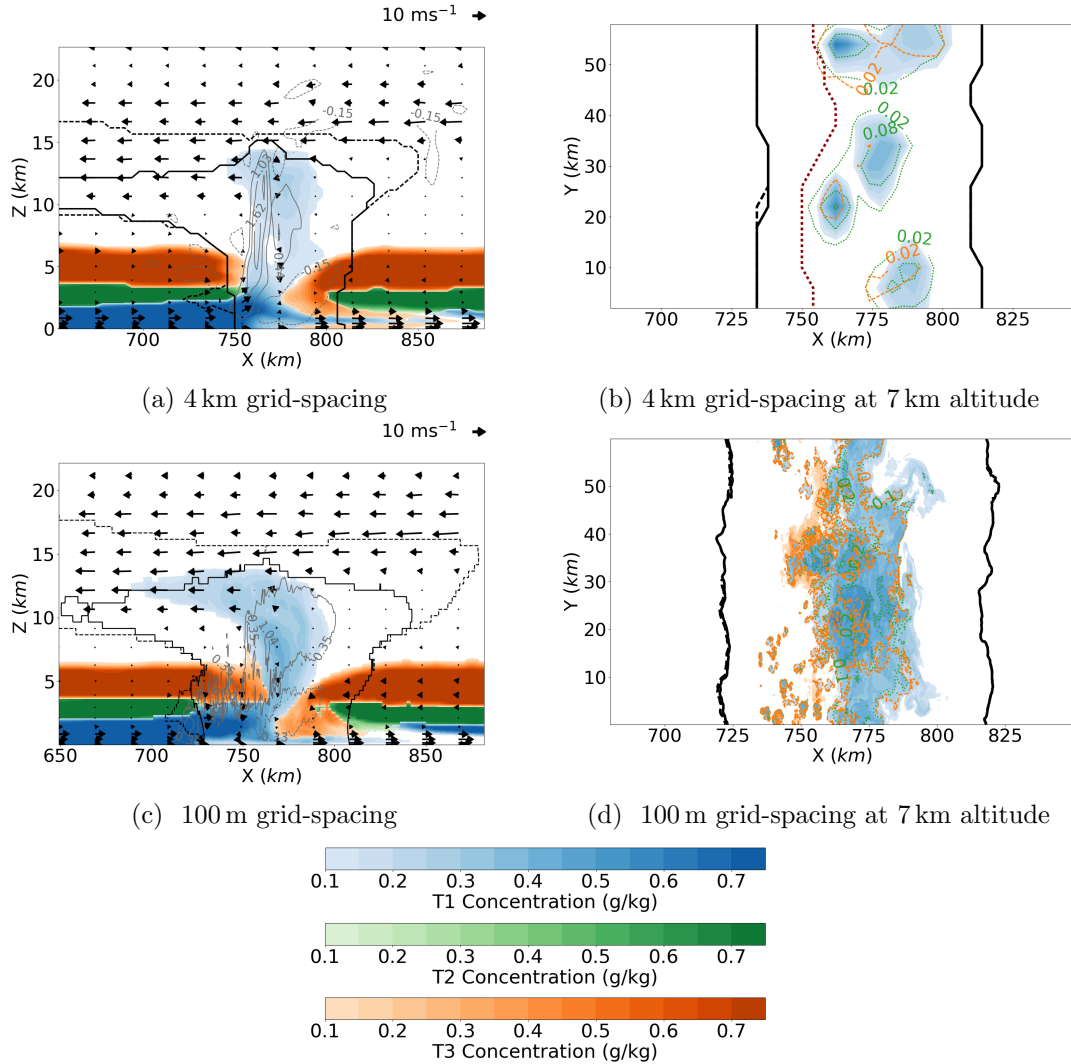
Figure 6.11: As in figures 6.3 and 6.6a for simulations with the control profile from the 2006 AMMA but with 4 km and 100 m grid-spacing at 5 hours after initiation. Concentrations of Tracer 1, 2 and 3 shown by blue, green and orange shading respectively. At each point only the tracer with the highest concentration (and above $0.1\,\mathrm{gkg}^{-1}$) is shown. Total liquid and solid water content where above $0.01\,\mathrm{gkg}^{-1}$ (dashed contours) and precipitable content where above $0.01\,\mathrm{gkg}^{-1}$ (solid contours). In (a) and (c) vertical velocity is shown by grey contours ($\mathrm{m\,s}^{-1}$). The arrows represent ($\bar{u}_r$, $\bar{w}$) where $\bar{u}_r$ are the system relative wind speeds. In (b) and (d) contour lines of green (dotted) and orange (dashed) represent concentrations of T2 and T3 (where above $0.1\,\mathrm{gkg}^{-1}$) respectively where T1 is shown by shaded contours.

(a) 4 km grid-spacing
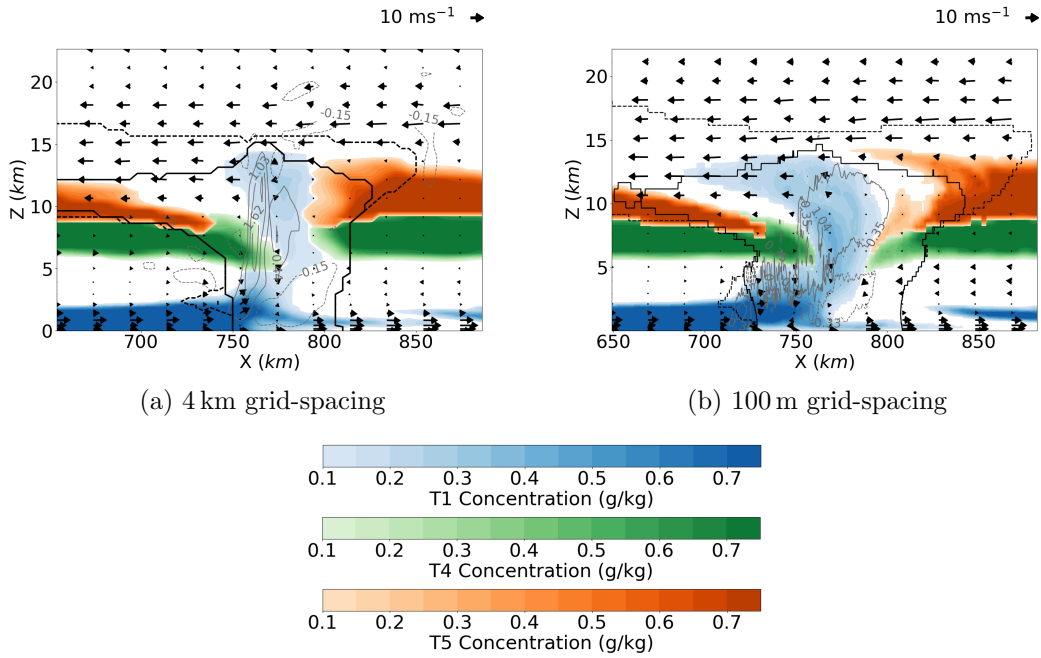
(b) 100 m grid-spacing

Figure 6.12: As in Figure 6.4, vertical cross-sections of Tracer 1, 4 and 5 from simulations with the control profile from the 2006 AMMA campaign but with 4 km and 100 m horizontal grid-spacing. The total liquid and solid water content is shown where above $0.01 \, \mathrm{gkg^{-1}}$ (dashed contours) and the precipitable content is shown where above $0.01 \, \mathrm{gkg^{-1}}$ (solid contours). The arrows represent $(\bar{u}_r, \bar{w})$ where $\bar{u}_r$ are the system relative wind speeds.

(a) 4 km grid-spacing
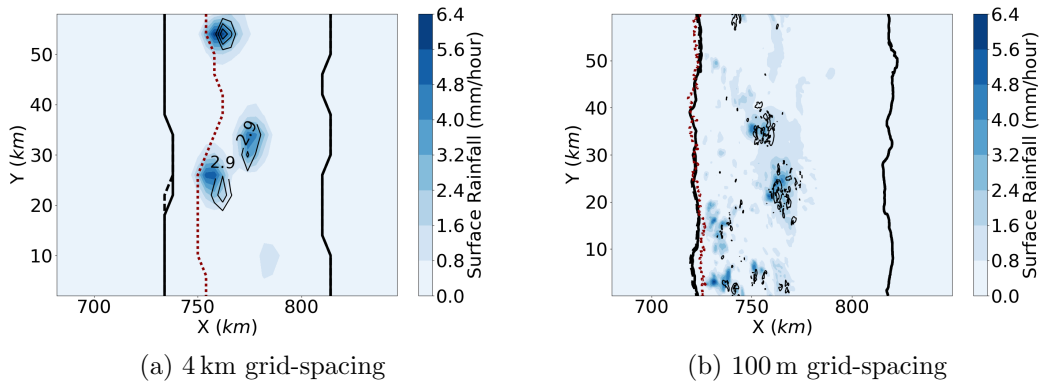
(b) 100 m grid-spacing

Figure 6.13: Similar to Figure 6.6a, surface rainfall rate at 5 hours (averaged over the next fifteen minutes) in the control simulation but with 4 km and 100 m horizontal grid-spacing. The thin black contours show vertical velocity at 7 km with minimum and maximum values of (a) -1.2 and $15.0 \, \mathrm{ms^{-1}}$ and (b) -5.7 to $19.0 \, \mathrm{ms^{-1}}$. The total liquid and solid water content where above $0.01 \, \mathrm{gkg^{-1}}$ (heavy dashed contours) and precipitable content where above $0.01 \, \mathrm{gkg^{-1}}$ (heavy solid contours) are plotted at 7 km. The front of the theoretical cold pool, as defined by Equation 2.10, is shown by a heavy red dotted line.

(a) $y = 32\,\text{km}$ (b) $y = 45\,\text{km}$
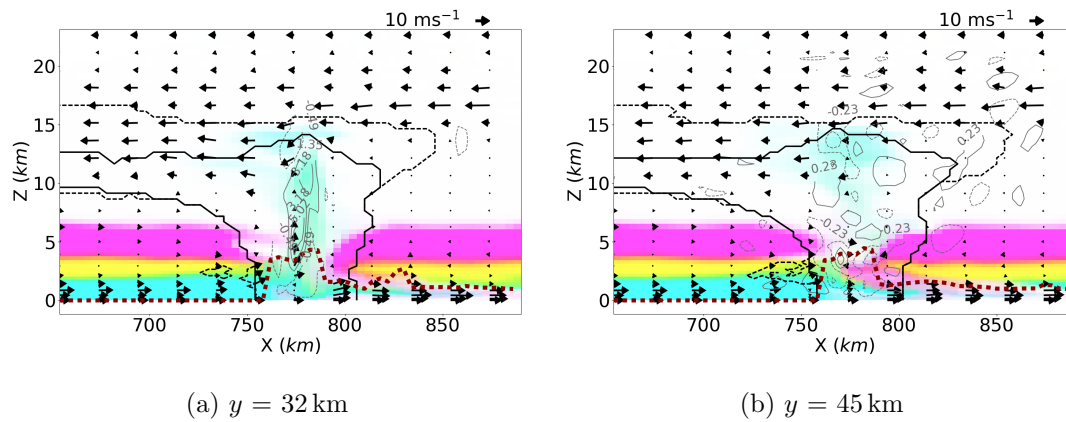
Figure 6.14: Similar to Figure 6.8, simulation with the control profile from the 2006 AMMA with 4 km horizontal grid-spacing. Vertical cross-sections at key points on the y-axis of (a) through a convective core and (b) a region with no convective core with coloured contours of tracer 1, 2 and 3 indicated by cyan, yellow and pink respectively. Vertical velocity is shown by grey contours (m s^{-1}). The arrows represent $(\bar{u}_r, \bar{w})$ where $\bar{u}_r$ are the system relative wind speeds. The cold pool height is shown by a red dotted line.

(a) $y = 22\,\text{km}$ (b) $y = 48\,\text{km}$
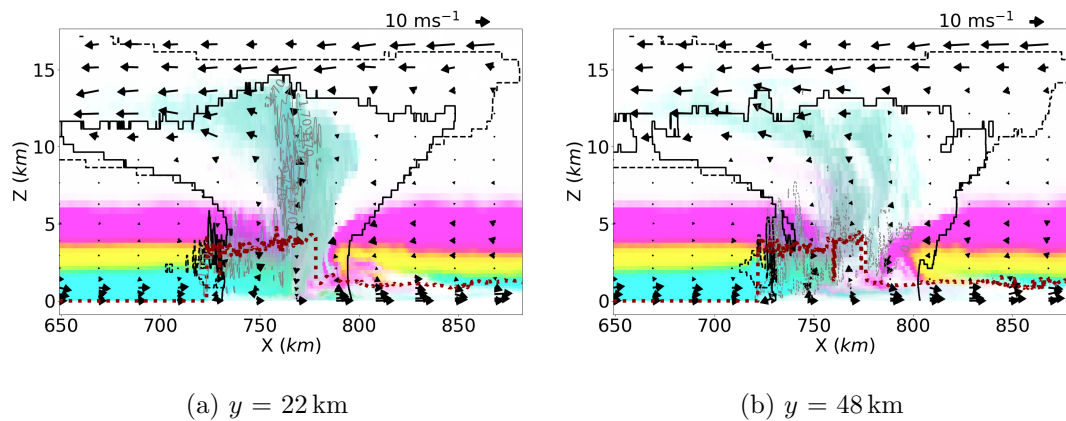
Figure 6.15: Similar to Figure 6.8, simulation with the control profile from the 2006 AMMA with 100 m horizontal grid-spacing. Vertical cross-sections at key points on the y-axis of (a) through a convective core and (b) a region with no convective core with coloured contours of tracer 1, 2 and 3 indicated by cyan, yellow and pink respectively. Vertical velocity is shown by grey contours (m s^{-1}). The arrows represent $(\bar{u}_r, \bar{w})$ where $\bar{u}_r$ are the system relative wind speeds. The cold pool height is shown by a red dotted line.

there is a deficit of T5 at that height with the 100 m grid-spacing when compared to the other cases, a result of the tracer having passed out of the region considered (from 750 to 850 km) but also due to being pushed up and over the anvil.

As the quantity of T1, T2 and T3 which moves upward increases with resolution, the ratio of T1 to both T2 and T3 were plotted in Figure 6.17 to understand whether the entrainment across grid-spacings is consistent. The updraft will mainly consist of convectively unstable T1 air so more entrainment occurs when there is more of T2 or T3 relative to T1 or when the ratio of T1/T2 is small. The ratio of the tracers is most similar between 100 m and 1 km simulations only diverging at 12 km where the concentrations of T2 and T3 become low and in the lowest 1 km near the surface. This result suggests that while entrainment is underestimated at 4 km this does not occur at so great an extent at 1 km grid-spacing.
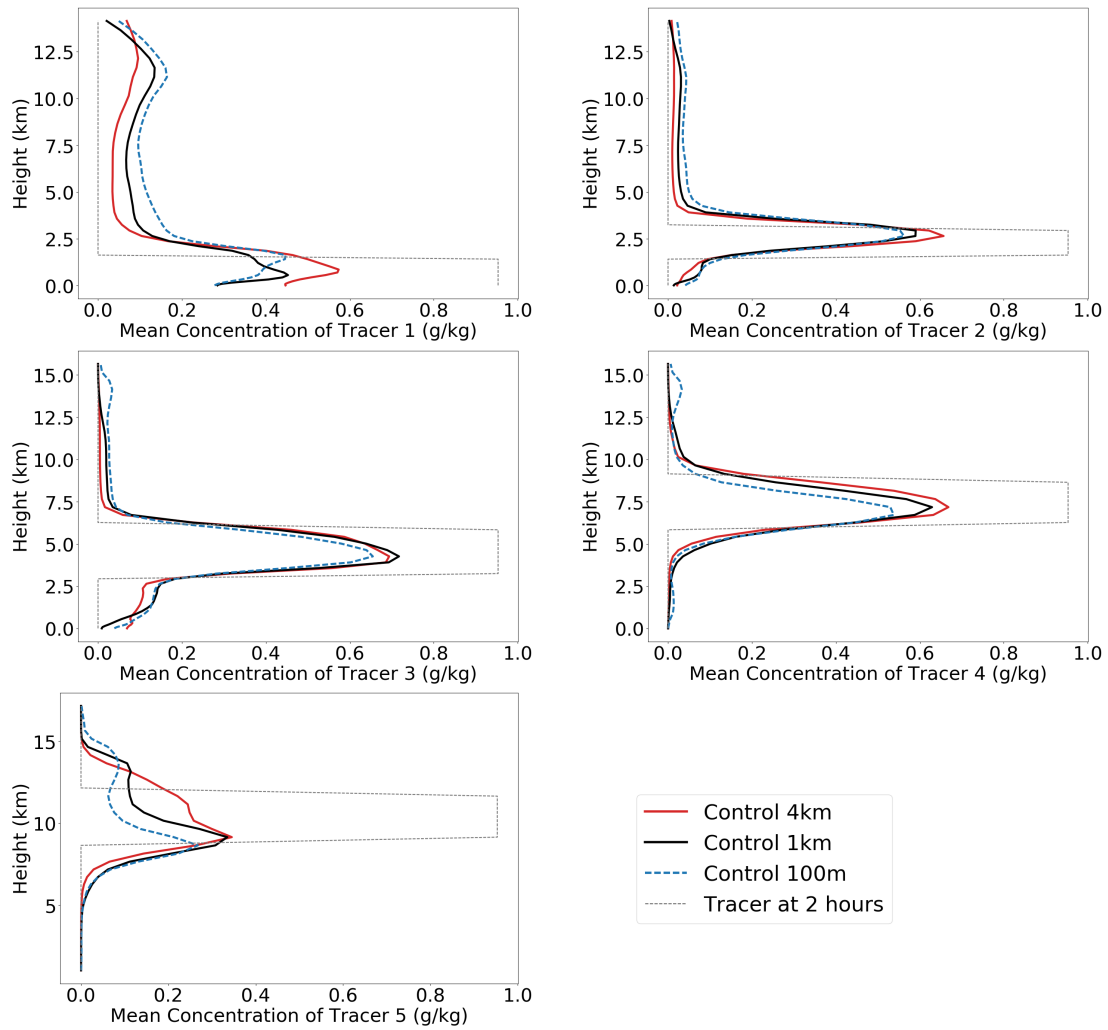
Figure 6.16: Vertical profiles of each of the Tracers at 5 hours. The tracer has been averaged over the horizontal range of 700 to 850 km at each height. The original tracer location is indicated by the dashed line.

Figure 6.17: Ratio of the sum of T1 to a) T2 and b) T3 at five hours. Tracers have been averaged over the horizontal range of 700 to 850 km at each height as in Figure 6.16.

6.2.3 Changes to Model Transport with Shear

Simulations with the 0600 and 1800 UTC wind profiles from Chapter 5 were also repeated with 4 km and 100 m resolution. These two profiles were selected as they offer the largest change in shear across the diurnal cycle. At 0600 UTC both the LLJ and the vertical wind shear between the level of the LLJ and the AEJ (ΔU) are at maximums of 6.7 and 16.5 ms^{-1} respectively across the four profiles. At 1800 UTC both are at their weakest values of 3.3 and 13.4 ms^{-1} respectively (Table 5.1). The time evolution of mean values of maximum vertical velocities, $\bar{w}_{max}$ and $\hat{w}_{max}$, maximum rain-rates $\hat{R}_{max}$ and mean rain-rates (where raining), $\bar{R}$, are plotted in Figure 6.18 (See Table 3.1 for details on variables). Despite there being larger differences between resolutions than between the changing profiles, there is a consistent trend in both vertical velocity and rainfall such that the 0600 UTC profile produces storms with stronger updrafts and higher rainfall across resolutions. Vertical y-averaged cross-sections of each of the 0600 and 1800 UTC simulations at each grid-spacing are shown in Figure 6.19. The 4 km grid-spacing storms appear to be consistently slower than those at finer grid-spacing.

The inclusion of tracers into the simulations provides an opportunity to compare how the transport of the different layers of inflowing air are affected by changes to the environmental wind conditions. As would be expected with a stronger LLJ at 0600 UTC there is a larger mean concentration of T1 above 1.5 km for all resolutions (except at 100 m below 6 km) than at 1800 (Figure 6.20). While a larger amount of T2 has moved above 4 km at 1800 than at 0600 UTC across all resolutions, the difference is at a maximum at 100 m. Due to the small amount of air marked by T2 that contains CAPE (Figure 6.1) it can not be claimed that this is entirely due to entrainment. There are similar quantities of T3 above 7 km at both 0600 and 1800 UTC at 4 km
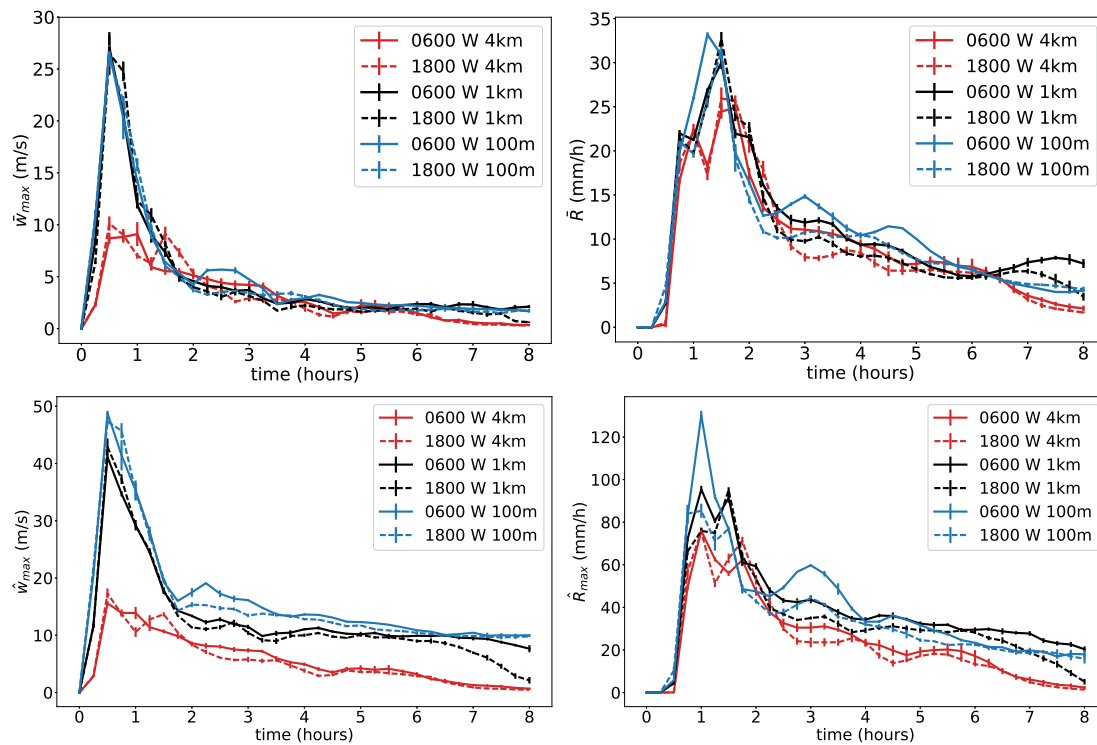
Figure 6.18: Comparing the time evolutions of (a) $\bar{w}_{max}$, (b) the mean rain rate (where raining), (c) $\hat{w}_{max}$ and (d) $\hat{R}_{max}$ with 4 km, 1 km and 100 m horizontal grid-spacing for the 0600 and 1800 UTC wind profiles. See Table 3.1 for further descriptions of variables. The mean of the repeated experiments for each environmental profile is marked with the standard error of the mean shown by a vertical bar.

(a) 0600 UTC at 4 km

(b) 1800 UTC at 4 km

(c) 0600 UTC at 1 km

(d) 1800 UTC at 1 km

(e) 0600 UTC at 100 m
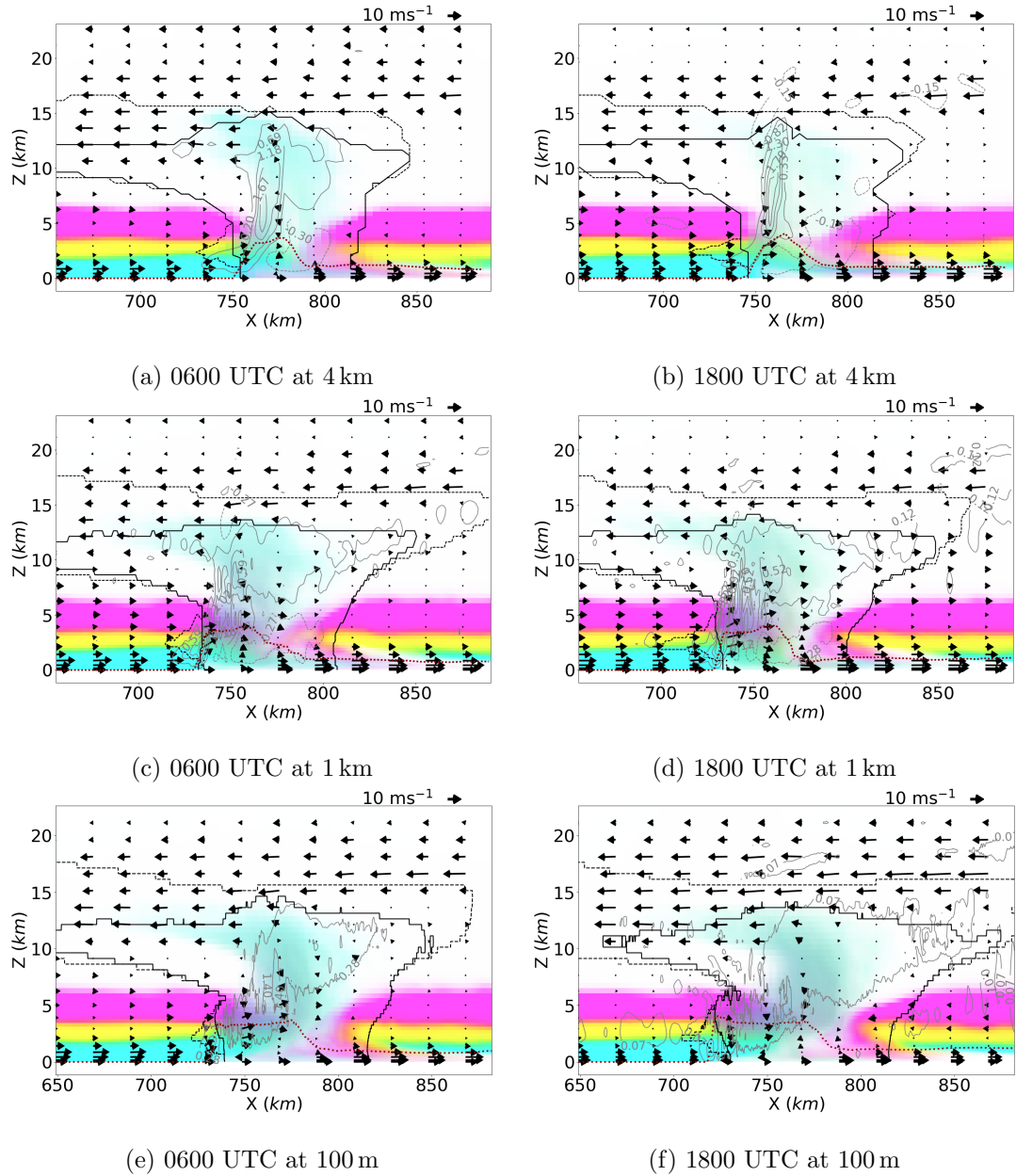
(f) 1800 UTC at 100 m

Figure 6.19: Simulations representative of 0600 and 1800 UTC at 4 km, 1 km and 100 m resolutions with tracers shown. Concentrations of Tracer 1, 2 and 3 shown by cyan, yellow and pink shading respectively. Total liquid and solid water content is shown where above $0.01\,\mathrm{gkg}^{-1}$ (dashed contours) and precipitable content is shown where above $0.01\,\mathrm{gkg}^{-1}$ (solid contours). Vertical velocity is shown by grey contours ($\mathrm{m\,s}^{-1}$). The arrows represent ($\bar{u}_r$, $\bar{w}$) where $\bar{u}_r$ are the system relative wind speeds.

grid-spacing with a small increase at 1800 at 1 km compared to 0600 UTC. However, at 100 m grid-spacing the 1800 UTC profile results in more of T3 being entrained and transported upwards. As was seen when varying the resolution in the control profile in Section 6.2.2, the higher resolutions result in T5b moving up and over the anvil at 1800 UTC, which is not seen at 4 km or in any resolution at 0600 UTC. This is likely due to the easterly winds above 200 hPa being at a maximum at 1800 UTC (Figure 6.1).

As discussed in the introduction, there are systematic errors in recent 4 km resolution CP4A simulations in response to shear (Fitzpatrick et al. 2020; Senior et al. 2021). At 4 km grid-spacing, squall-line dynamics are crudely resolved but mixing is not well represented. We now test whether the lack of mixing at coarser grid-spacing results in the simulated squall lines at these resolutions being less sensitive to shear. Mulholland et al. (2021) show through idealised simulations that stronger low-level shear promotes wider updrafts, less entrainment-driven dilution and larger buoyancy. We theorise that if shear supports undiluted updrafts, this may be masked at 4 km grid-spacing due to a general lack of entrainment and so dilution. It is therefore useful to consider ratios of T1 to T2 and T3 (particularly due to the differing propagation speeds of the storms) as this is an indicator for the dilution of the strongest convective cores (made up of the moist and convectively stable air with T1). Results in Figure 6.21 indicate that ratios are similar at 100 m and 1 km grid-spacing with 0600 UTC (higher shear) resulting in lower amounts of T2/T3 compared to T1 than at 1800 UTC. At 4 km the change in shear has very little impact on the ratio of T1 to T3 air, the latter of which has no CAPE and therefore is purely reliant on being mixed into convective cores. Thus, entrainment does not vary significantly with shear in our 4 km experiments. Although CP4A is run using a different model this result provides insight into one reason why those simulations produce higher cloud-top temperatures but no increases in rainfall with higher shear.

We now consider the least diluted convective cores using the 98th percentile (P98) of the equivalent potential temperature perturbation ($\Delta\theta_e$) from the base state. When comparing P98 of $\Delta\theta_e$, the finer the resolution the greater the change in θ_e at mid-levels (Figure 6.22). This is consistent both with the greater amounts of T1 and T2 which are present at mid-levels in the 100 m simulations and with Bryan and Morrison (2012), who found that smaller grid-spacing produced an increase of boundary layer air throughout the troposphere. The largest changes in $\Delta\theta_e$ occur in the 1800 UTC 4 km and 1 km experiments but this is above 16 km and so the height of the overshoot.

Vertical profiles of the 98th percentile of both T1 and T2 for each of the different resolutions were plotted in Figure 6.22 to better understand if the effects of the diurnal change in wind, and so wind-shear, on the strongest convective cores are consistently
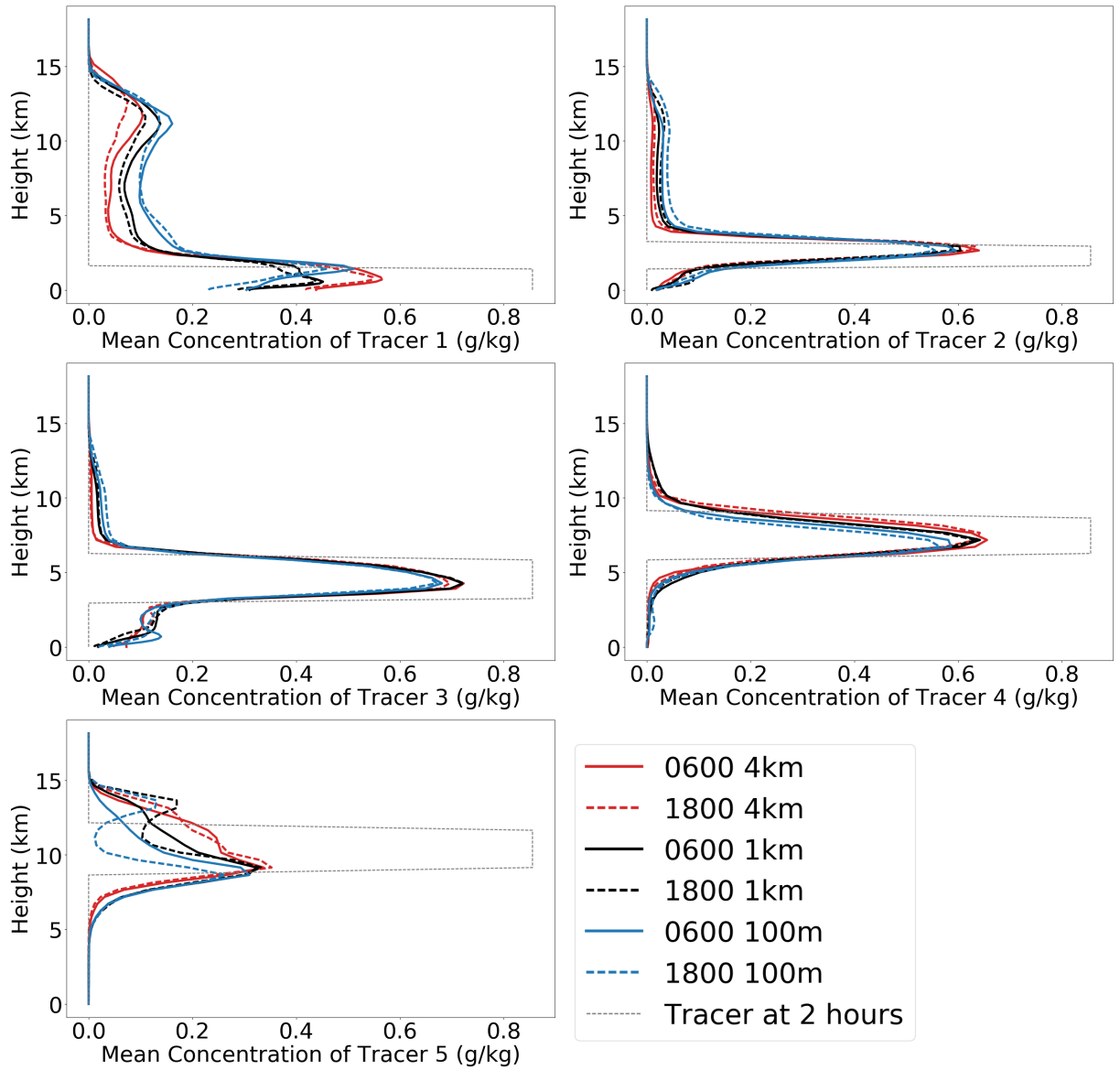
Figure 6.20: Vertical profiles of each of the Tracers at 5 hours with 4 km, 1 km and 100 m horizontal grid-spacing for the 0600 and 1800 UTC wind profiles. The tracers have been averaged over the horizontal range of 700 to 850 km at each height. The original tracer location is indicated by the dashed line.
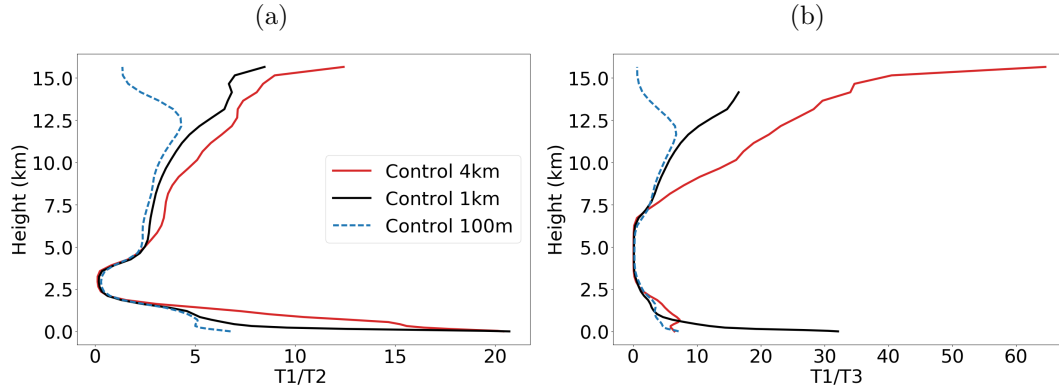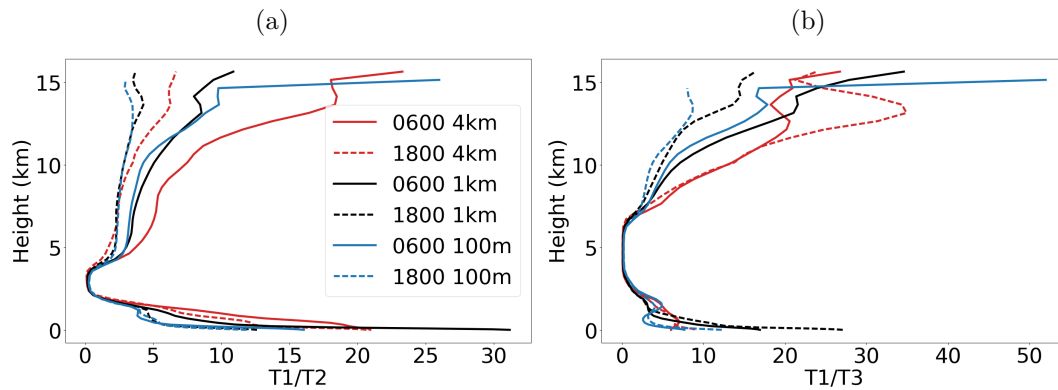
Figure 6.21: Ratio of the mean of T1 to the mean of a) T2 and b) T3 at five hours. Tracers have been averaged over the horizontal range of 700 to 850 km at each height as in Figure 6.16.

captured across resolution. Although at 4 km and 1 km grid-spacing there is an increase of the highest concentration of T1 at all heights in the troposphere, this does not hold at 100 m where the 0600 UTC case has the lowest 98th percentile of T1 at that resolution (Figure 6.22). As the mean concentration of T1 is higher at 0600 UTC but the 98th percentile is not, this suggests that there is a larger quantity of T1 but that it is spread out over a larger area at 0600 UTC in the 100 m simulation. The 0600 UTC profile results in higher values of the 98th percentile of T2 above 7.5 km for all resolutions with the magnitude of the change from 1800 UTC increasing with resolution. This holds for T3 except at 4 km resolution where it appears to decrease.

Figure 6.23 explores the effect of ΔU (where $= \Delta U = u_{AEJ} - u_{llj}$, the difference in wind speed between the AEJ and the LLJ) on the ratio of the 98th percentile of T1 to that of T2 and T3 in the strongest convective cores (those that reach the anvil). As the magnitude of ΔU increases, there is a consistent decrease of T2 compared to T1 across all resolutions and this is strongest at 4 km. For T3 this is also true at 100 m and 1 km grid-spacing while the reverse is found at 4 km. Thus, with greater shear there is lower concentration of air relative to the high-CAPE tracer 1 in the least dilute cores, i.e. higher shear leads to less diluted cores.

6.3   Conclusions

The previous chapters in this thesis have shown how the mean rainfall rates and updraft speeds of mature squall lines are dependent on both the thermodynamic and wind profiles of the environments they exist in. Furthermore, considering the relative inflow of convective instability and moisture into the storm can give an indication, at least

(a)

(b)

(c)

(d)
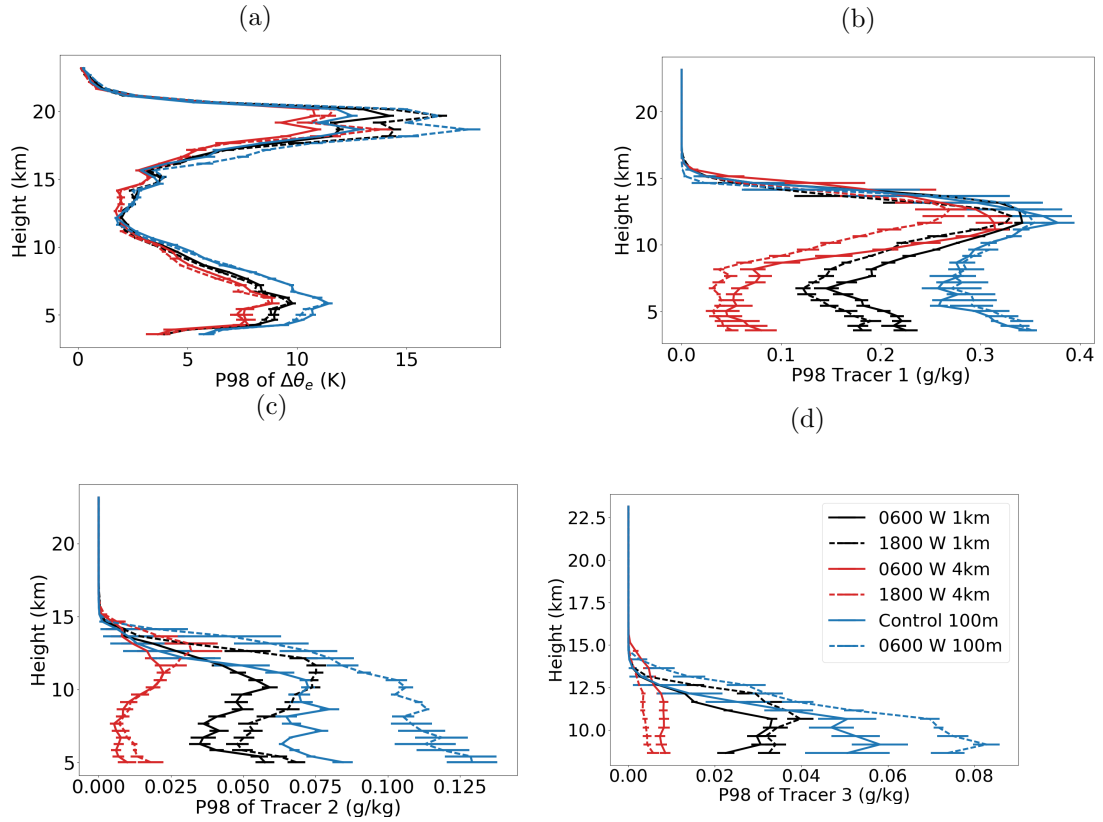
Figure 6.22: Vertical profiles for simulations initiated with the control, 0600 and 1800 UTC profiles at different resolutions at five hours including the 98th percentile (P98) of (a) θ_e perturbation at different heights, (b) Tracer 1, (c) Tracer 2 and (d) Tracer 3. Each of the tracers in panels (b - d) has been plotted from 2 km above the maximum height of their initial placement (see Table 6.1).

(a)

(b)
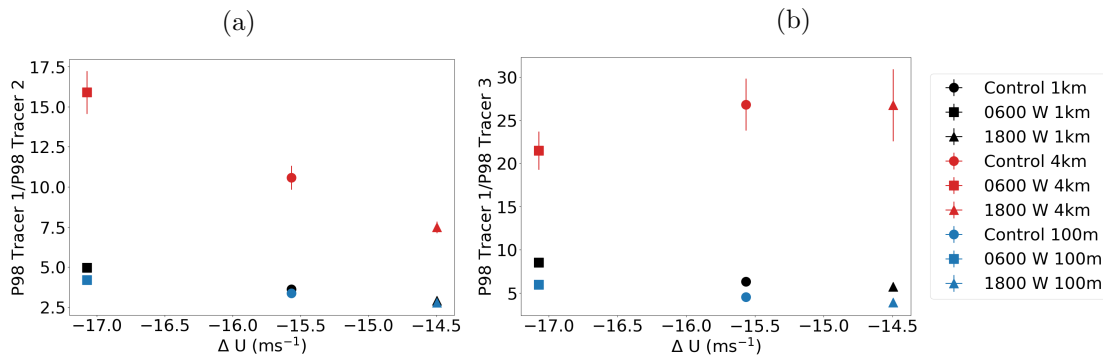
Figure 6.23: Statistics for simulations initiated with the control, 0600 and 1800 UTC profiles at different resolutions at five hours including ΔU vs the ratio of the 98th percentile of T1 and (a) 98th Percentile of T2 and (b) 98th Percentile of T2. All percentiles calculated between 7 and 10.5 km.

in these idealised simulations, of the mean updraft speeds and rainfall respectively. In order to better understand these results passive tracers were initiated in the simulations to gain insight into how air at different levels moves through the storm and whether layers of air are lifted up as is modelled in the layer-lifting model of convection (LLMC).

An additional aim was to diagnose where the air that forms both the cold pool and anvil predominantly comes from. The speed of the system, which is of great importance to the relative inflow of total mass, moisture and convective instability into the storm and therefore system intensity, is difficult to predict but is controlled by cold pool intensity. If the maintenance of the cold pool can be better understood, predicting its strength and therefore system intensity may be possible.

In the 2006 AMMA campaign control simulation with 1 km horizontal grid-spacing, both the cold pool and the updrafts and anvil are dominated by air from the lowest 1.5 km near the surface. While some air from above this and marked by T2 and T3 (from 1.5 km-6 km), is entrained upward, they are each approximately only 5-10% of the concentration of T1 in the anvil. Qualitatively it appears that inflowing air does not pass through the convective region unperturbed but either descends in layers or is transported upwards. As the anvil spreads outward, it forces the inflowing air at that level to ascend over, or descend below, the expanding anvil (T5B). The line of convection includes points of intense deep convection interjected with areas with much weaker ascent. The points with active deep convective cores had little evidence of mixing directly above the cold pool, with the convection being fed directly by the inflowing higher CAPE air and T3 air descending through the storm at other locations. At the rear of the storm, T3B air descends in a rear-inflow jet and then reverses to sit on top of T1 and below the undisturbed T2B at the back of the system. This results in a shallow, moist cold pool capped by dry air.

The 2006 AMMA Control profile was reused to initiate simulations with horizontal grid-spacing of 4 km and 100 m, which allowed a comparison of how convection is modelled at different horizontal resolutions. At 4 km grid-spacing the convective cores are not well resolved but there are 'blobby' regions of upward motion with rainfall produced without a clear line of convection. At 1 km there is a life-cycle of strong convective cores at the front with older dying convection at the rear and rainfall also lagging behind the strongest convection and weakening toward the rear of the storm. The line of convection is more consistent at 100 km and there is less difference between points with weak and strong convection along the line. The deepest convection occurs toward the rear of the system at this grid-spacing with new shallow convective cores appearing toward the front.

When the ratio of high CAPE T1 air is compared to that of T2 and T3 air, which has been transported upwards, they are similar for the 100 m and 1 km cases despite higher quantities of each tracer being transported upwards at 100 m. This does not hold at 4 km, where for T3 air, entrainment does not appear to vary with shear. There is a lack of consistency across resolutions in either the average (or ratio to T1) of T2 and T3 air that descends. This highlights that there are differences between the different resolutions in the make-up of the cold pool.

Through running simulations with varied shear at horizontal resolutions of 4 km, 1 km and 100 m with passive tracers it was possible to gain insight into how resolution captures the effect of shear on squall lines. Finer horizontal grid-spacing resulted in higher mean concentrations of air from the lower troposphere (surface to 6 km) to be convected upwards across all simulations.

Recent work has also shown that the 4 km horizontal grid-spacing in Unified Model simulations does not capture the observed increase of rainfall with shear in West Africa (Fitzpatrick et al. 2020; Senior et al. 2021). We investigated the dilution of updrafts across the three resolutions, to investigate whether the poor representation of mixing at coarse grid-spacing could affect the response to shear. At finer grid-spacing low shear resulted in increased entrainment of mid-level air into the updrafts which may explain the weaker updrafts and lower height of the anvils. At both 1 km and 100 m grid-spacing there was a consistent decrease in the dilution of the convective cores with greater vertical wind shear. This effect appears to be magnified at higher resolutions and may be underestimated at 4 km resolution, particularly for air with no CAPE, suggesting the lack of mixing at 4 km could be minimising the effects of shear on squall line intensity. Thus, despite different sub-grid schemes between the Cloud Model 1 (CM1) model and the Unified Model, the lack of representation of mixing and so entrainment seen in these experiments could be the reason changes in shear are not producing the same effects in 4 km climate simulations over Africa.

Chapter 7

Conclusions and Future Work

7.1 Summary

This thesis has focused on understanding the role of wind shear in organising and supporting deep moist convection in the West African monsoon (WAM), a region which experiences some of the most intense mesoscale convective systems (MCSs) in the world (Zipser et al. 2006). Such events are often poorly predicted due to their poor representation in global numerical weather prediction (NWP) models, the existence of a patchy observational network across much of Africa and an incomplete understanding of the processes involved. These poor predictions limit the usefulness, as well as the use of, modern numerical forecasting in a region which is increasingly vulnerable to extreme weather events due to both population growth and climate change. Weather forecasting in the tropics in general is far behind that of the extra-tropics and in Africa in particular where statistical ensemble post-processing adds almost no skill to forecasting (Vogel et al. 2020).

The poor representation of MCSs in numerical models is often a result of convection parametrisation schemes struggling to capture the genesis and evolution of convective structures over multiple grid-boxes (Fink et al. 2011). There is not a straightforward single explanation for this but rather it is due to a combination of issues including: little to no inclusion of surface conditions, or their effects, which can trigger and support convection (Klein and Taylor 2020); poor representation of entrainment and cold pools; parametrisation schemes (often fine-tuned for mid-latitudes) triggering too easily and so too early in the day and no inclusion of the effects of wind shear which plays a key role in the formation of MCSs. This culminates in rainfall predictions for the Sahel which are too widespread while failing to capture either the diurnal cycle or the most

intense rainfall (Randall et al. 2003; Stephens et al. 2010; Stratton et al. 2018). Finally, the direction and speed of MCSs are regularly incorrect, even in convection permitting models where much of the MCS dynamics is modelled explicitly (Crook et al. 2019).

A large body of literature exists which considers the role of shear in organising and promoting organised deep convection and particularly squall lines (Rotunno et al. 1988; Weisman et al. 1988; Bryan et al. 2006; Alfaro and Khairoutdinov 2015). It is widely accepted that vertical wind shear supports MCSs but the mechanisms behind how shear organises deep convection are still an active and debated area of research. Additionally, the majority of studies on the effects of shear have predominantly featured mid-latitude systems and have rarely focused on tropical Africa. Recent observational studies of the region have suggested that shear has played a key role in recent increases in extreme rainfall (Taylor et al. 2017) but this has not yet been reproduced by studies using numerical modelling where increases in shear have produced only higher anvils without accompanied increases in rainfall (Fitzpatrick et al. 2020; Senior et al. 2021). By focusing on understanding how changes in vertical wind shear impact organised convection in this complex region, this thesis provides important additions to the current gaps in the literature while also shedding light on the contradictions that occur there and in doing so enables a better understanding of the role of vertical wind shear in organised deep convection in general.

The key results from this thesis are presented in Chapters 4-6 and are based largely on idealised large-eddy simulation (LES) using the Cloud Model 1 (CM1). Chapter 3 describes the creation of a control profile obtained from radiosonde data from Niamey, measured during the 2006 African Monsoon Multidisciplinary Analysis (AMMA) campaign, that is representative of a nocturnal, pre-storm monsoon environment. With this environmental profile, convection was initiated with a cold line thermal that produced simulated squall lines which were consistent with observed squall lines in the region (Provod et al. 2016). In Chapter 4, this setup was used to explore the role of shear in recent and future decadal changes in MCSs and so test the findings of Taylor et al. (2017) in a controlled setting as well as consider the implications on Sahelian squall lines from future environmental changes. Recent decadal trends for the Sahel region were obtained from ECMWF Re-Analysis (ERA)-Interim data while future predictions were sourced from data from the Coupled Model Intercomparison Project 5 (CMIP5). In both cases, the most extreme trends available (regionally to match what was discussed in Taylor et al. (2017) for the former and the highest emission scenario for the latter) were applied to the control profile in order to minimise the signal-to-noise ratio. This provided an opportunity to test the relevant importance of recent and future predicted changes and how they impact upon mature squall lines.

The diurnal cycle of MCSs and rainfall in the WAM are pronounced (Parker et al. 2005a; Klein and Taylor 2020). However, although the nocturnal south-westerly low-level jet (LLJ) has been theorised to support organised convective systems, this has not yet been shown conclusively in the literature. In Chapter 5, through applying average diurnal variations from within the AMMA campaign radiosonde data from July-August 2006 to the control profile, it was possible to test the importance of diurnal changes in temperature, humidity and wind speeds to mature squall lines. This set of simulated squall lines produced from environmental profiles representative of different points in the day provided an opportunity to understand the role of shear in the diurnal cycle and in particular how the LLJ supports systems overnight and whether its decay in the morning accelerates the decay of storms which have sustained throughout the night.

The idealised simulations which are run throughout this study, representative of MCSs in the WAM, act as a bridge between past observations of these events and the multiple theories which explain what controls them. By constraining the initial set-up such that the thermodynamic and wind profiles were altered individually and in combination it was possible to analyse and compare the effects of each. This provided a set of simulated squall lines which could be used to isolate key processes and so examine the validity of different theories which attempt to explain the role of wind shear through dynamic organisation (Rotunno et al. 1988) and thermodynamic modulation (Alfaro 2017). The layer-lifting model of convection (LLMC) outlined in Alfaro (2017) quantifies both the inflow of air which is convectively unstable and which holds moisture relative to the total quantity of inflowing air into the storm, producing indices which are predictive of maximum vertical velocities and precipitation rates of the MCS. Although the LLMC has been tested in several studies it has generally been applied in idealised environments and often those representative of the mid-latitudes. This study focuses on applying the model to explain decadal and diurnal changes within the WAM, which is poorly represented by the parametrisation schemes in global numerical weather and climate models to better understand how these changes have occurred. To a lesser extent the theory of Rotunno et al. (1988) was also tested, which poses shear as having a dynamical role which counteracts the effects of the cold pool on convection.

Throughout this study it became apparent that diagnosing the mass transport through a MCS and in particular what layers of air make up the convective cores and the downdrafts and subsequent cold pools is vital to understanding what controls the severity of the systems which are produced. This is especially the case for the cold pool which affects the speed of the system and therefore the relative inflow of convective instability and moisture. In order to gain an understanding of the transport through the system and the relative contributions of air at different levels, passive tracers were added to

the simulations in Chapter 6. From studying the transport of the different tracers, conclusions could be made on how layers of air move through the systems including whether they remain undisturbed. Simulations were then repeated with different wind profiles and at different resolutions to investigate how mass transport depends on both the horizontal grid-spacing of the model and the vertical shear profile, and how shear effects depend on the resolution in the model.

7.2 Conclusions

To analyse the effects of both decadal and diurnal variations in wind shear, temperature and humidity we adapted the initial profile in idealised simulations representative of squall lines in the WAM (Chapters 4 and 5). Thermodynamic changes dominated the effects of shear in both cases. However, increases in vertical wind shear resulted in higher vertical velocities and mean rainfall. Our results support the findings of Taylor et al. (2017) that the recent decadal strengthening of the LLJ and the African easterly jet (AEJ) have driven recent changes in storm intensity in the Sahel as well as the often conjectured role of the LLJ in the diurnal cycle of MCS in the region. An increase in humidity might be expected to increase moderate and severe storms, whereas shear is more compatible with the increase in severe and not moderate storms seen in Taylor et al. (2017). Additionally, although the diurnal wind cycle is not a dominant factor in the diurnal cycle of MCSs, it still plays a role in controlling their severity and decay.

CMIP5 trends were applied to the initial control profile to produce squall lines representative of the end of this century. The predicted thermodynamic trends resulted in shorter-lived squall lines. This is consistent with the increase in convective inhibition (CIN) predicted across the CMIP5 models and suggests that large-scale convergence and synoptic variability may play an important role for storms in a future climate and more work is needed to understand this relationship.

When multiple sets of reanalysis data for recent decades were compared in Chapter 4 for the Sahel region there were differences, including in the sign, of decadal trends in both humidity and shear. This shows the real need for an improvement of measurements in the region especially as the analysis of the current thermodynamic profiles is vital for understanding past trends in squall line intensity as well as initiating models accurately for the future. Despite there being large disparities across the CMIP5 predictions due to differences in model physics, increased shear is an expected product of a strengthened Saharan heat low (SHL) (Dong and Sutton 2015; Evan et al. 2015) and so an increase in storm intensity is expected in the future (Taylor et al. 2017).

The skill of the LLMC as an indicator of vertical ascent and rain-rates in the simulated
storms was explored (Chapters 4 and 5). When considering recent ERA-Interim trends,
the diagnostics of Alfaro (2017) were an excellent indicator for squall line average ascent
and rain-rates while maximum values of both were not as well correlated. For the set
of experiments which explored the diurnal cycle, the LLMC was found to correlate well
with upward mass flux but not with average maximum ascent rates due to variations
in storm organisation. The lack of correlation appeared to be linked to differences
in cold pool structure, with cooler low-level environments producing cold pools with
weaker temperature deficits, more compact storms and a circulation that was more like
a wave than a density current (Crook and Moncrieff 1988). Furthermore, similarly to
the findings of Parker (2008), these weak wave-like cold pools had ratios of cold pool
speed to shear which were close to 1.

Our analysis shows that by moving with the AEJ storms maximise their system-relative
inflow of convective available potential energy (CAPE). Whether there are mechanisms
that create a tendency for storms to move at a speed that minimises the system-relative
inflow of CAPE, or whether this is simply because storms move with the AEJ and this
maximises the inflow, is unclear. Our results also show some measure of reconciliation
between the theories of Alfaro (2017) and Rotunno et al. (1988) as storms in which the
cold pool intensity was comparable with shear strength were more compact, resulting
in a more efficient storm with higher mean rainfall rates that were not reflected in the
precipitation rate index of the LLMC. Thus, the LLMC and theory of Rotunno et al.
(1988) appear useful in explaining our results, with the LLMC explaining mass fluxes
and rainfall, and the theory of Rotunno et al. (1988) indicating differences in storm
organisation and structure.

For the diurnal experiments, the LLMC correlates better with total rainfall than with
the mean, which can again be understood partly as mean rainfall rates are a function
of storm area whilst the total rainfall is not. However, total rainfall is not as well
predicted as mass flux and our analysis shows that this can largely be explained by
variations in thermodynamics affecting microphysical processes.

In summary, the LLMC provides useful scalings for squall line ascent rates and mean
and bulk rainfall measures, with results showing these properties are strongly controlled
by shear, a parameter that is not usually accounted for in parametrisations, but that
has had more attention in recent years (Moncrieff et al. 2017). However, differences
in microphysics and storm organisation are not accounted for in the LLMC and this
is particularly clear when the thermodynamic profile is varied rather than the wind
profile alone. To correctly account for both longer term environmental trends as well
as the diurnal cycle, our results indicate that convection parametrisation schemes need

to capture the shear effects, which is something they currently struggle with.

By adding passive tracers to the idealised simulations, we found in Chapter 6 that in-flowing air does not pass through the convective region unperturbed but either descends in layers or is transported upward. This finding, which suggests a large proportion of some layers descend independent of their CAPE and water vapour mixing ratio, may provide some further insight into why the LLMC is an imperfect representation of how the system relative inflow controls the eventual rainfall in an MCS.

Finally, simulations with the control pre-storm profile and specific wind shear profiles were run with passive tracers at multiple horizontal grid-spacings of 4 km, 1 km and 100 m. Although increased horizontal resolution alone produces greater quantities of each tracer to be transported upwards, when the ratio of low-level, high CAPE air to mid-level, lower CAPE air is computed the ratio is similar in the upper troposphere at both 1 km and 100 m resolutions while 4 km simulations differ more. Recent work by Mulholland et al. (2021) has shown that low-level shear results in stronger horizontal mass flux into the leading edge of the cold pool which produces wider updrafts, less entrainment-driven dilution and larger buoyancy than those with weak low-level shear. Our results support this finding with increased shear resulting in less diluted updrafts at both 1 km and 100 m grid-spacing. However, these results were less consistent at 4 km which suggests the poorer representation of mixing at 4 km could be minimising the effects of shear on squall line intensity. This result, although produced in a different model, does shed some light on why convection-permitting 4 km climate simulations over the African continent using the Unified Model are not seeing increases in the highest intensity rainfall with greater shear (Senior et al. 2021) as shown in recent observational studies (Taylor et al. 2017).

7.2.1 Sahelian Squall Line Schematic

The findings in this thesis have been drawn together to produce the schematic in Figure 7.1 which highlights the unique traits of Sahelian Squall Lines. The most obvious difference between this and the classic versions is the anvil cloud which spreads out to the west due to the Tropical Easterly Jet which begins around 300 hPa. Additionally, the Sahelian squall lines produced in our simulations had clear slant-wise ascent which initiated ahead of the cold pool as well as individual deep convective cores. An important aspect of the squall lines that was seen in Chapter 6 was their three-dimensional nature with areas of ascent interspaced with layers of descending low-θ_e air.
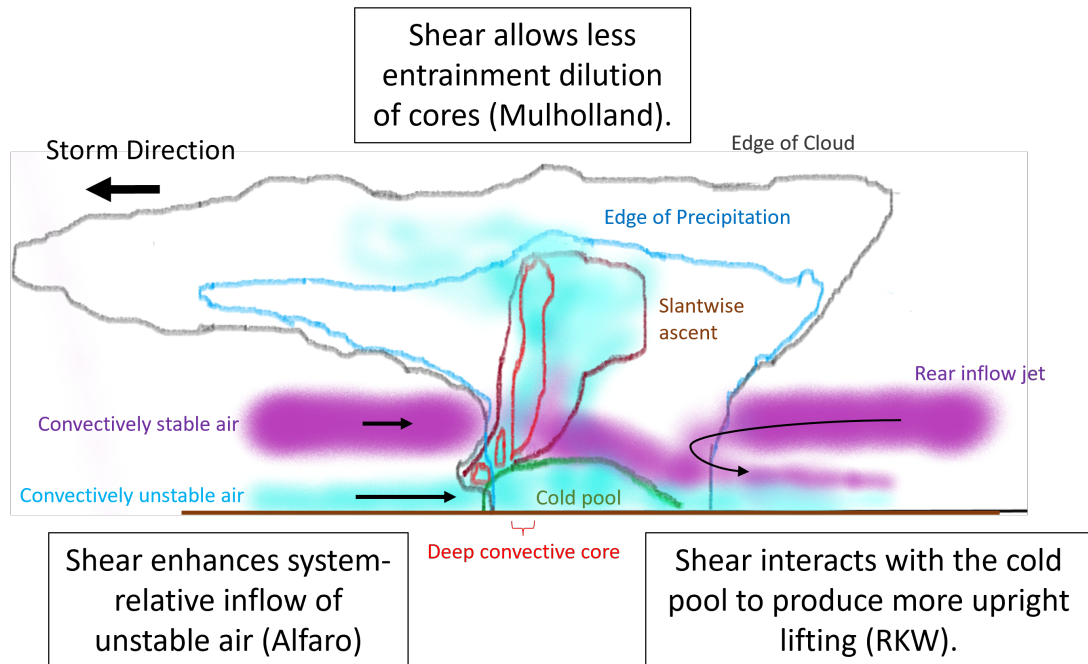
Figure 7.1: Schematic of a West African Squall Line showing the inflow of convectively unstable near-surface air (light blue) and convectively stable air (purple). There is an area of weaker slantwise-ascent (dark red outline) and the strongest deep convective cores (red) are interspaced along the line of the storm with areas of strong descent.

7.3 Future Work

7.3.1 Further Development of Theoretical and Conceptual Models

Throughout this thesis the LLMC has been shown as a useful tool in predicting how changes in the environmental profile in wind, temperature and humidity impact the intensity of MCSs. However, despite the LLMC producing several correlations above 0.95 for mean rainfall and line-averaged maximum updraft speeds across longer-term decadal trends in this project, it does not provide a consistent indicator of squall line intensity, particularly on a diurnal time-frame. It is also noteworthy that the change in vertical shear in the trends applied from both ERA-Interim and CMIP5 data is equivalent in the former, and smaller in the latter, than the variability within the diurnal cycle applied in Chapter 5 which was drawn only from radiosonde data over a two month period. This thesis has used best estimates to represent both the past and what we can expect in the future, and applied these to a current pre-storm profile, but a diurnal cycle will be present in both. In this section, we discuss the next steps which would be undertaken to gain further insight into the successes, failures and complexities of different theories for the efficiency and character of MCSs.

The first step would be to use a more idealised profile to allow an easier comparison with theory as well as the opportunity to analyse a larger parameter space of both shear and thermodynamic profiles. By changing only the wind profile, the following could be investigated:

- whether it is merely the effect of changes in the LLJ (and so changes in the inflow of low-level air relative to mid-level air) rather than changes in shear which have impacted squall line intensity. This could be explored through manipulating the wind profile such that wind-shear is held constant but the maximum of the LLJ and AEJ are altered.

- the role of the mean system-relative inflow of CAPE and moisture. This could be examined through the inclusion of tracers to explore what air feeds updrafts.

- how the maximum of the AEJ influences the propagation speed of the storm and whether the simulated squall lines still tend towards a speed which maximises their w_{ll} when the wind profile is varied.

A set of experiments which included a larger variety of thermodynamic and wind profiles would allow for further testing of the LLMC and an opportunity to gain a better understanding of how the system relative-inflow of moisture relates to the eventual rainfall.

While testing whether the LLMC predicted mean and total rainfall rates for the diurnal profile experiments in Chapter 5, alternative scalings were considered including the system-relative inflow of moisture,

$$q_{in} = \left(\int_0^{z_{tr}} \rho(z) \left| u_{env} - \mathrm{PS} \right| q_v dz \right), \qquad (7.1)$$

and the fractional system-relative inflow of moisture relative to that of total mass,

$$q_{ll} = \left(\int_0^{z_{tr}} \rho(z) \left| u_{env} - \mathrm{PS} \right| q_v dz \right) \left(\int_0^{z_{tr}} \rho(z) \left| u_{env} - \mathrm{PS} \right| dz \right)^{-1}. \qquad (7.2)$$

the latter of which provided the best indicator of total rainfall and was better correlated with the mean rainfall than PR_{ll} (see Table 7.1 and Figure 7.2). However, the success of the indicators were not consistent when the experiments with recent ERA-Interim decadal trends in thermodynamics were considered (Table 7.1). Differences in CAPE_{ll} (and so PR_{ll}) are the strongest indicator of total and mean rainfall for the decadal

Table 7.1: Table comparing correlation co-efficient for PR_{ll}, ΔU, $C/\Delta U$, q_{in} and q_{ll} for the mean (of the five repeated experiments in each case) and total rainfall across the Diurnal experiments in Chapter 5 and the ERA-Interim experiments which represent recent decadal trends (Chapter 4). The correlations are calculated for the mean values of each set of random experiments.

	Rainfall	PR_{ll}	ΔU	$C/\Delta U$	q_{in}	q_{ll}	$CAPE_{ll}$
Diurnal	$\bar{R}$	-0.19	0.72	-0.48	-0.1	0.48	-0.14
	R_{tot}	0.42 (0.72*)	0.51	0.12	0.4	0.94	0.47
ERA-I	$\bar{R}$	0.98	0.28	-0.75	0.27	0.79	0.99
	R_{tot}	0.91	0.17	-0.62	0.45	0.71	0.95

* If cases with the 1800 thermodynamics are ignored.
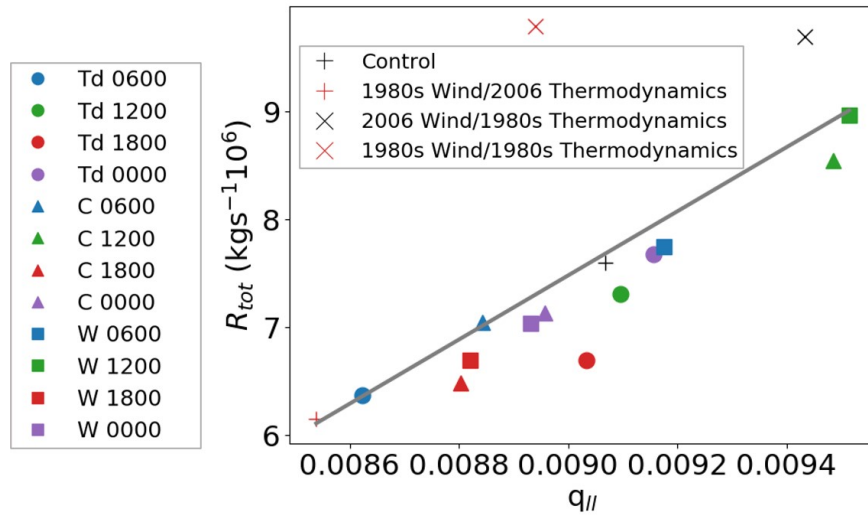
Figure 7.2: Comparing q_{ll} to the total domain rainfall for (a) all Diurnal runs and (b) the ERA-Interim experiments.

changes in rainfall while as previously stated q_{ll} and ΔU are the best indicators for total rainfall and mean rainfall respectively over the diurnal time-frame. Due to the limited number of profiles considered in the ERA-Interim experiments the results here are not conclusive. So future work should analyse flows of mass and water through the squall line (see Chapter 6) to test the assumptions contained in Alfaro (2017) and potentially generate an improved theory of layer-lifting convection.

7.3.2 Diagnosing Mass Transport

It would be useful to repeat the set of passive tracer experiments in Chapter 6 so that T2, currently placed from 1.5 to 3 km so as to include no CAPE while also splitting the

area of T1, currently defined from 0-1.5km, so that this region included two different tracers. This would allow for a better understanding of whether the mid-level air is truly entrained or moved upwards due to the small amount of CAPE included. Additionally, multiple tracers in the lowest level would provide further insight into the composition of the cold pool.

Finally, there was insufficient time to fully analyse the full set of passive tracer experiments which also included the diurnal thermodynamic change experiments. However, these combined with additional experiments which included a larger variety of both thermodynamic profiles would allow for an investigation of the suggestion in Provod et al. (2016) that mid-level dryness may strengthen cold pools.

7.3.3 Testing the Role of Shear in more Realistic Environments

The idealised simulations in this study ignore influences such as large-scale convergence, variations in the synoptic state and diurnal cycle, including surface fluxes and radiation. Additionally, the squall lines in this study have all been infinitely long lines so extending the analysis to 3-dimensional squall lines would be valuable. Thus, further work is required on exploring the role of wind shear in organised deep convection in less idealised settings including operational models and observations. Initially, the properties of the squall lines produced in such models would be analysed. For instance, recent work has shown that the MCSs do not travel fast enough when deep convection is parametrised (Crook et al. 2019). Eventually, the impact of additional key parameters of the environment including African Easterly Waves, seasonality and synoptic variability could be considered.

This would provide an opportunity to investigate if storm intensities in these more realistic scenarios could be explained by the role shear plays in the LLMC, the rate of entrainment and in dynamically effecting the cold pool. These investigations would also indicate whether parametrisation schemes could be adapted to include the effects of shear. Such adaptations would be challenging, but if there is a robust impact of shear on updraft widths and entrainment dilution this could, for example, be included in the parametrisation scheme. Another application is satellite based nowcasting with recent work (Hill et al. 2020; Roberts et al. 2021) showing the need and potential for satellite based nowcasting in Africa. An improved understanding of the dependence of MCSs on the environment could help predict storm growth and decay in such systems through the application of information from NWP as currently nowcasting systems essentially only extrapolate storms forward in time.

Finally, better understanding of the role of wind shear in MCSs could inform the use of climate predictions including what changes to extremes we expect in the future in the WAM. Current convection permitting, 4.5km resolution modelling over Africa (CP4A) simulations are likely under-estimating future extremes as they are missing the effects of shear which is projected to increase. Additionally, such further work could inform the setup of CP4A for new sets of runs including the minimum horizontal grid-spacing which would capture shear effects. As decision making becomes more reliant on climate projections of high impact weather, predictions are being increasingly based on convection permitting climate runs. The efficacy of such runs, including in the set-up and interpretation of any results, is dependent on understanding what controls the severity of squall lines.

References

Abdou, K., Parker, D. J., Brooks, B., Kalthoff, N., and Lebel, T. 2010. The diurnal cycle of lower boundary-layer wind in the West African Monsoon. *Quarterly Journal of the Royal Meteorological Society*, **136**(SUPPL. 1), 66–76. ISSN 00359009. doi: 10.1002/qj.536.

Agustí-Panareda, A., Vasiljevic, D., Beljaars, A., Bock, O., Guichard, F., Nuret, M., Mendez, A. G., Andersson, E., Bechtold, P., Fink, A., Hersbach, H., Lafore, J. P., Ngamini, J. B., Parker, D. J., Redelsperger, J. L., and Tompkins, A. M. 2009. Radiosonde humidity bias correction over the West African region for the special AMMA reanalysis at ECMWF. *Quarterly Journal of the Royal Meteorological Society*, **135**(640), 595–617. ISSN 00359009. doi: 10.1002/qj.396.

Agustí-Panareda, A., Beljaars, A., Cardinali, C., Genkova, I., and Thorncroft, C. 2010. Impacts of Assimilating AMMA Soundings on ECMWF Analyses and Forecasts. *Weather and Forecasting*, **25**(4), 1142–1160. ISSN 08828156. doi: 10.1175/2010WAF2222370.1.

Alfaro, D. A. 2017. Low-tropospheric shear in the structure of squall lines: Impacts on latent heating under layer-lifting ascent. *Journal of the Atmospheric Sciences*, **74**(1), 229–248. ISSN 15200469. doi: 10.1175/JAS-D-16-0168.1.

Alfaro, D. A. and Khairoutdinov, M. 2015. Thermodynamic constraints on the morphology of simulated midlatitude squall lines. *Journal of the Atmospheric Sciences*, **72**(8), 3116–3137. ISSN 15200469. doi: 10.1175/JAS-D-14-0295.1.

American Meteorological Society, A. M. S. Richardson number, 2012. URL `https://glossary.ametsoc.org/wiki/Richardson{_}number`.

American Meteorological Society, A. M. S. Virtual Temperature, 2021a. URL `https://glossary.ametsoc.org/wiki/Virtual{_}temperature`.

American Meteorological Society, A. M. S. Convective Available Po-

tential Energy, 2021b. URL https://glossary.ametsoc.org/wiki/
Convective{_}available{_}potential{_}energy.

American Meteorological Society, A. M. S. Convective Instability, 2021c. URL https:
//glossary.ametsoc.org/wiki/Conditional{_}instability.

American Meteorological Society, A. M. S. Convective Inhibition, 2021d. URL https:
//glossary.ametsoc.org/wiki/Convective{_}inhibition.

American Meteorological Society, A. M. S. Saharan air layer, 2021e. URL https:
//glossary.ametsoc.org/wiki/Saharan{_}air{_}layer.

American Meteorological Society, A. M. S. Mesoscale Convective System, 2021f. URL
https://glossary.ametsoc.org/wiki/Mesoscale{_}convective{_}system.

American Meteorological Society, A. M. S. Potential Instability, 2021g. URL https:
//glossary.ametsoc.org/wiki/Potential{_}instability.

American Meteorological Society, A. M. S. Monsoon, 2021h. URL https://glossary.
ametsoc.org/wiki/Monsoon.

American Meteorological Society, A. M. S. Turbulence Kinetic Energy, 2021i. URL
https://glossary.ametsoc.org/wiki/Turbulence{_}kinetic{_}energy.

Baidu, M. Ongoing Analysis by Michael Baidu, 2021. URL eembai@leeds.ac.uk.

Bannon, P. R. 2002. Theoretical foundations for models of moist convection. *Journal
of the Atmospheric Sciences*, **59**(12), 1967–1982. ISSN 00224928. doi: 10.1175/
1520-0469(2002)059⟨1967:TFFMOM⟩2.0.CO;2.

Barnes, G. M. and Sieckman, K. 1984. The environment of fast- and slow-moving
tropical mesoscale convective cloud lines. *Monthly Weather Review*, **112**(9), 1782–
1794. ISSN 09240136. doi: 10.1175/1520-0493(1984)112⟨1782:TEOFAS⟩2.0.CO;2.

Bauer, P., Thorpe, A., and Brunet, G. 2015. The quiet revolution of numerical weather
prediction. *Nature*, **525**(7567), 47–55. ISSN 14764687. doi: 10.1038/nature14956.

Becker, T. and Hohenegger, C. 2021. Entrainment and Its Dependency on Envi-
ronmental Conditions and Convective Organization in Convection-Permitting Sim-
ulations. *Monthly Weather Review*, **149**(2), 537–550. ISSN 0027-0644. doi:
10.1175/mwr-d-20-0229.1.

Benjamin, T. B. 1968. Gravity currents and related phenomena. *Journal of Fluid
Mechanics*, **31**(2), 209–248. ISSN 14697645. doi: 10.1017/S0022112068000133.

Berrisford, P., Dee, D., Poli, P., Brugge, R., Fielding, K., Fuentes, M., Kallberg, P.,
Kobayashi, S., Uppala, S., and Simmons, A. The ERA-Interim archive, version 2.0.
Technical report, European Centre for Medium Weather Forecasting, 2011.

Berthou, S., Kendon, E. J., Rowell, D. P., Roberts, M. J., Tucker, S., and Stratton,
R. A. nov 2019a. Larger Future Intensification of Rainfall in the West African Sahel in
a Convection-Permitting Model. *Geophysical Research Letters*, **46**(22), 13299–13307.
ISSN 19448007. doi: 10.1029/2019GL083544.

Berthou, S., Rowell, D. P., Kendon, E. J., Roberts, M. J., Stratton, R. A., Crook,
J. A., and Wilcox, C. 2019b. Improved climatological precipitation characteristics
over West Africa at convection-permitting scales. *Climate Dynamics*, **53**(3-4), 1991–
2011. ISSN 14320894. doi: 10.1007/s00382-019-04759-4.

Bevere, L., Schwartz, M., Sharan, R., and Zimmerli, P. Natural catastrophes and man-
made disasters in 2017: a year of record-breaking losses. Technical Report 1, Swiss
Re Institute, 2018.

Biasutti, M., Held, I. M., Sobel, A. H., and Giannini, A. 2008. SST forcings and Sahel
rainfall variability in simulations of the twentieth and twenty-first centuries. *Journal
of Climate*, **21**(14), 3471–3486. ISSN 08948755. doi: 10.1175/2007JCLI1896.1.

Biggerstaff, M. I. and Houze Jr., R. A. 1993. Kinematics and Microphysics of the
Transition Zone of the 10–11 June 1985 Squall Line. *Journal of Atmospheric Sciences*,
50(18), 3091–3110. doi: 10.1175/1520-0469(1993)050⟨3091:KAMOTT⟩2.0.CO;2.

Birch, C. E., Parker, D. J., Marsham, J. H., Copsey, D., and Garcia-Carreras, L. 2014.
A seamless assessment of the role of convection in the water cycle of the west African
Monsoon. *Journal of Geophysical Research*, **119**(6), 2890–2912. ISSN 21562202. doi:
10.1002/2013JD020887.

Brooks, I. The Tephigram. Technical report, University of Leeds, 2011. URL `http:
//www.met.reading.ac.uk/{~}sgs02rpa/TEACHING/Tephigram.pdf`.

Brown, R. G. and Zhang, C. 1997. Variability of midtropospheric moisture and its
effect on cloud-top height distribution during TOGA COARE. *Journal of the Atmo-
spheric Sciences*, **54**(23), 2760–2774. ISSN 00224928. doi: 10.1175/1520-0469(1997)
054⟨2760:VOMMAI⟩2.0.CO;2.

Browning, K. A. and Ludlam, F. H. 1962. Airflow in convective storms. *Quarterly
Journal of the Royal Meteorological Society*, **88**(376), 117–135. ISSN 1477870X. doi:
10.1002/qj.49708837602.

Bryan, G. H. The governing equations for CM1. Technical Report January 2003, National Center for Atmospheric Research, Boulder, Colorado, USA, 2017.

Bryan, G. H. and Fritsch, J. M. 2000. Moist absolute instability: The sixth static stability state. *Bulletin of the American Meteorological Society*, **81**(6), 1207–1230. ISSN 00030007. doi: 10.1175/1520-0477(2000)081⟨1287:MAITSS⟩2.3.CO;2.

Bryan, G. H. and Fritsch, J. M. 2002. A benchmark simulation for moist nonhydrostatic numerical models. *Monthly Weather Review*, **130**(12), 2917–2928. ISSN 00270644. doi: 10.1175/1520-0493(2002)130⟨2917:ABSFMN⟩2.0.CO;2.

Bryan, G. H. and Morrison, H. 2012. Sensitivity of a simulated squall line to horizontal resolution and parameterization of microphysics. *Monthly Weather Review*, **140**(1), 202–225. ISSN 00270644. doi: 10.1175/MWR-D-11-00046.1.

Bryan, G. H., Wyngaard, J. C., and Fritsch, J. M. 2003. Resolution requirements for the simulation of deep moist convection. *Monthly Weather Review*, **131**(10), 2394–2416. ISSN 00270644. doi: 10.1175/1520-0493(2003)131⟨2394:RRFTSO⟩2.0.CO;2.

Bryan, G. H., Knievel, J. C., and Parker, M. D. 2006. A multimodel assessment of RKW theory's relevance to squall-line characteristics. *Monthly Weather Review*, **134** (10), 2772–2792. ISSN 00270644. doi: 10.1175/MWR3226.1.

Burpee, R. W. 1972. The Origin and Structure of Easterly Waves in the Lower Troposphere of North Africa. *Journal of the Atmospheric Sciences*, **29**(1), 77–90. ISSN 0022-4928. doi: 10.1175/1520-0469(1972)029⟨0077:toasoe⟩2.0.co;2.

Burpee, R. W. 1974. Characteristics of North African Easterly Waves During the Summers of 1968 and 1969. *Journal of Atmospheric Sciences*, **31**(6), 1556–1570. doi: 10.1175/1520-0469(1974)031⟨1556:CONAEW⟩2.0.CO;2.

Chong, M. 2010. The 11 august 2006 squall-line system as observed from MIT doppler radar during the AMMA SOP. *Quarterly Journal of the Royal Meteorological Society*, **136**(SUPPL. 1), 209–226. ISSN 00359009. doi: 10.1002/qj.466.

Coniglio, M. C. and Stensrud, D. J. 2001. Simulation of a progressive derecho using composite initial conditions. *Monthly Weather Review*, **129**(7), 1593–1616. ISSN 00270644. doi: 10.1175/1520-0493(2001)129⟨1593:SOAPDU⟩2.0.CO;2.

Cook, K. H. 1999. Generation of the African easterly jet and its role in determining West African precipitation. *Journal of Climate*, **12**(5 I), 1165–1184. ISSN 08948755. doi: 10.1175/1520-0442(1999)012⟨1165:GOTAEJ⟩2.0.CO;2.

Correia, J. and Arritt, R. W. 2008. Thermodynamic properties of mesoscale convective systems observed during BAMEX. *Monthly Weather Review*, **136**(11), 4242–4271. ISSN 00270644. doi: 10.1175/2008MWR2284.1.

Cotton, W. R., Bryan, G. H., and Van den Heever, S. C. *Storm and cloud dynamics*, volume 99. Academic press, 2010. ISBN 0080916651. doi: https://doi.org/10.1016/S0074-6142(10)09908-0. URL https://www.sciencedirect.com/science/article/pii/S0074614210099080.

Crook, J., Klein, C., Folwell, S., Taylor, C. M., Parker, D. J., Stratton, R., and Stein, T. may 2019. Assessment of the Representation of West African Storm Lifecycles in Convection-Permitting Simulations. *Earth and Space Science*, **6**(5), 818–835. ISSN 23335084. doi: 10.1029/2018EA000491.

Crook, N. A. and Moncrieff, M. W. 1988. The Effect of Large-Scale Convergence on the Generation and Maintenance of Deep Moist Convection. *Journal of Atmospheric Sciences*, **45**(23), 3606–3624. doi: 10.1175/1520-0469(1988)045⟨3606:TEOLSC⟩2.0. CO;2.

Crutcher, H. L. and Eskridge, R. E. Development of a method to modify solar-induced humidity biases in the US radiosonde data from the period 1961–1973. Preprints. In *Eighth Symp. on Meteorological Observations and Instrumentation, Anaheim, CA*, pages 143–147. American Meteorological Society, 1993.

Cullmann, J., Dilley, M., Fowler, J., Grasso, F. V., Kabat, P., Lúcio, F., Nullis, C., and Repnik, M. 2019. 2019 State of climate services. *WMO-No. 1242*, page 44. URL https://library.wmo.int/index.php?lvl=notice{_}display{&}id=21609{#}.XgWKsUf0mub.

Deardorff, J. W. 1980. Stratocumulus-capped mixed layers derived from a three-dimensional model. *Boundary-Layer Meteorology*, **18**(4), 495–527. ISSN 00068314. doi: 10.1007/BF00119502.

Derbyshire, S. H., Beau, I., Bechtold, P., Grandpeix, J.-Y. Y., Piriou, J.-M. M., Redelsperger, J.-L. L., and Soares, P. M. M. oct 2004. Sensitivity of moist convection to environmental humidity. *Quarterly Journal of the Royal Meteorological Society*, **130**(604), 3055–3079. ISSN 0035-9009. doi: https://doi.org/10.1256/qj.03.130.

Dong, B. and Sutton, R. 2015. Dominant role of greenhouse-gas forcing in the recovery of Sahel rainfall. *Nature Climate Change*, **5**(8), 757–760. ISSN 17586798. doi: 10.1038/nclimate2664.

Durran, D. R. *IUTAM Symposium on Advances in Mathematical Modelling of Atmosphere and Ocean Dynamics: Proceedings of the IUTAM Symposium held in Limerick, Ireland, 2–7 July 2000*, volume 61. Springer Science & Business Media, 2001. ISBN 0792370759.

Durran, D. R. *Numerical Methods for Wave Equations in Geophysical Fluid Dynamics*, volume 32. Springer Science & Business Media, 2013. ISBN 0387983767.

Durran, D. R. and Klemp, J. B. 1983. A compressible model for the simulation of moist mountain waves. *Monthly Weather Review*, **111**(12), 2341–2361. ISSN 00270644. doi: 10.1175/1520-0493(1983)111⟨2341:ACMFTS⟩2.0.CO;2.

Duvel, J. P. 1989. Convection over Tropical Africa and the Atlantic Ocean during Northern Summer. Part I: Interannual and Diurnal Variations. *Monthly Weather Review*, **117**(12), 2782–2799. doi: 10.1175/1520-0493(1989)117⟨2782:COTAAT⟩2.0.CO;2.

Evan, A. T., Flamant, C., Lavaysse, C., Kocha, C., and Saci, A. 2015. Water vapor-forced greenhouse warming over the Sahara desert and the recent recovery from the Sahelian drought. *Journal of Climate*, **28**(1), 108–123. ISSN 08948755. doi: 10.1175/JCLI-D-14-00039.1.

Fankhauser, J. C. 1988. Estimates of Thunderstorm Precipitation Efficiency from Field Measurements in CCOPE. *Monthly Weather Review*, **116**(3), 663–684. doi: 10.1175/1520-0493(1988)116⟨0663:EOTPEF⟩2.0.CO;2.

Feng, Z., Leung, L. R., Houze Jr, R. A., Hagos, S., Hardin, J., Yang, Q., Han, B., and Fan, J. 2018. Structure and Evolution of Mesoscale Convective Systems: Sensitivity to Cloud Microphysics in Convection-Permitting Simulations Over the United States. *Journal of Advances in Modeling Earth Systems*, **10**(7), 1470–1494. doi: https://doi.org/10.1029/2018MS001305. URL `https://agupubs.onlinelibrary.wiley.com/doi/abs/10.1029/2018MS001305`.

Fierro, A. O., Simpson, J., LeMone, M. A., Straka, J. M., and Smull, B. F. 2009. On How Hot Towers Fuel the Hadley Cell: An Observational and Modeling Study of Line-Organized Convection in the Equatorial Trough from TOGA COARE. *Journal of the Atmospheric Sciences*, **66**(9), 2730–2746. ISSN 00224928. doi: 10.1175/2009JAS3017.1.

Fink, A. H. and Reiner, A. 2003. Spatiotemporal variability of the relation between African Easterly Waves and West African Squall Lines in 1998 and 1999. *Journal of Geophysical Research: Atmospheres*, **108**(11). ISSN 01480227. doi: 10.1029/2002jd002816.

Fink, A. H., Agustí-Panareda, A., Parker, D. J., Lafore, J.-P., Ngamini, J.-B., Afies-
imama, E., Beljaars, A., Bock, O., Christoph, M., Didé, F., Faccani, C., Fourrié,
N., Karbou, F., Polcher, J., Mumba, Z., Nuret, M., Pohle, S., Rabier, F., Tompkins,
A. M., and Wilson, G. jan 2011. Operational meteorology in West Africa: observa-
tional networks, weather analysis and forecasting. *Atmospheric Science Letters*, **12**
(1), 135–141. ISSN 1530-261X. doi: 10.1002/asl.324.

Fitzpatrick, R. G., Parker, D. J., Marsham, J. H., Rowell, D. P., Guichard, F. M.,
Taylor, C. M., Cook, K. H., Vizy, E. K., Jackson, L. S., Finney, D., Crook, J.,
Stratton, R., and Tucker, S. 2020. What drives the intensification of mesoscale
convective systems over the West African Sahel under climate change? *Journal of
Climate*, **33**(8), 3151–3172. ISSN 08948755. doi: 10.1175/JCLI-D-19-0380.1.

Fovell, R. G. and Dailey, P. S. 1995. The temporal behavior of numerically simulated
multicell-type storms. Part I: models of behavior. *Journal of Atmospheric Sciences*,
52(11), 2073–2095. ISSN 0022-4928. doi: 10.1175/1520-0469(1995)052⟨2073:ttbons⟩
2.0.co;2.

Fovell, R. G. and Tan, P. H. 1998. The temporal behavior of numerically sim-
ulated multicell-type storms. Part II: The convective cell life cycle and cell re-
generation. *Monthly Weather Review*, **126**(3), 551–577. ISSN 00270644. doi:
10.1175/1520-0493(1998)126⟨0551:TTBONS⟩2.0.CO;2.

French, A. J. and Parker, M. D. 2010. The response of simulated nocturnal convective
systems to a developing low-level jet. *Journal of the Atmospheric Sciences*, **67**(10),
3384–3408. ISSN 00224928. doi: 10.1175/2010JAS3329.1.

Gallus, W. A. and Johnson, R. H. 1995. The Dynamics of Circulations
within the Trailing Stratiform Regions of Squall Lines. Part II: Influence of
the Convective Line and Ambient Environment. *Journal of Atmospheric Sci-
ences*, **52**(12), 2188–2211. doi: 10.1175/1520-0469(1995)052⟨2188:TDOCWT⟩
2.0.CO;2. URL https://journals.ametsoc.org/view/journals/atsc/52/12/
1520-0469{_}1995{_}052{_}2188{_}tdocwt{_}2{_}0{_}co{_}2.xml.

Garcia-Carreras, L., Marsham, J. H., Parker, D. J., Bain, C. L., Milton, S., Saci, A.,
Salah-Ferroudj, M., Ouchene, B., and Washington, R. 2013. The impact of convective
cold pool outflows on model biases in the Sahara. *Geophysical Research Letters*, **40**
(8), 1647–1652. ISSN 00948276. doi: 10.1002/grl.50239.

Garcia-Carreras, L., Parker, D. J., Marsham, J. H., Rosenberg, P. D., Brooks, I. M.,
Lock, A. P., Marenco, F., Mcquaid, J. B., and Hobby, M. 2015. The turbulent

structure and diurnal growth of the Saharan atmospheric boundary layer. *Journal of the Atmospheric Sciences*, **72**(2), 693–713. ISSN 15200469. doi: 10.1175/JAS-D-13-0384.1.

Georg, G. A., Dudhia, J., and Stauffer, D. R. A description of the Fifth-generation Penn State/NCAR Mesoscale Model (MM5). Technical Report December, National Center for Atmospheric Research, 1994.

Gilmore, M. S. and Wicker, L. J. 1998. The Influence of Midtropospheric Dryness on Supercell Morphology and Evolution. *Monthly Weather Review*, **126**(4), 943–958. ISSN 00270644. doi: 10.1175/1520-0493(1998)126⟨0943:TIOMDO⟩2.0.CO;2.

Haiden, T., Rodwell, M. J., Richardson, D. S., Okagaki, A., Robinson, T., and Hewson, T. 2012. Intercomparison of Global Model Precipitation Forecast Skill in 2010/11 Using the SEEPS Score. *Monthly Weather Review*, **140**(8), 2720–2733. ISSN 00270644. doi: 10.1175/MWR-D-11-00301.1.

Hill, P. G., Stein, T. H. M., Roberts, A. J., Fletcher, J. K., Marsham, J. H., and Groves, J. nov 2020. How skilful are Nowcasting Satellite Applications Facility products for tropical Africa? *Meteorological Applications*, **27**(6), e1966. ISSN 1350-4827. doi: https://doi.org/10.1002/met.1966. URL `https://doi.org/10.1002/met.1966`.

Hodges, K. I. and Thorncroft, C. D. 1997. Distribution and statistics of african mesoscale convective weather systems based on the ISCCP meteosat imagery. *Monthly Weather Review*, **125**(11), 2821–2837. ISSN 00270644. doi: 10.1175/1520-0493(1997)125⟨2821:DASOAM⟩2.0.CO;2.

Houze Jr., R. A. 1977. Structure and dynamics of a tropical squall–line system. *Monthly Weather Review*, **105**(12), 1540–1567. ISSN 1520-0493.

Houze Jr., R. A. 1989. Observed structure of mesoscale convective systems and implications for large-scale heating. *Quarterly Journal of the Royal Meteorological Society*, **115**(487), 425–461. ISSN 1477870X. doi: 10.1002/qj.49711548702.

Houze Jr., R. A. 2014. Mesoscale convective systems. *International Geophysics*, **104**, 237–286. ISSN 00746142. doi: 10.1016/B978-0-12-374266-7.00009-3.

James, R. P. and Markowski, P. M. 2010. A numerical investigation of the effects of dry air aloft on deep convection. *Monthly Weather Review*, **138**(1), 140–161. ISSN 00270644. doi: 10.1175/2009MWR3018.1.

Kalapureddy, M. C., Lothon, M., Campistron, B., Lohou, F., and Saïd, F. 2010. Wind profiler analysis of the African Easterly Jet in relation with the boundary layer and

the Saharan heat-low. *Quarterly Journal of the Royal Meteorological Society*, **136** (SUPPL. 1), 77–91. ISSN 00359009. doi: 10.1002/qj.494.

Kendon, E. J., Stratton, R. A., Tucker, S., Marsham, J. H., Berthou, S., Rowell, D. P., and Senior, C. A. 2019. Enhanced future changes in wet and dry extremes over Africa at convection-permitting scale. *Nature Communications*, **10**(1), 1–14. ISSN 20411723. doi: 10.1038/s41467-019-09776-9.

Kilpatrick, T. J. and Xie, S. P. 2015. ASCAT observations of downdrafts from mesoscale convective systems. *Geophysical Research Letters*, **42**(6), 1951–1958. ISSN 19448007. doi: 10.1002/2015GL063025.

Kingsmill, D. E. and Houze Jr., R. A. apr 1999. Kinematic characteristics of air flowing into and out of precipitating convection over the west Pacific warm pool: An airborne Doppler radar survey. *Quarterly Journal of the Royal Meteorological Society*, **125** (556), 1165–1207. ISSN 0035-9009. doi: 10.1002/qj.1999.49712555605.

Klein, C. and Taylor, C. M. 2020. Dry soils can intensify mesoscale convective systems. *Proceedings of the National Academy of Sciences of the United States of America*, **117**(35), 21132–21137. ISSN 10916490. doi: 10.1073/pnas.2007998117.

Klein, C., Nkrumah, F., Taylor, C. M., and Adefisan, E. A. 2021. Seasonality and Trends of Drivers of Mesoscale Convective Systems in Southern West Africa. *Journal of Climate*, **34**(1), 71–87. doi: 10.1175/JCLI-D-20-0194.1.

Klemp, J. B. and Durran, D. R. 1983. An Upper Boundary Condition Permitting Internal Gravity Wave Radiation in Numerical Mesoscale Models. *Monthly Weather Review*, **111**(3), 430–444. ISSN 09240136. doi: 10.1175/1520-0493(1983)111⟨0430: aubcpi⟩2.0.co;2.

Klemp, J. B. and Lilly, D. K. Numerical Simulation of Hydro-static Mountain Waves. *Journal of Atmospheric Sciences*, **35**(1), 78–107. doi: 10.1175/1520-0469(1978)035⟨0078:NSOHMW⟩2.0.CO;2. URL https://journals.ametsoc.org/view/journals/atsc/35/1/ 1520-0469{_}1978{_}035{_}0078{_}nsohmw{_}2{_}0{_}co{_}2.xml.

Klemp, J. B. and Wilhelmson, R. B. 1978. The Simulation of Three-Dimensional Convective Storm Dynamics. *Journal of Atmospheric Sciences*, **35**(6), 1070–1096. doi: 10.1175/1520-0469(1978)035⟨1070:TSOTDC⟩2.0.CO;2.

Kniffka, A., Knippertz, P., Fink, A. H., Benedetti, A., Brooks, M. E., Hill, P. G., Maranan, M., Pante, G., and Vogel, B. 2020. An evaluation of operational and research weather forecasts for southern West Africa using observations from the DAC-

CIWA field campaign in June–July 2016. *Quarterly Journal of the Royal Meteorological Society*, **146**(728), 1121–1148. ISSN 1477870X. doi: 10.1002/qj.3729.

Knippertz, P. 2008. Dust emissions in the West African heat trough - the role of the diurnal cycle and of extratropical disturbances. *Meteorologische Zeitschrift*, **17**(5), 553–563. ISSN 09412948. doi: 10.1127/0941-2948/2008/0315.

Lafore, J. P. and Moncrieff, M. W. 1989. A numerical investigation of the organization and interaction of the convective and stratiform regions of tropical squall lines. *Journal of the Atmospheric Sciences*, **46**(4), 521–544. ISSN 00224928. doi: 10.1175/1520-0469(1989)046⟨0521:ANIOTO⟩2.0.CO;2.

Laing, A. G., Trier, S. B., and Davis, C. A. 2012. Numerical Simulation of Episodes of Organized Convection in Tropical Northern Africa. *Monthly Weather Review*, **140**(9), 2874–2886. ISSN 00270644. doi: 10.1175/MWR-D-11-00330.1.

Langhans, W., Schmidli, J., and Schär, C. 2012. Bulk convergence of cloud-resolving simulations of moist convection over complex terrain. *Journal of the Atmospheric Sciences*, **69**(7), 2207–2228. ISSN 00224928. doi: 10.1175/JAS-D-11-0252.1.

Lavaysse, C., Flamant, C., Janicot, S., Parker, D. J., Lafore, J. P., Sultan, B., and Pelon, J. 2009. Seasonal evolution of the West African heat low: A climatological perspective. *Climate Dynamics*, **33**(2-3), 313–330. ISSN 09307575. doi: 10.1007/s00382-009-0553-4.

Lebel, T., Diedhiou, A., and Laurent, H. 2003. Seasonal cycle and interannual variability of the Sahelian rainfall at hydrological scales. *Journal of Geophysical Research: Atmospheres*, **108**(8). ISSN 01480227. doi: 10.1029/2001jd001580.

Lebo, Z. J. and Morrison, H. 2015. Effects of horizontal and vertical grid spacing on mixing in simulated squall lines and implications for convective strength and structure. *Monthly Weather Review*, **143**(11), 4355–4375. ISSN 15200493. doi: 10.1175/MWR-D-15-0154.1.

LeMone, M. A. 1983. Momentum Transport by a Line of Cumulonimbus. *Journal of Atmospheric Sciences*, **40**(7), 1815–1834. doi: 10.1175/1520-0469(1983)040⟨1815:MTBALO⟩2.0.CO;2.

Letkewicz, C. E. and Parker, M. D. 2011. Impact of environmental variations on simulated squall lines interacting with terrain. *Monthly Weather Review*, **139**(10), 3163–3183. ISSN 00270644. doi: 10.1175/2011MWR3635.1.

Ludlam, F. H. Severe Local Storms: A Review. In *Severe Local Storms*, pages 1–32. American Meteorological Society, Boston, MA, 1963. ISBN 978-1-940033-56-3. doi: 10.1007/978-1-940033-56-3_1.

Maranan, M., Fink, A. H., and Knippertz, P. 2018. Rainfall types over southern West Africa: Objective identification, climatology and synoptic environment. *Quarterly Journal of the Royal Meteorological Society*, **144**(714), 1628–1648. ISSN 1477870X. doi: 10.1002/qj.3345.

Market, P. S., Allen, S., Scofield, R., Kuligowski, R., and Gruber, A. 2003. Precipitation efficiency of warm-season midwestern mesoscale convective systems. *Weather and Forecasting*, **18**(6), 1273–1285. ISSN 08828156. doi: 10.1175/1520-0434(2003)018⟨1273:PEOWMM⟩2.0.CO;2.

Markowski, P. and Richardson, Y. *Mesoscale Meteorology in Midlatitudes*, volume 2. John Wiley & Sons, 2010. ISBN 9780470682104. doi: 10.1002/9780470682104.

Marsham, J. H., Dixon, N. S., Garcia-Carreras, L., Lister, G. M., Parker, D. J., Knippertz, P., and Birch, C. E. 2013. The role of moist convection in the West African monsoon system: Insights from continental-scale convection-permitting simulations. *Geophysical Research Letters*, **40**(9), 1843–1849. ISSN 00948276. doi: 10.1002/grl.50347.

Mathon, V. and Laurent, H. 2001. Life cycle of Sahelian mesoscale convective cloud systems. *Quarterly Journal of the Royal Meteorological Society*, **127**(572), 377–406. ISSN 00359009. doi: 10.1256/smsqj.57207.

Mathon, V., Diedhiou, A., and Laurent, H. 2002a. Relationship between easterly waves and mesoscale convective systems over the Sahel. *Geophysical Research Letters*, **29**(8). ISSN 19448007. doi: 10.1029/2001GL014371.

Mathon, V., Laurent, H., and Lebel, T. 2002b. Mesoscale convective system rainfall in the Sahel. *Journal of Applied Meteorology*, **41**(11), 1081–1092. ISSN 08948763.

Mechem, D. B., Houze Jr., R. A., and Chen, S. S. jul 2002. Layer inflow into precipitating convection over the western tropical Pacific. *Quarterly Journal of the Royal Meteorological Society*, **128**(584), 1997–2030. ISSN 0035-9009. doi: https://doi.org/10.1256/003590002320603502.

Meynadier, R., Bock, O., Guichard, F., Boone, A., Roucou, P., and Redelsperger, J.-L. 2010. West African Monsoon water cycle: 1. A hybrid water budget data set. *Journal of Geophysical Research: Atmospheres*, **115**(D19). doi: https://doi.org/10.1029/2010JD013917.

Moncrieff, M. W. 1978. The dynamical structure of two-dimensional steady convection in constant vertical shear. *Quarterly Journal of the Royal Meteorological Society*, **104**(441), 543–567. ISSN 1477870X. doi: 10.1002/qj.49710444102.

Moncrieff, M. W. jan 1981. A theory of organized steady convection and its transport properties. *Quarterly Journal of the Royal Meteorological Society*, **107**(451), 29–50. ISSN 0035-9009. doi: https://doi.org/10.1002/qj.49710745103.

Moncrieff, M. W. 1992. Organized Convective Systems: Archetypal Dynamical Models, Mass and Momentum Flux Theory, and Parametrization. *Quarterly Journal of the Royal Meteorological Society*, **118**(507), 819–850. ISSN 1477870X. doi: 10.1002/qj.49711850703.

Moncrieff, M. W. 2013. The Multiscale Organization of Moist Convection and the Intersection of Weather and Climate. *Climate Dynamics: Why Does Climate Vary*, pages 3–26. doi: 10.1029/2008GM000838.

Moncrieff, M. W. and Green, J. S. 1972. The propagation and transfer properties of steady convective overturning in shear. *Quarterly Journal of the Royal Meteorological Society*, **98**(416), 336–352. ISSN 1477870X. doi: 10.1002/qj.49709841607.

Moncrieff, M. W. and Miller, M. J. apr 1976. The dynamics and simulation of tropical cumulonimbus and squall lines. *Quarterly Journal of the Royal Meteorological Society*, **102**(432), 373–394. ISSN 0035-9009. doi: https://doi.org/10.1002/qj.49710243208.

Moncrieff, M. W., Liu, C., and Bogenschutz, P. 2017. Simulation, modeling, and dynamically based parameterization of organized tropical convection for global climate models. *Journal of the Atmospheric Sciences*, **74**(5), 1363–1380. ISSN 15200469. doi: 10.1175/JAS-D-16-0166.1.

Morrison, H., Curry, J. A., and Khvorostyanov, V. I. 2005. A new double-moment microphysics parameterization for application in cloud and climate models. Part I: Description. *Journal of the Atmospheric Sciences*, **62**(6), 1665–1677. ISSN 00224928. doi: 10.1175/JAS3446.1.

Muetzelfedt, M. R., Plant, R. S., Clark, P. A., Stirling, A. J., and Woolnough, S. J. 2021. A climatology of tropical wind shear produced by clustering wind profiles from a climate model. *Geoscientific Model Development Discussions*, (in review), 1–27. doi: 10.5194/gmd-2020-388. URL `https://gmd.copernicus.org/preprints/gmd-2020-388/`.

Mulholland, J. P., Peters, J. M., and Morrison, H. 2021. How does vertical wind shear influence entrainment in squall lines? *Journal of the Atmospheric Sciences*, **13**(1), 152–154. ISSN 00191035. doi: 10.1016/0019-1035(70)90124-7.

Nicholls, S. D. and Mohr, K. I. 2010. An analysis of the environments of intense convective systems in West Africa in 2003. *Monthly Weather Review*, **138**(10), 3721–3739. ISSN 00270644. doi: 10.1175/2010MWR3321.1.

Normand, C. W. B. 1938. On instability from water vapour. *Quarterly Journal of the Royal Meteorological Society*, **64**(273), 47–70. ISSN 0035-9009.

Ooyama, K. 1969. Numerical Simulation of the Life Cycle of Tropical Cyclones. *Journal of Atmospheric Sciences*, **26**(1), 3–40. doi: 10.1175/1520-0469(1969)026⟨0003: NSOTLC⟩2.0.CO;2.

Orlanski, I. 1976. A simple boundary condition for unbounded hyperbolic flows. *Journal of Computational Physics*, **21**(3), 251–269. ISSN 10902716. doi: 10.1016/0021-9991(76)90023-1.

Panosetti, D., Schlemmer, L., and Schär, C. 2018. Convergence behavior of idealized convection-resolving simulations of summertime deep moist convection over land. *Climate Dynamics*, **55**(1-2), 215–234. ISSN 14320894. doi: 10.1007/s00382-018-4229-9.

Panosetti, D., Schlemmer, L., and Schär, C. 2019. Bulk and structural convergence at convection-resolving scales in real-case simulations of summertime moist convection over land. *Quarterly Journal of the Royal Meteorological Society*, **145**(721), 1427–1443. ISSN 1477870X. doi: 10.1002/qj.3502.

Pante, G. and Knippertz, P. 2019. Resolving Sahelian thunderstorms improves mid-latitude weather forecasts. *Nature Communications*, **10**(1), 1–9. ISSN 20411723. doi: 10.1038/s41467-019-11081-4.

Panthou, G., Vischel, T., and Lebel, T. 2014. Recent trends in the regime of extreme rainfall in the Central Sahel. *International Journal of Climatology*, **34**(15), 3998–4006. ISSN 10970088. doi: 10.1002/joc.3984.

Parker, D. J. and Diop-Kane, M. *Meteorology of tropical West Africa: The forecasters' handbook*. John Wiley & Sons, 2017. ISBN 1118391306. doi: 10.1002/9781118391297.

Parker, D. J., Burton, R. R., Diongue-Niang, A., Ellis, R. J., Felton, M., Taylor, C. M., Thorncroft, C. D., Bessemoulin, P., and Tompkins, A. M. 2005a. The diurnal cycle of the West African monsoon circulation. *Quarterly Journal of the Royal Meteorological Society*, **131**(611), 2839–2860. ISSN 00359009. doi: 10.1256/qj.04.52.

Parker, D. J., Thorncroft, C. D., Burton, R. R., and Diongue-Niang, A. 2005b. Analysis of the African easterly jet, using aircraft observations from the JET2000 experiment. *Quarterly Journal of the Royal Meteorological Society*, **131**(608), 1461–1482. ISSN 00359009. doi: 10.1256/qj.03.189.

Parker, D. J., Fink, A., Janicot, S., Ngamini, J. B., Douglas, M., Afiesimama, E., Agustí-Panareda, A., Beljaars, A., Dide, F., Diedhiou, A., Lebel, T., Polcher, J., Redelspergerk, J. L., Thorncroft, C., and Wilson, G. A. 2008. The Amma radiosonde program and its implications for the future of atmospheric monitoring over Africa. *Bulletin of the American Meteorological Society*, **89**(7), 1015–1027. ISSN 00030007. doi: 10.1175/2008BAMS2436.1.

Parker, M. D. 2008. Response of simulated squall lines to low-level cooling. *Journal of the Atmospheric Sciences*, **65**(4), 1323–1341. ISSN 00224928. doi: 10.1175/2007JAS2507.1.

Parker, M. D. and Johnson, R. H. 2004. Structures and dynamics of quasi-2D mesoscale convective systems. *Journal of the Atmospheric Sciences*, **61**(5), 545–567. ISSN 00224928. doi: 10.1175/1520-0469(2004)061⟨0545:SADOQM⟩2.0.CO;2.

Petch, J. C., Brown, A. R., and Gray, M. E. 2002. The impact of horizontal resolution on the simulations of convective development over land. *Quarterly Journal of the Royal Meteorological Society*, **128**(584 PART B), 2031–2044. ISSN 00359009. doi: 10.1256/003590002320603511.

Peters, K., Hohenegger, C., and Klocke, D. 2019. Different representation of mesoscale convective systems in convection-permitting and convection-parameterizing NWP models and its implications for large-scale forecast evolution. *Atmosphere*, **10**(9), 503. ISSN 20734433. doi: 10.3390/atmos10090503.

Provod, M., Marsham, J. H., Parker, D. J., and Birch, C. E. 2016. A characterization of cold pools in the West African Sahel. *Monthly Weather Review*, **144**(5), 1923–1934. ISSN 15200493. doi: 10.1175/MWR-D-15-0023.1.

Randall, D., Khairoutdinov, M., Arakawa, A., and Grabowski, W. 2003. Breaking the cloud parameterization deadlock. *Bulletin of the American Meteorological Society*, **84**(11), 1547–1564. ISSN 00030007. doi: 10.1175/BAMS-84-11-1547.

Reed, R. J., Norquist, D. C., and Recker, E. E. 1977. The Structure and Properties of African Wave Disturbances as Observed During Phase III of GATE. *Monthly Weather Review*, **105**(3), 317–333. doi: 10.1175/1520-0493(1977)105⟨0317:TSAPOA⟩2.0.CO;2.

Rickenbach, T., Ferreira, R. N., Guy, N., and Williams, E. 2009. Radar-observed squall line propagation and the diurnal cycle of convection in Niamey, Niger, during the 2006 African monsoon and multidisciplinary analyses intensive observing period. *Journal of Geophysical Research Atmospheres*, **114**(3), 1–8. ISSN 01480227. doi: 10.1029/2008JD010871.

Rienecker, M. M., Suarez, M. J., Gelaro, R., Todling, R., Bacmeister, J., Liu, E., Bosilovich, M. G., Schubert, S. D., Takacs, L., Kim, G. K., Bloom, S., Chen, J., Collins, D., Conaty, A., Da Silva, A., Gu, W., Joiner, J., Koster, R. D., Lucchesi, R., Molod, A., Owens, T., Pawson, S., Pegion, P., Redder, C. R., Reichle, R., Robertson, F. R., Ruddick, A. G., Sienkiewicz, M., and Woollen, J. 2011. MERRA: NASA's modern-era retrospective analysis for research and applications. *Journal of Climate*, **24**(14), 3624–3648. ISSN 08948755. doi: 10.1175/JCLI-D-11-00015.1.

Roberts, A. J., Marsham, J. H., and Knippertz, P. 2015. Disagreements in low-Level moisture between (Re)analyses over summertime West Africa. *Monthly Weather Review*, **143**(4), 1193–1211. ISSN 15200493. doi: 10.1175/MWR-D-14-00218.1.

Roberts, A. J., Fletcher, J. K., Groves, J., Marsham, J. H., Parker, D. J., Blyth, A. M., Adefisan, E. A., Ajayi, V. O., Barrette, R., de Coning, E., Dione, C., Diop, A., Foamouhoue, A. K., Gijben, M., Hill, P. G., Lawal, K. A., Mutemi, J., Padi, M., Popoola, T. I., Rípodas, P., Stein, T. H., and Woodhams, B. J. 2021. Nowcasting for Africa: advances, potential and value. *Weather*, pages 1–7. ISSN 14778696. doi: 10.1002/wea.3936.

Rotunno, R., Klemp, J. B., and Weisman, M. L. 1988. A theory for strong, long-lived squall lines. *Journal of the Atmospheric Sciences*, **45**(3), 463–485. ISSN 00224928. doi: 10.1175/1520-0469(1988)045⟨0463:ATFSLL⟩2.0.CO;2.

Rowell, D. P. and Milford, J. R. 1993. On the Generation of African Squall Lines. *Journal of Climate*, **6**(6), 1181–1193. ISSN 08948755. doi: 10.1175/1520-0442(1993) 006⟨1181:OTGOAS⟩2.0.CO;2.

Russell, J. O., Aiyyer, A., White, J. D., and Hannah, W. jan 2017. Revisiting the connection between African Easterly Waves and Atlantic tropical cyclogenesis. *Geophysical Research Letters*, **44**(1), 587–595. ISSN 0094-8276. doi: https://doi.org/10. 1002/2016GL071236. URL https://doi.org/10.1002/2016GL071236.

Savitzky, A. and Golay, M. J. 1964. Smoothing and Differentiation of Data by Simplified Least Squares Procedures. *Analytical Chemistry*, **36**(8), 1627–1639. ISSN 15206882. doi: 10.1021/ac60214a047.

Schultz, D. M., Schumacher, P. N., and Doswell, C. A. 2000. The intricacies of instabilities. *Monthly Weather Review*, **128**(12), 4143–4148. ISSN 00270644. doi: 10.1175/1520-0493(2000)129⟨4143:TIOI⟩2.0.CO;2.

Schumacher, R. S. and Johnson, R. H. 2005. Organization and Environmental Properties of Extreme-Rain-Producing Mesoscale Convective Systems. *Monthly Weather Review*, **133**(4), 961–976. ISSN 00270644. doi: 10.1175/MWR2899.1. URL https://journals.ametsoc.org/view/journals/mwre/133/4/mwr2899.1.xml.

Senior, C. A., Marsham, J. H., Berthou, S., Burgin, L. E., Folwell, S. S., Kendon, E. J., Klein, C. M., Jones, R. G., Mittal, N., Rowell, D. P., Tomassini, L., Vischel, T., Becker, B., Birch, C. E., Crook, J., Dougill, A. J., Finney, D. L., Graham, R. J., Hart, N. C. G., Jack, C. D., Jackson, L. S., James, R., Koelle, B., Misiani, H., Mwalukanga, B., Parker, D. J., Stratton, R. A., Taylor, C. M., Tucker, S. O., Wainwright, C. M., Washington, R., and Willet, M. R. 2021. Convection permitting regional climate change simulations for understanding future climate and informing decision making in Africa. *Bulletin of the American Meteorological Society*, pages 1–46. doi: 10.1175/BAMS-D-20-0020.1.

Serdeczny, O., Adams, S., Baarsch, F., Coumou, D., Robinson, A., Hare, W., Schaeffer, M., Perrette, M., and Reinhardt, J. 2017. Climate change impacts in Sub-Saharan Africa: from physical changes to their social repercussions. *Regional Environmental Change*, **17**(6), 1585–1600. ISSN 1436378X. doi: 10.1007/s10113-015-0910-2.

Sherwood, S. C. 2000. On moist instability. *Monthly Weather Review*, **128**(12), 4139–4142. ISSN 00270644. doi: 10.1175/1520-0493(2000)129⟨4139:OMI⟩2.0.CO;2.

Stensrud, D. J. *Parameterization Schemes: Keys to Understanding Numerical Weather Prediction Models*. Cambridge University Press, 2009 edition, 2007. ISBN 0521865409. doi: 10.1017/cbo9780511812590.

Stephens, G. L., L'Ecuyer, T., Forbes, R., Gettlemen, A., Golaz, J. C., Bodas-Salcedo, A., Suzuki, K., Gabriel, P., and Haynes, J. 2010. Dreary state of precipitation in global models. *Journal of Geophysical Research Atmospheres*, **115**(24). ISSN 01480227. doi: 10.1029/2010JD014532.

Stevens, B. 2005. Atmospheric moist convection. *Annual Review of Earth and Planetary Sciences*, **33**, 605–643. ISSN 00846597. doi: 10.1146/annurev.earth.33.092203.122658.

Stratton, R. A., Senior, C. A., Vosper, S. B., Folwell, S. S., Boutle, I. A., Earnshaw, P. D., Kendon, E., Lock, A. P., Malcolm, A., Manners, J., Morcrette, C. J., Short, C., Stirling, A. J., Taylor, C. M., Tucker, S., Webster, S., and Wilkinson, J. M. 2018. A

Pan-African Convection-Permitting Regional Climate Simulation with the Met Office Unified Model: CP4-Africa. *Journal of Climate*, **31**(9), 3485–3508. doi: 10.1175/JCLI-D-17-0503.1. URL `https://journals.ametsoc.org/view/journals/clim/31/9/jcli-d-17-0503.1.xml`.

Sullivan, P. P., McWilliams, J. C., and Moeng, C. H. 1994. A subgrid-scale model for large-eddy simulation of planetary boundary-layer flows. *Boundary-Layer Meteorology*, **71**(3), 247–276. ISSN 00068314. doi: 10.1007/BF00713741.

Takahashi, H. and Luo, Z. 2012. Where is the level of neutral buoyancy for deep convection? *Geophysical Research Letters*, **39**(15), 1–6. ISSN 00948276. doi: 10.1029/2012GL052638.

Taylor, C. M., Harrisa, P. P., and Parker, D. J. 2010. Impact of soil moisture on the development of a Sahelian mesoscale convective system: A case-study from the AMMA special observing period. *Quarterly Journal of the Royal Meteorological Society*, **136**(SUPPL. 1), 456–470. ISSN 00359009. doi: 10.1002/qj.465.

Taylor, C. M., Birch, C. E., Parker, D. J., Dixon, N., Guichard, F., Nikulin, G., and Lister, G. M. 2013. Modeling soil moisture-precipitation feedback in the Sahel: Importance of spatial scale versus convective parameterization. *Geophysical Research Letters*, **40**(23), 6213–6218. ISSN 00948276. doi: 10.1002/2013GL058511.

Taylor, C. M., Belusic, D., Guichard, F., Parker, D. J., Vischel, T., Bock, O., Harris, P. P., Janicot, S., Klein, C., and Panthou, G. 2017. Frequency of extreme Sahelian storms tripled since 1982 in satellite observations. *Nature*, **544**(7651), 475–478. ISSN 14764687. doi: 10.1038/nature22069.

Taylor, K. E., Stouffer, R. J., and Meehl, G. A. 2012. An overview of CMIP5 and the experiment design. *Bulletin of the American Meteorological Society*, **93**(4), 485–498. ISSN 00030007. doi: 10.1175/BAMS-D-11-00094.1.

Thorncroft, C. and Hodges, K. 2001. African Easterly Wave Variability and Its Relationship to Atlantic Tropical Cyclone Activity. *Journal of Climate*, **14**(6), 1166–1179. doi: 10.1175/1520-0442(2001)014⟨1166:AEWVAI⟩2.0.CO;2.

Thorncroft, C. D. and Blackburn, M. 1999. Maintenance of the African easterly jet. *Quarterly Journal of the Royal Meteorological Society*, **125**(555), 763–786. ISSN 00359009. doi: 10.1002/qj.49712555502.

Thorpe, A. J., Miller, M. J., and Moncrieff, M. W. 1982. Two-dimensional convection in non-constant shear: A model of mid-latitude squall lines. *Quarterly Journal of the Royal Meteorological Society*, **108**(1978), 739–762. ISSN 1477870X. doi: 10.1002/qj.49710845802.

Trenberth, K. E., Stepaniak, D. P., Hurrell, J. W., and Fiorino, M. 2001. Quality of reanalyses in the tropics. *Journal of Climate*, **14**(7), 1499–1510. ISSN 08948755. doi: 10.1175/1520-0442(2001)014⟨1499:QORITT⟩2.0.CO;2.

Trzeciak, T. M., Garcia-Carreras, L., and Marsham, J. H. 2017. Cross-Saharan transport of water vapor via recycled cold pool outflows from moist convection. *Geophysical Research Letters*, **44**(3), 1554–1563. ISSN 19448007. doi: 10.1002/2016GL072108.

Varble, A., Morrison, H., and Zipser, E. 2020. Effects of under-resolved convective dynamics on the evolution of a squall line. *Monthly Weather Review*, **148**(1), 289–311. ISSN 15200493. doi: 10.1175/MWR-D-19-0187.1.

Verrelle, A., Ricard, D., and Lac, C. 2015. Sensitivity of high-resolution idealized simulations of thunderstorms to horizontal resolution and turbulence parametrization. *Quarterly Journal of the Royal Meteorological Society*, **141**(687), 433–448. ISSN 1477870X. doi: 10.1002/qj.2363.

Vizy, E. K. and Cook, K. H. 2012. Mid-twenty-first-century changes in extreme events over northern and tropical Africa. *Journal of Climate*, **25**(17), 5748–5767. ISSN 08948755. doi: 10.1175/JCLI-D-11-00693.1.

Vizy, E. K. and Cook, K. H. 2018. Mesoscale convective systems and nocturnal rainfall over the West African Sahel: role of the Inter-tropical front. *Climate Dynamics*, **50**(1-2), 587–614. ISSN 14320894. doi: 10.1007/s00382-017-3628-7.

Vogel, P., Knippertz, P., Fink, A. H., Schlueter, A., and Gneiting, T. 2018. Skill of global raw and postprocessed ensemble predictions of rainfall over Northern Tropical Africa. *Weather and Forecasting*, **33**(2), 369–388. ISSN 15200434. doi: 10.1175/WAF-D-17-0127.1.

Vogel, P., Knippertz, P., Fink, A. H., Schlueter, A., and Gneiting, T. 2020. Skill of global raw and postprocessed ensemble predictions of rainfall in the tropics. *Weather and Forecasting*, **35**(6), 2367–2385. ISSN 15200434. doi: 10.1175/WAF-D-20-0082.1.

Wang, Y. 2002. An explicit simulation of tropical cyclones with a triply nested movable mesh primitive equation model: TCM3. Part II: Model refinements and sensitivity to cloud microphysics parameterization. *Monthly Weather Review*, **130**(12), 3022–3036. ISSN 00270644. doi: 10.1175/1520-0493(2002)130⟨3022:AESOTC⟩2.0.CO;2.

Weisman, M. L. 1992. The role of convectively generated rear-inflow jets in the evolution of long-lived mesoconvective systems. *Journal of the Atmospheric Sciences*, **49**(19), 1826–1847. ISSN 00224928. doi: 10.1175/1520-0469(1992)049⟨1826:TROCGR⟩2.0.CO;2.

Weisman, M. L. and Klemp, J. B. 1986. Characteristics of Isolated Convective
Storms. *Mesoscale Meteorology and Forecasting*, pages 331–358. doi: 10.1007/
978-1-935704-20-1_15.

Weisman, M. L. and Rotunno, R. 2004. "A theory for strong long-lived squall lines"
revisited. *Journal of the Atmospheric Sciences*, **61**(4), 361–382. ISSN 00224928. doi:
10.1175/1520-0469(2004)061⟨0361:ATFSLS⟩2.0.CO;2.

Weisman, M. L., Klemp, J. B., and Rotunno, R. 1988. Structure and evolution of
numerically simulated squall lines. *Journal of the Atmospheric Sciences*, **45**(14),
1990–2013. ISSN 00224928. doi: 10.1175/1520-0469(1988)045⟨1990:SAEONS⟩2.0.
CO;2.

Weisman, M. L., Skamarock, W. C., and Klemp, J. B. 1997. The resolution dependence
of explicitly modeled convective systems. *Monthly Weather Review*, **125**(4), 527–548.
ISSN 00270644. doi: 10.1175/1520-0493(1997)125⟨0527:TRDOEM⟩2.0.CO;2.

Wilhelmson, R. B. and Ching-Sen Chen. 1982. A simulation of the development of
successive cells along a cold outflow boundary. *Journal of the Atmospheric Sciences*,
39(7), 1466–1483. ISSN 1098-6596. doi: 10.1175/1520-0469(1982)039⟨1466:asotdo⟩
2.0.co;2.

World Health Organisation. Public Health Risk Assessment and Interventions: Flood-
ing disaster Nigeria, November 2012. Technical Report November, World Health
Organisation, 2012.

Wu, M. L. C., Reale, O., Schubert, S. D., Suarez, M. J., Koster, R. D., and Pegion,
P. J. 2009. African easterly jet: Structure and maintenance. *Journal of Climate*, **22**
(17), 4459–4480. ISSN 08948755. doi: 10.1175/2009JCLI2584.1.

Yang, G.-Y. and Slingo, J. 2001. The Diurnal Cycle in the Tropics. *Monthly Weather
Review*, **129**(4), 784–801. ISSN 00270644. doi: 10.1175/1520-0493(2001)129⟨0784:
TDCITT⟩2.0.CO;2.

Zhang, G., Cook, K. H., and Vizy, E. K. 2016. The diurnal cycle of warm season
rainfall over West Africa. Part I: Observational analysis. *Journal of Climate*, **29**(23),
8423–8437. ISSN 08948755. doi: 10.1175/JCLI-D-15-0874.1.

Zipser, E. J. 1977. Mesoscale and Convective-Scale Downdrafts as Distinct Com-
ponents of Squall-Line Structure. *Monthly Weather Review*, **105**(12), 6. doi:
10.1175/1520-0493(1977)105⟨1568:MACDAD⟩2.0.CO;2.

Zipser, E. J., Cecil, D. J., Liu, C., Nesbitt, S. W., and Yorty, D. P. 2006. Where are the most: Intense thunderstorms on Earth? *Bulletin of the American Meteorological Society*, **87**(8), 1057–1071. ISSN 00030007. doi: 10.1175/BAMS-87-8-1057.